WISSENSCHAFTLICHE MITTEILUNGEN

aus dem Institut für Meteorologie der Universität Leipzig

BAND 60

M. Wendisch (Hrsg.)

Meteorologische Arbeiten XXVII

Jahresbericht 2021

UNIVERSITÄT LEIPZIG

Wissenschaftliche Mitteilungen

aus dem
Institut für Meteorologie der Universität Leipzig

ISBN **978-3-9823985-0-1**

Meteorologische Arbeiten (XXVII) und Jahresbericht 2021 des Instituts für Meteorologie der Universität Leipzig

Hrsg.: Manfred Wendisch

Leipzig 2022

Band 60

Wissenschaftliche Mitteilungen aus dem Institut für Meteorologie der Universität Leipzig Bd. 60 (2022)

Schäfer, M., Jha, S. S, M., Ehrlich, A., Jäkel, E., Thoböll, J., Wendisch, M.: Forest albedo in the context of different cloud situations derived from irradiance measurements at the Leipzig floodplain crane - A pilot study 1

Vogl, T., Schimmel, W., Seifert, P., Kalesse-Los, Radenz, M., H., Ansmann, A., Baars, H., Barja, B. , Bühl, J., Engelmann, R., Floutsi, A., Foth, A. , Gong, X., Hajipour, M., Henning, S., Jimenez, C., Ohneiser, K., Stratmann, F., Tatzelt, C., Teisseire, A., Wex, H., Witthuhn, J., Zamorano, F.: The DACAPO-PESO campaign to obtain dynamics, aerosol, cloud and precipitation observations in the pristine environment of the Southern Ocean 9

Vaishnav, R., Jacobi, Ch., Schmölter, E., Berdermann, J., Codrescu, M., Dühnen, H.: The response of the ionospheric peak electron density (NmF2) to solar activity 23

Lonardi, M., Ehrlich, A., Schäfer, M., Thoböll, J., Wendisch, M.: Tethered balloon measurements in Ny-Ålesund 35

Ehrlich, A., Stapf, J., Emmanouilidis, A., Wolf, K., Schäfer, M., Kalesse-Los, H.: Investigating the potential to retrieve cloud droplet number concentration from ship-based measurements of spectral solar radiance during EUREC^4 A 41

Röttenbacher, J., Luebke, A. E., Müller, H., Ehrlich, A., Schäfer, M.Kirbus, B., Wendisch, M. : CIRRUS-HL: Overview of LIM contributions 52

Kandieva, K., Jacobi, Ch., Pogoreltsev, A., Merzlyakov. E.: The sensitivity of the MUAM model to variability of non-orographic gravity wave distributions 65

Mehrdad, S., Sudhakar, D., Jacobi, C.: Analyzing the sensitivity of large scale circulation to the regional radiation forcing over Europe using deep learning . 78

Dipu, S., Quaas J.: Exploring aerosol-cloud interaction in Southeast Pacific marine stratocumulus during VOCALS regional experiment 92

Linke, O., Quaas, J.: Variation of cloud horizontal sizes and cloud fraction over Europe 1985–2018 in high-resolution satellite data 106

Jahresbericht des Instituts für Meteorologie 2021 119

Projekte 119
Publikationen 163
Mitgliedschaften in Gremien, Redaktionskollegien 172
Mitarbeitende 174

Anzahl Studierende 176
Abschlussarbeiten 177
Ausgaben 179

Forest albedo in the context of different cloud situations derived from irradiance measurements at the Leipzig floodplain crane - A pilot study

Schäfer, M.[1,✉], **Jha, S. S.**[1], **Ehrlich, A.**[1], **Jäkel, E.**[1], **Thoböll, J.**[1]
Wendisch, M.[1]

[1] *Leipzig Institute for Meteorology, University of Leipzig, Leipzig, Germany*
✉*e-mail: michael.schaefer@uni-leipzig.de*

Summary: The surface albedo significantly modulates the atmospheric energy budget and, thus, vertical radiation, energy, and mass fluxes. Therefore, it regulates the local and regional effects of climate warming. Over a forest canopy, the surface albedo mainly depends on the seasonal leaf state. Furthermore, for certain surface types, such as snow, it has been shown that the surface albedo changes as a function of cloudiness. A similar effect is expected over forest surfaces, leading to complex feedback loops between forest surfaces and climate. To investigate these processes, a pilot study was performed at the Leipzig floodplain crane to observe the forest canopy albedo under different atmospheric conditions in 2021. First analyses revealed a dependency of the forest albedo from the cloud state, which is slightly stronger in the near-infrared wavelength range compared to the visible wavelength range.

Zusammenfassung: Der atmosphärische Strahlungshaushalt und damit auch die vertikale Strahlungsverteilung, Energie- und Massenflüsse werden signifikant durch die Bodenalbedo gesteuert. Diese regulieren somit lokale und regionale Effekte der Klimaerwärmung. Über einem Wald hängt die Bodenalbedo hauptsächlich vom saisonalen Blattstatus ab. Zudem wurde für bestimmte Bodentypen wie Schneeoberflächen gezeigt, dass die Bodenalbedo eine Funktion der Bewölkung ist. Ähnlicher Effekte werden für Waldoberflächen erwartet, welche zu komplexen Rückkopplungseffekten zwischen Waldoberflächen und dem Klima führen. Um diese Prozesse zu untersuchen wurde im Jahr 2021 eine Vorstudie am Leipziger Auwaldkran durchgeführt, um die Waldalbedo unter verschiedenen atmosphärischen Bedingungen zu beobachten. Erste Analysen zeigen, dass auch die Albedo des Waldes von den Bewölkungsbedingungen abhängt. Der Effekt ist dabei etwas stärker im nah-infrarotem als im sichtbaren Wellenlängenbereich zu beobachten.

1 Introduction

The surface albedo strongly modulates the atmospheric energy budget and, thus, vertical radiation, energy, and mass fluxes. Therefore, it can regulate the local and regional effects of climate warming (e.g. Davin et al., 2014; Kala and Hirsch, 2020). Over a forest canopy, the surface albedo mainly depends on the leaf state, which changes with meteorological seasons. However, also extreme weather conditions such as droughts or

floods influence the leaf state (leaf orientation, e.g., Yanagy and Costa, 2011), the aerosol production (e.g., BVOC emissions, Mentel et al., 2013) and, therefore, the surface albedo on a shorter time scale, which in turn feeds back to the energy budget.

Furthermore, for certain surface types, such as snow, it has been shown that the surface albedo changes as a function of cloudiness (Gardner and Sharp, 2010; Stapf et al., 2020). This is important because the modification of the spectral distribution of solar irradiance by clouds can significantly modify the broadband albedo (Gardner and Sharp, 2010). An increased liquid water path in the atmosphere leads to higher absorption of the downward irradiance in the near-infrared wavelength range, which results in an increased surface broadband albedo. Furthermore, in case of clouds, the direct and diffuse components of the downward irradiance are redistributed to a predominant diffuse component, which further increases the potential for absorption within the near-infrared wavelength range insight clouds. If a similar effect could be demonstrated over forest surfaces, potential feedback loops between forest surfaces and climate would be much more complex.

Assuming, a future climate will be characterized by an increased number of extreme events with longer periods of either cloud-free or cloudy conditions (droughts, extended winter inversion), these differences of the surface albedo are key to better understand possible feedbacks on the local energy budget and vertical exchange of energy, mass, and momentum. Such feedbacks may buffer or even amplify the stable meteorological conditions of extreme periods. However, forests may directly react on extreme weather events by a changing forest-canopy albedo, which needs to be decoupled from the cloud-albedo effect. Furthermore, forest reactions like pollen expectoration, biogenic emissions, and new particle formation are expected in such cases. Depending on the energy budget, turbulent mass fluxes will then redistribute the biogenic aerosol and lead to an exchange with the boundary layer above the canopy where aerosol particles may become relevant as cloud condensation nuclei, which opens another biogenic-atmospheric feedback mechanism.

To investigate if similar effects can be found over a forest like it is discussed by Gardner and Sharp (2010) or Stapf et al. (2020) for Arctic conditions, a pilot study has been performed at the Leipzig floodplain crane in the summer of 2021 to observe the forest albedo under different atmospheric conditions. Spectral irradiance measurements have been obtained at a fixed location at the top of the crane from which the spectral albedo was derived. The cloudiness was characterized by daily observations.

Here, we will give a brief introduction of the pilot study, including descriptions of the measurement site and instrumentation in Sect. 2. Preliminary results from the measurements are discussed in Sect. 3. Subsequently, the potential of this instrument setup to study albedo-vegetation interactions will be evaluated and used to identify gaps in the instrumentation, which have to be filled in future studies.

2 Measurement site and instrumentation

2.1 Leipzig floodplain crane

The following information within this section on the history and specifications of the Leipzig floodplain crane are taken from https://www.auwaldstation.de. The Leipzig floodplain crane (Ger. Leipziger Auwaldkran, LAK) was installed under supervision

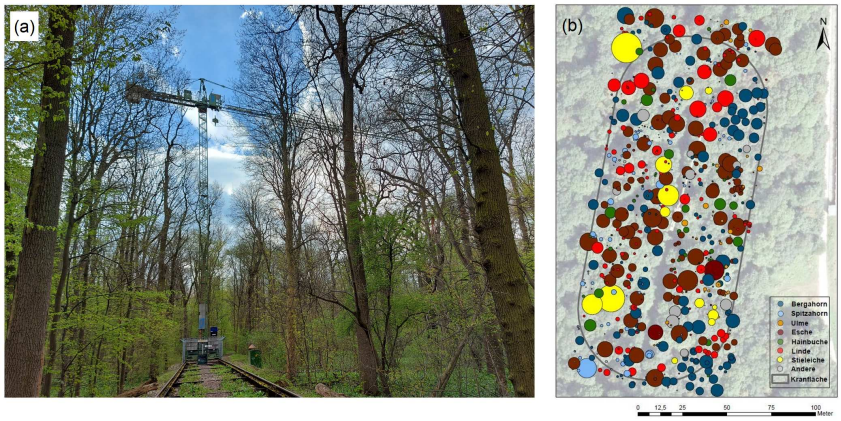

Fig. 1: ***(a)*** *Photo of the Leipzig floodplain crane taken on 29 April 2021.* ***(b)*** *Overview of the distribution and size of the different species in the area that can be reached by the gondola of the Leipzig floodplain crane. Graphic by Ronny Richter, iDIV, https://www.auwaldstation.de/projekte/beobachtungsplattform/der-leipziger-auwaldkran-und-aktuelle-baumkronenforschung/.*

of Prof. Wilfried Morawetz in March 2001. It is located within the Leipzig floodplain north-west of Leipzig, slightly south-west of the Leipzig Auensee at 51.36° N and 12.31° E. After a heavy damage during the century flood in the year 2013, it was reconstructed by the research center iDiv of the German Research Foundation (Deutsche Forschungsgemeinschaft, DFG) under supervision of Prof. Christian Wirth. Figure 1a shows a recent photo of the Leipzig floodplaine crane taken on 29 April 2021.

The floodplaine crane reaches 40 m in altitude with a 45 m long crane boom. A gondola is installed at the crane boom to reach the tree tops. The crane itself is installed on rails and can be moved along a horizontal distance of about 120 m. Therefore, tree tops in an oval area of 210 m length and 90 m width can be reached. This includes 800 trees of different species. Figure 1b shows an overview of the distribution and size of the different species in the area that can be reached by the gondola. These species include the common ash (Fraxinus excelsior), the pedunculate oak (Quercus robur), sycamore maple (Acer pseudoplatanus), Norway maple (Acer platanoides), small-leaved lime (Tilia cordata), and hornbeam (Carpinus betulus).

2.2 Spectral irradiance measurement system

To investigate the spectral albedo at the Leipzig floodplain crane it is planned to develop a new measurement system including measurements of the up-and downward spectral irradiance in the visible and near-infrared wavelength range and measurements of the broadband up- and downward irradiance in the solar and terrestrial wavelength range. The system shall be completed by an all-sky imager.

However, to clarify the needs for such a new measurement system with respect to, e.g., sensitivity, power consumption, or installation, the pilot study was performed with the existing COmpact RAdiation Measurement System (CORAS, Brückner et al., 2014), which initially was designed for non-autonomous field studies.

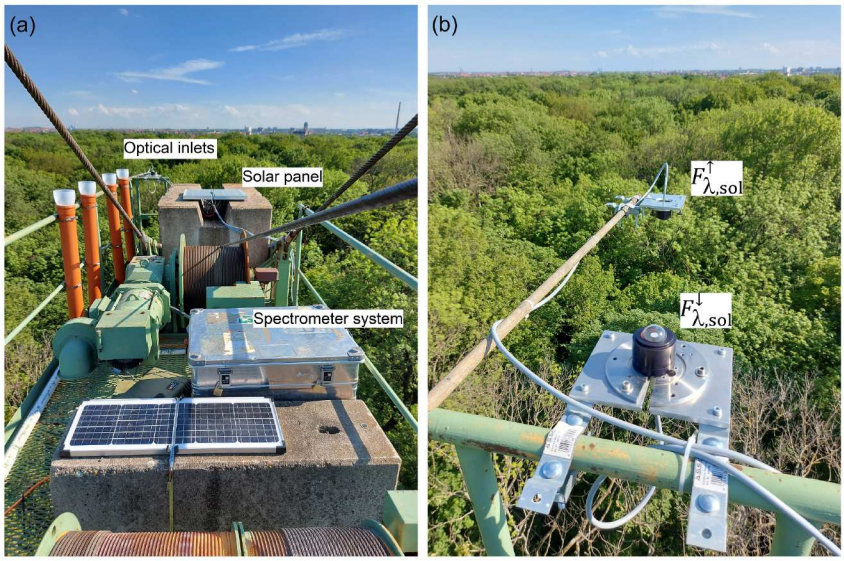

Fig. 2: Photos of the ***(a)*** *spectral irradiance measurement system on the platform of the Leipzig floodplain crane and* ***(b)*** *the up- and downward facing optical irradiance inlets.*

CORAS is a ground–based version of the albedometer introduced by Wendisch et al. (2001), which was designed as a modular system to measure spectral radiometric quantities from airborne platforms. The instrumentation setup installed on the tail platform of the Leipzig floodplain crane is illustrated in Fig. 2. The main parts are the spectrometers and data acquisition installed in a weatherproof box, the optical irradiance inlets, which are connected by optical fibres to the spectrometers, and the power supply, which is realized by a solar panel and batteries.

Two up- and downward–facing optical inlets collect down- and upward irradiance ($F^{\downarrow}_{\lambda}$, $F^{\uparrow}_{\lambda}$). The collected radiation from the inlets is transferred via two bifurcated optical fibers to the spectrometer system. The fibres are isolated with a specific synthetic material adjusted to humid conditions (Brückner et al., 2014).

CORAS consists of four grating spectrometers; per optical inlet one sensitive to the visible and near-infrared wavelength range (VNIR, $\lambda = 400 - 1000$ nm) and one sensitive to the shortwave-infrared wavelength range (SWIR, $\lambda = 1000 - 2200$ nm). The incoming radiation is spectrally dispersed by a grating and detected by a single–line photo-diode array. Data acquisition from CORAS is realized with one computer in a sequential order.

3 Measurements

The pilot study was carried out from 2 June 2021 to 15 December 2021. However, due to the high power consumption of CORAS (120 W) and no permanent power supply at the crane, it was not possible to perform measurements over a full daily cycle each day. Therefore, the daily measurement time was reduced to one hour starting at noon. The rest of the daytime was used to recharge the main battery (400 Wh) by a 200 W solar panel. However, if overcast conditions prevailed for several days, the solar panel did not provide sufficient power to recharge the main battery, which led to data loss for single days. To buffer such cases, the batteries were manually recharged and exchanged weekly. Especially at the end of the measurement period (November, December) with

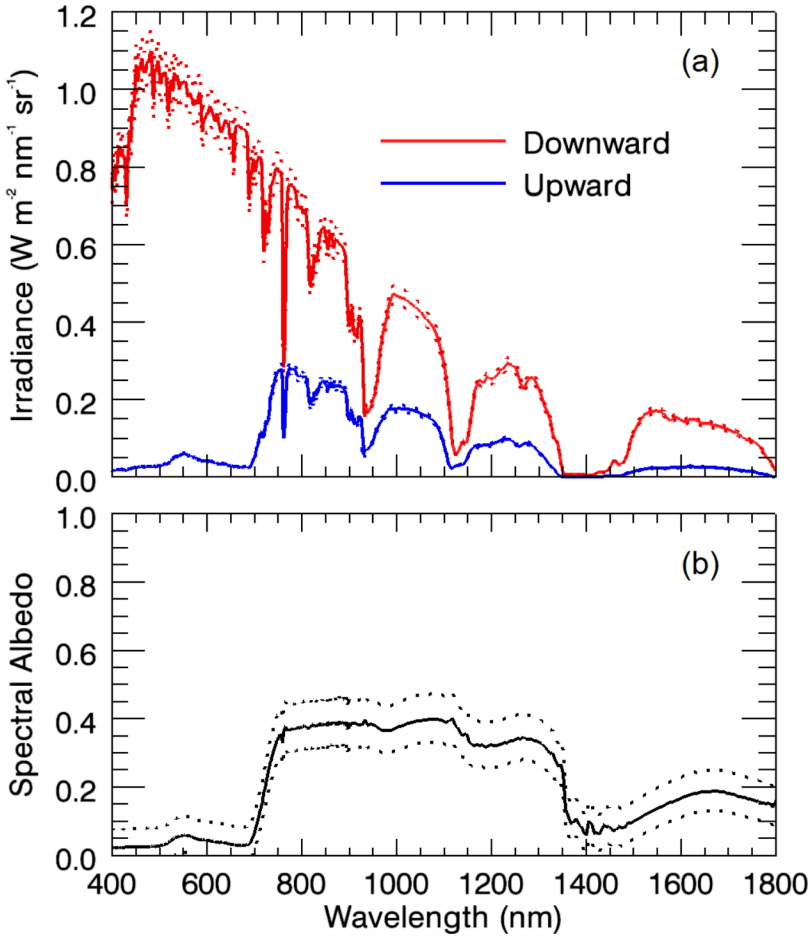

Fig. 3: ***(a)*** *Spectral up- (blue) and downward (red) irradiance measured at the Leipzig floodplain crane on 2 June 2021, 12:00 local time, 32° solar zenith angle.* ***(b)*** *Spectral albedo derived from spectral irradiance displayed in (a). Dotted lines represent measurement uncertainties.*

low Sun conditions the number of data gaps increased. However, for the full period of measurements, irradiance data on 51 different days were collected.

3.1 Spectral irradiance and albedo

Figure 3a shows example measurements of the spectral downward (red) and upward (blue) irradiance. While the shape of the downward measured irradiance spectrum is mainly influenced by atmospheric absorption bands, the upward irradiance is clearly shaped by the imprint of vegetation features. It shows low irradiance below 700 nm followed by the steep vegetation step.

The spectral albedo calculated from the upward and the downward irradiance is displayed in Fig. 3b. For values up to about 700 nm the albedo shows the same behaviour like the upward irradiance, starting with low values at small wavelengths followed by the steep vegetation step. However, for the wavelength range between 800 nm and 1300 nm the influence of the atmospheric absorption bands almost vanishes.

However, the main focus of the pilot study was to investigate, if a dependency of the forest albedo on the presence of clouds can be identified. For this, a first test is

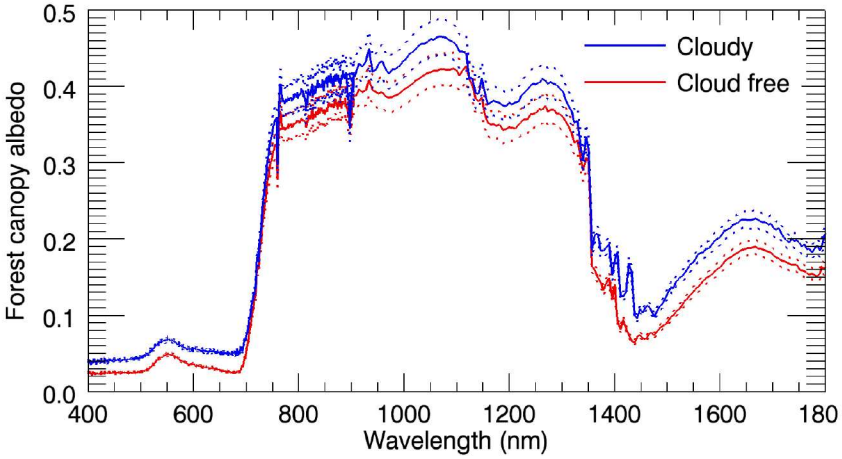

Fig. 4: ***(a)*** *Spectral albedo measured during cloud-free conditions on 9 September 2021 (red) and during overcast conditions on 10 September 2021 (blue) at 12:00 local time, 48° solar zenith angle. Dotted lines represent measurement uncertainties.*

performed by comparing the spectral albedo for the two extreme cases of fully cloud-free and fully cloudy conditions. The particular times were identified manually. One important requirement for the comparison was that these two cases appeared in close temporal collocation to avoid large differences of solar zenith angle, atmospheric and forest conditions. A further requirement was that the crane was located at the same position on the rail with equal horizontal orientation of its boom to observe the same part of the forest canopy in both cases. Several of these combinations were found.

Figure 4 shows a selected case with cloud-free measurements performed on 9 September 2021 and overcast conditions measured on 10 September 2021. In general, larger albedo was observed in the cloudy case compared to the cloud-free case. A more detailed spectral comparison reveals differences in the albedo spectra of 0.02 in the visible wavelength range to up to 0.05 in the near-infrared wavelength range. The broadband albedo is 0.17 for the cloud-free case and increased to 0.2 for the cloudy case. Similar differences were found for the other identified cases, while the differences were negligible for inter-comparisons of cloud-free measurements or cloudy measurements only.

Although the presented measurement case is still based on preliminary results and need further evaluation, it already implies a good potential of the measurements at the Leipzig floodplain crane.

3.2 Temporal variation of the forest canopy albedo

At the moment only data of one hour per day with an increasing number of data gaps until the end of the period exist. However, to gain statistical significance and to consider also cloud fractions in between the maxima of overcast and cloud-free conditions, a time series of the whole measurement period was analyzed.

Since the cloudiness at the site was not recorded automatically, the cloud fraction data for the following analysis were taken from satellite observations with Sentinel 5P. An advantage of this method is that the cloud fraction is then also available with high resolution in decimal values between 0 (cloud free) and 1 (cloudy).

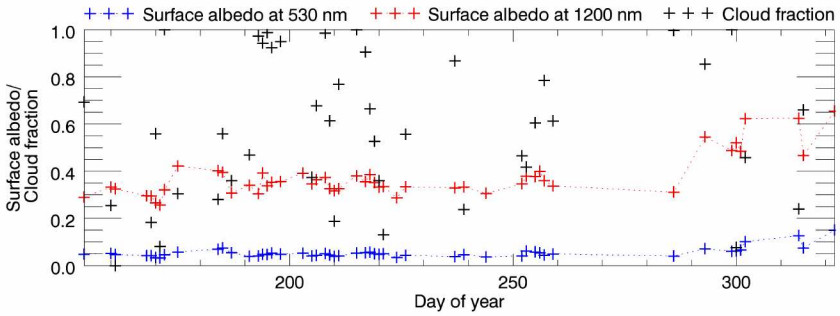

*Fig. 5: **(a)** Time series of forest canopy albedo at 530 nm (blue) and 1200 nm (red) measured with CORAS at 12:00 local time and mean cloud fraction (black) observed by Sentinel 5P in the time period from June to November 2021.*

Figure 5 shows the forest canopy albedo observed by CORAS at 530 nm (blue crosses) and at 1200 nm (red crosses) and the cloud fraction observed by Sentinel 5P (black crosses) during the whole period of the pilot study. The forest canopy albedo is fluctuating around a rather constant average value over most of the measurement period until it is rising while approaching the end of the measurement period. This increase of the forest canopy albedo at the end of the measurement period is related to the change of the vegetation structure from a state of trees with many healthy green leaves via a time when the leaves turn yellow until the trees have lost almost all their leaves.

However, besides this increase of the forest canopy albedo at the end of the measurement phase, the forest canopy albedo shows constant fluctuations around a mean value. These fluctuations are most likely related to changes in the cloudiness. Comparing the time series of the averaged broadband albedo with the time series of the mean cloud fraction indicates a slight correlation. In both time series, when the averaged broadband albedo has a peak to higher values, often also in the mean cloud fraction a peak with higher values is observed. For minima in the albedo values it behaves vice versa. This hints to a measurable dependency of the forest canopy albedo from the state of cloudiness and is worth to be analysed by a longer time series with measurements during a full daily cycle.

4 Summary and conclusions

To investigate the forest canopy albedo as a function of the cloudiness, it is planned to develop a new measurement system including measurements of the up-and downward spectral irradiance in the visible and near-infrared wavelength range and measurements of the broadband up- and downward irradiance in the solar and terrestrial wavelength range. The system shall be completed by an all-sky imager. However, to clarify the needs for such a new measurement system with respect to, e.g., sensitivity, power supply, or installation, a pilot study was performed at the Leipzig floodplain crane to observe the forest canopy albedo under different atmospheric conditions in the year 2021. For this pilot study, measurements at a fixed location at the top of the crane including irradiance observations were performed with the existing COmpact RAdiation measurement System (CORAS).

First analysis reveal a similar behaviour of the forest canopy albedo like it was described by Gardner and Sharp (2010) or Stapf et al. (2020) for Arctic surfaces; an increasing cloudiness leads to a higher surface albedo compared to the cloud-free state. For the measurements at the Leipzig floodplain crane this was demonstrated by comparing albedo spectra of both cases; cloud-free and cloudy conditions. Furthermore, it was shown that the time series of the forest canopy albedo and cloud fraction hints to such a dependency, although the variations in the forest canopy albedo need to be disentangled from seasonal variations.

However, the findings within this study are based on a preliminary analysis using a dataset with only one hour measurement time per day. A more comprehensive data set including complementary measurements to characterize cloud properties are required to quantify the interaction between clouds and vegetation. It needs to be a system, which covers a full daily cycle of irradiance measurements with high temporal resolution. Furthermore, the system must be able to automatically record the state of cloudiness in parallel and to allow the retrieval of the cloud microphysical properties from measurements of the transmitted radiation. Such a new system is currently in planning and might be operational by the end of 2022. As soon as it is established the continuously gathered data will allow to parameterize the forest canopy albedo as a function of the cloud state.

Acknowledgements: Special thanks to Ronny Richter, Tom Künne, and Julia Behrens for their always great support at the measurement site.

References

Brückner, M., Pospichal, B., Macke, A., and Wendisch, M.: A new multispectral cloud retrieval method for ship-based solar transmissivity measurements, J. Geophys. Res., 119, 11.338–11.354, 2014.

Davin, E., Seneviratne, S., Ciais, P., Olioso, A., and Wang, T.: Preferential cooling of hot extremes from cropland albedo management, Proc. Natl. Acad. Sci. Unit. States Am., 111, 9757–9761, 2014.

Gardner, A. S. and Sharp, M. J.: A review of snow and ice albedo and the development of a new physically based broadband albedo parameterization, J. Geophys. Res., 115, F01 009, doi:10.1029/2009JF001444, 2010.

Kala, J. and Hirsch, A. L.: Could crop albedo modification reduce regional warming over Australia?, Weather and Climate Extremes, 30, 100 282, doi:10.1016/j.wace.2020.100282, 2020.

Mentel, T. F., Kleist, E., Andres, S., et al.: Secondary aerosol formation from stress-induced biogenic emissions and possible climate feedbacks, Atmos. Chem. Phys., 13, 8755–8770, 2013.

Stapf, J., Ehrlich, A., Jäkel, E., Lüpkes, C., and Wendisch, M.: Reassessment of shortwave surface cloud radiative forcing in the Arctic: consideration of surface-albedo–cloud interactions, Atmos. Chem. Phys., 20, 9895–9914, doi:10.1038/s41586-018-0555-7, 2020.

Wendisch, M., Müller, D., Schell, D., and Heintzenberg, J.: An airborne spectral albedometer with active horizontal stabilization, J. Atmos. Oceanic Technol., 18, 1856–1866, 2001.

Yanagy, S. N. M. and Costa, M. H.: Modeling radiative transfer in tropical rainforest canopies: sensitivity of simulated albedo to canopy architectural and optical parameters, An. Acad. Bras. Ciênc., 83, 9895–9914, doi:10.1590/S0001-37652011000400010, 2011.

The DACAPO-PESO campaign: Dynamics, Aerosol, Cloud and Precipitation Observations in the Pristine Environment of the Southern Ocean – an overview

Vogl, T.[1,✉], Schimmel, W.[1], Seifert, P.[2], Kalesse-Los, H.[1], Radenz, M.[2] Ansmann, A.[2], Baars, H.[2], Barja, B.[3], Bühl, J.[2], Engelmann, R.[2], Floutsi, A.[2], Foth, A.[1], Gong, X.[2], Hajipour, M.[2], Henning, S.[2], Jimenez, C.[2], Ohneiser, K.[2], Stratmann, F.[2], Tatzelt, C.[2], Teisseire, A.[2], Wex, H.[2], Witthuhn, J.[1], Zamorano, F.[3]

[1] *University of Leipzig, Leipzig Institute for Meteorology LIM, Leipzig, Germany*
[2] *Leibniz Institute for Tropospheric Research (TROPOS) Leipzig, Germany*
[3] *University of Magallanes, Atmospheric Research Laboratory LIA-UMAG, Punta Arenas, Chile*
✉*e-mail: teresa.vogl@uni-leipzig.de*

Summary: This article gives an overview of the DACAPO-PESO field experiment, which has taken place in Punta Arenas, Chile, from November 2018 to November 2021, and showcases first exciting research results that have already emerged from it.

Zusammenfassung: In diesem Artikel wird ein Überblick über das DACAPO-PESO Experiment gegeben, welches von November 2018 bis November 2021 in Punta Arenas, Chile, stattgefunden hat. Außerdem werden erste spannende Forschungsergebnisse vorgestellt, die bereits daraus gewonnen wurden.

1 Introduction

Punta Arenas, Chile (53°S, 71°W), is located at the southern tip of South America, in the Southern hemispheric mid-latitudinal west wind zone (Fig. 1). With the nearest landmasses (New Zealand) having a distance of roughly 8,000 km towards the direction of the prevailing Westerly winds, the aerosol conditions are dominated by clean Pacific Ocean air masses. Therefore, Punta Arenas as a clean and pristine place in all atmospheric heights is especially well-suited for comparison of atmospheric processes in more aerosol-polluted places in the Northern Hemisphere.
Furthermore, given the general lack of high-quality long-term ground-based remote sensing observations of aerosols and clouds in this region, mainly due to the absence of substantial land masses below 40°S latitude, measurements in the Southern mid-latitudes are extremely useful for better understanding aerosol-cloud-precipitation interactions. For example, the Southern midlatitudes and Sub-Antarctica are a region of large uncertainties in estimates of cloud properties in global climate models, because the supercooled liquid water (SLW) content is underestimated, causing shortwave radiation biases (e.g. Kay et al., 2016). Increasing the SLW content in the models improves these biases, but the reason why parameterizations valid for the Northern Hemisphere are seemingly not

applicable to the Southern Hemisphere is unclear. Aerosol-cloud-interaction and clouds in general still make up the largest uncertainty in climate models (Forster et al., 2021), and it is well known that the number of ice nucleating particles (INPs) varies strongly across Northern and Southern hemispheres (e.g. Gong et al., 2020).

Motivated by the need for an improved process understanding and the current lack of

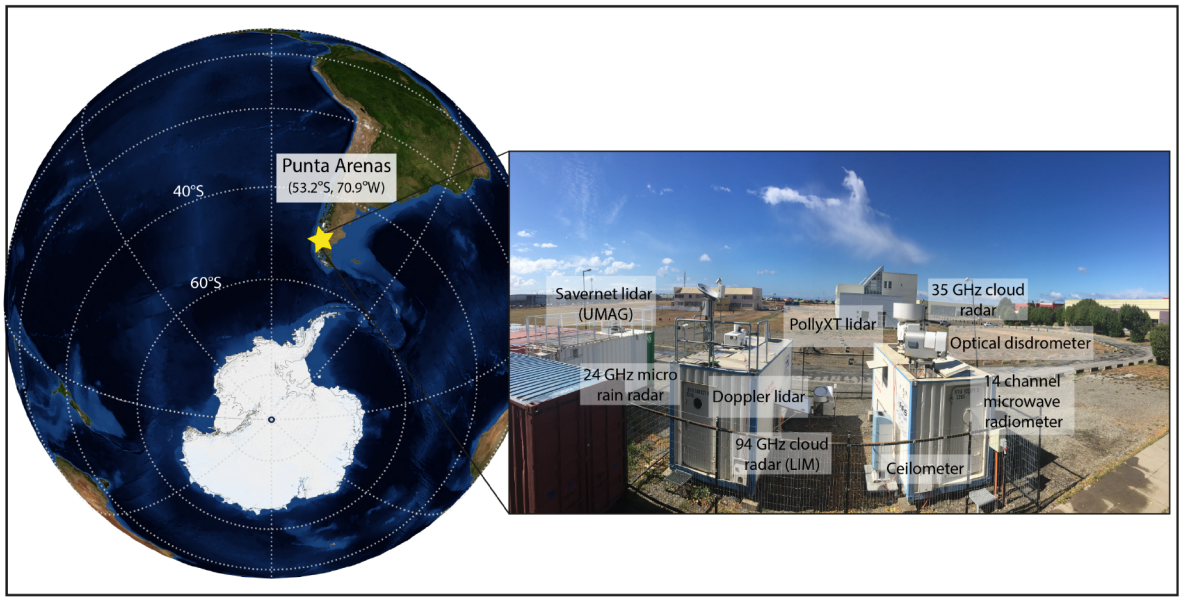

Figure 1: *The location of Punta Arenas on the globe (indicated by a yellow star) in Chile, South America, and the LACROS observational facility, which was enhanced by instruments by the Leipzig Institute for Meteorology (LIM) and the University of Magallanes (UMAG). Figure 1 from Floutsi et al. (2021).*

high-quality continuous aerosol-cloud-precipitation datasets for the Southern Ocean region, the project DACAPO-PESO (Dynamics, Aerosol, Cloud and Precipitation Observations in the Pristine Environment of the Southern Ocean) was realized by Leibniz Institute of Tropospheric Research (TROPOS), Leipzig, Germany and partners from University of Leipzig and University of Magallanes, Punta Arenas, Chile (http://dacapo.tropos.de). In the frame of this project, a large suite of remote sensing and in-situ instruments has been deployed over a period of more than two years in Punta Arenas. This article will give an overview of the field experiment and showcase some research highlights that have already emerged from it.

2 Instrumentation deployed during the DACAPO-PESO field experiment

In the frame of DACAPO-PESO, the Leipzig Aerosol and Cloud Remote Observations System (LACROS) has been operated on the campus of University of Magallanes (53°S, 71°W) in the 3-year period from austral spring of 2018 to austral spring 2021. LACROS comprises a set of state-of-the-art remote-sensing instruments such as a 35-GHz scanning polarimetric cloud radar, multi-wavelength polarization Raman lidars, Doppler lidar, micro rain radar, microwave radiometer, laser disdrometer, as well as sensors for direct and diffuse solar and terrestrial radiation. Until

September 2019, LACROS was enhanced by a 94-GHz Doppler radar of University of Leipzig. A picture of the site can be seen in Fig. 1. In addition, the TROPOS mobile radiation observatory (MORDOR; https://www.tropos.de/en/research/projects-infrastructures-technology/technology-at-tropos/remote-sensing/radiation-measurement-station-bsrn last access: 2022-04-29) performed radiation measurements during the LACROS deployment. The global horizontal irradiance (GHI), diffuse horzontal irradiance (DHI) and direct horizontal irradiance (DNI) were measured with Class A instruments of the type MS-80 (pyranometer) and MS-56 (pyrheliometer), respectively, from the manufacturer EKO Instruments. The measurement uncertainty under clear skies for this class of pyranometers and pyrheliometers was about 2 % (Fountoulakis et al., 2021).
In-situ aerosol instrumentation was installed on the 620-m high peak of Cerror Mirador mountain, 10 km upwind of the LACROS site. At Cerror Mirardor, particle number size distributions in the range from 10 nm to 10 μm were measured using a TROPOS-type mobility particle size spectrometer (MPSS) Wiedensohler et al., 2012 and an aerodynamic particle sizer. Cloud condensation nuclei (CCN) number concentrations at supersaturations (SS) of 0.1 %, 0.2 %, 0.3 %, 0.5 %, and 0.7 % are measured utilizing a CCN counter. In addition, filter samples were collected from 8 May 2019 to 11 March 2020. These filter samples were used for subsequent laboratory measurements of INPs (see Gong et al., 2022 for details).

3 Research highlights

3.1 Evaluation of the Aeolus winds at Punta Arenas using scanning Doppler cloud radar and radio soundings

Aeolus is an Earth Explorer mission of the European Space Agency and aims to measure vertically resolved wind profiles of one wind component (mainly west-east direction) with the goal to improve numerical weather prediction. It is the first European satellite mission having a lidar on-board and the first space mission ever utilizing a HSRL Doppler lidar. Thus, intensive validation efforts are needed – especially in remote places like in Southern South America.
Next to many other instruments, the scanning Doppler cloud radar MIRA-35 was deployed as part of LACROS during DACAPO-PESO. After intensive algorithm development, horizontal winds could be derived from the Velocity-Azimuth-Display (VAD) cloud radar scans performed every 60 minutes in cloudy regions above the measurement site as schematically shown in Fig. 2. These wind products could then be used to validate the *Aeolus* wind products during the two weekly overpasses and delivered valuable input for the algorithm and instrument developers of *Aeolus*. The wind profiles for the overpass indicated in Fig. 2 are shown in Fig. 3. Furthermore, occasional radiosondes have been launched once a week since the beginning of 2020 for the direct evaluation of *Aeolus* winds and to cross-check the radar-derived horizontal winds. From Fig. 3. one can see that a good agreement between the observations is found at the top of the cloud layer and in the local boundary layer showing the great capabilities of Aeolus. For some atmospheric regions in clear sky, for which also no ground-based Doppler observations and no Aeolus Mie winds are available, sporadic offsets of the Aeolus Rayleigh winds in

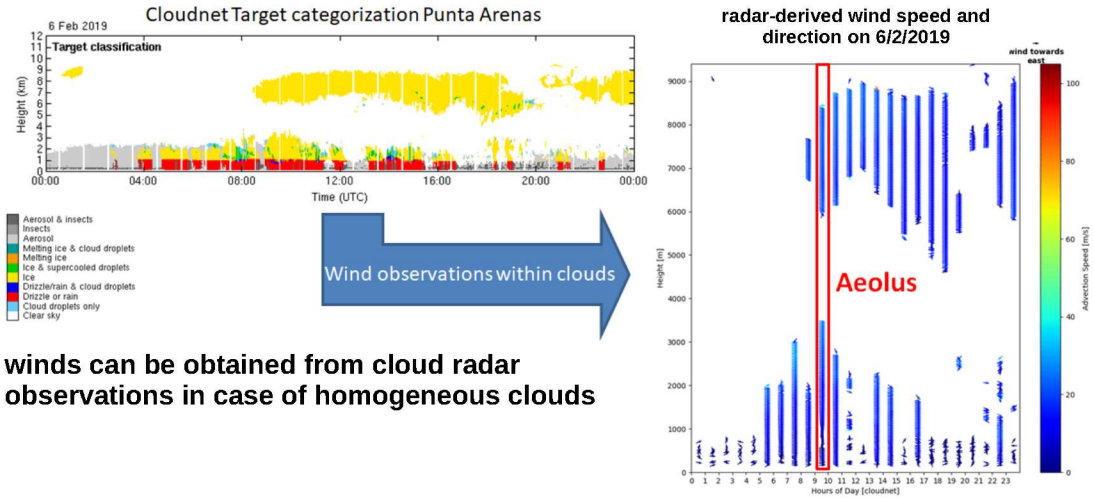

Figure 2: *Sketch for the retrieval of vertical profiles of the horizontal wind vector from scanning Doppler cloud radar. Left, top: Cloudnet Target classification for 6 February 2019. In regions of cloud or precipitation occurrence, e.g. yellow (ice) or red (drizzle), wind speed from radar velocity-azimuth display (VAD) scans can be derived, as shown in the right panel: Cloud radar derived horizontal wind vector for the same day. The overpass time of (satellite) Aeolus is indicated as well.*

comparison to the model data is detected. The reasons for this mismatch are still under investigation.

In general, a good agreement between Aeolus and cloud radar was found, considering the uncertainties of Aeolus and the distance between the two measurement (57 km). Long-term studies have shown that the systematic error is low with the most recent Aeolus algorithms and thus provide proof that space-borne wind profiling is possible and valuable. The radar-derived winds were found to agree very well with the radiosonde winds and thus give confidence for the reliability of this methodology.

3.2 Advection of biomass burning aerosols towards Punta Arenas

During the first 14 months of the DACAPO-PESO campaign, lofted aerosol layers were observed occasionally in the generally clean free troposphere above Punta Arenas. Two events were studied and presented in detail in Floutsi et al. (2021), based on observations from the multiwavelength Raman lidar PollyXT. The lidar observations in combination with a HYSPLIT backward trajectory analysis allowed the identification of the observed aerosol. In the first case (4 and 5 February 2019), the lofted aerosol layers originated from Central and Central-South Chile, and were identified as smoke layers mixed with soil dust, while in the second case (11 March 2019), several geometrically and optically thin smoke layers were observed after long-range transport from Australia. The smoke advection from Central and Central-South Chile affected significantly the available CCN and INP in the lower troposphere. Both CCN and INP concentrations were higher than usual for the first case, and likely contributed to the characteristics of an ice cloud that

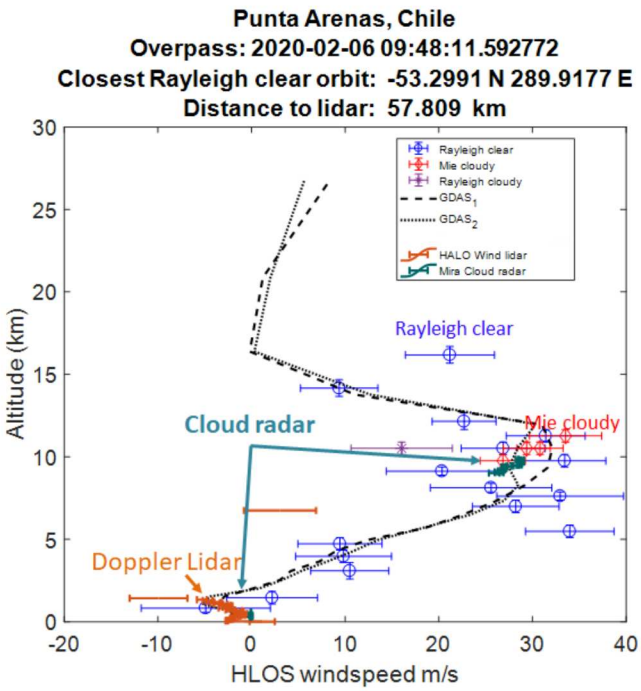

Figure 3: *Comparison of the Aeolus-derived horizontal line-of-sight (HLOS) wind speedto the ones derived from scanning Doppler cloud radar (turquoise) and Doppler lidar(brownish). For Aeolus, wind derived in clear sky regions with the so-called Rayleightechnology (blue) as well as in clouds with the so-called Mie technology (red) andRayleigh one (purple) are shown. For comparison, winds form the Global Data AssimilationSystem (GDAS) are presented, too. A good agreement between the observations is found at the top of the cloud layer and in the local boundary layer showing the great capabilities of Aeolus. For some atmospheric regions in clear sky, for which also no ground-based Doppler observations and no Aeolus Mie winds are available, sporadic offsets of the Aeolus Rayleigh winds in comparison to the model data is detected. The reasons for this mismatch are still under investigation.*

was observed only a couple of hours later. In addition, smoke particles advected from Australia at high altitudes were found to likely facilitate the formation of ice crystals. A long-term analysis of the occurrence of lofted layers was also performed, and, similarly to the ALPACA campaign (i.e. the "Aerosol Lidar Measurement at Punta Arenas in the Frame of Chilean–German Cooperation" which had taken place in Punta Arenas in October 2009, Foth et al., 2019), it was found that lofted aerosol layers in the troposphere were observed more frequently than expected during 2019.

3.3 Australian wildfire smoke in the stratosphere over Punta Arenas during DACAPO-PESO: the decay phase in 2020/21 and impact on ozone depletion

Record-breaking wildfires raged in South-Eastern Australia in late December 2019 and early January 2020 (Ohneiser et al., 2020, 2022). Rather strong pyrocumulonimbus (pyroCb) convection developed over the fire areas and lifted enormous amounts of biomass-burning smoke into the tropopause region. They caused the strongest wildfire-related stratospheric aerosol perturbation ever observed around the globe. The multiwavelength

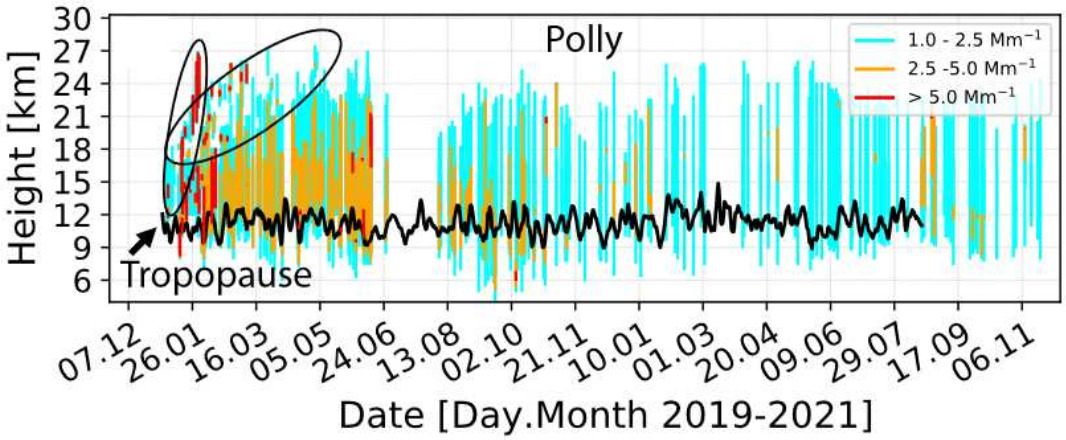

Figure 4: *Overview of Polly XT observations of the UTLS smoke layers (colored bars from layer base to top, one bar per day) from 15 November 2019 to 15 November 2021. Black ellipses indicate the smoke layers showing a fast ascent.*

polarization Raman lidar Polly-XT, which is part of LACROS, was used to monitor this major record-breaking event until the end of 2021. A unique dynamical feature, an anticyclonic, smoke-filled vortex with 1000 km horizontal width and 5 km vertical extent, which ascended by about 500 m per day, was observed over the full last week of January 2020. The key results of the long-term study are as follows: The smoke layers extended, on average, from 9 to 24 km in height. The smoke partly ascended to more than 30 km height as a result of self-lifting processes. Clear signs of a smoke impact on the record-breaking ozone hole over Antarctica in September–November 2020 were found. A slow decay of the stratospheric perturbation detected by means of the 532 nm aerosol optical thickness (AOT) yielded an e-folding decay time of 19–20 months. The maximum upper tropospheric lower stratospheric (UTLS) smoke AOT was around 1.0 over Punta Arenas in January 2020 and thus two to three orders of magnitude above the stratospheric aerosol background of 0.005. After two months with strongly varying smoke conditions, the 532 nm UTLS AOT decreased to 0.03–0.06 from March–December 2020 and to 0.015–0.03 throughout 2021. The particle extinction coefficients were in the range of 10–75 Mm^{-1} in January 2020, and later on mostly between 1 and 5 Mm^{-1} (Fig. 4). Combined lidar-photometer retrievals revealed typical smoke extinction-to-backscatter ratios of 69 ± 19 sr (at 355 nm), 91 ± 17 sr (at 532 nm), and 120 ± 22 sr (at 1064 nm). An ozone reduction of 20–25 % in the 15–22 km height range was observed over Antarctic and New Zealand-based ozonesonde stations in the smoke-polluted air. This smoke-ozone anti-correlation was potentially caused by an enhanced formation of ozone-depleting polar stratospheric clouds on the additional smoke-related particle surface area of 1-5 μm^2 cm^{-3}.

3.4 Ground-based aerosol characterization, including CCN at Cerror Mirardor

In order to gain knowledge on the annual cycle of aerosol particle and CCN number concentrations and the hypothesized seasonality of their sources, long-term in-situ observations at Cerra Mirardor mountain station were carried out. These measurements are also of values for ground truthing the remote sensing observations and retrievals.

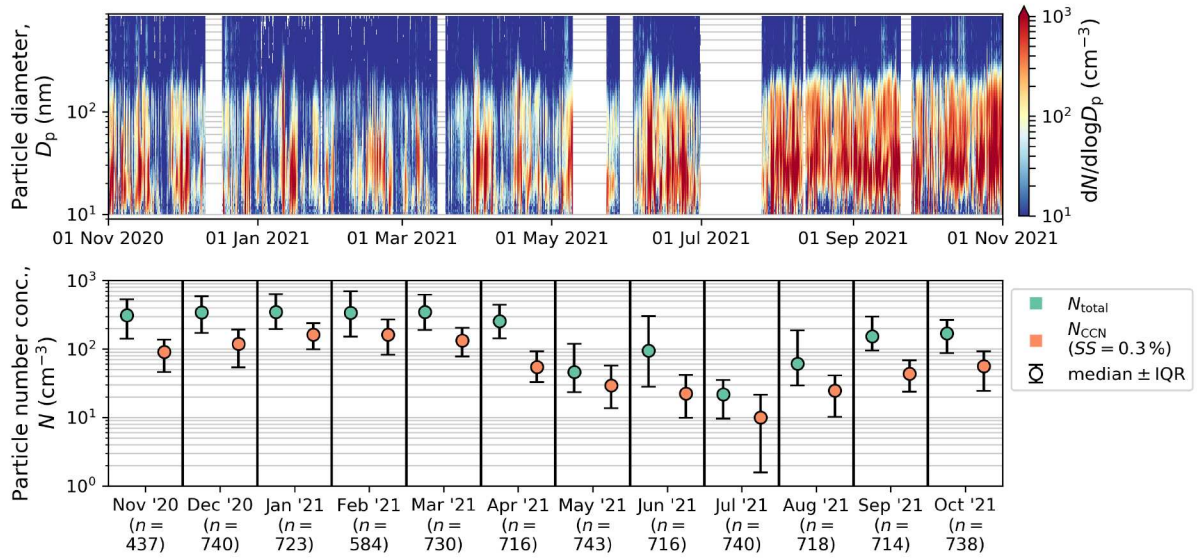

Figure 5: *Top panel: Time series of the particle number size distribution (PNSD) measured at the top of Cerror Mirador between November 2020 and November 2021. Gaps in the PNSD data are due to the instrumentation being unavailable. In the lower panel, monthly averages of the PNSD-derived Ntotal (green) and the CCN number concentration (N_{CCN}) at a 0.3 % SS (orange) are given as median values and their respective inter-quartile ranges (IQR). The number of averaged values, n, is given in the lower panel for reference.*

Particle number size distribution measurements were performed with a combination of a Mobility Particle Size Spectrometer (homebuilt TROPOS) and an Aerodynamic Particle Sizer (APS 3321,TSI, MN, USA) in a particle size range 10 nm to 10000 nm along with the total number concentration (CPC-3772, TSI, MN, USA). The CCN number concentration (CCN-100, DMT, Boulder, USA) was measured at five supersaturation steps.

Atmospheric aerosol particles are important for their radiative effects in the atmosphere, and for their role in the formation of droplets and primary ice in clouds. Total particle number concentrations (N_{total}) were measured at Cerro Mirador with combined measurements from a TROPOS-type MPSS (mobility particle size spectrometer, Wiedensohler et al. (2012), using a concensation particle counter CPC, model 3772, TSI Inc.) and an APS (aerodynamic particle sizer, model 3321, TSI Inc.). CCN were measured using a CCN-counter (model CCN-100, DMT Inc.). More information can be found in Gong et al. (2022). For the measurement period between November 2020 and November 2021, both N_{total} and the CCN number concentration at a SS of 0.3 % ($N_{CCN,\ 0.3}$) covered roughly 2 orders of magnitude when taking the natural variability (indicated by the errorbars in Fig. 5) into consideration. The lowest monthly median values ($N_{total} \approx 20$ cm^{-3} and $N_{CCN,\ 0.3} \approx 10$ cm^{-3}) were found for July 2021, coinciding with the end of the Southern hemispheric winter (May–July). In contrast, concentrations during the summer months (December–February) were roughly one order of magnitude higher ($N_{total} \approx 200$ cm^{-3} and $N_{CCN,\ 0.3} \approx 100$ cm^{-3}).

3.5 A strong continental source of ice-nucleating particles (INPs) at Cerror Mirardor

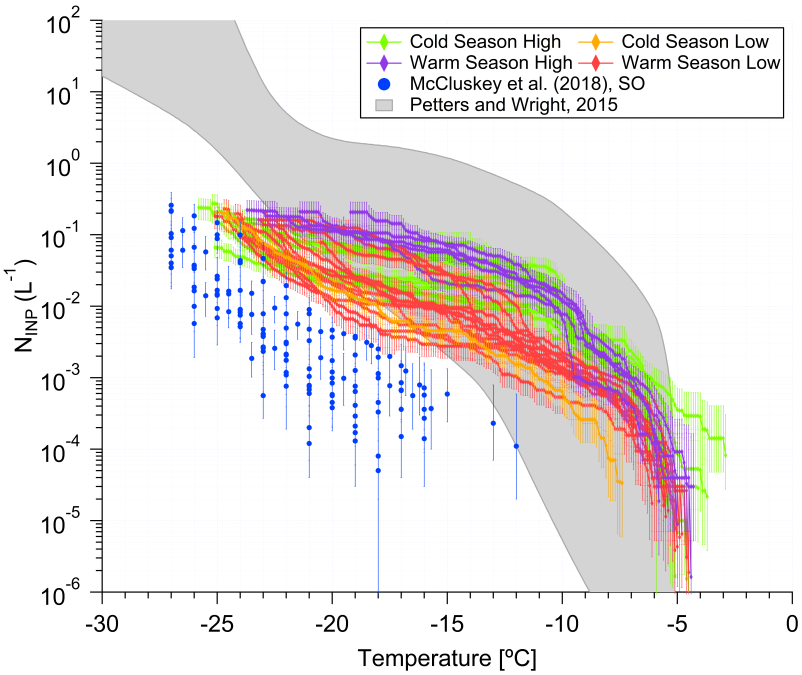

Figure 6: *Spectra of INP concentrations for all examined samples are shown, with the color coding indicating that there were high and low values throughout the year. The gray background shows typical midlatitude continental concentrations, while the blue dots show typical data from the Southern Ocean (SO), free of continental sources.*

INP are important as they are responsible for the formation of primary ice in clouds, and with this they influence cloud radiative processes and the formation or precipitation. To obtain INP concentrations, filter samples were collected at Cerro Mirador, and evaluated off-line at TROPOS, using well proven cold-stages (Gong et al., 2022). At the Cerror Mirardor mountain station, Gong et al. (2022) found unexpectedly high INP number concentrations, comparable to typical continental values, without an annual cycle, but with the typically observed high variability over roughly two orders of magnitude at any freezing temperature (Fig. 6). A large fraction of > 80 % (median value) of all INP was biogenic in nature (for freezing temperatures above -16 °C). An INP parameterization developed for a forest ecosystem (Tobo et al., 2013) was best able to describe the measured data, with 50 % of the predicted INP concentrations within a factor of two of the measured values, but further large deviations of roughly up to plus or minus one order of magnitude. In order to find an explanation for times with high INP concentrations, a range of parameters was investigated, including aerosol parameters and meteorological conditions and air mass back-trajectories. Precipitation was the only parameter which might explain the presence of high INP concentrations because rain drops can disperse bio-aerosol from the soil and from plants into the atmosphere. A comparison with lidar data from the boundary layer showed that particle number concentrations for particles with diameters larger than 500 nm agreed well when continental conditions were assumed in the lidar retrieval. This in turn means that reasonable INP concentrations for the

boundary layer may be obtained based on these lidar data and the above mentioned INP parameterization.

3.6 Hemispheric contrasts in stratiform mixed-phase cloud properties observed with LACROS

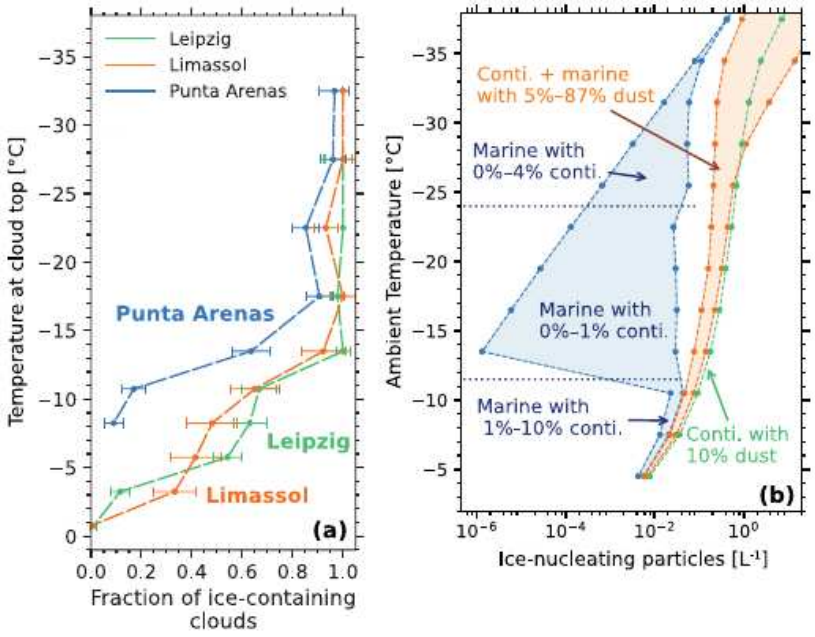

Figure 7: *(a) Fraction of clouds containing ice at a given cloud-top temperature for three different locations: Leipzig (green), Limassol (orange) and Punta Arenas (blue). Only free-tropospheric and turbulent clouds are shown after filtering out gravity wave clouds and boundary layer coupling. (b) Estimated profiles of INP concentrations based on averaged lidar optical data, airmass source and well-established INP parameterizations. At Punta Arenas (blue), the strong increase of INP concentrations for T warmer than -10° C is related to high boundary layer aerosol concentrations.*

The synergistic Cloudnet dataset obtained from the multi-year LACROS observations at Punta Arenas is used to investigate hemispheric contrasts of ice formation in supercooled stratiform clouds. At Punta Arenas, the fraction of ice-containing clouds for a given cloud-top temperature was found to be lower than at two Northern Hemispheric stations (Leipzig, Germany and Limassol, Cyprus) as shown in Fig 7. The low frequency of ice-forming clouds at Punta Arenas at temperatures colder than -15° C can in part be related to orographic gravitiy waves, which create areas of persistent saturation with respect to liquid in the updraft regions. Ice crystals in turn are only observable in the downwind regions. These wave clouds could be identified using the autocorrelation function of the vertical air velocity within the clouds (Radenz et al., 2021). Wave-driven clouds were identified in 30 % of all considered clouds colder than -15° C for the DACAPO-PESO data set. Furthermore, a correlation was found between the surface-coupling of the cloud and the occurrence of ice formation: If a cloud was coupled to the aerosol-laden boundary layer, the probability of ice formation was higher by a fraction of 0.3 to 0.4. Still, even if both gravity wave and boundary layer effects were taken into

account, the probability of ice formation is smaller in clouds over Punta Arenas than for their Northern-hemispheric counterparts (Fig. 7a). This difference is likely related to the lower abundance of INPs in the free troposphere over Punta Arenas.

3.7 Deriving supercooled liquid water beyond lidar attenuation from vertically-pointing cloud radar observations using artificial neural networks

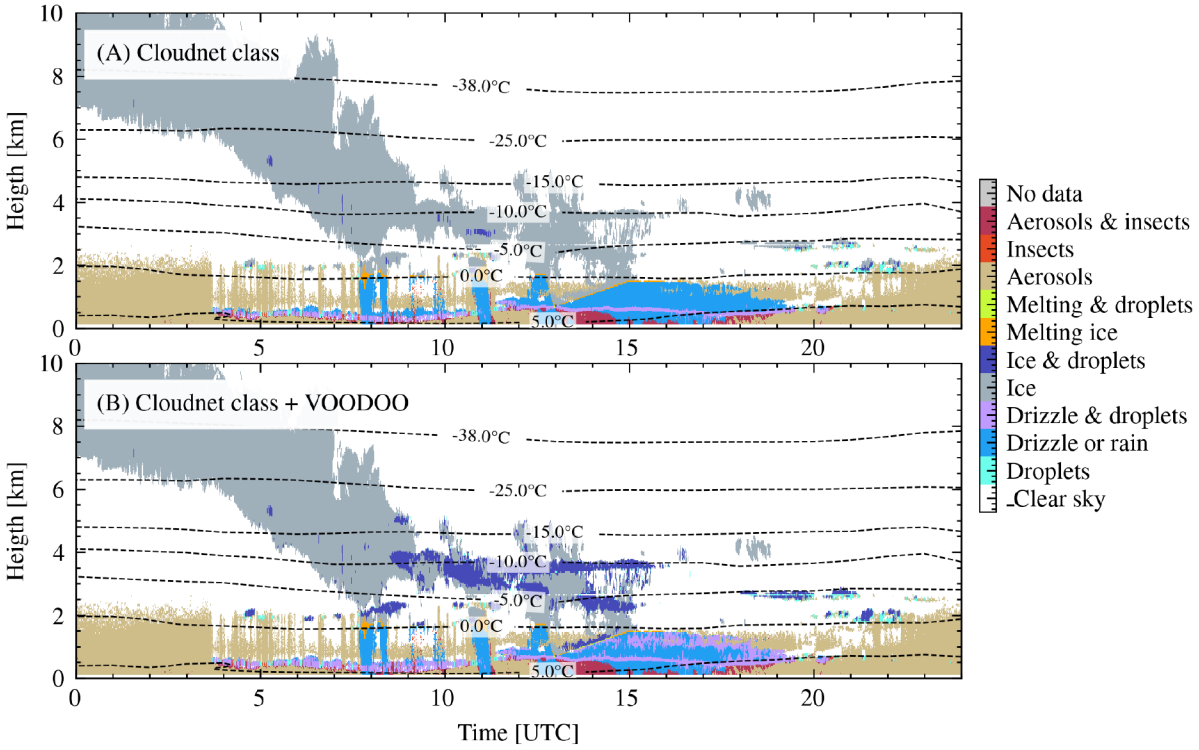

Figure 8: *Example of Cloudnet target classification (top). The lidar was attenuated by the low level liquid cloud at 500 m, (class:Drizzle & rain). VOODOO machine-learning technique (bottom). VOODOO is augmenting the liquid detection of Cloudnet and is able to predict multiple liquid layers between 1 – 4 km altitude (dark blue). Observations were made on 13 March, 2019 in Punta Arenas, Chile.*

The DACAPO-PESO data set was used to develop a novel tool to compute the likelihood for the presence of cloud droplets (CD) using ground-based radar measurements from RPG-FMCW-94-DP Doppler cloud radar, Jenoptik CHM15kx ceilometer, RPG-HATPRO-G2 microwave radiometer and weather model data from the European Centre for Medium-Range Weather Forecasts (ECMWF). Data sets of vertically-pointing Doppler cloud radars and lidars provide insights into cloud properties at high temporal and spatial resolution. However, the identification of liquid CD usually relies on lidar observations, which suffer from complete attenuation at an approximate optical thickness of $\tau > 3$. Since cloud radars can penetrate multiple liquid layers, they can potentially be used to expand the identification of cloud phase to the entire vertical column beyond the lidar signal attenuation height. VOODOO (reVealing supercOOled liquiD beyOnd lidar attenuatiOn) is a deep convolutional neural network (CNN) approach, which uses Doppler radar spectra as input to directly compute the likelihood for the presence of CD at

each data point. VOODOO utilizes concepts of computer vision to relate morphologies in a series of multiple consecutive radar Doppler spectra to the presence of CD. The optimization was done by supervised learning using the Cloudnet target classification (Illingworth et al., 2007) in regions where both radar and lidar signals are available as a-priori ground-truth. Validation was done on suitable case studies as well as long-term observations from two locations, Punta Arenas, Chile (Radenz et al., 2021) and Leipzig, Germany. The PyTorch implementation is freely-available via Zenodo (Schimmel, 2022) and the VOODOO technique is described in detail in Schimmel et al. (2022).

The deep learning approach VOODOO overcomes the issue of droplet underestimation in mixed-phase clouds caused by complete lidar signal attenuation. VOODOO has the potential to drastically improve the hydrometeor phase classification, as displayed in Fig. 8 which shows that VOODOO was able to identify multiple additional mixed-phase layers between 1 and 4 km . The planned fusion of Cloudnet and VOODOO will surely benefit further cloud microphysical and radiative retrievals and thus the cloud remote-sensing community in general.

3.8 Development of a novel machine-learning-based riming retrieval

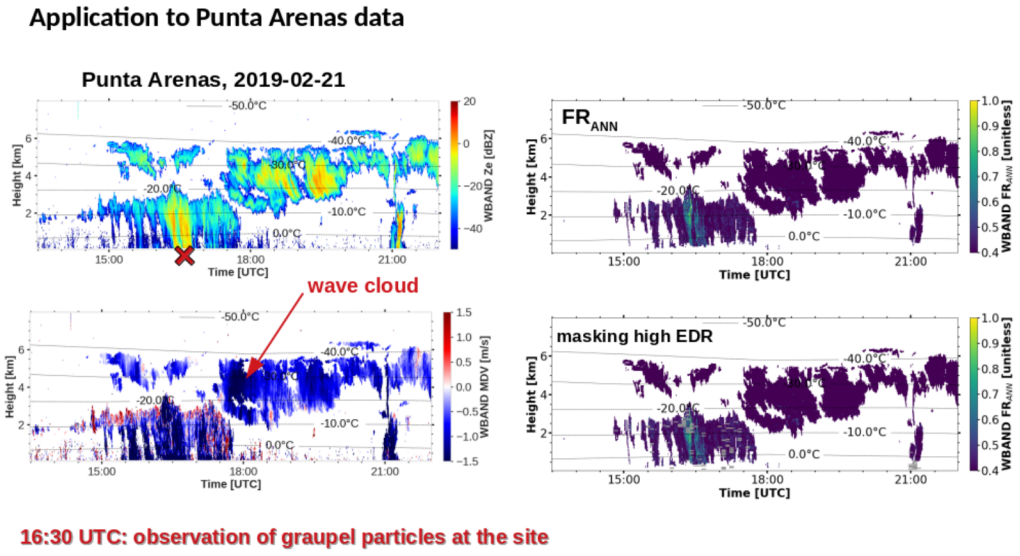

Figure 9: *Radar moments measured by the 94 GHz radar and ANN predictions of riming during a case observed on 21 February 2019: Top left panel shows the equivalent radar reflectivity in dBZ, bottom left panel the mean Doppler velocity. The right-hand panels show the rime fraction FR_{ANN} predicted by the ANN: Top panels shows the raw prediction, and the bottom panel the predictions when pixels with high turbulent eddy dissipation rate (EDR) are masked (grey dashes). The red cross marks the time (16:30 UTC) when graupel particles were observed at the site.*

Riming, i.e. the accretion and freezing of supercooled liquid water (SLW) on ice particles in mixed-phase clouds, is an important pathway for precipitation formation. During this process, droplets of SLW collide with ice hydrometeors and freeze upon contact to the ice surface. This leads to the formation of graupel and hail particles.

Detecting and quantifying riming using ground-based cloud radar observations is of great interest, and the data set acquired during DACAPO-PESO was used to develop and test a method that works even in orographically influenced cloud systems: Artificial neural networks (ANNs) were used to predict riming using ground-based zenith-pointing cloud radar variables as input features. More details on the method can be found in Vogl et al. (2022).
Fig. 9 shows a case study observed on 21 February 2019. A precipitating cloud system with cloud top around 2.5 to 3 km is present from around 15 to 18 UTC. Above, a mid-level cloud with top around 6 km and varying cloud base is observed. At 16:30 UTC, marked by the red cross in Fig. 9, graupel particles were observed at the ground on-site. The predicted rime mass fraction FR_{ANN} maximum is reached around 16:30 UTC, coinciding with the observation of graupel particles. This signal is persistent even if observation points with high turbulent eddy dissipation rate, which masks fingerprints of riming in the cloud radar observations, are excluded.

3.9 Development of a new method to derive the vertical distribution of particle shape

Advancement of the understanding of mixed-phase clouds requires knowledge of microphysical ice growth processes. The transition from pristine to aggregated or rimed particles is a key process in the growth of hydrometeors. A new approach was developed by Teisseire et al. (2022) that uses polarimetric variables from the scanning polarimetric cloud radar MIRA-35, which is part of LACROS, in the 45° slated linear depolarization configuration, to derive the vertical distribution of particle shape (VDPS) between top and base of mixed-phase cloud systems.
The polarimetric parameter SLDR was selected for this study due to its strong sensitivity to shape and low sensitivity to the wobbling effect of particles at different antenna elevation angles. For the VDPS method, elevation scans from 90° to 30° elevation angle were deployed to estimate the vertical profile of the particle shape by means of the polarizability ratio, which is a measure of the density-weighted axis ratio. Results were obtained by retrieving the best fit between observed SLDR-vs-elevation dependencies and respected values simulated with a spheroid scattering model. The applicability of the new method is demonstrated by case studies of isometric, columnar and oblate hydrometeor shapes, which were obtained from measurements during DACAPO-PESO at Punta Arenas. The identified hydrometeor shapes are demonstrated to fit well to the cloud and thermodynamic conditions which prevailed at the times of observations. The VDPS results reveal that the shape gradient ranges in general from a pristine columnar or dendritic state at cloud top toward a more isometric shape at cloud base. Either aggregation or riming processes contribute to this vertical change of microphysical properties. The new height-resolved identification of hydrometeor shape and its gradient is a helpful tool to understand complex processes such as riming or aggregation, which occur particularly in mixed-phase clouds.

4 Summary and conclusions

The DACAPO-PESO data set offers the great opportunity to comprehensibly study aerosol-cloud-precipitation interactions in a unique location in the Southern hemispheric mid-latitudes. As shown, many exciting research results have already been published or are well on the way to be published soon. The following studies were conducted. During DACAPO-PESO, lofted layers of long-range transported smoke were occasionally observed in the clean free troposphere of Punta Arenas. In this study, two events of smoke originating from regional sources in South America and from Australia were captured by the PollyXT lidar and discussed in detail. The in-situ aerosol measurements revealed a strong seasonal cycle (ratio winter/summer 1/10) with in general significantly lower values compared to middle Europe. Continental biological aerosol, the aerosolization of which is most likely driven by raindrops, is the main source of highly ice active INPs in the southernmost Patagonia regions. Regarding contrasts in shallow supercooled clouds, a frequently occurring liquid-only clouds could be attributed to updrafts in gravity waves. When excluding these clouds, a slightly higher frequency of ice-containing clouds in the northern hemisphere can be linked to a higher abundance of ice-nucleating particles. Finally, we show that machine learning techniques can be used to improve current state-of-the-art multi-sensor remote-sensing retrievals in determining the amount and location of mixed-phase cloud volumes and are well suited to retrieve the rime mass fraction form Doppler radar data.

References

Floutsi, A. A., Baars, H., Radenz, M., et al.: Advection of Biomass Burning Aerosols towards the Southern Hemispheric Mid-Latitude Station of Punta Arenas as Observed with Multiwavelength Polarization Raman Lidar, Remote Sens., 13, doi:10.3390/rs13010138, 2021.

Forster, P., Storelvmo, T., Armour, K., et al.: The Earth's energy budget, climate feedbacks and climate sensitivity, in: Climate Change 2021: The Physical Science Basis. Contribution of Working Group I to the Sixth Assessment Report of the Intergouvernmental Panel on Climate Change, edited by Masson-Delmotte, V., Zhwi, P., Pirani, A., et al., Camebridge University Press, 2021.

Foth, A., Kanitz, T., Engelmann, R., et al.: Vertical aerosol distribution in the southern hemispheric midlatitudes as observed with lidar in Punta Arenas, Chile (53.2° S and 70.9° W), during ALPACA, Atmos. Chem. Phys., 19, 6217–6233, doi:10.5194/acp-19-6217-2019, 2019.

Fountoulakis, I., Kosmopoulos, P., Papachristopoulou, K., et al.: Effects of Aerosols and Clouds on the Levels of Surface Solar Radiation and Solar Energy in Cyprus, Remote Sens., 13, doi:10.3390/rs13122319, 2021.

Gong, X., Wex, H., van Pinxteren, M., et al.: Characterization of aerosol particles at Cabo Verde close to sea level and at the cloud level – Part 2: Ice-nucleating particles in air, cloud and seawater, Atmos. Chem. Phys., 20, 1451–1468, doi:10.5194/acp-20-1451-2020, 2020.

Gong, X., Radenz, M., Wex, H., et al.: Significant continental source of ice-nucleating particles at the tip of Chile's southernmost Patagonia region, Atmos. Chem. Phys. Discuss., 2022, 1–29, doi:10.5194/acp-2022-71, 2022.

Illingworth, A. J., Hogan, R. J., O'Connor, E., et al.: Cloudnet: Continuous Evaluation of Cloud Profiles in Seven Operational Models Using Ground-Based Observations, B. Am. Meteorol. Soc., 88, 883–898, doi:10.1175/BAMS-88-6-883, 2007.

Kay, J. E., Bourdages, L., Miller, N. B., et al.: Evaluating and improving cloud phase in the Community Atmosphere Model version 5 using spaceborne lidar observations, J. Geophys. Res. Atmos., 121, 4162–4176, doi:10.1002/2015jd024699, 2016.

Ohneiser, K., Ansmann, A., Baars, H., et al.: Smoke of extreme Australian bushfires observed in the

stratosphere over Punta Arenas, Chile, in January 2020: optical thickness, lidar ratios, and depolarization ratios at 355 and 532 nm, Atmos. Chem. Phys., 20, 8003–8015, doi:10.5194/acp-20-8003-2020, 2020.

Ohneiser, K., Ansmann, A., Kaifler, B., et al.: Australian wildfire smoke in the stratosphere: the decay phase in 2020/21 and impact on ozone depletion, Atmos. Chem. Phys. Discuss., 2022, 1–41, doi:10.5194/acp-2021-1097, 2022.

Radenz, M., Bühl, J., Seifert, P., et al.: Hemispheric contrasts in ice formation in stratiform mixed-phase clouds: Disentangling the role of aerosol and dynamics with ground-based remote sensing, Atmospheric Chemistry and Physics Discussions, 2021, 1–34, doi:10.5194/acp-2021-360, 2021.

Schimmel, W.: pyLARDA3 v0.1, doi:10.5281/zenodo.5970206, 2022.

Schimmel, W., Kalesse-Los, H., Maahn, M., et al.: Identifying cloud droplets beyond lidar attenuation from vertically-pointing cloud radar observations using artificial neural networks, Atmos. Meas. Tech. Discuss., 2022, 1–35, doi:10.5194/amt-2022-149, 2022.

Teisseire, A., Seifert, P., Bühl, J., and Radenz, M.: Determination of the vertical distribution of in-cloud particle shape using SLDR-mode 35-GHz scanning cloud radar, in prep. for Atmos. Meas. Tech. Discuss., 2022.

Tobo, Y., Prenni, A. J., DeMott, P. J., et al.: Biological aerosol particles as a key determinant of ice nuclei populations in a forest ecosystem, J. Geophys. Res. Atmos., 118, 10,100–10,110, doi:https://doi.org/10.1002/jgrd.50801, 2013.

Vogl, T., Maahn, M., Kneifel, S., et al.: Using artificial neural networks to predict riming from Doppler cloud radar observations, Atmos. Meas. Tech., 15, 365–381, doi:10.5194/amt-15-365-2022, 2022.

Wiedensohler, A., Birmili, W., Nowak, A., et al.: Mobility particle size spectrometers: harmonization of technical standards and data structure to facilitate high quality long-term observations of atmospheric particle number size distributions, Atmos. Meas. Tech., 5, 657–685, doi:10.5194/amt-5-657-2012, 2012.

The response of the ionospheric peak electron density (NmF2) to solar activity)

Vaishnav, R.[1,✉], Jacobi, Ch.[1], Schmölter, E.[2], Berdermann, J.[2]
Codrescu, M.[3], Dühnen, H.[2]

[1] *Institute for Meteorology, Leipzig University, Stephanstr. 3, 04103 Leipzig, Germany*
[2] *German Aerospace Center, Kalkhorstweg 53, 17235 Neustrelitz, Germany*
[3] *Space Weather Prediction Centre, National Oceanic and Atmospheric Administration, Boulder, Colorado, USA*
✉*e-mail: rajesh_ishwardas.vaishnav@uni-leipzig.de*

Summary: The ionospheric peak electron density NmF2, simulated with the Coupled Thermosphere Ionosphere Plasmasphere electrodynamics (CTIPe) model was used to study the ionospheric response to solar flux in years of low (2008) and high (2013) solar activity. The CTIPe NmF2 was compared to the Whole Atmosphere Community Climate Model with Thermosphere and Ionosphere Extension (WACCM-X) and the Constellation Observing System for Meteorology, Ionosphere, and Climate (COSMIC) NmF2 in March and July of 2008 and 2013. The comparison shows that the CTIPe NmF2 is lower than the COSMIC and WACCM-X NmF2. Both models successfully reproduce the semi-annual variations seen in the COSMIC observations. Analysis of the 27-day variations of the CTIPe NmF2 shows that the midnight NmF2 deviations are stronger than the midday deviations. In addition, at low solar activity, the 27-day variations of NmF2 are larger in the Southern Hemisphere, while at high solar activity, the 27-day variations of NmF2 are larger at the equator and in the Northern Hemisphere.

An ionospheric delay was estimated with CTIPe simulated NmF2 at the 27-day solar rotation period during low and high solar activity. During low (high) solar activity, an ionospheric delay of about 12 (34) hours is predicted indicating an increasing ionospheric delay with solar activity.

Zusammenfassung: Die maximale ionosphärische Elektronendichte NmF2, die mit dem Coupled Thermosphere Ionosphere Plasmasphere electrodynamics (CTIPe) Modell simuliert wurde, wurde zur Untersuchung der ionosphärischen Reaktion in Jahren mit geringer (2008) und hoher (2013) Sonnenaktivität verwendet. CTIPe vorhergesagte NmF2 wurde mit derjenigen des Whole Atmosphere Community Climate Model with Thermosphere and Ionosphere Extension (WACCM-X) und Messwerten des Constellation Observing System for Meteorology, Ionosphere, and Climate (COSMIC) im März und Juli der Jahre 2008 und 2013 verglichen. Der Vergleich zeigt, dass NmF2 aus CTIPe geringer ist als das COSMIC gemessene und von WACCM-X simulierte. Beide Modelle reproduzieren erfolgreich die von COSMIC beobachteten halbjährlichen Schwankungen. Die Analyse der 27-tägigen Schwankungen des CTIPe NmF2 zeigt, dass die mitternächtlichen NMF2-Abweichungen stärker sind als diejenigen am Mittag. Außerdem sind bei geringer Sonnenaktivität die 27-Tage-Abweichungen von NmF2 in der

Südhemisphäre größer, während bei hoher Sonnenaktivität die 27-Tage-Abweichungen von NmF2 am Äquator und in der Nordhemisphäre größer sind.

Die ionosphärische Verzögerung während geringer und hoher Sonnenaktivität wurde für die 27-tägige Sonnenrotation mit CTIPe simuliert. Bei geringer (hoher) Sonnenaktivität wird eine ionosphärische Verzögerung von etwa 12 (34) Stunden beobachtet, was auf eine zunehmende ionosphärische Verzögerung mit zunehmender Sonnenaktivität hinweist.

1 Introduction

The thermospheric and ionospheric parameters, in particular the total electron content (TEC) and the peak electron density of the F2 region (NmF2), are mainly controlled by transport processes, photoionization and photodissociation of the main species O, O_2 and N_2 and depend on the intensity of incident extreme ultraviolet (EUV) and UV radiation from the Sun on various time scales, including the well-understood period of quasi-solar rotation (SR) and the 11-year solar cycle (SC) or longer (e.g. Jakowski et al., 1991; Afraimovich et al., 2008; Liu and Chen, 2009; Chen et al., 2015). Variations in solar irradiance are observed by satellites, and they have significant implications for the peformance of global navigation satellite systems (GNSS) and satellite communications. Therefore, it is important to characterise the influence of solar radiation on the thermosphere-ionosphere region. EUV can vary by more than a factor of 2 between solar minimum and maximum.

Since continuous observations of the whole EUV spectrum were not available prior to the TIMED/SEE mission starting in 2002 (Woods et al., 2000), solar EUV proxies, e.g., the F10.7 solar radio flux at 10.7 cm (Tapping, 2013) and Mg-II index, are used to represent solar activity.

The 27-day variations in solar flux are significantly modulated and amplified at higher solar activity compared to low solar activity, leading to a corresponding modulation in the thermosphere/ionosphere system (Kutiev et al., 2013).

The 27-day variations in solar and geomagnetic activity contribute significantly to the 27-day variations in the NmF2. However, the role of geomagnetic activity is complex. Ma et al. (2012) have studied the 27-day variations of NmF2 in detail using ionosonde observations. They show that the 27-day variations of solar irradiance and geomagnetic activity caused by the solar rotation are the main factors for the 27-day variations of the ionosphere. Apart from solar activity and geomagnetic activity, the 27-day variations in the lower ionosphere (D region), especially in winter when solar activity is low, are due to lower atmospheric influences (planetary waves) (Pancheva et al., 1991). But the D region contributes only weakly to the ionospheric electron density. There is a considerable influence of lower atmosphere waves (planetary waves, tides, and gravity waves) on the entire ionosphere, including TEC and NmF2. These effects are more prominent during solar maximum. In this article we focus on the fluctuations of NmF2 under different solar activity.

The relationship between solar flux and ionospheric parameters is important for monitoring and modeling solar variability in particular with respect to space weather applications, and has been studied by many researchers (e.g. Kane, 1992; Rishbeth, 1998; Forbes et al., 2000; Oinats et al., 2008; Astafyeva et al., 2008; Min et al., 2009; Ma

et al., 2012). An ionospheric lag of about 17 hours to 2 days in thermosphere-ionosphere parameters such as NmF2, TEC, temperature, and neutral densities with respect to solar EUV flux measurements and EUV proxies (e.g., F10.7 index, Mg-II index, etc.) has been extensively reported by various authors (e.g. Jakowski et al., 1991; Afraimovich et al., 2008; Liu and Chen, 2009; Unglaub et al., 2012; Chen et al., 2015; Jacobi et al., 2016; Vaishnav et al., 2019, 2021b; Schmölter et al., 2018, 2020, 2021, 2022; Ren et al., 2018, 2019, see also references therein), and it was reported that this lag may vary with solar activity and season.

The physical mechanism of ionospheric delay in TEC and neutrals against solar flux has been studied by several authors (e.g. Jakowski et al., 1991; Vaishnav et al., 2021a, 2022; Ren et al., 2018; Schmölter et al., 2022) by using numerical physics-based models such as the Coupled Thermosphere Ionosphere Plasmasphere electrodynamics (CTIPe, Fuller-Rowell and Rees, 1980) model, or the Thermosphere Ionosphere Electrodynamics-General Circulation Model (TIE-GCM, Richmond et al., 1992). The delay in the ionosphere is mainly due to the difference in response times between quasi-instantaneous ionization and slower recombination in the ionospheric F region (Ren et al., 2018). In addition, eddy diffusion, electrodynamics, and lower atmospheric forcings also influence the ionospheric delay (Vaishnav et al., 2021a). In addition to solar activity, geomagnetic activity may also play an important role in the ionospheric delay (Schmölter et al., 2020).

The present study aims to investigate the effects of 27-day variations in the peak electron density of the F2 region and solar and geomagnetic parameters in years of low (2008) and high (2013) solar activity. We also investigate an ionospheric delay in NmF2 during various solar activity conditions under ideal atmospheric conditions. In Section 2, we present our data sources, and the CTIPe model used for the analyses. In Section 3, we examine the 27-day variability of solar activity, geomagnetic activity, and NmF2, as well as the ionospheric delay under different solar activity conditions. Section 4 concludes the paper.

2 Data and model description

2.1 Data sources

The F10.7 solar radio flux is one of the most commonly used indices of solar activity (Tapping, 2013). We use the daily values of the F10.7 index. The F10.7 index values are available in the LISIRD database (Dewolfe et al., 2010). In addition, as a measure of geomagnetic activity, we used the daily Ap indices from the OMNIWeb Plus database (https://omniweb.gsfc.nasa.gov/, NASA, 2022).

2.2 FORMOSAT-3/COSMIC

The Constellation Observing System for Meteorology, Ionosphere, and Climate/Formosa Satellite Mission 3 (COSMIC/FORMOSAT-3, hereafter COSMIC) was a joint Taiwan U.S. occultation satellite mission, a constellation of six microsatellites launched on April 2006, initially in 500 km orbit and later in 800 km orbit and at an inclination of 72° (Anthes et al., 2008). COSMIC provides neutral and ionospheric parameters via the COSMIC Data Analysis and Archive Center (CDAAC).

In this study, electron density profiles (ionPrf) for 2008 and 2013 have been used (http://cdaacwww.cosmic.ucar.edu/cdaac/rest/tarservice/data/cosmic2013/ionPrf).

2.3 CTIPe model

The CTIPe model is a global, time-dependent model of the upper atmosphere that self-consistently solves the primitive continuity, momentum, and energy equations to calculate wind components, global temperature, and neutral composition, and which is also used to calculate plasma production, loss, and transport. The model consists of four components, namely a neutral thermosphere model (Fuller-Rowell and Rees, 1980), a mid- and high-latitude ionosphere convection model (Quegan et al., 1982), a plasmasphere and low-latitude ionosphere model (Millward et al., 1996), and an electrodynamics model (Richmond et al., 1992). Calculations are performed at a resolution of 2°/18° in latitude/longitude. In the vertical direction, the atmosphere is divided into 15 logarithmic pressure levels at an interval of one scale height, starting with a lower boundary at 1 Pa (about 80 km altitude) up to over 500 km altitude at pressure level 15. The model requires several external forcing factors such as solar UV and EUV radiation, Weimer electric field, TIROS /NOAA auroral precipitation, and tidal forcing at the lower boundary. The F10.7 index is used as a solar proxy to calculate ionization, heating, and oxygen dissociation in the ionosphere. A detailed description of the model can be found in Codrescu et al. (2008, 2012).

2.4 WACCM-X

The National Center for Atmospheric Research (NCAR) Whole Atmosphere Community Climate Model with thermosphere and ionosphere extension (WACCM-X) is a global numerical model of the entire atmosphere, from the surface to an altitude of about 600 km, depending on solar activity. The first version of WACCM-X was described by Liu et al. (2010). WACCM-X is an atmospheric component of the NCAR Community Earth System Model that links the atmosphere, ocean, land surface, sea ice, land ice, and carbon cycle components through flux and state information exchange (Hurrell et al., 2013). Recent extensions of WACCM-X include a fully coupled ionosphere, including electric field effects and ion transport. The vertical resolution in the mesosphere and thermosphere is one-quarter of a scale height and the horizontal resolution is 1.9°/2.5° in latitude and longitude, respectively. A detailed description of the new version (version 2.0) of WACCM-X can be found in Liu et al. (2018a).

3 Results

In this work, we focused on the variability of NmF2 during different solar activity conditions. For this purpose, we performed two types of model experiments. In the first experiment, we used more realistic atmospheric conditions from March and July 2008 and 2013, using the solar, geomagnetic, and other realistic inputs with the default model settings. The model simulations from the first experiment are used in Sections 3.1 and 3.2. The second experiment was conducted with only one day of constant atmospheric conditions on March 15, 2013, and we varied only F10.7 in an artificial manner for

a 27-day solar rotation period to observe the effects of solar flux. This experiment is described in more detail in Section 3.3. In general, we used ionospheric electron density profiles between 170 and 400 km to derive the peak election density NmF2.

3.1 NmF2 comparisons

Figure 1 shows maps of monthly mean NmF2 from COSMIC (top panel), WACCM-X (middle panel), and CTIPe (middle panel) in March and July 2008 and 2013. The white lines indicate the dip equator. Longitudinal and latitudinal variations are evident from the figure. The maximum of NmF2 is seen in the low latitude region around the dip equator. In general, the effect of solar activity can be seen in COSMIC NmF2 and is well reproduced in the WACCM-X and CTIPe models. In 2008, solar activity was very low, so the overall WACCM-X NmF2 was lower than in 2013, showing a strong dependence on solar activity. In addition, NmF2 is larger in March than in July. This feature is observed in both low and high solar activity years. This is due to the semi-annual fluctuations of NmF2 (e.g., Qian et al., 2013). In addition, NmF2 is higher in March in the Northern Hemisphere, while NmF2 is higher in July in the Southern Hemisphere. These variations are due to the winter-summer asymmetry of equatorial ionization anomalies (EIA) resulting from electrodynamic, thermodynamic, and chemical processes (e.g., Lin et al., 2007). Liu et al. (2018b) presented the new development of the WACCM-X. They showed that the climatological characteristics of the ionospheric peak densities and heights (NmF2 and hmF2) of WACCM-X are in general agreement with the results obtained from the COSMIC data. They also found that NmF2 values predicted by WACCM-X are smaller and EIA are closer to the magnetic equator than observations from COSMIC and ionosondes.

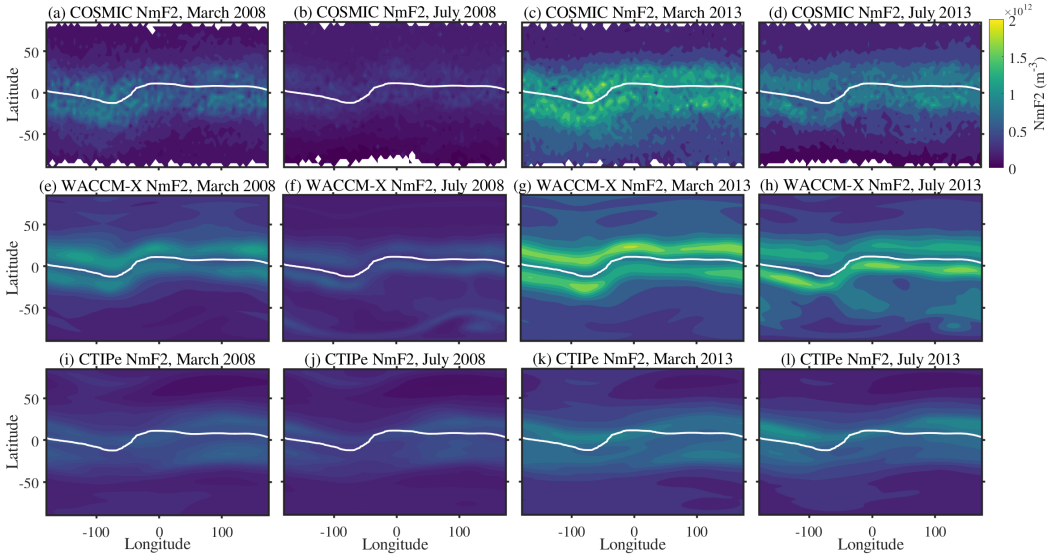

Figure 1: *Variations of NmF2 observed from COSMIC (a-d, upper panel), simulated with WACCM-X (e-h, lower panel), and with CTIPe (i-l, lower panel) during March and July 2008 and 2013. The month and year are indicated in the respective figure title. The white lines indicate the dip equator.*

The bottom panels in Figure 1(i-l) shows the NmF2 simulated by CTIPe. Compared

to the WACCM and COSMIC NmF2, the CTIPe NmF2 is generally lower. It lacks some climatological features clearly seen in the COSMIC and WACCM-X NmF2. The underestimation could be a consequence of the model limitations (e.g., grid resolution, and solar EUV flux input) highlighted by Codrescu et al. (2008, 2012). NmF2 varies with solar activity and also shows the slightly larger NmF2 in March compared to July indicates the semi-annual variations, as seen in COSMIC and WACCM-X NmF2, although they are not that clearly expressed in this model.

Diurnal variations of NmF2 as a function of time for the WACCM-X and CTIPe models in March and July 2008 and 2013 at $50°N/18°E$ are shown in Figure 2. The figure shows the monthly mean values of NmF2 with standard deviations. Most of the time CTIPe underestimates the WACCM-X NmF2, except in July 2008 from 10:00 UT to 14:00 UT as shown in Figure 2(b). The bias is due to the physical processes included in both CTIPe and WACCM-X models. The diurnal variations look similar in March of both years, except for the magnitude. The semi-annual variations can be seen in the figure, and the NmF2 values are larger in March than in July.

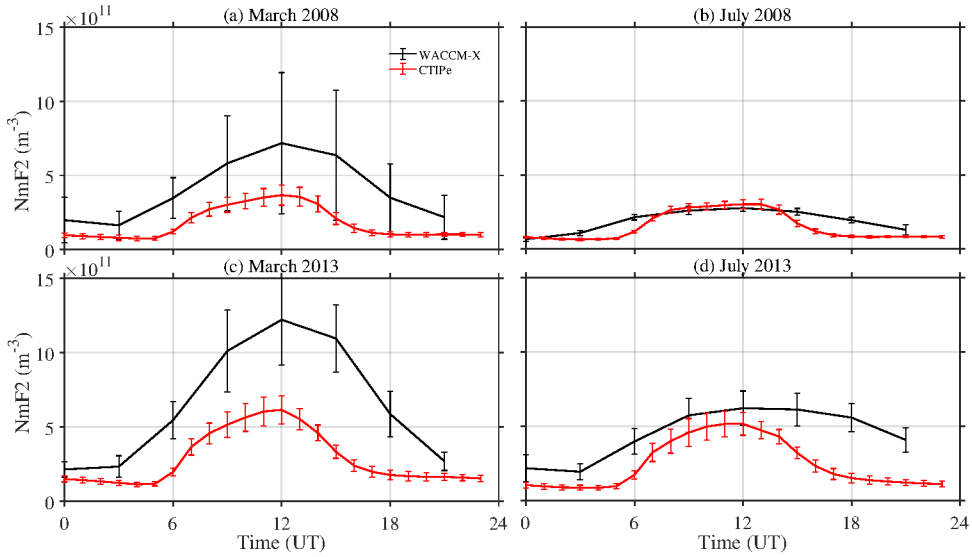

Figure 2: *Diurnal variations of mean NmF2 with standard deviation simulated with WACCM-X (upper panel) and CTIPe (lower panel) at* $50°N/18°E$ *during (a) March 2008, (b) July 2008, (c) March 2013, and (d) July 2013.*

3.2 The 27-day variations

We used the F10.7 index (Ap index) to represent solar (geomagnetic) activity. To focus only on the 27-day variations that represent the dominant oscillation in the solar proxies, we first performed a smoothing procedure similar to Ma et al. (2012). In this method, a 33 days moving average with one day step was calculated to isolate the 27-day variations. The relative changes can be determined using equation 1:

$$\Delta A_i = (A_i - \mu)/\mu. \tag{1}$$

A_i represents the time series of F10.7, Ap, and NmF2, and μ represents the 33 day moving averages of A_i. To focus only on the 27-day variations, we applied a bandpass

filter between 22 and 33 days to filter out the unfiltered ΔF10.7, ΔAp, and ΔNmF2 from Eq. 1, which we refer to below as the filtered time series (after bandpass filtering) and denote by Δ_{27}F10.7, Δ_{27}Ap, and Δ_{27}NmF2. The relative deviations of ΔF10.7 and ΔAp in 2008 and 2013 are shown in Figure 3. The gray (black) curve shows the unfiltered (filtered) deviations.

Figure 3(a-b) shows the deviations in the filtered and unfiltered time series of ΔF10.7. The ΔF10.7 and Δ_{27}F10.7 deviations show a similar response to the 27-day solar rotation period. The deviations are much larger during the high solar activity period than during the low solar activity period. It can also be seen that the 27-day variations are more pronounced in 2013. The deviations are weaker during June to August 2013. Since the period of solar rotation changes frequently, we cannot reconstruct the similar variations from the filtered time series (see Ma et al., 2012).

A similar analysis of the Ap index shows the 27-day variations in the filtered time series (Figure 3(d-e)). In 2008, the 27-day fluctuations are stronger than in 2013, and there are several short-term fluctuations in the Ap index that result in different dominant periods shorter than the 27-day fluctuations. We also performed a spectral analysis of ΔF10.7 and ΔAp (not shown). In ΔF10.7, the dominant period in 2008 and 2013 are 27 days. In ΔAp, the 27-day period is the dominant period, however shorter periods such as 13.5 days and 9 days are also present. These periods are dominant in 2008, while they are less so in 2013.

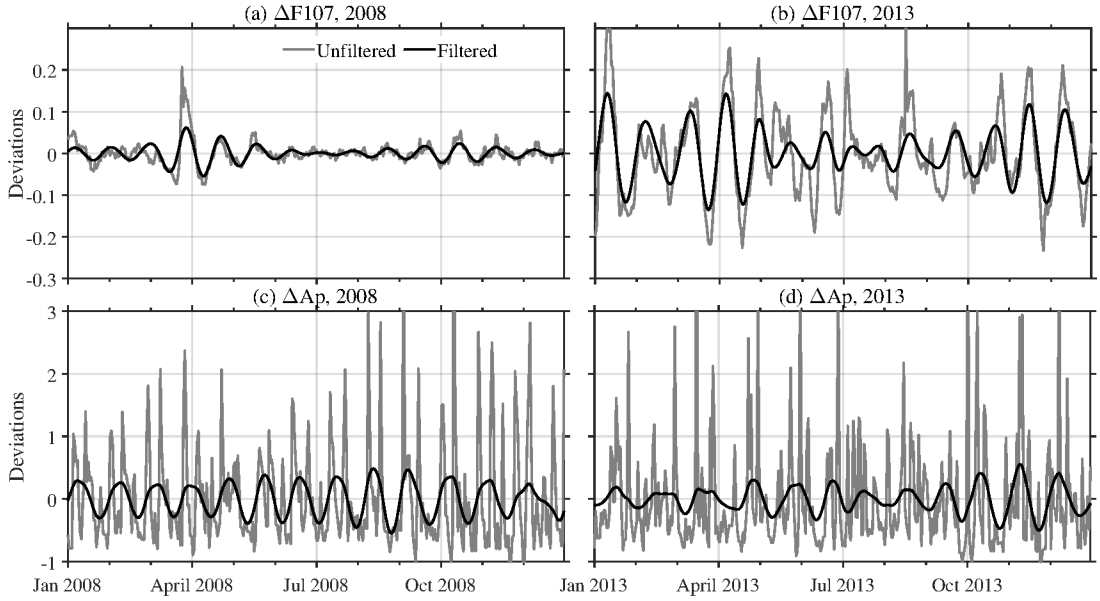

Figure 3: *The time series of unfiltered (gray) and filtered (black) relative deviations of the ΔF10.7 index (top panel, a-b) and ΔAp indices (bottom panel, c-d) during 2008 (left panel) and 2013 (right panel).*

Vaishnav et al. (2019) reported a dominant 27-day period in several solar proxies and TEC. This is the dominant mode of solar variability. Therefore, in this study, we examine the 27-day variations of CTIPe NmF2 at 0°/18°E, 30°N/18°E, and 30°S/18°E. We first performed the smoothing and filtering mentioned above to filter out the signal at periods longer than 33 days. To examine the difference between Δ_{27}NmF2 variations during low (2008) and high (2013) solar activity, we used averaged Δ_{27}NmF2 values.

Figure 4 shows the Δ_{27}NmF2 at the three grid points above for midday (11:00-13:00 LT) and midnight (23:00-01:00 LT) in low and high solar activity years along with the Δ_{27}F10.7. Figure 4(a-b) shows that in 2008, the changes in Δ_{27}NmF2 are larger at 30°S during both midday and midnight from July to October 2008, while the changes during midnight are larger at 0° from January to April 2008 and after October 2008. In Δ_{27}F10.7, the larger variation is observed in March-April. During this period, the variations are in phase with the lag during the midday period, and similar for the midnight period, except for 0°, which is 180° out of phase. Similarly, in May 2013, we found a phase deviation of 180° for 30°S with respect to Δ_{27}F10.7 during midday and midnight (Figure 4(b-d)). In 2013, the deviations for midday are larger at 0°, 30°N through April, and in November and December. In November-December, the deviations are again out of phase at 30°S with Δ_{27}F10.7 during midday and during midnight, similar holds for 0° and 30°S (Figure 4(d)).

Overall, the midnight Δ_{27}NmF2 variations are stronger than the midday ones. It is also interesting to note that at low solar activity the Δ_{27}NmF2 variations are larger at 30°S, while at high solar activity the Δ_{27}NmF2 variations are larger at 0° and 30°N during midday.

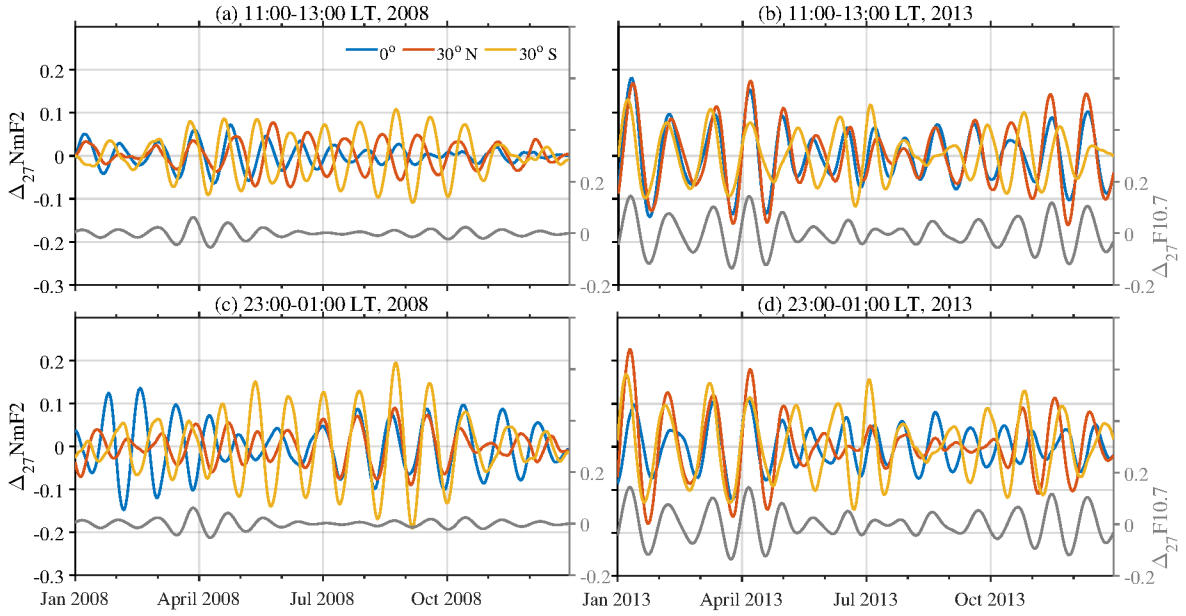

Figure 4: *Day to day variations of Δ_{27}NmF2 during 2008 (left panel, a-c) and 2013 (right panel, b-d). The upper (lower) panel shows the midday (midnight) variations at 0°/18°E, 30°N/18°E, and 30°S/18°E. The right y-axis represents the Δ_{27}F10.7 (gray curve).*

Ma et al. (2012) used 18 years of ionosonde data over 11 stations to examine the 27-day variations. They reported that the normalized standard deviation of the midnight 27-day variations of NmF2 is larger than that of midday, which is also observed for the Δ_{27}NmF2 simulated by CTIPe. They also suggest that the 27-day solar rotation is the main cause of the 27-day variations in the ionosphere.

3.3 Ionospheric delay in NmF2 under different solar activity conditions

An ionospheric lag compared to solar flux has been found in various ionospheric parameters (e.g. Jakowski et al., 1991; Liu and Chen, 2009; Jacobi et al., 2016; Vaishnav et al., 2019, 2022; Schmölter et al., 2020, 2022; Ren et al., 2018, and references therein). Overall, recent studies using physics based numerical models of the global thermosphere-ionosphere suggest that the ionospheric delay process is influenced by several factors, including solar, geomagnetic, and electrodynamic ones, eddy diffusion, and lower atmospheric forcings.

In this work, we focus on the study of the ionospheric delay in NmF2 to solar irradiance. For this purpose, we performed two experiments with the CTIPe model simulations in different ranges of the F10.7 index at a cycle of 27 days under ideal conditions. The model was run for 30 days with input parameters held constant to achieve diurnal reproducibility, and inputs were changed after this spin-up period. We used constant atmospheric conditions for March 15, 2013, and ran the model varying the F10.7 index for the 27-day solar rotation period. The F10.7 index was chosen for low (70-90 sfu) and high (150-190 sfu) solar activity. We calculated the time delay using the hourly simulated NmF2 and F10.7. The F10.7 index was interpolated to hourly data using a sine function (Vaishnav et al., 2021a).

Figure 5 shows the daily variations of NmF2 (black curve) during (a) low and (b) high solar activity together with the F10.7 index (gray curve) at $50°N$. The figure shows that NmF2 follows solar activity in the ascending phase of the solar rotation period and increases with solar activity. In the descending phase of the solar rotation period, the behaviour of NmF2 changes and NmF2 does not return to the initial values, which is due to the imbalance of the production and loss processes of electrons in the F2 region. Further, the ionospheric delay in NmF2 is calculated using the F10.7 index and shown in the figure. The ionospheric delay at low solar activity is about 12 hours, as shown in Figure 5(a). After the zero day, the recombination processes are balanced by the photoionization rates, resulting in a delay of about 12 hours. Compared to low solar activity, an ionospheric delay of about 34 hours is observed at high solar activity (Figure 5(b)). Again, the values of NmF2 do not return to initial values after a complete cycle, and the difference between the production and loss processes is much larger, leading to a longer delay compared to low solar activity. This suggests that solar activity plays an important role in the ionospheric delay of NmF2, and the ionospheric delay increases with increasing solar activity.

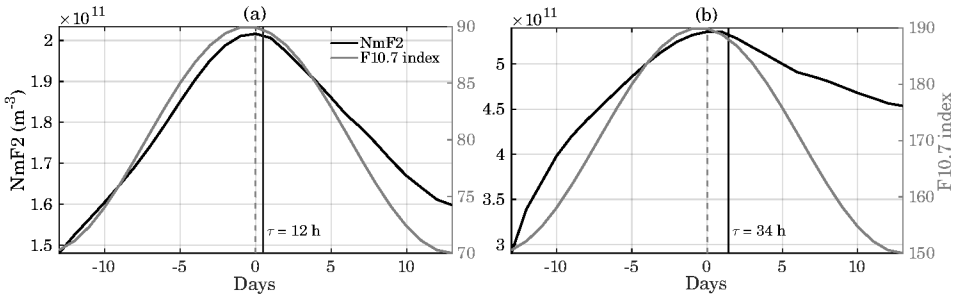

Figure 5: *Time series of model-simulated NmF2 during (a) low (70-90 sfu), and (b) high (150-190 sfu) solar activity. The right y-axis represents the input F10.7 index.*

4 Conclusions

We studied the ionospheric response to solar variability using the CTIPe simulated ionospheric peak electron density NmF2 for 2008 and 2013 under low and high solar activity conditions. The CTIPe NmF2 was compared to the observed COSMIC and the modeled WACCM-X NmF2 in March and July of 2008 and 2013. The CTIPe NmF2 is lower than the COSMIC and WACCM-X NmF2 during the periods studied. Both models successfully reproduce the semi-annual variations that can be seen in the COSMIC NmF2.

The CTIPe model simulated NmF2 was used to examine the 27-day fluctuations at $0°/18°E$, $30°N/18°E$, and $30°S/18°E$. We found that the 27-day variations in midnight NmF2 are stronger than the midday variations, which is consistent with observations. The analysis also shows that at low solar activity the 27-day variations of NmF2 are larger at $30°S$, while at high solar activity the 27-day variations of NmF2 are larger at $0°$ and $30°N$ during midday.

In addition, the ionospheric delay was estimated with the model simulated NmF2 during low and high solar activity. An ionospheric delay of about 12 hours is observed during low solar activity and 34 hours during high solar activity. This shows that the ionospheric delay increases with increasing solar activity.

Here, we discussed the 27-day variations of NmF2 at low (2008) and high (2013) solar activity and focused on the ionospheric delay of NmF2 at moderate and high solar activity. In future studies, we will further investigate the effects and main roles of the different processes affecting the ionospheric delay and their physical mechanisms using modelling and observations. In addition, the 27-day variations in solar activity and geomagnetic activity contribute to the 27-day variations in peak electron density (NmF2). Therefore, further studies are needed to understand the complexity of these factors and their role in the delayed ionospheric response.

Acknowledgements Daily F10.7 index and Ap index can be downloaded from https://omniweb.gsfc.nasa.gov/ (NASA, 2022). The study has been supported by Deutsche Forschungsgemeinschaft (DFG) through grants nos. JA 836/48-1 and SCHM 3761/1-1.

References

Afraimovich, E. L., Astafyeva, E. I., Oinats, A. V., Yasukevich, Y. V., and Zhivetiev, I. V.: Global electron content: a new conception to track solar activity, Annales Geophysicae, 26, 335–344, doi:10.5194/angeo-26-335-2008, 2008.

Anthes, R. A., Bernhardt, P. A., Chen, Y., et al.: The COSMIC/FORMOSAT-3 Mission: Early Results, Bulletin of the American Meteorological Society, 89, 313–334, doi:10.1175/bams-89-3-313, 2008.

Astafyeva, E. I., Afraimovich, E. L., Oinats, A. V., Yasukevich, Y. V., and Zhivetiev, I. V.: Dynamics of global electron content in 1998-2005 derived from global GPS data and IRI modeling, Advances in Space Research, 42, 763–769, doi:10.1016/j.asr.2007.11.007, 2008.

Chen, Y., Liu, L., Le, H., and Zhang, H.: Discrepant responses of the global electron content to the solar cycle and solar rotation variations of EUV irradiance, Earth, Planets and Space, 67, doi:10.1186/s40623-015-0251-x, 2015.

Codrescu, M. V., Fuller-Rowell, T. J., Munteanu, V., Minter, C. F., and Millward, G. H.: Validation of the

Coupled Thermosphere Ionosphere Plasmasphere Electrodynamics model: CTIPE-Mass Spectrometer Incoherent Scatter temperature comparison, Space Weather, 6, doi:10.1029/2007sw000364, 2008.

Codrescu, M. V., Negrea, C., Fedrizzi, M., et al.: A real-time run of the Coupled Thermosphere Ionosphere Plasmasphere Electrodynamics (CTIPe) model, Space Weather, 10, doi:10.1029/2011sw000736, 2012.

Dewolfe, A. W., Wilson, A., Lindholm, D. M., et al.: Solar Irradiance Data Products at the LASP Interactive Solar Irradiance Datacenter (LISIRD), in: AGU Fall Meeting Abstracts, 2010.

Forbes, J. M., Palo, S. E., and Zhang, X.: Variability of the ionosphere, Journal of Atmospheric and Solar-Terrestrial Physics, 62, 685–693, doi:10.1016/s1364-6826(00)00029-8, 2000.

Fuller-Rowell, T. J. and Rees, D.: A Three-Dimensional Time-Dependent Global Model of the Thermosphere, Journal of the Atmospheric Sciences, 37, 2545–2567, doi:10.1175/1520-0469(1980)037<2545:atdtdg>2.0.co;2, 1980.

Hurrell, J. W., Holland, M. M., Gent, P. R., et al.: The Community Earth System Model: A framework for collaborative research, Bulletin of the American Meteorological Society, 94, 1339–1360, doi:10.1175/bams-d-12-00121.1, 2013.

Jacobi, C., Jakowski, N., Schmidtke, G., and Woods, T. N.: Delayed response of the global total electron content to solar EUV variations, Advances in Radio Science, 14, 175–180, doi:10.5194/ars-14-175-2016, 2016.

Jakowski, N., Fichtelmann, B., and Jungstand, A.: Solar activity control of ionospheric and thermospheric processes, Journal of Atmospheric and Terrestrial Physics, 53, 1125–1130, doi:10.1016/0021-9169(91)90061-B, 1991.

Kane, R. P.: Sunspots, solar radio noise, solar EUV and ionospheric foF2, Journal of Atmospheric and Terrestrial Physics, 54, 463–466, doi:10.1016/0021-9169(92)90025-G, 1992.

Kutiev, I., Tsagouri, I., Perrone, L., et al.: Solar activity impact on the Earth's upper atmosphere, Journal of Space Weather and Space Climate, 3, A06, doi:10.1051/swsc/2013028, 2013.

Lin, C. H., Liu, J. Y., Fang, T. W., et al.: Motions of the equatorial ionization anomaly crests imaged by FORMOSAT-3/COSMIC, Geophysical Research Letters, 34, L19 101, doi:10.1029/2007gl030741, 2007.

Liu, H.-L., Foster, B. T., Hagan, M. E., et al.: Thermosphere extension of the Whole Atmosphere Community Climate Model, Journal of Geophysical Research: Space Physics, 115, A12 302, doi:10.1029/2010ja015586, 2010.

Liu, H.-L., Bardeen, C. G., Foster, B. T., et al.: Development and Validation of the Whole Atmosphere Community Climate Model With Thermosphere and Ionosphere Extension (WACCM-X 2.0), Journal of Advances in Modeling Earth Systems, 10, 381–402, doi:10.1002/2017ms001232, 2018a.

Liu, J., Liu, H., Wang, W., et al.: First Results From the Ionospheric Extension of WACCM-X During the Deep Solar Minimum Year of 2008, Journal of Geophysical Research: Space Physics, 123, 1534–1553, doi:10.1002/2017ja025010, 2018b.

Liu, L. and Chen, Y.: Statistical analysis of solar activity variations of total electron content derived at Jet Propulsion Laboratory from GPS observations, Journal of Geophysical Research: Space Physics, 114, doi:10.1029/2009ja014533, 2009.

Ma, R., Xu, J., Wang, W., and Lei, J.: The effect of ~27 day solar rotation on ionospheric F2 region peak densities (NmF2), Journal of Geophysical Research: Space Physics, 117, A03 303, doi:10.1029/2011ja017190, 2012.

Millward, G., Moffett, R., Quegan, S., and Fuller-Rowell, T.: A coupled thermosphere-ionosphere-plasmasphere model (CTIP), STEP handbook on ionospheric models, pp. 239–279, 1996.

Min, K., Park, J., Kim, H., et al.: The 27-day modulation of the low-latitude ionosphere during a solar maximum, Journal of Geophysical Research: Space Physics, 114, 1–8, doi:10.1029/2008JA013881, 2009.

NASA: OMNIWeb Plus database, available at: `http://omniweb.gsfc.nasa.gov/`, last access: 15 April 2022, 2022.

Oinats, A. V., Ratovsky, K. G., and Kotovich, G. V.: Influence of the 27-day solar flux variations on the ionosphere parameters measured at Irkutsk in 2003-2005, Advances in Space Research, 42, 639–644, doi:10.1016/j.asr.2008.02.009, 2008.

Pancheva, D., Schminder, R., and Laštovička, J.: 27-day fluctuations in the ionospheric D-region, Journal

of Atmospheric and Terrestrial Physics, 53, 1145–1150, doi:10.1016/0021-9169(91)90064-e, 1991.

Qian, L., Burns, A. G., Solomon, S. C., and Wang, W.: Annual/semiannual variation of the ionosphere, Geophysical Research Letters, 40, 1928–1933, doi:10.1002/grl.50448, 2013.

Quegan, S., Bailey, G. J., Moffett, R. J., et al.: A theoretical study of the distribution of ionization in the high-latitude ionosphere and the plasmasphere: first results on the mid-latitude trough and the light-ion trough, Journal of Atmospheric and Terrestrial Physics, 44, 619–640, doi:10.1016/0021-9169(82)90073-3, 1982.

Ren, D., Lei, J., Wang, W., et al.: Does the Peak Response of the Ionospheric F2 Region Plasma Lag the Peak of 27-Day Solar Flux Variation by Multiple Days?, Journal of Geophysical Research: Space Physics, pp. 1–11, doi:10.1029/2018JA025835, 2018.

Ren, D., Lei, J., Wang, W., et al.: A Simulation Study on the Time Delay of Daytime Thermospheric Temperature Response to the 27-Day Solar EUV Flux Variation, Journal of Geophysical Research: Space Physics, 124, 9184–9193, doi:10.1029/2019ja027000, 2019.

Richmond, A. D., Ridley, E. C., and Roble, R. G.: A thermosphere/ionosphere general circulation model with coupled electrodynamics, Geophysical Research Letters, 19, 601–604, doi:10.1029/92GL00401, 1992.

Rishbeth, H.: How the thermospheric circulation affects the ionospheric F2-layer, Journal of Atmospheric and Solar-Terrestrial Physics, 60, 1385–1402, doi:10.1016/s1364-6826(98)00062-5, 1998.

Schmölter, E., Berdermann, J., Jakowski, N., Jacobi, C., and Vaishnav, R.: Delayed response of the ionosphere to solar EUV variability, Advances in Radio Science, 16, 149–155, doi:10.5194/ars-16-149-2018, 2018.

Schmölter, E., Berdermann, J., Jakowski, N., and Jacobi, C.: Spatial and seasonal effects on the delayed ionospheric response to solar EUV changes, Annales Geophysicae, 38, 149–162, doi:10.5194/angeo-38-149-2020, 2020.

Schmölter, E., Berdermann, J., and Codrescu, M.: The Delayed Ionospheric Response to the 27-day Solar Rotation Period Analyzed With GOLD and IGS TEC Data, Journal of Geophysical Research: Space Physics, 126, doi:10.1029/2020ja028861, 2021.

Schmölter, E., Heymann, F., Savigny, C., and Berdermann, J.: The Height-Dependent Delayed Ionospheric Response to Solar EUV, Journal of Geophysical Research: Space Physics, 127, doi:10.1029/2021ja030118, 2022.

Tapping, K. F.: The 10.7 cm solar radio flux (F10.7), Space Weather, 11, 394–406, doi:10.1002/swe.20064, 2013.

Unglaub, C., Jacobi, C., Schmidtke, G., Nikutowski, B., and Brunner, R.: EUV-TEC proxy to describe ionospheric variability using satellite-borne solar EUV measurements, Advances in Radio Science, 10, 259–263, doi:10.5194/ars-10-259-2012, 2012.

Vaishnav, R., Jacobi, C., and Berdermann, J.: Long-term trends in the ionospheric response to solar extreme-ultraviolet variations, Annales Geophysicae, 37, 1141–1159, doi:10.5194/angeo-37-1141-2019, 2019.

Vaishnav, R., Jacobi, C., Berdermann, J., Codrescu, M., and Schmölter, E.: Role of eddy diffusion in the delayed ionospheric response to solar flux changes, Annales Geophysicae, 39, 641–655, doi:10.5194/angeo-39-641-2021, 2021a.

Vaishnav, R., Schmölter, E., Jacobi, C., Berdermann, J., and Codrescu, M.: Ionospheric response to solar extreme ultraviolet radiation variations: comparison based on CTIPe model simulations and satellite measurements, Annales Geophysicae, 39, 341–355, doi:10.5194/angeo-39-341-2021, 2021b.

Vaishnav, R., Jacobi, C., Berdermann, J., Schmölter, E., and Codrescu, M.: Delayed ionospheric response to solar extreme ultraviolet radiation variations: A modeling approach, Advances in Space Research, 69, 2460–2476, doi:10.1016/j.asr.2021.12.041, 2022.

Woods, T., Bailey, S., Eparvier, F., et al.: TIMED Solar EUV experiment, Physics and Chemistry of the Earth, Part C: Solar, Terrestrial & Planetary Science, 25, 393–396, doi:10.1016/s1464-1917(00)00040-4, 2000.

Tethered balloon measurements during Arctic autumn conditions in the framework of HALO-(AC)^3

Lonardi, M.[1,✉], Ehrlich, A.[1], Schäfer, M.[1], Thoböll, J.[1], Wendisch, M.[1]

[1] *University of Leipzig, Leipzig Institute for Meteorology (LIM), Leipzig, 04103, Germany*
✉*e-mail: michael.lonardi@uni-leipzig.de*

Summary: The BalloonbornE moduLar Utility for profilinG the lower Atmosphere (BELUGA) was deployed in autumn 2021 in the Arctic at the AWIPEV research station in Ny-Ålesund (Svalbard). In-situ profiles of thermodynamic parameters, broadband radiation, turbulence, aerosol particle concentrations, and cloud microphysical structure, were performed. Additionally, samples of ice nucleating particles were collected. Thermal infrared radiation profiles are presented for different cloud conditions. The data provides the base for studying the vertical distribution of cloud radiative effects, and extends the common view of the bi-modal distribution of the Arctic surface energy budget.

Zusammenfassung: Das Fesselballonsystem BalloonbornE moduLar Utility for profilinG the lower Atmosphere (BELUGA) wurde im Herbst 2021 an der Forschungsstation Ny-Ålesund in der Arktis eingesetzt. Es wurden In-situ Profile von thermodynamischen Parametern, breitbandiger Strahlung, Turbulenz, Aerosolpartikelkonzentrationen und der mikrophysikalischer Wolkenstruktur erstellt. Zusätzlich wurden Proben von eiskeimbildenden Partikeln gesammelt. Strahlungsprofile wurden unter verschiedenen Wolkenbedeckungen gemessen und quantifizieren die vertikale Verteilung der Wolkenstrahlungseffekte. Die Profilmessungen erweitern damit die für bodennahe Messungen bekannte modale Verteilung des Energiehaushalts der Arktis.

1 Introduction

The tethered balloon system BELUGA (BalloonbornE moduLar Utility for profilinG the lower Atmosphere; Egerer et al., 2019) was deployed at the AWIPEV research station in Ny-Ålesund (Svalbard) for an extensive measurement period in autumn 2021 in cooperation with the Institute for Tropospheric Research (TROPOS) and the Alfred Wegener Institute (AWI). The deployment of BELUGA in Ny-Ålesund succeeds the operation of the balloon from the sea ice (Egerer et al., 2019; Lonardi et al., 2021) and extends the series of tethered-balloon operations in Ny-Ålesund (e.g., Ferrero et al., 2019, Pasquier et al., in review) and in Svalbard (e.g., Cappelletti et al., in review).

The site was chosen for the relative ease of access combined with a comprehensive setup providing time series of radiosoudings (e.g., Maturilli et al., 2013), cloudiness and cloud phase retrieved with ground-based remote sensing (e.g., Nomokonova et al., 2019), surface thermodynamics (e.g., Mazzola et al., 2016), radiation budget (e.g., Maturilli

Figure 1: *(a) The broadband radiation payload on BELUGA and (b) a profile measurement during the polar night.*

et al., 2015), and aerosol particle concentrations (e.g., Lupi et al., 2016). In particular, the daily radiosoundings yeld a valuable dataset for radiative transfer simulations and for the cross validation of some of the observed quantities. Furthermore, the area is subject to intense high-resolution Large-Eddy Simulations (LES) modelling activities by $(AC)^3$ (e.g., Kiszler et al., in review).

2 Overview

The balloon deployment lasted from 17 September to 15 November 2021 (Fig. 1). The BELUGA system followed to a large extent the setup and the techniques adopted during MOSAiC (Multidisciplinary drifting Observatory for the Study of Arctic Climate; Shupe et al., 2022) by Lonardi et al. (2021). Some changes had to be applied to operate in the specific conditions provided by Ny-Ålesund and to extend the research objectives.

A total of 48 flights was performed over 19 days, reaching typically up to 1000-1500 m above ground level (Fig. 2). Profiles were obtained in cloud free and cloudy conditions, with four profiles crossing the cloud layer (on 30 September and 8 November 2021). Snow covered the site from 13 October.

The significant flexibility gained by a potential 24/7 access to the measurement site proved to be important when facing harsh weather conditions that inhibited BELUGA operations during longer periods. The observations were also constrained by commercial

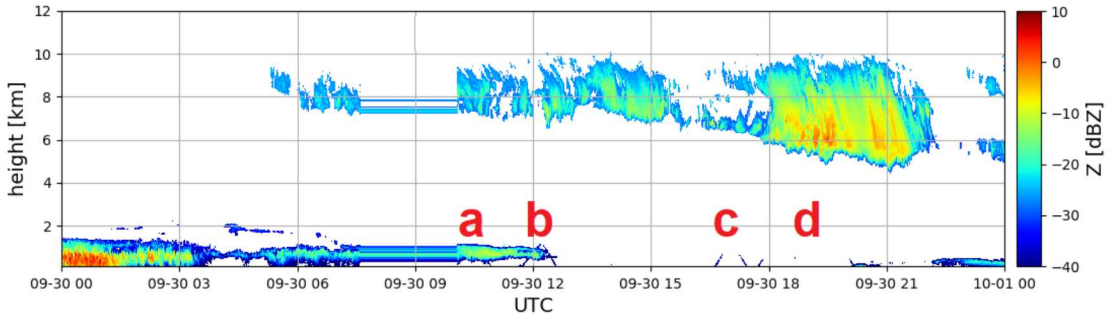

Figure 2: *Radar retrieval on 30 September 2021. BELUGA is partially detected while performing three profiles (a-c) and a two-hours stationary filter sampling (d).*

flights reaching Ny-Ålesund airport, which required the balloon to be at the ground (Fig. 3). BELUGA was also not operated during intermittently strong katabatic winds from the local glaciers. As a result, the balloon had to be stored overnight for safety reasons.

Additionally, the onset of the polar night, combined with cold temperatures (down to -20°C) and strong wind chill (down to -35°C) posed a serious challenge to the personnel in the field. Particular care had to be taken for the staff to be safe and relatively comfortable in such a hazardous environment, further facing the potential threat of polar bear encounters. Great effort was also successfully put in place to avoid to be hit by the ongoing COVID-19 pandemic, still relatively significant at the time.

The measured quantities were almost analogous to the setup presented by Lonardi et al. (accepted) for MOSAiC. An extended meteorological package (EP) served to monitor the basic thermodynamic parameters. A broadband radiation package (BP) measured up- and downwards terrestrial irradiances. An ultrasonic anemometer package (UP) measured 3D-winds to retrieve local energy dissipation rates. Unfortunately, the instrument was heavily damaged on 20 October 2021 and had to be substituted by an hot-wire anemometer package (HP) measuring 1D-wind. The Cubic Aerosol Measurement Platform (CAMP) was used to quantify the vertical distribution of aerosol particles in two different size ranges. The Video Ice Particle Sampler (VIPS) was operated, on a single flight, to characterize the phase of cloud particles. Two additional instruments complemented the setup with in-situ sampling at a fixed height. A cloud water sampler (CWS) was used, to collect water within the cloud. Unfortunately, the sampling efficiency turned out to be too low for in-cloud observations. The high-volume and light-weight balloon-borne filter sampler (HALFBAC) was used to collect ice nucleating particles (INP) for offline chemical analysis.

3 Radiation measurements

LIM in particular operated the broadband radiation measurements to study the vertical change of terrestrial and solar irradiances. Observations of solar irradiances were discontinued due to a low-to-none presence of the solar radiation during the polar night. A total of 39 radiation flights was obtained under various cloud conditions. Figure 4 shows an ensemble of the measured net terrestrial irradiance. Derived heating rates (not shown) from the three different types of scenario generally match with the case studies

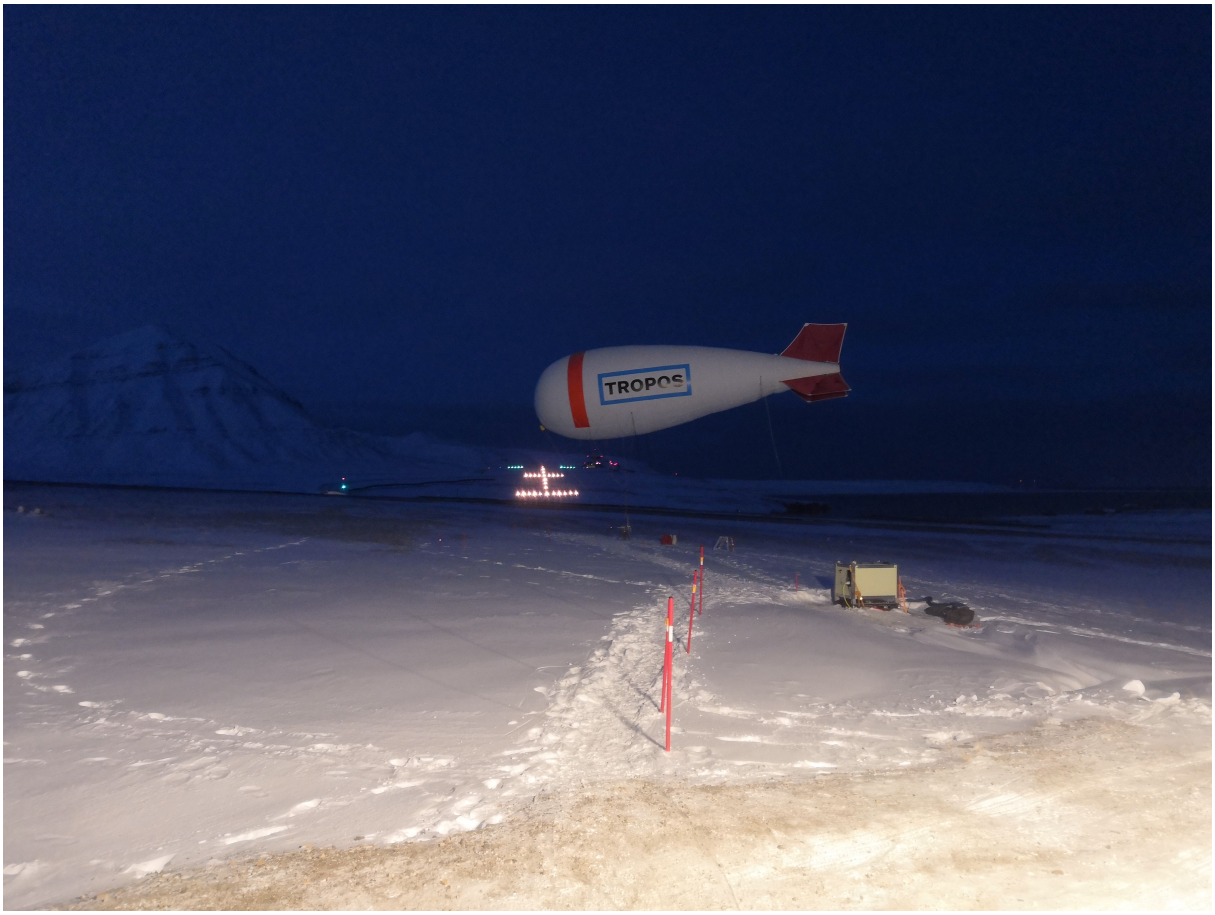

Figure 3: *View of BELUGA at the measurement site in November 2021. The lights in the background mark the runway of Ny-Ålesund airport. The mountain (left) and the open water (dark area on the right) showcase the typical geography of the area surrounding the research site.*

by Egerer et al. (2019).

In particular, 17 cases feature cloud free conditions (Fig. 4, green lines), while 18 cases represent an scenario with elevated clouds (Fig. 4, red lines), with clouds above the maximum height in reach of BELUGA. The cloud top was reached by BELUGA (Fig. 4, blue lines) only four times.

The opposing scenarios, with and without clouds, provide a base to study the vertical distribution of the cloud radiative effect (CRE). This extends the ground-based measurements of the radiation energy budget in Ny-Ålesund. In cloud free conditions, the net terrestrial irradiances are strongly negative and decrease with altitude. Furthermore, a large variability is observed among the single profiles as a result of the variations of temperature and humidity profiles due to seasonality and synoptic activity. In turn, under cloudy conditions there is no significant vertical variation in the total irradiance. As a result, the cloud radiative effect becomes stronger with altitude.

Profiles through clouds (Fig. 4, blue lines) were obtained 4 times during two distinct days (30 September and 8 November 2021). These complement the dataset by Lonardi et al. (2022) and allow for a similar analysis of single-layer clouds as presented by Lonardi et al. (accepted). Additionally, in at least one of these cases (30 September)

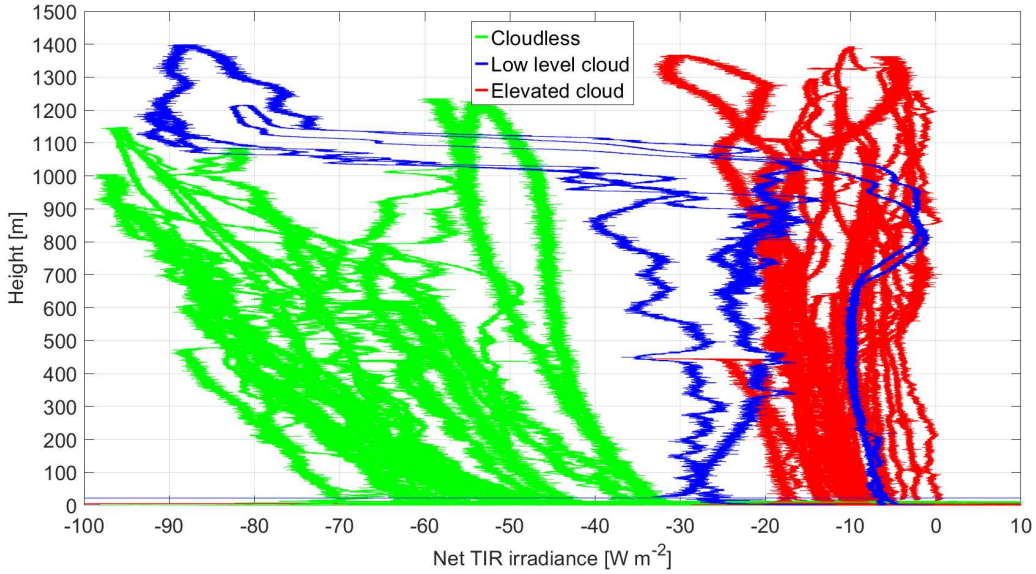

Figure 4: *Ensemble of profiles of net terrestrial irradiance. An immediate visual distinction can be made between the structure of the profiles obtained during cloud free (green), low level cloud (blue), and elevated cloud (red) conditions.*

there is a good agreement between balloon in-situ measurements, Cloudnet remote sensing retrievals, and simulations by the ICOsahedral Non-hydrostatic model (ICON). This case is currently being evaluated by a cross-cutting team within $(AC)^3$.

4 Summary and outlook

The operation of BELUGA in Ny-Ålesund during autumn 2021 provided a significant number of profiles combining thermodynamic properties, terrestrial radiation, turbulence, and aerosol particles, additionally complemented by stationary INP measurements.

Balloon-borne observations are complemented by the Ny-Ålesund time series of radiosoudings, cloudiness and cloud phase, surface thermodynamics, radiation budget, and aerosol particle concentrations.

By comparing opposing scenarios, with and without clouds, the measurements of terrestrial radiation can be used to study the vertical distribution of CRE.

A follow up tethered balloon campaign was conducted in spring 2022 and extended the autumn dataset with cold and dry spring conditions. This period was also partly covered by the airborne observations of the HALO-$(AC)^3$ campaign.

5 Acknowledgements

The authors and the BELUGA team are grateful for the invaluable support provided by the staff of AWIPEV and Kings Bay. In particular, we wish to personally thank G. Tran, Y. Dulong, F. Rader, and W. Ruhe for their efforts in providing coordination and on-site support. We also thank S. Jacobsen and V. Sand for their flexibility in ensuring the fundamental airspace clearance, and E. Havenstrøm for the logistic support at the harbour storage site.

References

Egerer, U., Gottschalk, M., Siebert, H., Ehrlich, A., and Wendisch, M.: The new BELUGA setup for collocated turbulence and radiation measurements using a tethered balloon: First applications in the cloudy Arctic boundary layer, Atmospheric Measurement Techniques, 12, doi:10.5194/amt-12-4019-2019, 2019.

Ferrero, L., Ritter, C., Cappelletti, D., et al.: Aerosol optical properties in the Arctic: The role of aerosol chemistry and dust composition in a closure experiment between Lidar and tethered balloon vertical profiles, Science of the Total Environment, 686, doi:10.1016/j.scitotenv.2019.05.399, 2019.

Lonardi, M., Ehrlich, A., and Wendisch: Tethered balloon broadband radiation profiles during MOSAiC, Wiss. Mitteil. Inst. f. Meteorolo. Univ. Leipzig, 59, 48–53, URL https://nbn-resolving.org/urn:nbn:de:bsz:15-qucosa2-780112, 2021.

Lonardi, M., Pilz, C., Siebert, H., Ehrlich, A., and Wendisch, M.: [dataset] Tethered balloon-borne measurements of terrestrial radiation during MOSAiC leg 4 in July 2020., doi:10.1594/PANGAEA.944200, URL https://doi.pangaea.de/10.1594/PANGAEA.944200, 2022.

Lupi, A., Busetto, M., Becagli, S., et al.: Multi-seasonal ultrafine aerosol particle number concentration measurements at the Gruvebadet observatory, Ny-Ålesund, Svalbard Islands, Rendiconti Lincei, 27, doi:10.1007/s12210-016-0532-8, 2016.

Maturilli, M., Herber, A., and König-Langlo, G.: Climatology and time series of surface meteorology in Ny-Ålesund, Svalbard, Earth System Science Data, 5, doi:10.5194/essd-5-155-2013, 2013.

Maturilli, M., Herber, A., and König-Langlo, G.: Surface radiation climatology for Ny-Ålesund, Svalbard (78.9° N), basic observations for trend detection, Theoretical and Applied Climatology, 120, doi:10.1007/s00704-014-1173-4, 2015.

Mazzola, M., Viola, A. P., Lanconelli, C., and Vitale, V.: Atmospheric observations at the Amundsen-Nobile Climate Change Tower in Ny-Ålesund, Svalbard, Rendiconti Lincei, 27, doi:10.1007/s12210-016-0540-8, 2016.

Nomokonova, T., Ebell, K., Löhnert, U., et al.: Statistics on clouds and their relation to thermodynamic conditions at Ny-Ålesund using ground-based sensor synergy, Atmospheric Chemistry and Physics, 19, doi:10.5194/acp-19-4105-2019, 2019.

Shupe, M. D., Rex, M., Blomquist, B., et al.: Overview of the MOSAiC expedition- Atmosphere, Elementa: Science of the Anthropocene, 10, doi:10.1525/elementa.2021.00060, 2022.

Investigating the potential to retrieve cloud droplet number concentration from ship-based measurements of spectral solar radiance during EUREC^{4}A

Ehrlich, A.[1,✉], Stapf, J.[1], Emmanouilidis, A.[1], Wolf, K.[1,a], Schäfer, M.[1], Kalesse-Los, H.[1]

[1] *Leipzig Institute for Meteorology, Leipzig University, Germany*
[a] *now at: Institute Pierre-Simon Laplace, Sorbonne Université, Paris, France*
✉*e-mail: a.ehrlich@uni-leipzig.de*

Summary: Ship-based cloud remote sensing observations made onboard R/V Meteor during the ElUcidating the RolE of Cloud-Circulation Coupling in ClimAte, EUREC^{4}A, campaign are presented and used to calculate cloud droplet number concentrations. The calculation is based on cloud liquid water path LWP and droplet effective radius r_{eff} retrieved from spectral measurements of transmitted solar radiance. It is shown that measurement uncertainties and retrieval assumptions impact the accuracy of the results. A case study indicates that the retrieval of LWP and r_{eff} is most affected by 3D-radiative effects in case of shallow cumulus and drizzle, which violates the adiabatic theory and plan-parallel geometry on which the radiative transfer simulations of the retrieval are based. Depending on the cloud thickness, the retrieval of r_{eff} might suffers from ambiguity.

These retrieval uncertainties and their implications on the estimated cloud droplet number concentration are investigated by a sensitivity study. The analysis showed that most of the uncertainty is introduced by r_{eff}, whereas LWP contributes significantly to the uncertainty only for thin clouds. Therefore, it is concluded that only selected cloud cases, which do not violate the retrieval assumption, such as stratiform cloud layers, are suited to apply the retrieval approach in further studies.

Zusammenfassung: Fernerkundungsmessungen von Wolken auf dem Forschungsschiff R/V Meteor während der ElUcidating the RolE of Cloud-Circulation Coupling in ClimAte, EUREC^{4}A, Kampagne werden vorgestellt und zur Berechnung der Tröpfchenanzahlkonzentration verwendet. Die Berechnung basiert auf Messungen des Flüssigwasserpfads LWP und dem effektiven Tröpfchenradius r_{eff}, welche aus spektralen Messungen der transmittierten solaren Strahldichte abgeleitet wurden. Es wird gezeigt, dass Messunsicherheiten und Annahmen bei der Ableitung der Wolkeneigenschaften die Genauigkeit der Ergebnisse beeinflussen. Eine Fallstudie zeigt, dass die Ableitung von LWP und r_{eff} am stärksten durch 3-dimensionale Strahlungseffekte von flachen Cumuli und Nieselregen beeinflusst wird. Beides wiederspricht den Idealisierungen von adiabatischen Wolken und einer planparallelen Geometrie, auf denen die Strahlungstransfersimulationen des Verfahrens beruhen. Abhängig von der Wolkendicke kann die Ableitung von r_{eff} zusätzlich durch Mehrdeutigkeiten beeinflusst sein.

In einer Sensitivitätsstudie wurde der Einfluss dieser Unsicherheiten auf die Berechnung von der Tröpfchenanzahlkonzentration untersucht. Die Analyse ergab, dass der größte Teil der Unsicherheit durch Retrievalunsicherheit von r_{eff} verursacht wird, wogegen LWP nur bei dünnen Wolken einen wesentlichen Beitrag leistet. Deshalb wird geschlussfolgert, dass nur ausgewählte Wolkenfälle, die die Annahmen der Methode nicht verletzen, wie z. B. stratiforme Wolkenschichten, geeignet sind, um die Methode in weiteren Studien anzuwenden.

1 Introduction

The cloud droplet number concentration CDNC is a key parameter, which significantly regulates the cloud radiative effects (Wolf et al., 2019). Therefore, estimates of the CDNC from observations are highly desired either from satellite or ground-based instruments (Grosvenor et al., 2018). Ground-based measurements of transmitted solar spectral radiance or irradiance have frequently been used to derive cloud properties of liquid clouds and cirrus (e.g., Brückner et al., 2014; Schäfer et al., 2013; LeBlanc et al., 2015). The spectral measurements are often converted into spectral ratios or normalized radiances to reduce the impact of calibration uncertainties. However, other studies such as, e.g. Fielding et al. (2014, 2015) or Merk et al. (2016), use absolute radiances or a combination of passive and active remote sensing to characterize clouds.

The adiabatic cloud theory provides a basis to calculate the CDNC from observed cloud properties (Brenguier et al., 2000). This approach has previously been applied for active ground-based and passive satellite remote sensing observations, using the retrieved cloud liquid water path LWP, cloud droplet effective radius r_{eff}, and adiabaticity factor. Here, we apply this approach to ship-based observations including passive spectral solar radiance measurements. The observations and uncertainties are presented with respect to their effect on the retrieval of LWP and r_{eff}. The CDNC retrieval theory is then adapted to the transmissivity observations and tested by a sensitivity study and furthermore applied to potential cloud cases.

2 Passive solar cloud remote sensing during EUREC^{4}A

2.1 Spectral solar radiance measurements

The COmpact RAdiation measurements System spectrometer system (CORAS, Brückner et al., 2014) was deployed during EUREC^{4}A in January and February 2020 on the research vessel R/V Meteor. CORAS was configured to measure spectral solar radiance in zenith viewing directions with a sampling frequency of about 6 s. Individual measurements were obtained with an integration time of 300 – 500 ms. The setup consisted of two separate radiance inlets; one of them was installed on the stabilized cloud radar platform correcting for ship motion, the second one was installed on the microwave radiometer which was operated non-stabilized.

The radiance optical inlets feature an opening angle of 2°, which results in a cross track resolution of about 35 m assuming a cloud base at 1 km altitude. The zenith radiance of the stabilized inlet is analyzed by two separated grating spectrometers, which cover the visible (380 – 1000 nm) and near-infrared (900 – 2000 nm) wavelength range. The

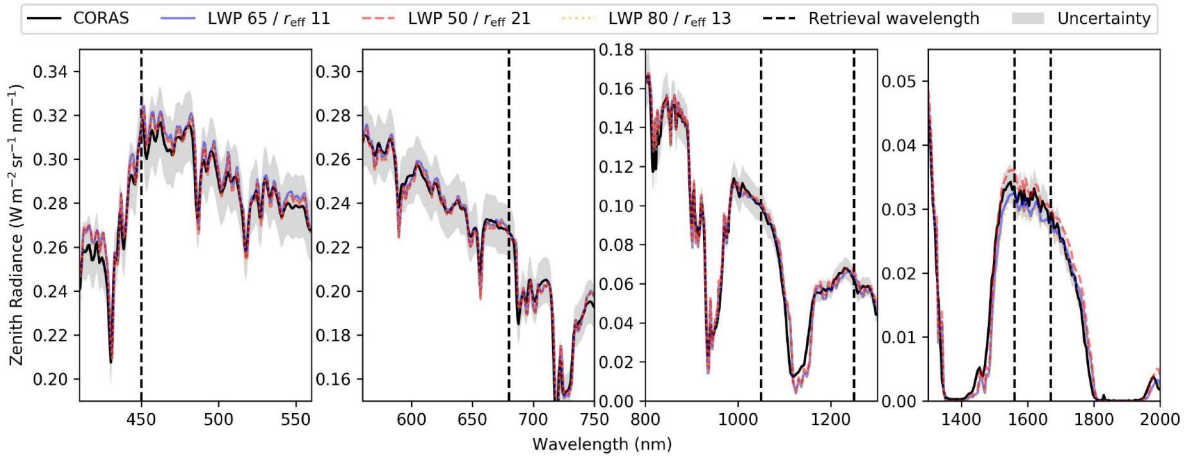

Figure 1: *Spectral zenith radiance observed by CORAS for a homogeneous stratocumulus field on 24 January 2020 around 14:20 UTC compared to radiative transfer simulations using three different combinations of LWP and* r_{eff}. *Uncertainties (gray area) and potential wavelengths used in a cloud and CDNC retrieval (vertical lines) are shown.*

non-stabilized radiance is available only for the near-infrared wavelength range, which is sufficient for most common cloud retrievals. The spectral resolution of the spectrometers was quantified by the full width at half maximum of the individual wavelength and is 2 – 3 nm in the visible and, 15 nm near-infrared range, respectively.

In order to monitor changes in the radiometric calibration of the instrument, transfer calibrations with a portable integrating sphere were regularly performed in the course of the campaign. Significant changes due to the temperature dependence of the system and the deposition of sea salt on the inlets were observed and corrected. The uncertainties of the measured radiance amount up to 8 % and are mostly dominated by the radiometric calibration as discussed in Brückner et al. (2014). For ratios of two different wavelengths the uncertainties are significantly reduced but might be prone to spectral shifts of the radiometric calibration over time, which was indicated by the transfer calibrations to introduce spectral uncertainties of about 1 %. During EUREC^{4}A the near-infrared spectrometer sometimes have been overexposed, in particular at cloud edges, where cloud side effects enhance the solar irradiance. These data were filtered carefully.

An example of the observed radiance is shown in Fig. 1. The radiance spectra obtained from the two spectrometers were merged at 990 nm. Using a LWP of 65 g m^{-2} as derived from the simultaneous microwave radiometer measurements and assuming a cloud droplet effective radius $r_{\mathrm{eff}} = 11\ \mu$m, radiative transfer simulations with the library of radiative transfer (libRadtran, Emde et al., 2016) were performed. The simulated spectral radiances were then compared to the observations. To test the sensitivity of the spectral radiance with respect to the assumed r_{eff} and LWP, two other combinations of LWP and r_{eff} typical for trade wind cumulus were simulated ($LWP = 50\,\mathrm{g\,m^{-2}}$ and $r_{\mathrm{eff}} = 21\,\mu$m as well as $LWP = 80\,\mathrm{g\,m^{-2}}$ and $r_{\mathrm{eff}} = 13\,\mu$m, cf. Fig. 1). The simulations show almost identical radiances except for the wavelength around 1600 nm. This illustrates the ambiguity of zenith radiance with respect to their dependence on LWP, cloud particle size and also cloud droplet number concentration.

2.2 Retrieval of liquid water path and effective droplet radius

Different approaches to retrieve LWP and r_{eff} have been applied to estimate the retrieval uncertainties. All retrievals are based on spectral radiance measured by CORAS and look-up tables derived from radiative transfer simulations by libRadtran. In the simulations, clouds were constructed by the sub-adiabatic cloud model with adiabaticity factor of 0.7 and a range of LWP and r_{eff} covering the conditions experienced during EUREC^{4}A. Cloud boundaries were obtained from cloud radar observations on R/V Meteor. The retrievals use either the classic ratio method (Brückner et al., 2014) or a combination of cloud transmissity at eight wavelengths. The eight wavelengths approach includes the six wavelengths used in Brückner et al. (2014) and add measurements at 500 nm and 860 nm wavelength to improve the sensitivity to LWP. To constrain the retrieval, for both approaches, an option prescribing the LWP with observations from the microwave radiometer are tested. The ratio method was applied in two version. One using the original wavelength combination by (Brückner et al., 2014). A second version using an alternative wavelength combination, 500 nm and 860 nm, was tested. As a benchmark, LWP obtained by a passive microwave radiometer (HATPRO) are used.

Figure 2 compares LWP and r_{eff} as retrieved by all different approaches for a time period observed on 2 February 2020. The period was characterized by the presence of shallow cumulus and thin strato-cumulus with low $LWP < 100\,\text{g}\,\text{m}^{-2}$ and a deeper cloud field with LWP reaching up to $400\,\text{g}\,\text{m}^{-2}$ as indicated by the microwave radiometer. The highest LWP of around $400\,\text{g}\,\text{m}^{-2}$ are reached during around 12:15 – 12:30 UTC when the cloud radar still observed hydrometeors at lowest radar range gate (300 m) which likely did not evaporate before reaching the surface. Thus, the LWP from the microwave radometer might be less trustworthy if the radiometer radome got wet. It also has to be noted that the microwave radiometer was not corrected for the cloud-free offset, which typically ranges up to $30\,\text{g}\,\text{m}^{-2}$. However, depending on the retrieval approach, the retrieved LWP significantly differ. Both ratio retrievals overestimate the LWP of the shallow cumulus after 13:00 UTC, while they partly underestimate the LWP of the thick cloud field. The transmissivity approach shows more reasonable results, especially for shallow cumulus periods and in cloud-free conditions. The results of the retrievals, which are constrained by the LWP naturally match the LWP of the microwave radiometer best.

The retrieved r_{eff} was not filtered for spurious results, e.g., overestimations in r_{eff} close to 25 μm, which is linked to cloud edges and cloud-free conditions. In general, the shallow cumulus shows smaller r_{eff} than the deeper cloud field. Comparing the different retrieval approaches indicates that the unconstrained methods, except the one using 500 nm and 860 nm, result in higher r_{eff} than the methods that are constrained by the LWP from the microwave radiometer. These results demonstrate the sensitivity of the retrieval with respect to the choice of wavelength. This is partly linked to spectral measurement uncertainties. In addition, the vertical weighting functions of the transmissivity retrievals, and therefore, the retrieved r_{eff} depend on the location of the chosen wavelengths in the water absorption band.

This sensitivity study suggests that although nadir radiances measured by CORAS are ambiguous as a function of cloud LWP, a high information content and sensitivity is found with respect to r_{eff}, when an estimate of cloud LWP is given and used to constrain the retrieval. LWP estimates, for example provided by the microwave radiometer, allows

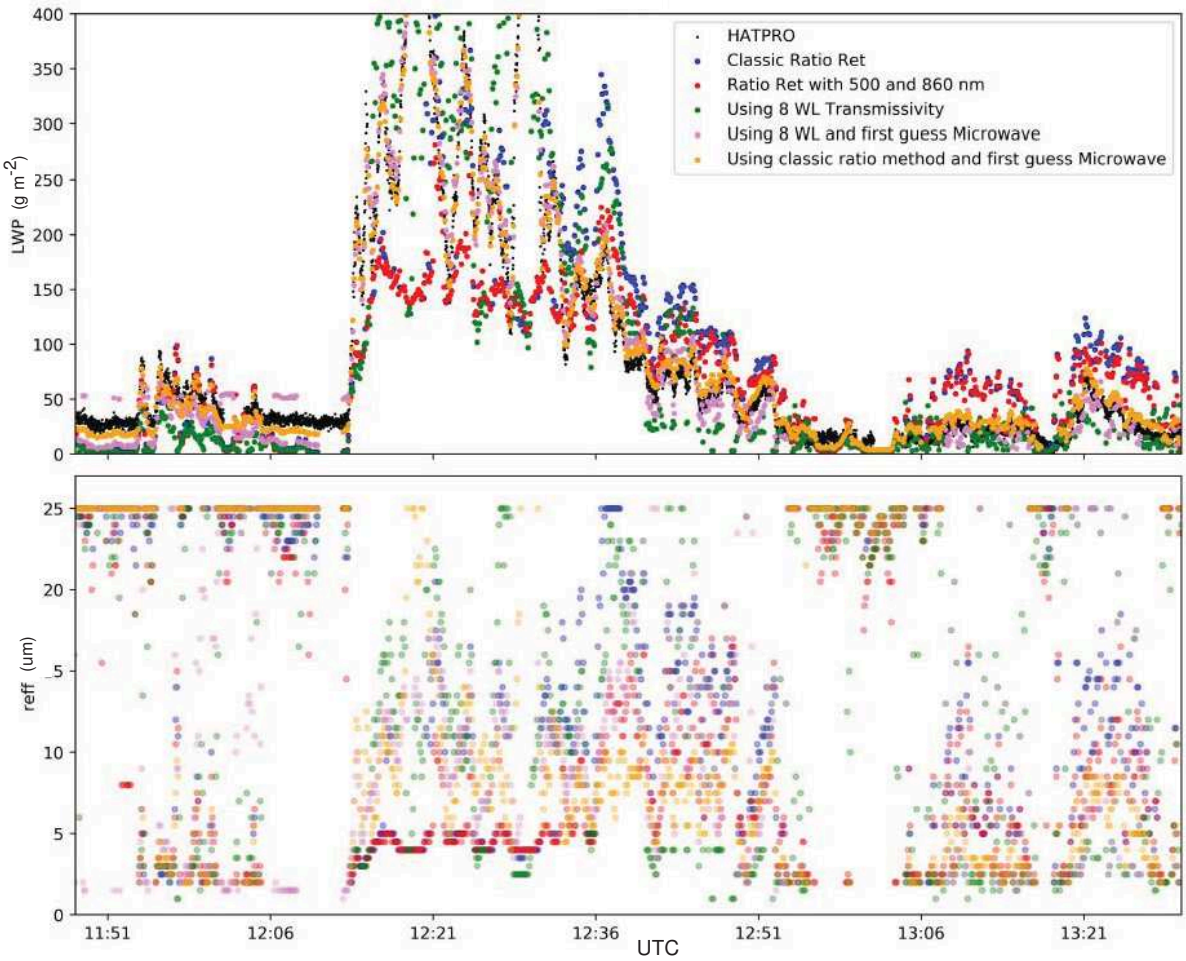

Figure 2: *Time series of LWP and r_{eff} retrieved by different methods using spectral radiance from CORAS measured onboard R/V Meteor on 2 February 2020. For LWP, the passive microwave radiometer measurements (HATPRO) are included.*

pre-separating between low and high LWP. However, the LWP threshold is not fixed and, based on thresholds, ranges between $20\,\mathrm{g\,m^{-2}}$ and $60\,\mathrm{g\,m^{-2}}$ depending on solar zenith angle and r_{eff}. Unfortunately, shallow trade wind cumulus as observed frequently during EUREC^{4}A often falls into this LWP ambiguity range.

3 CDNC Retrieval from ground based transmissivity measurements

3.1 Theory

For retrieving the cloud droplet number concentration N in stratiform clouds from satellite remote sensing, Brenguier et al. (2000) and Wood (2006) proposed a relation, which links N to the cloud liquid water path LWP and the cloud effective radius $\tilde{r}_{\mathrm{eff}}$ based on reflectivity retrievals:

$$N = \frac{3 \cdot \sqrt{2}}{4 \cdot \pi \cdot \rho_{\mathrm{w}}} \cdot \sqrt{f_{\mathrm{ad}} \cdot \Gamma_{\mathrm{ad}}} \cdot \frac{\sqrt{LWP}}{\tilde{r}_{\mathrm{eff}}^3} \tag{1}$$

with ρ_w the density of liquid water, f_{ad} the degree of adiabaticity, and Γ_{ad} the adiabatic rate of increase of liquid water content with respect to height.

In this relation $\tilde{r}_{eff}$ should not be mistaken with r_{eff}, the effective cloud droplet radius retrieved from transmissivity measurements as used in Section 2. Here, $\tilde{r}_{eff}$ represents the cloud droplet radius at cloud top $\tilde{r}_{eff} = r(h_{top})$, to consider the high sensitivity of satellite retrievals to cloud top layers. Vertical weighting functions of reflectivity retrievals are presented by Platnick (2000) and were shown to not penetrate deep into the clouds. Platnick (2000) also showed that the weighting functions for transmissivity measurements are more uniform and weights the profile of particle sizes equally. Therefore, retrievals based on transmissivity provide an estimate of the mean droplet radius averaged over the entire $r_{eff} = \overline{r}$.

The profile of cloud particle radius in stratiform clouds can be calculated by:

$$r(h) = B \cdot h^{1/3} \quad \text{with} \quad B = \left(\frac{3}{4 \cdot \pi \cdot \rho_w} \cdot \frac{\Gamma_{ad}}{N} \right)^{1/3} \tag{2}$$

From that, $\overline{r}$ can be derived by integration of $r(h)$:

$$r_{eff} = \overline{r} = \frac{1}{h} \cdot \int_0^{h_{top}} B \cdot h^{1/3} \mathrm{d}h, \tag{3}$$

$$r_{eff} = B \cdot \frac{3}{4} \cdot h_{top}^{1/3}, \tag{4}$$

$$r_{eff} = \frac{3}{4} \cdot \tilde{r}_{eff}. \tag{5}$$

This conversion of the reflectivity-based cloud effective radius into the transmissivity-based cloud droplet radius is used to convert Eq. 1 into a relation for calculating N from transmissivity measurements:

$$N = \left(\frac{3}{4} \right)^4 \cdot \frac{\sqrt{2}}{\pi \cdot \rho_w} \cdot \sqrt{f_{ad} \cdot \Gamma_{ad}} \cdot \frac{\sqrt{LWP}}{r_{eff}^3}. \tag{6}$$

To calculate N, measurements of LWP, r_{eff} and assumptions on the adiabaticity factor f_{ad} are required. As discussed by, e.g., Wolf et al. (2019) for reflectivity-based retrieval and Merk et al. (2016) for ground-based observations, these three parameters can be obtained by different combinations of remote sensing measurements. For example, passive spectral solar and microwave radiometer measurements, and active lidar and radar observations were combined. Here, LWP from the microwave radiometer is applied. r_{eff} is obtained from the constrained ratio retrieval of CORAS. Radar and lidar (ceilometer) cloud boundaries are used to calculate the cloud height H, which in combination with LWP is used to derive f_{ad}:

$$\Gamma_{obs} = f_{ad} \cdot \Gamma_{ad} = \frac{2 \cdot LWP}{H^2}. \tag{7}$$

This reduces Eq. 6 to:

$$N = \left(\frac{3}{4} \right)^4 \cdot \frac{2}{\pi \cdot \rho_w \cdot H} \cdot \frac{LWP}{r_{eff}^3}. \tag{8}$$

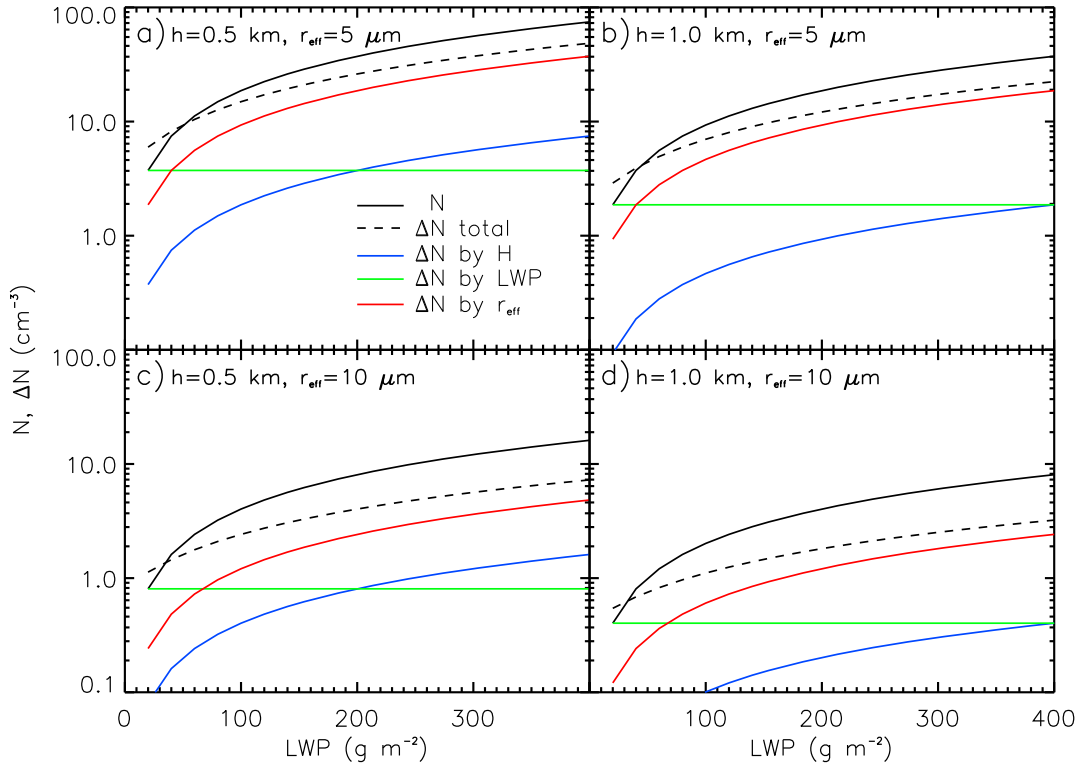

Figure 3: *Cloud droplet number concentration N and uncertainty ΔN calculated for different combinations of H, r_{eff}, and LWP.*

3.2 Sensitivity study

To analyse the potential of a CDNC retrieval and the impact of the measurement uncertainties on the retrieved cloud properties, a sensitivity study based on Eq. 8 was performed. For different combinations of H, r_{eff}, and LWP, representing the typical range of sub-tropical boundary layer clouds, the cloud droplet number concentration N was calculated. The uncertainty ΔN was estimated by Gaussian uncertainty propagation assuming that cloud altitude is measured with an uncertainty of $\Delta H = 50\,\mathrm{m}$, cloud particle size is retrieved with uncertainty of $\Delta r_{\mathrm{eff}} = 1\,\mu\mathrm{m}$, and LWP is derived with an uncertainty of $\Delta LWP = 20\,\mathrm{g\,m^{-2}}$. To estimate, which quantity contributes most to the total uncertainty ΔN, also separate uncertainties by each of the measured cloud properties were calculated.

Figure 3 shows N and ΔN for four clouds in dependence of LWP. In all cases, the total uncertainty may exceed 100 % for cloud with small LWP and low N, respectively. For higher LWP and N, absolute uncertainties increase but relatively uncertainties decrease to about 50 %. For most clouds, the strongest impact on the total uncertainty results from uncertainties of r_{eff}. Only for small LWP, the uncertainty of LWP is dominant. While LWP contributes linear to the calculation of N, the dependence on r_{eff} is cubic (compare Eq. 8) and, therefore, is more prone to uncertainties. This holds especially for clouds

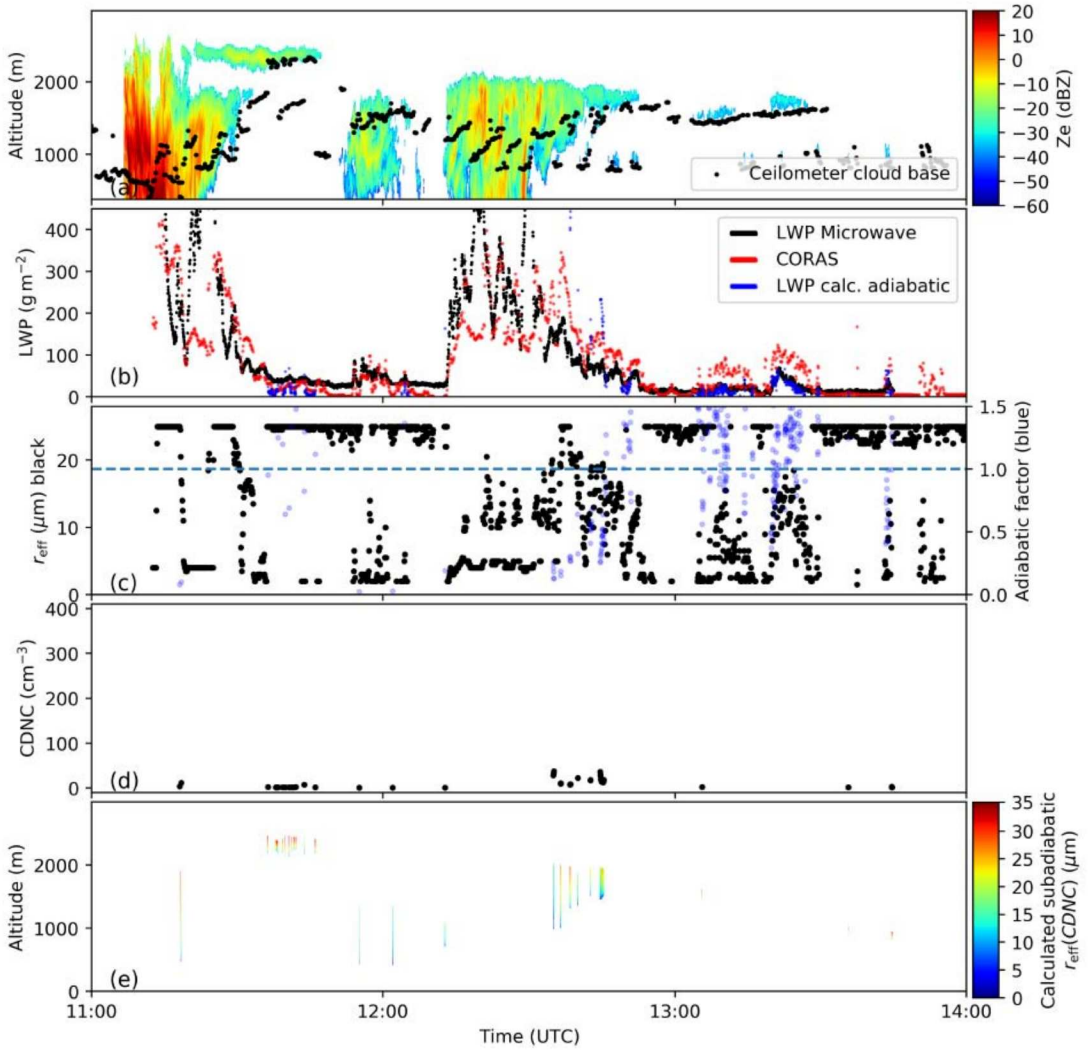

Figure 4: *Time series of cloud radar reflectivity and ceilometer cloud base altitude (a), LWP retrieved from CORAS and microwave radiometer (b), retrieved* r_{eff} *and* f_{ad} *(c), retrieved (g m-2) (d) and calculated profile of cloud droplet effective radius (e) for 2 February 2020,* 11 – 14 *UTC.*

with small droplets (i.e. small r_{eff}) as indicated when comparing the different cases in Fig. 3.

These calculations suggest that the accuracy of the retrieval of N strongly depends on a quantitative estimation of the cloud droplet effective radius. While an accurate retrieval of LWP is important only for thin clouds, the geometrical thickness of the cloud is less critical. This indicates that the accuracy of the retrieval of cloud properties as discussed in Section 2.2 may limit the potential to retrieve N. Especially the uncertainty of r_{eff} in case of broken clouds, which are affected by 3D radiative effects, will not allow for deriving a reasonable N.

4 Potential cloud cases

The retrieval approach introduced above is based on several assumptions, which in reality might be violated. Horizontal homogeneous cloud layers are assumed in the plane parallel

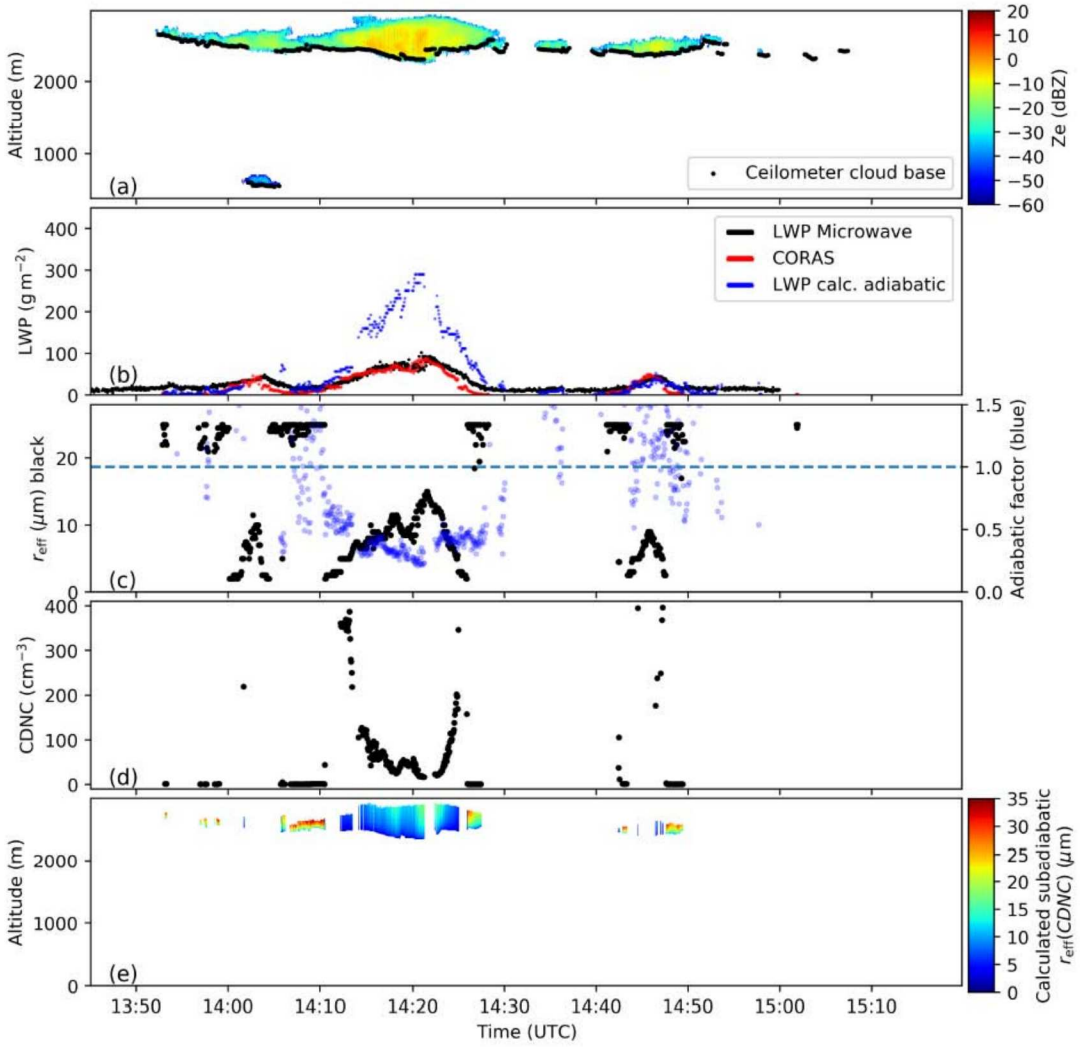

Figure 5: *Time series of radar reflectivity and ceilometer cloud base altitude (a), LWP retrieved from CORAS and microwave radiometer (b), retrieved r_{eff} and f_{ad} (c), retrieved CDNC (d) and calculated profile of cloud droplet effective radius (e) for 24 January 2020.*

radiative transfer simulations of the cloud retrieval of r_{eff}. As outlined by Fielding et al. (2014) for heterogeneous cumulus, three-dimensional (3D) radiative transfer is required to account for 3D radiative effects. Depending on the solar zenith angle and the aspect ratios of cloud height to width, the photon path length through the cloud side does change and may affect the absorption by cloud droplets imprinted in the zenith radiance. In this case, one-dimensional plane-parallel simulations inadequately represent the transmitted radiation.

The CDNC retrieval assumes the adiabatic cloud model which is not valid in the presence of drizzle. Therefore, precipitating clouds have to be filtered from the analysis. The cloud base height is often difficult do determine in case of full signal attenuation of the lidar observations, as is cloud top altitude from radar reflectivity. Due to these measurement uncertainties of the cloud boundaries, also the adiabatic factor can be biased and become non-physically. Often cases with $f_{\mathrm{ad}} > 1$ were observed for which a calculation of N using the adiabatic theory is not possible (Merk et al., 2016).

These constrains limit the number of potential cloud cases from EUREC^{4}A. Here two cases with stratiform clouds are presented. Figure 4 shows a time series of all relevant cloud parameters measured on 2 February 2020. The three hour period is characterized by a sequence of warm convection, which partly formed precipitation. In the core of the convective cell, LWP up to 400 g m^{-2} were observed. Due to the drizzle, LWP derived from CORAS and the microwave radiometer differ significantly and the retrieved r_{eff} become non-reliable. Additionally, for this cloud, r_{eff} varies around the ambiguity range of the transmissicity retrieval, which is obvious by the absence of any solution between 7-11 μm. For smaller trade wind cumuli at low altitudes, 3D-radiative effects biased the retrieval by CORAS. Therefore, N was calculated only for short periods of the time series, e.g., the stratiform cloud layer in about 2200 m altitude observed around 11:30 UTC.

A second case, where only stratiform clouds were observed, is presented in Figure 5. For this almost ideal scenario, LWP retrieved by CORAS and the microwave radiometer agree well. The retrieved r_{eff} ranged between 4 μm in thinner cloud parts and 15 μm in the thicker parts of the cloud layer. In this section of the cloud the retrieved N become more reliable and range around 50 cm^{-3}. However, also here the retrieval of N seems to fail when the cloud layer becomes thin and LWP decreases below 30 g m^{-2}, which agrees with the sensitivity study presented in Section 3.2.

5 Summary and conclusions

Spectral solar irradiance measurements on board of R/V Meteor obtained during the EUREC^{4}A campaign are presented and used in combination with active and passive microwave remote sensing to estimate the cloud droplet number concentration. The ship-based measurements turned out to be challenging due to a non-stable radiometric calibration caused by temperature effects and deposition of sea salt, which results in a higher measurement uncertainty compared to ground-based observations (Brückner et al., 2014). The measurement uncertainty impacts the retrieval of cloud properties using transmissivity based retrieval such as presented by Brückner et al. (2014) or LeBlanc et al. (2015). Therefore, different approaches to derive LWP and r_{eff} were tested. The case study indicated that retrieval uncertainties can result from 3D-radiative effects in case of shallow cumulus and drizzle, which violates the adiabatic theory on which the radiative transfer simulations of the retrieval are based. Due to the range of LWP present during the measurements, which falls into the ambiguity range of the retrieval, the retrieval of r_{eff} may partly fail. However, synergistic approaches that combine active and passive remote sensing similar to Fielding et al. (2015) are possible.

An approach to calculate the cloud droplet number concentration N from ground-based observations using r_{eff} retrieved from the spectral irradiance measurements is presented. The approach is based on common reflectivity-based retrieval of N (e.g., Merk et al., 2016; Wolf et al., 2019) and was converted for the r_{eff} observed by transmissivity-based retrieval. A sensitivity study showed that the uncertainty of N is dominated by the uncertainty of r_{eff}, This indicates that the limitation of the retrieval of LWP and r_{eff} can significantly bias the retrieval of N. Therefore, data need to be filtered for 3D-radiative effects, the ambiguity range of the retrieval and drizzle. This was demonstrated by two cases. Cloud sections, which can potentially be used to retrieve N were identified. These

sections are mostly limited to non-precipitating stratiform clouds. As discussed by e.g., Fielding et al. (2015) and Merk et al. (2016), further analysis is required to refine the retrieval approach and select the most suited approach to combine the different passive and active measurements.

References

Brenguier, J.-L., Pawlowska, H., Schüller, L., et al.: Radiative properties of boundary layer clouds: Droplet effective radius versus number concentration, J. Atmos. Sci., 57, 803–821, doi:10.1175/1520-0469(2000)057<0803:RPOBLC>2.0.CO;2, 2000.

Brückner, M., Pospichal, B., Macke, A., and Wendisch, M.: A new multispectral cloud retrieval method for ship-based solar transmissivity measurements, J. Geophys. Res. Atmos., 119, 11,338–11,354, doi:10.1002/2014JD021775, 2014.

Emde, C., Buras-Schnell, R., Kylling, A., et al.: The libRadtran software package for radiative transfer calculations (version 2.0.1), Geosci. Model Dev., 9, 1647–1672, doi:10.5194/gmd-9-1647-2016, 2016.

Fielding, M. D., Chiu, J. C., Hogan, R. J., and Feingold, G.: A novel ensemble method for retrieving properties of warm cloud in 3-D using ground-based scanning radar and zenith radiances, J. Geophys. Res., 119, 10,912–10,930, doi:10.1002/2014JD021742, 2014.

Fielding, M. D., Chiu, J. C., Hogan, R. J., et al.: Joint retrievals of cloud and drizzle in marine boundary layer clouds using ground-based radar, lidar and zenith radiances, Atmos. Meas. Tech., 8, 2663–2683, doi:10.5194/amt-8-2663-2015, 2015.

Grosvenor, D. P., Sourdeval, O., Zuidema, P., et al.: Remote Sensing of Droplet Number Concentration in Warm Clouds: A Review of the Current State of Knowledge and Perspectives, Rev. Geophys., 56, 409–453, doi:10.1029/2017RG000593, 2018.

LeBlanc, S. E., Pilewskie, P., Schmidt, K. S., and Coddington, O.: A spectral method for discriminating thermodynamic phase and retrieving cloud optical thickness and effective radius using transmitted solar radiance spectra, Atmos. Meas. Tech., 8, 1361–1383, doi:10.5194/amt-8-1361-2015, 2015.

Merk, D., Deneke, H., Pospichal, B., and Seifert, P.: Investigation of the adiabatic assumption for estimating cloud micro- and macrophysical properties from satellite and ground observations, Atmos. Chem. Phys., 16, 933–952, doi:10.5194/acp-16-933-2016, 2016.

Platnick, S.: Vertical photon transport in cloud remote sensing problems, J. Geophys. Res., 105, 22 919–22 935, doi:10.1029/2000JD900333, 2000.

Schäfer, M., Bierwirth, E., Ehrlich, A., Heyner, F., and Wendisch, M.: Retrieval of cirrus optical thickness and assessment of ice crystal shape from ground-based imaging spectrometry, Atmos. Meas. Tech., 6, 1855–1868, doi:10.5194/amt-6-1855-2013, 2013.

Wolf, K., Ehrlich, A., Jacob, M., et al.: Improvement of airborne retrievals of cloud droplet number concentration of trade wind cumulus using a synergetic approach, Atmos. Meas. Tech., 12, 1635–1658, doi:10.5194/amt-12-1635-2019, 2019.

Wood, R.: Relationships between optical depth, liquid water path, droplet concentration and effective radius in an adiabatic layer cloud, personal note, 2006.

CIRRUS-HL: Overview of LIM contributions

Röttenbacher, J.[1,✉] **and Luebke, A. E.**[1,✉]
Müller H.[1], **Ehrlich, A.**[1], **Schäfer, M.**[1], **Kirbus B.**[1], **Wendisch, M.**[1]

[1] *Leipzig Institute for Meteorology, Universität Leipzig, Leipzig, Germany*
✉*e-mail: johannes.roettenbacher@uni-leipzig.de, anna.luebke@uni-leipzig.de*

Summary: From June to July 2021, the Leipzig Institute for Meteorology (LIM) participated in the Cirrus in High Latitudes (CIRRUS-HL) campaign. Utilizing the German High Altitude Long Range Research Aircraft (HALO), 24 research flights were conducted out of Oberpfaffenhofen, Germany. The initial goal of the campaign was to sample high-latitude cirrus clouds with a combination of in-situ and remote sensing instrumentation. However, due to the global coronavirus pandemic, the flights had to be carried out from southern Germany instead of northern Sweden. Thus, the flight time in Arctic latitudes was limited. Therefore, more objectives concerning midlatitude cirrus were included in the campaign goals. LIM contributed to CIRRUS-HL with measurements by the Broadband AirCrAft RaDiometer Instrumentation (BACARDI) and the Spectral Modular Airborne Radiation measurement sysTem (SMART). While BACARDI measured broadband solar and terrestrial upward and downward irradiance, SMART measured spectrally resolved solar upward radiance as well as upward and downward irradiance.

Zusammenfassung: Von Juni bis Juli 2021 nahmen einige Mitarbeitende des LIM an der CIRRUS-HL Kampagne teil. Mit dem deutschen Forschungsflugzeug HALO (High Altitude Long Range Research Aircraft) wurden 24 Forschungsflüge von Oberpfaffenhofen, Deutschland, aus durchgeführt. Ursprüngliches Ziel der Kampagne war es, Zirruswolken in hohen Breitengraden mit einer Kombination aus In-situ- und Fernerkundungsinstrumenten zu untersuchen. Aufgrund der weltweiten Corona-Pandemie mussten die Flüge jedoch von Süddeutschland statt von Nordschweden aus durchgeführt werden. Daher wurden weitere Ziele in Bezug auf Zirruswolken in mittleren Breiten in die Ziele der Kampagne aufgenommen. Das LIM-Team betrieb die breitbandigen und spektralen Strahlungssensoren BACARDI (Broadband AirCrAft RaDiometer Instrumentation) und SMART (Spectral Modular Airborne Radiation measurement sysTem), wobei BACARDI die breitbandige solare und terrestrische Auf- und Abwärtsstrahlung und SMART die spektral aufgelöste solare Auf- und Abwärtsstrahlung sowie die Aufwärtsstrahlungsdichte maß.

1 Introduction

The impact of cirrus clouds on our current and changing climate is a critical point for comprehending the Earth's climate system. In particular, cirrus clouds in the Arctic present a key uncertainty of the Arctic energy budget as it might switch from a warming to a cooling effect depending on the changing properties of clouds moving between ocean and ice covered surfaces and the sensitivity of the larger climate system to perturbations. Midlatitude cirrus clouds were studied with the German High Altitude Long Range Research Aircraft (HALO) in the MidLatitude Cirrus (ML-CIRRUS) airborne campaign in 2014. Building onto that successful mission and the established extensive instrument payload, the CIRRUS-HL campaign was carried out in June and July 2021 to probe Arctic cirrus clouds. The scope of the mission is to study formation, properties, and climate impacts of cirrus clouds in high latitudes, compare them to midlatitude cirrus and investigate the aviation impact on cirrus. The main objectives were to quantify ice crystal properties, the impact of the aerosol particles and the radiative effects of cirrus clouds.

Due to the impact of the ongoing coronavirus pandemic on the logistics of the campaign, the original spring time frame for the campaign and measurements based out of Kiruna, Sweden, could not be realized. Instead, the campaign was shifted to Oberpfaffenhofen, Germany, and moved to the summer. This compelled the scientists to reevaluate their flight strategies, and the major goals of the mission could still be achieved while incorporating further research objectives.

A team of scientists from the Leipzig Institute for Meteorology (LIM) participated in this study with two remote sensing packages on board. The following sections provide more details on the goals of the campaign, an overview of the campaign results, information on the instruments operated by LIM and a case study demonstrating how the measurements from these instruments can be used for future analyses.

2 Campaign overview and instrumentation

The CIRRUS-HL campaign resulted in 24 measurement flights with a total of 146 flight hours. Figure 1 illustrates an overview of the flight tracks from the campaign. In order to accommodate more time spent measuring in the Arctic, several flight days included double flights, wherein HALO would refuel in the Arctic to extend the measurement time in high latitudes. However, HALO also took advantage of its home base in Oberpfaffenhofen and managed to also fly in midlatitude cirrus systems and obtain measurements collocated with ground-based stations across Germany in Jülich, Leipzig, Munich and Lindenberg.

The research flights were designed to follow one or more of the seven objectives of CIRRUS-HL, which comprise Arctic in-situ cirrus in ice supersaturated regions (ISSR), Arctic frontal cirrus, midlatitude in-situ cirrus, midlatitude frontal cirrus, embedded contrails in cirrus, contrail cirrus hotspots and exemplary cases of cirrus influenced by soot.

The LIM team operated two passive radiation sensors on board HALO. Both instruments are described in the following subsections, and for reference, their respective

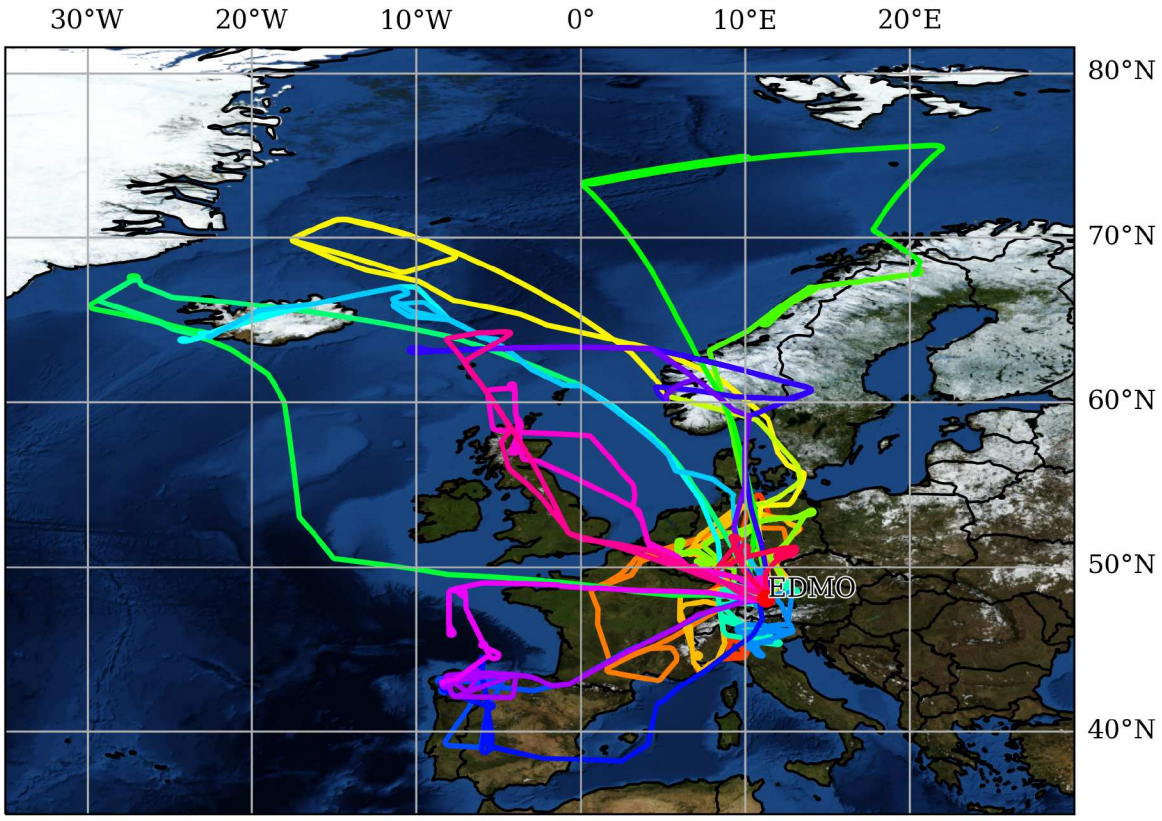

Figure 1: *Flight tracks from all 24 research flights during CIRRUS-HL (background: NASA Visible Earth).*

positions on the aircraft can be seen in Fig. 2. In addition, Table 1 provides an overview of both instruments and key specifications.

Figure 2: *HALO during landing with the locations of the different radiation sensors. Photo: Andreas Minikin; Instrument photos: Roger Riedel, Hanno Müller.*

Table 1: *Overview of instrument specifications.*

Instrument	**Time resolution**	**FOV**	**Wavelength range**	**Vertical resolution**	**Measured quantity**	**Derived/retrieved parameters**
BACARDI	0.1 s	180°	0.2 – 3.6 µm (pyranometer); 4.5 – 42 µm (pyrgeometer)	integrated	Up- and downward broadband solar and terrestrial irradiance	Albedo, net irradiance, heating rate profiles
SMART	0.3 s	180°, 2° (radiance)	0.3 – 2.2 µm	integrated	Up- and downward spectral irradiance, upward spectral radiance	Cloud top reflectivity, spectral net irradiance, albedo

2.1 Overview of instrumentation

The majority of the instrumentation on board HALO for the CIRRUS-HL campaign is designed for in-situ measurements (Voigt et al., 2017). Thirteen in-situ instruments with inlets on the fuselage of the aircraft were installed to measure water vapor, water content and different aerosols. Eight more cloud probe instruments employing various measurement techniques were installed along the wings of HALO. These cloud probes provide valuable information concerning cloud particle number concentrations and images of cloud particles to determine particle sizes and shapes. In addition to the remote sensing instruments operated by LIM, the WALES lidar (name derived from WAter vapor Lidar Experiment in Space; Wirth et al., 2009) and the spectral imager (specMACS; Ewald et al., 2016) were also part of the payload. A schematic overview is shown in Fig. 3 where a) shows the instruments located inside the aircraft with inlets or windows on the fuselage of HALO and b) shows the particle and in-situ probes mounted on the wings of HALO. A more detailed description of each instrument is given on the campaign website https://cirrus-hl.de/instruments.

2.2 BACARDI

The radiometer package on HALO, the Broadband AirCrAft RaDiometer Instrumentation (BACARDI), consists of two sets of Kipp and Zonen pyranometers (CMP 22) and pyrgeometers (CGR-4) mounted to the fuselage of the aircraft. The upward and downward solar ($0.2 - 3.6\,\mu m$) and terrestrial ($4.5 - 42\,\mu m$) irradiances at flight level are measured using this configuration of four radiometers. Based on these measurements, the radiative forcing of cirrus clouds can be calculated with the help of radiative transfer simulations. Because the instruments measure the irradiance of the full sky, including cloudy and cloud-free areas, simulations are performed using the libRadtran package (Emde et al., 2016) to calculate the irradiance of the cloud-free case in order to isolate cloud radiative effects alone (Luebke et al., 2022). A more detailed description of the instrument as well as the measurement uncertainties and post-processing are provided in Luebke et al. (2022). Postprocessed data from the BACARDI instrument for the CIRRUS-HL campaign are published on the HALO Database (https://halo-db.pa.op.dlr.de/).

2.3 SMART

During CIRRUS-HL, the Spectral Modular Airborne Radiation measurement sysTem (SMART; Wolf et al., 2019) measured downward and upward irradiance as well as upward nadir radiance in the spectral range between 0.3 µm and 2.2 µm. The spectral resolution (Full Width at Half Maximum (FWHM)) of the instrument is $2 - 3$ nm for wavelengths below 1.0 µm and 10 –15 nm for longer wavelengths. The integration time was set to 300 ms resulting in a temporal resolution of 3.3 Hz. The radiance sensor has a field of view of $2\,^\circ$, which together with the temporal resolution results in a footprint of approximately $422\,m \times 349\,m$, assuming an aircraft speed of $220\,m\,s^{-1}$ and an altitude of 10 km. Notably, the optical inlet for the downward irradiance is mounted to a leveling platform to actively maintain a horizontal position. The two inlets for upward irradiance and radiance were mounted in a fixed position. With this setup, the spectrally resolved solar radiative budget at flight altitude was derived.

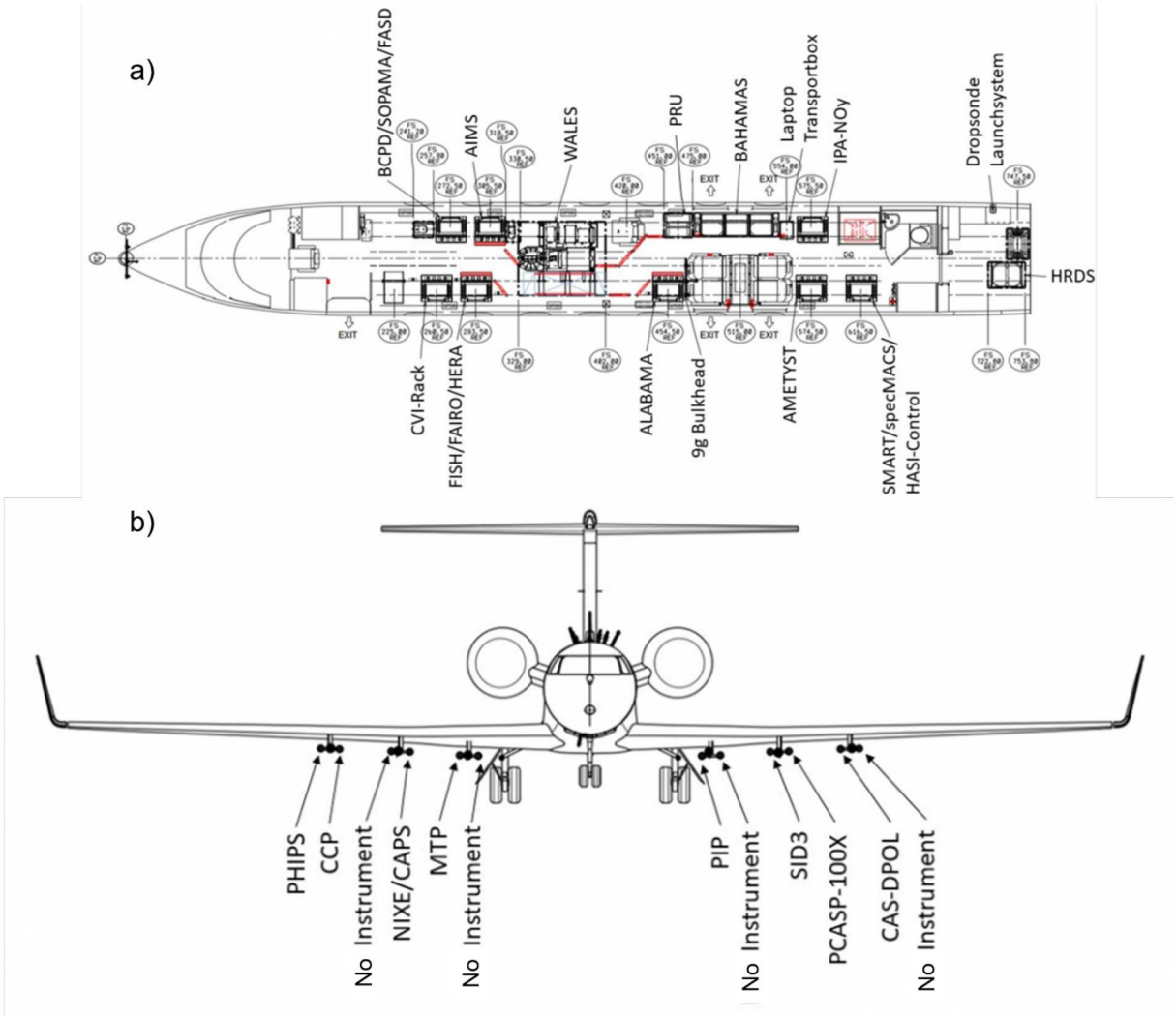

Figure 3: *Schematic depicting the position of measurement instruments a) on board HALO and b) attached to the wings during the CIRRUS-HL campaign. See https://cirrus-hl.de/instruments for details on the abbreviations and instruments.*

3 Case study of measurements

To demonstrate how the observations of the SMART and BACARDI instruments are used to study cirrus cloud radiative effects, a case study from the double flight on 29 June 2021 is used, which comprises Research Flights (RF) 05 and 06. However, we consider only RF05 here. The overall goal of this particular flight was to sample an Arctic cirrus system just east of Greenland and north of Iceland, which could be accommodated by a refueling stop in Bergen, Norway at the end of RF05. The synoptic conditions east of Greenland were dominated by a strong high pressure ridge located between Iceland and Scandinavia. This caused a southwesterly flow, lifting an air mass east of Greenland and forming a warm front. Cirrus clouds formed along the associated ridge. An in-situ, Lagrangian, staircase flight pattern was chosen to probe this system over the course of approximately 2 hours. With this strategy, different vertical layers of the cirrus system could be observed. The flight track with the different sections of the staircase pattern and an impression of the cloud field can be seen in Fig. 4.

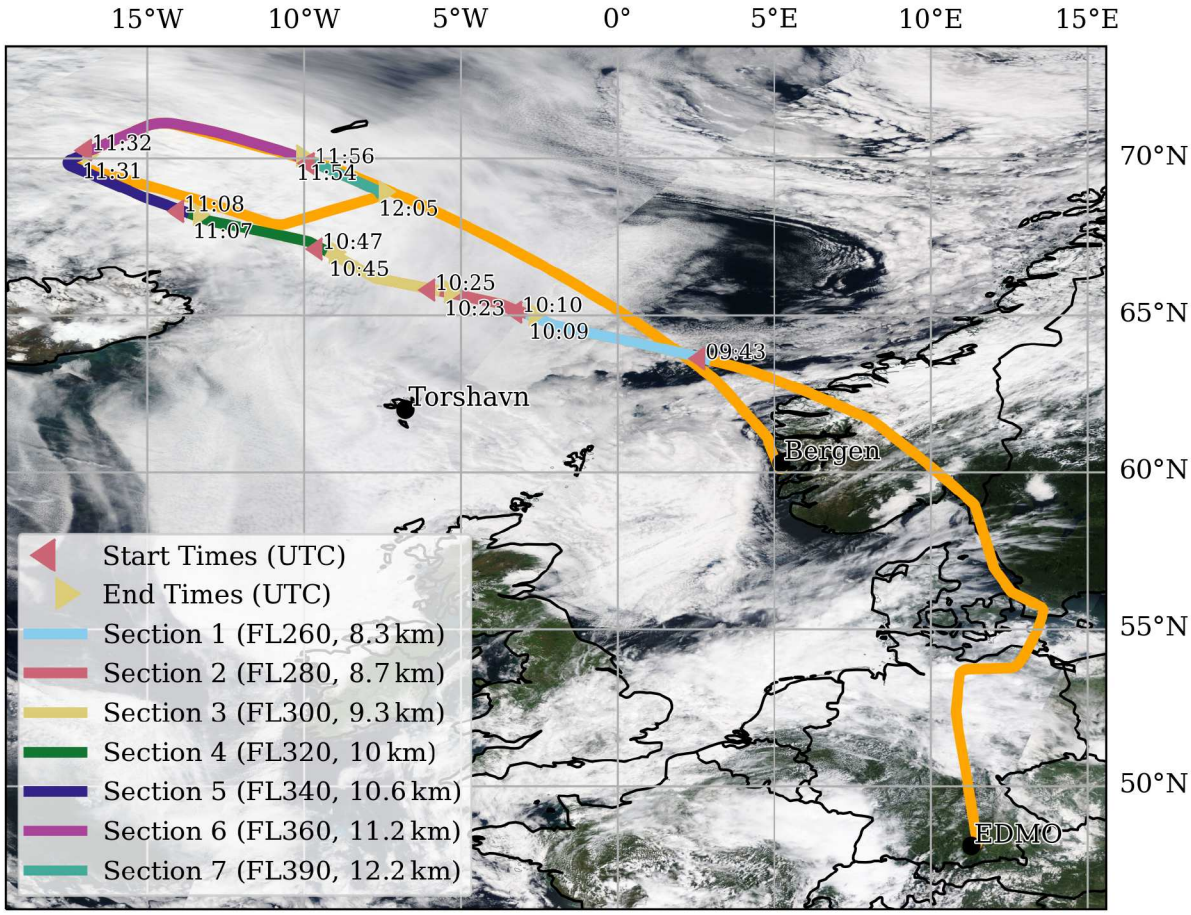

Figure 4: *HALO flight track of RF05 on 29 June 2021 starting from Oberpfaffenhofen (EDMO) towards the north of Iceland. Colors depict the position of HALO according to the sections defined by altitude. The satellite image is the corrected reflectance from the MODIS instrument on board Terra retrieved on 29 June 2021.*

The staircase pattern started at FL260, which was below the cirrus cloud deck. A cloud-free atmosphere was observed under HALO at this time. The aircraft first ascended into a thin cirrus cloud layer. As HALO continued to climb, the aircraft was persistently in clouds until FL320, where the cirrus cloud became more patchy. Some thicker cirrus cloud was encountered, but became thinner and intermittent at FL360. At FL390, HALO completed the pattern and was above the cirrus cloud layer.

3.1 BACARDI

Figure 5 provides time series of observed and simulated upward and downward, solar and terrestrial irradiance, respectively, throughout RF05. The simulations, which represent the cloud-free case, are shown as a reference. The points where the simulations and observations match indicate flight sections with cloud-free observations of either the upward or downward irradiance. From Fig. 5, it is clear that large sections of the flight were in cloudy conditions. Although the irradiance observations can be used to infer the cloud situation, additional observations of the clouds above or below the aircraft provide necessary contextual information. Thus, the following interpretations of the data are subject to some uncertainty and require further analysis for confirmation.

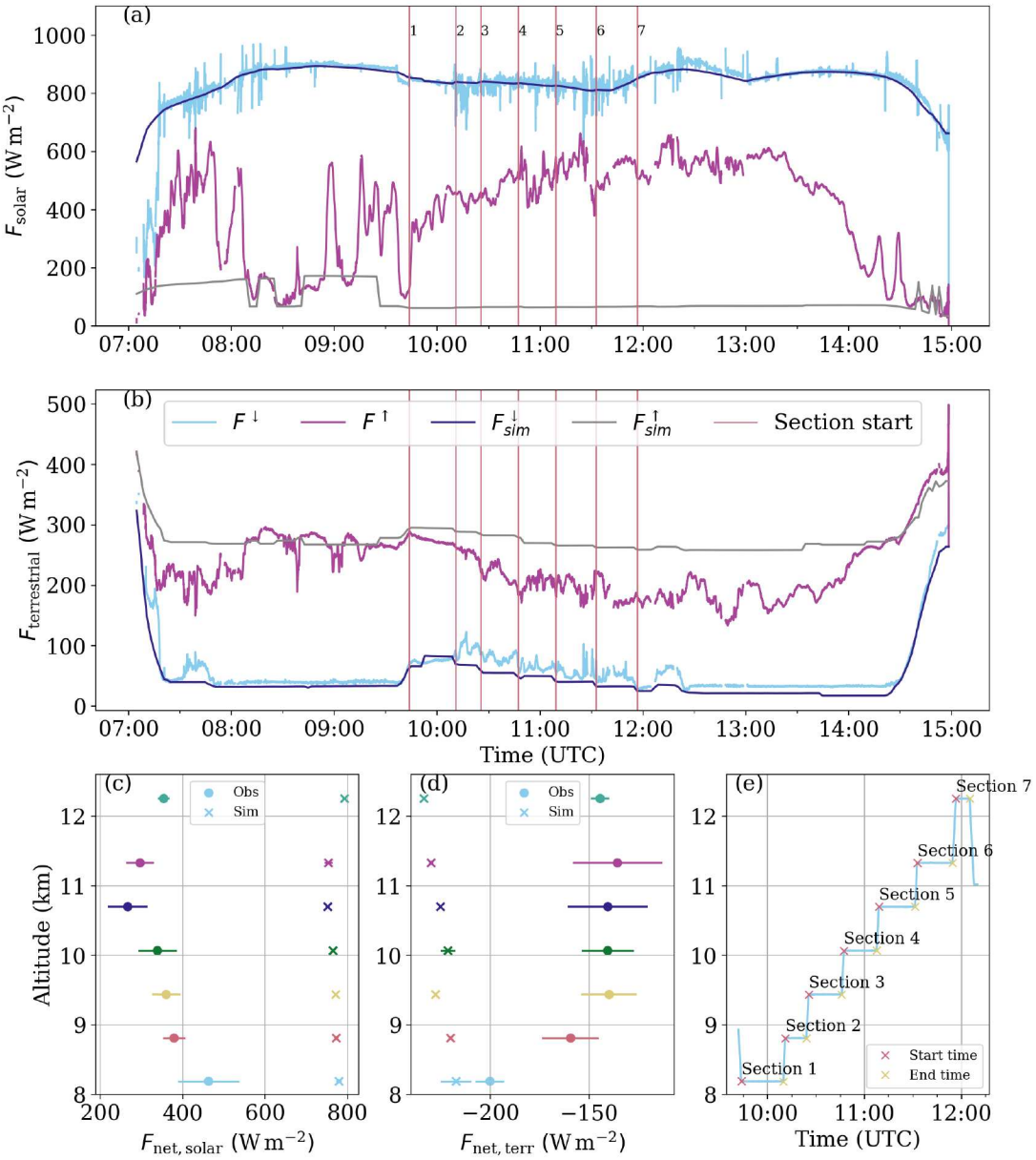

Figure 5: *BACARDI observations from RF05 on 29.06.2021. (a) and (b) depict time series of solar and terrestrial irradiance observations and cloud-free simulations, respectively, for the whole flight. (c) and (d) show the observed and simulated mean net solar and terrestrial irradiance for each flight section during the staircase flight pattern. Bars indicate the standard deviation for each level. (e) illustrates the different altitude sections over the same time period for reference.*

Figure 5 (c) and (d) depict the mean net irradiance (F_{net}) for each of the sections during the in-situ, Langrangian staircase sequence. Simulations of F_{net} for the cloud-free case are also shown for reference. In general, the observed net solar irradiance ($F_{\text{net,solar}}$) is decreasing with altitude. This is due to the fact that with higher altitude, the cloud layer below HALO becomes thicker and increases the reflection of solar irradiance. The cloud layer above becomes thinner and transmits more incoming solar irradiance. In this case, we see that the upward solar irradiance is increasing while the downward component remains relatively stable, even as the aircraft moves into and under cirrus cloud layers.

In Flight Section 5, just below 11 km, there is a sharper decrease in $F_{\text{net,solar}}$. The cirrus clouds in this section were reported to first become thicker, which increases the amount of solar radiation being reflected by the lower clouds and reduces the transmitted solar radiation, thus decreasing $F_{\text{net,solar}}$. However, $F_{\text{net,solar}}$ increases again as the aircraft exits this layer into thin, intermittent clouds, where the upward solar irradiance could be less intense, however confirmation of this assumption depends on the cloud situation below HALO. The fact that the simulated $F_{\text{net,solar}}$ is much higher than the observations suggests that there is also a stratitform cloud layer at lower altitudes, which increases the upward solar irradiance relative to a case where there are no clouds below HALO. This stratus cloud layer is likely to also be changing and affecting the upward irradiance.

In the terrestrial net irradiance ($F_{\text{net,terr}}$), the profile in Fig. 5(d) first increases sharply with altitude, but then stabilizes around 10 km (Flight Section 4). In the lower altitudes of the profile (Flight Sections 1–3), Fig. 5(b) shows that the downward terrestrial irradiance is not decreasing as rapidly as the upward component. This coincides with HALO entering the base of the cirrus cloud. The upward irradiance decreases due to the emission of terrestrial radiation by the cirrus cloud layer, which is colder than the surface. The emitted downward terrestrial irradiance only decreases slowly as the cloud base temperature is only slightly warmer than the temperature of the higher cirrus cloud layers. In the higher part of the profile (Flight Sections 4–7), the upward terrestrial irradiance continues to decrease with altitude, but the cirrus cloud is reported to be more intermittent and thin, with only some denser samples. Thus, the upward terrestrial irradiance decreases more slowly than at the lower altitudes of the profile. At the same time, the cold atmosphere above the cirrus cloud layer continues to impact the downward terrestrial irradiance, particularly as HALO nears the top of the layer. Both effects compensate for each other and stabilize $F_{\text{net,terr}}$ until Flight Section 7, when HALO is above the clouds completely, and the magnitude of the cooling increases ($F_{\text{net,terr}}$ decreases).

Similar to the $F_{\text{net,solar}}$ profile around 11 km, $F_{\text{net,terr}}$ is also affected by the very dense cirrus cloud layer and transition to patchier, thinner cirrus clouds. This is not obvious in the mean $F_{\text{net,terr}}$, but is indicated by the larger standard deviation bars in Flight Sections 5 and 6, where it is demonstrated that the terrestrial fluxes are fluctuating as the density of the cloud within and between layers changes too. In the case of both $F_{\text{net,solar}}$ and $F_{\text{net,terr}}$, additional information about the microphysical and macrophysical properties of the cloud can help to more clearly interpret the observations.

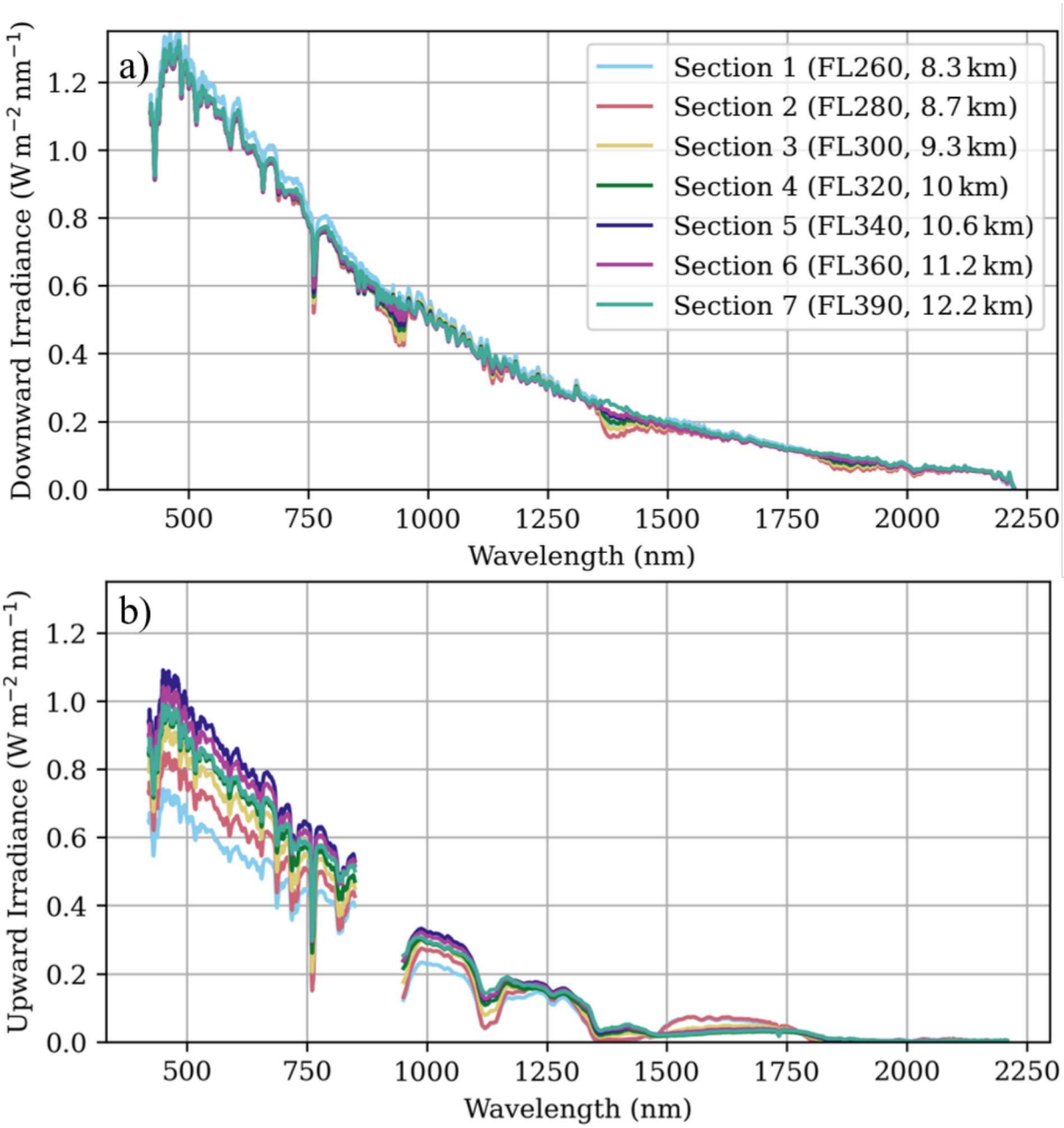

Figure 6: *Average SMART spectra for each section of the staircase pattern, (a) downward irradiance, (b) upward irradiance.*

3.2 SMART

The broadband measurements by BACARDI were complemented by spectral information provided by the irradiance measured with SMART in the solar part of the spectrum from 0.3 nm – 2200 nm. The spectral information allows for conclusions to be made on the cirrus cloud microphysical properties and their representation in radiative transfer models.

Figure 6 shows the average spectral downward irradiance (a) and upward irradiance (b) for each section of the staircase pattern. The variability of the downward irradiance indicates the presence/absence of cirrus clouds above HALO but is also is caused by the changing solar zenith angle. Flight Section 1 shows the highest values because it

includes parts with no cloud above and is located further south with a lower solar zenith angle than Section 7, which is exclusively above cloud. Apart from this, the different sections do not show significant differences in most of the spectrum. This shows that the extinction by the optically thin cirrus cloud does not attenuate the incoming solar radiation significantly. However, in particular wavelength ranges absorption by atmospheric trace gases is obvious.

The first notable absorption line at 760 nm corresponds to an oxygen absorption line, which becomes more pronounced the lower the altitude of HALO. Three broader sections can be identified at around 900 nm, 1350 nm and 1850 nm. They all correspond to water vapour absorption bands with centers at 940 nm, 1380 nm and 1870 nm. With increasing altitude and thus less cirrus cloud above the aircraft, the dip in the spectrum gets less pronounced. This can be explained by the decrease in the absolute amount of water vapour above the aircraft, which directly correlates with the amount of cirrus clouds. In addition, the path a photon needs to travel decreases with increasing altitude, thus decreasing the chance of it being absorbed inside the cirrus clouds.

The upward irradiance in Fig. 6(b) shows a higher variability between the different sections. Different processes lead to the change of the upward irradiance, which does not follow a steady increase with altitudes as would be the case for a homogeneous cirrus cloud. In this case, a lower stratiform cloud layer increased the reflectivity from altitudes below the cirrus cloud. As the cloud optical thickness of this stratiform cloud might change along the flight track, the upward irradiance becomes variable. In the wavelength range between 1500 and 1700 nm, the absorption by cloud particles dominates the spectral pattern. For the high flight section, when HALO is above the cirrus clouds, the upward irradiance is reduced compared to lower altitudes. This indicates the absorption by ice crystals and the presence of cirrus clouds. In this spectral range, the large ice crystals of the cirrus cloud absorb solar radiation more strongly than the small liquid droplets of the low stratiform cloud. To disentangle the different effects and quantify the radiative effect of the cirrus cloud, a sensitivity study using radiative transfer simulations is required.

4 Conclusions and outlook

CIRRUS-HL provides a new data set for analyzing the microphysical and radiative properties of Arctic and midlatitude cirrus clouds. Here, spectral and broadband irradiance measurements by BACARDI and SMART are presented for an Arctic cirrus cloud north of Iceland. The irradiances reveal the complexity of this case, which was caused by a low level liquid cloud layer and the heterogeneity of the cirrus cloud. Comparison with radiative transfer simulation of cloud-free conditions with profiles of up- and downward irradiance illustrate the solar radiative effect by the cirrus cloud, which is often superimposed by the reflection of radiation by the lower stratiform cloud. In the terrestrial wavelength range, the effect of the low cloud is less important. This illustrates, that different spectral ranges need to be analysed to separate the radiative effects of both cloud layers. Similarly, the spectrally resolved measurements of SMART can be used in combination with radiative transfer simulations to extract the radiative effects of ice crystals. To interpret the radiation measurements, the full HALO instrumentation of CIRRUS-HL can be used to combine remote sensing measurements with in-situ measurements of

ice particle size, shape and number. By constraining the influence of the lower-cloud albedo with model analyses, these data can be used to assess the impact of ice crystal properties, such as ice crystal shape, on the radiative effect of Arctic cirrus clouds. It is envisioned to compare the CIRRUS-HL observations with numerical weather forecast models and cirrus cases observed in the central Arctic during the recent HALO campaign HALO-(AC)³.

References

Emde, C., Buras-Schnell, R., Kylling, A., et al.: The libRadtran software package for radiative transfer calculations (version 2.0.1), Geosci. Model Dev., 9, 1647–1672, doi:10.5194/gmd-9-1647-2016, 2016.

Ewald, F., Kölling, T., Baumgartner, A., Zinner, T., and Mayer, B.: Design and characterization of specMACS, a multipurpose hyperspectral cloud and sky imager, Atmos. Meas. Tech., 9, 2015–2042, doi:10.5194/amt-9-2015-2016, 2016.

Luebke, A. E., Ehrlich, A., Schäfer, M., Wolf, K., and Wendisch, M.: An assessment of macrophysical and microphysical cloud properties driving radiative forcing of shallow trade-wind clouds, Atmospheric Chemistry and Physics, 22, 2727–2744, doi:10.5194/acp-22-2727-2022, 2022.

Voigt, C., Schumann, U., Minikin, A., et al.: ML-CIRRUS: The Airborne Experiment on Natural Cirrus and Contrail Cirrus with the High-Altitude Long-Range Research Aircraft HALO, Bull. Amer. Meteor. Soc., 98, 271–288, doi:10.1175/BAMS-D-15-00213.1, 2017.

Wirth, M., Fix, A., Mahnke, P., et al.: The airborne multi-wavelength water vapor differential absorption lidar WALES: system design and performance, App. Phys. B, 96, doi:10.1007/s00340-009-3365-7, 2009.

Wolf, K., Ehrlich, A., Jacob, M., et al.: Improvement of airborne retrievals of cloud droplet number concentration of trade wind cumulus using a synergetic approach, Atmospheric Measurement Techniques, 12, 1635–1658, doi:10.5194/amt-12-1635-2019, 2019.

The sensitivity of the MUAM model to the variability of non-orographic gravity wave distributions

K.Kandieva[1,✉], Ch.Jacobi[1], A. Pogoreltsev[2,†], E. Merzlyakov[3]

[1]*Institute of Meteorology, Stephanstr. 3, 04103, Leipzig*
[2]*Russian State Hydrometeorological University, St. Petersburg*
[3]*Institute for Experimental Meteorology, Obninsk*
[✉]*e-mail: kanykeikandieva@gmail.com*

Summary: Numerical experiments with the Middle and Upper Atmosphere Model with modified parameterization settings were carried out to study the response of the mesosphere/lower thermosphere (MLT) wind circulation to the non-orographic gravity waves (GWs) originating from the lower atmosphere. The modification of the phase speed spectrum controls the height of the zonal wind reversal due to strengthening of the westerly winds. The simulation results obtained for various latitudinal distributions of the intensity of non-orographic GWs at the source level show that the zonal circulation is most sensitive to GW variability at high latitudes. The latitudinal distribution of GW intensity, produced by the global distribution of convective processes and seasonal variations in GW sources, and modified phase speed spectrum made it possible to simulate the major zonal circulation structures observed by MLT wind radar.

Zusammenfassung: Numerische Experimente mit dem Middle and Upper Atmosphere Model mit modifizierten Parametrisierungseinstellungen wurden durchgeführt, um die Reaktion der Zirkulation der in der Mesosphäre / unteren Thermosphäre (MLT) auf nicht-orographische Schwerewellen (SW) zu untersuchen, die von der unteren Atmosphäre ausgehen. Die Modifikation des Phasengeschwindigkeitsspektrums steuert die Höhe der zonalen Windumkehr aufgrund der Verstärkung der Westwinde. Die Simulationsergebnisse für verschiedene Breitenverteilungen der Intensität nicht-orographischer SW in Quellenhöhe zeigen, dass die zonale Zirkulation am stärksten auf SW-Variabilität in hohen Breiten reagiert. Die Breitenverteilung der SW-Intensität, die durch die globale Verteilung konvektiver Prozesse und saisonaler Variationen der SW-Quellen erzeugt wird, und das modifizierte Phasengeschwindigkeitsspektrum ermöglichten es, die wichtigsten zonalen Zirkulationsstrukturen zu simulieren, die von einem MLT-Windradar beobachtet wurden.

1. Introduction

A wide range of waves of various spatial and temporal scales exist in the Earth's atmosphere – from slow planetary waves to fast mesoscale internal gravity waves (IGWs). They transfer energy and momentum upward from their lower atmosphere sources, leading to the interaction of atmospheric layers (e.g., Pogoreltsev et al., 2007). Vertically propagating IGWs dissipate in the mesosphere and thermosphere and, thus, having a significant impact on the energy and dynamics of the upper atmosphere.

IGWs, unlike planetary waves, have smaller spatial and temporal scales and their whole spectrum cannot be explicitly resolved by general circulation models. The main way to reproduce them in numerical circulation models is to use parametrizations. One of the main tasks of most IGW parametrizations is the need to set the global distribution of IGW intensity in the upper troposphere. It is known that IGW sources, such as convective processes, have a non-uniform distribution over the globe, and wave sources and wave filtering in the atmosphere are subject to seasonal changes (Gavrilov and Fukao, 1999), leading to differences in wave characteristics in the winter and summer hemispheres. Therefore, it is necessary to take into account the observed inhomogeneity of the wave source distributions in numerical general circulation models of the middle atmosphere. An equally important task of IGW parametrization is to set a realistic wave spectrum at the wave source level.

In this paper, we study the sensitivity of the Middle and Upper Atmosphere Model (MUAM) to modifications of the phase speed spectrum, and various observed forms of horizontal inhomogeneities of non-orographic IGW sources in the lower atmosphere. MUAM is a 3D non-linear mechanistic general circulation model of the middle and upper atmosphere (Pogoreltsev et al., 2007), and is an extension of the COMMA-LIM (Cologne Model of the Middle Atmosphere - Leipzig Institute for Meteorology) model (Fröhlich et al, 2003). COMMA-LIM is based on the original COMMA model developed earlier at the University of Cologne (Jakobs et al., 1986; Ebel et al., 1995). The model has a horizontal resolution of 5.625^{o} x 5^{o} in longitude/latitude. The MUAM version with 56 vertical levels (upper level at about 300 km) is used. The lower boundary conditions at the 1000 hPa level are zonally averaged climatological fields of the geopotential height and temperature calculated from the Japanese 55-year reanalysis (JRA-55) data for 2010 - 2019 (Kobayashi et al., 2015). Since MUAM is a low-resolution model, the lower levels up to 50 km are nudged with zonally averaged temperature fields from the JRA-55 reanalysis data for 2010 – 2019. The most recent MUAM version uses climatological 3D distributions of ozone (Suvorova and Pogoreltsev, 2011) and water vapor in the troposphere taking into account longitudinal variations (Ermakova et al. 2017). Besides, the MUAM accounts for processes related to the latent heat release due to condensation of the

water vapor (Ermakova et al., 2019), the parametrizations of orographic waves (Gavrilov and Koval 2013; Gavrilov et al. 2015), and normal atmospheric modes (Pogoreltsev et al. 2014), and non-orographic IGW parametrizations.

The non-orographic IGW parametrization in MUAM combines two schemes, namely an updated Lindzen-type gravity wave scheme (Jacobi et al., 2006), and a modified spectral parametrization by Yigit and Medvedev (2009). The Lindzen-type approach by Jakobs et al. (1986) was modified for an atmosphere with strongly varying background wind and temperature profiles (in which tidal fluctuations and/or planetary waves are taken into account). These conditions imply the possible existence of several convectively unstable layers, in which the IGW amplitudes cease to grow with height, and IGWs propagate upward with increasing amplitudes with height between these layers. The Lindzen-type scheme (due to its limitations to the short-wavelength approximation) is not able to describe IGWs with relatively large vertical wavelengths that propagate into the upper thermosphere. Therefore, this parameterization is applied to IGWs with low phase velocities of 5 - 30 m s^{-1}, that reach the saturation effect at mesosphere and lower thermosphere (MLT) heights up to 100 km. Yigit and Medvedev's (2009) spectral parametrization is applied to faster waves with phase speeds of 30-125 m s^{-1}. The full width at half maximum of the spectrum function is located at 75 m s^{-1}. The GW spectrum includes 30 harmonics. The eddy diffusion coefficient to be specified in this parametrization is calculated using the Lindzen scheme. The horizontal momentum flux in the troposphere was set equal to 10^{-7} m^2 s^{-2}.

2. Results

2.1 Effect of the phase speed modification

We first assess the sensitivity of MUAM to modifications of the phase speed spectrum. Gravity wave parameters for the spectral parametrization remain the same for all numerical experiments. Changes in the IGW parameters are implemented solely into the Lindzen-type scheme. The experiments are summarized in Table 1. For EXP1, the range of horizontal phase speeds varies from 5 to 30 m s^{-1} (step 5 m s^{-1}). The IGW spectrum is distributed in such a way that the "weight" coefficient of the wave decreases at high and low phase speeds. This distribution is consistent with existing ideas about the IGW spectra in the atmosphere (Fritts and Alexander, 2003). In total, the IGW spectrum consists of 48 harmonics. Wave harmonics are divided into 8 groups propagating in horizontal directions with azimuths with a difference of 45^0.

For EXP2 the horizontal phase speeds ranging from 5 to 30 m s^{-1} were increased by the background flow U_0, as in the WACCM3 model (Whole Atmosphere Community Climate Model, Version 3)(Garcia et al., 2007). Other properties of the GW spectrum were the same like in EXP1. For both numerical experiments, the IGW

amplitude distribution function over latitude is constant and equal to a_{const} = 0.0125 ms^{-1} and IGW sources has been set at a level of 10 km.

Fig. 1 shows the latitudinal dependence of the IGW intensity and the corresponding analytical equations. The latitude-altitude distributions of the zonal mean zonal wind and the divergence of the zonal momentum flux for January are shown in Fig. 2. For EXP1, Fig. 2a, we can distinguish westerly winds from 0 to 20 km in both hemispheres, and, at 20 to 80 km, of easterly winds in the summer hemisphere and westerly winds in the winter hemisphere. At altitudes from 80 to 120 km in both hemispheres, a change in the direction of the zonal wind to the opposite is observed (wind reversal). An analysis of the results obtained for EXP2, Fig. 2b, shows that an increase in horizontal phase speeds by the background flow leads to changes in wind speeds at different heights and latitudes. The contribution of the modified phase speed spectrum is expressed in strengthening of the stratospheric-mesospheric westerly jet in the winter hemisphere. The wind reversal occurs at an altitude of 100 km at middle latitudes, which is 20 km higher than for EXP1. A comparison of the zonal structure for EXP1 and EXP2 shows that the wind reversal for EXP2 occurs a bit lower due to intensification of the westerly jet (80 – 110 km) in the summer hemisphere. This effect is accompanied by a decrease in the area of maximum zonal wind speeds of the easterly jet. To interpret the changes in zonal circulation the zonal momentum flux divergence is shown in Fig. 2c,d. According to Lindzen's approach, the divergence of the zonal momentum flux makes it possible to estimate the acceleration of the mean flow due to the breaking of the IGWs. Thus, a significant intensification in the observed westerly winds between 80 - 100 km (Fig. 2b) is caused by the increased number of dissipated westward GWs compared to EXP1. In the winter hemisphere the eastward GWs with low phase speeds are completely filtered out up to 100 km.

Table 1: *Summary of experiments and related IGW parameterization parameters.*

	Lindzen-type scheme paarameters			
	Phase speeds (m s^{-1})		IGW intensity distribution	
	[5, 10, 15, 20, 25, 30]	[5, 10, 15, 20, 25,30] + U_0	Distribution according to Fig.2	Amplitude *a* (m s^{-1})
EXP1	+		1	0.0125
EXP2		+	1	0.0125
EXP3		+	2	0.0125
EXP4		+	3	0.00625

EXP5		+	2+3	0.017, 0.01

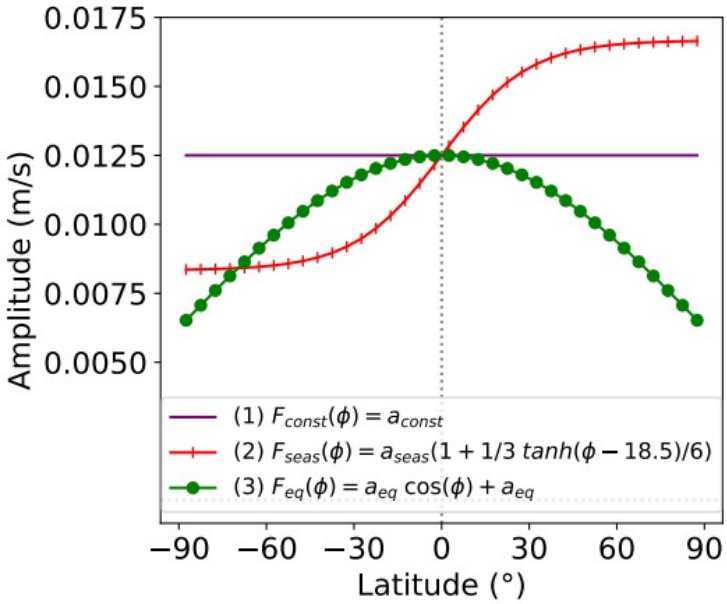

Figure 1. Latitudinal distributions of IGW amplitudes for January.

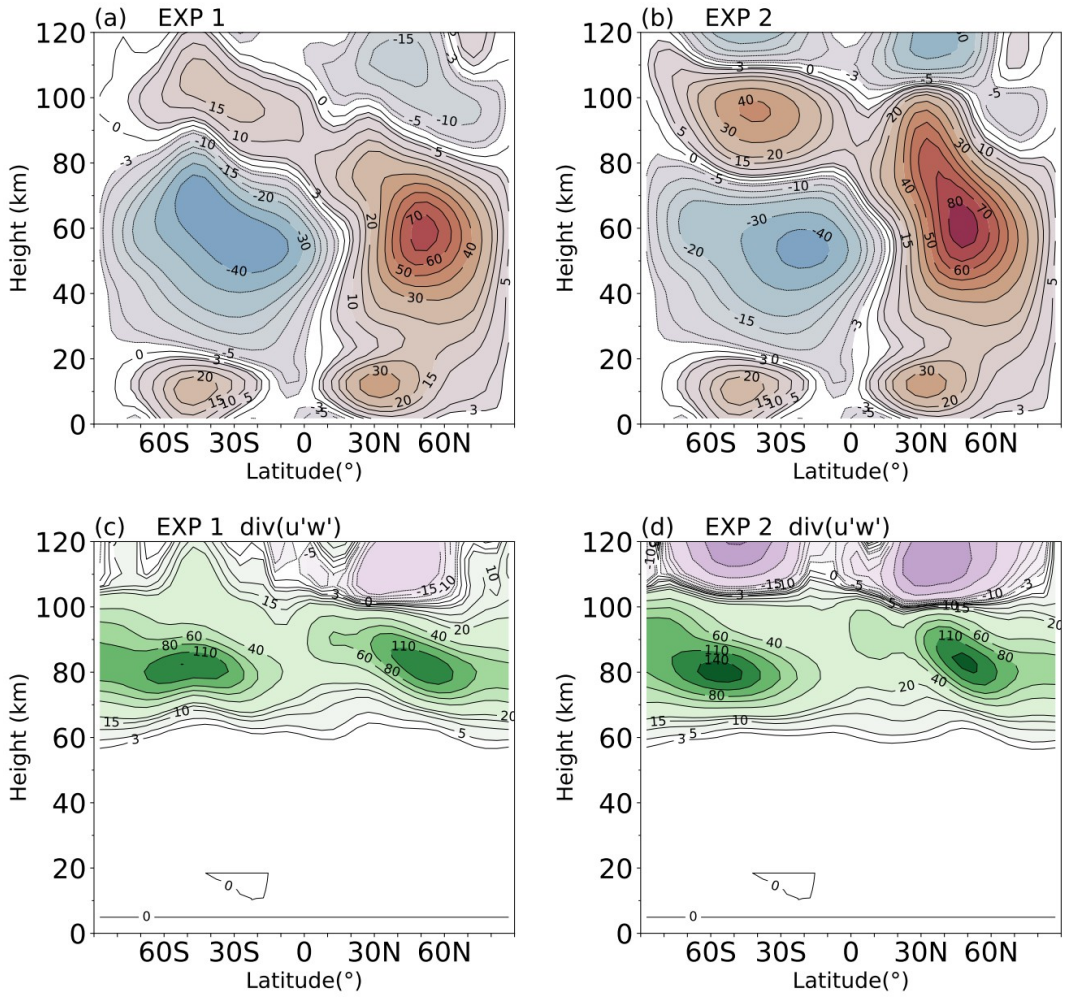

Figur

e 2. January (a) and (b) zonal mean zonal wind (ms^{-1}), (c) and (d) zonal momentum flux divergence ($ms^{-2}day^{-1}$) for EXP1 and EXP2.

2.2 Effect of modification of latitudinal IGW intensity distribution

The numerical experiments using the settings of the IGW spectrum for EXP2 were carried out with different latitude dependencies of the IGW amplitudes defined at the level of wave sources. Observations show that IGW amplitudes in the troposphere–stratosphere are larger in winter than in summer, and the seasonal differences are greater at high latitudes (Gavrilov et al., 2001). EXP3 was carried out taking into account these features for January conditions. In EXP3 the seasonal IGW amplitude variation was specified by distribution (2) in Fig. 1, where a_{seas} = 0.0125 m s^{-1}.

Another factor affecting the latitudinal distribution of IGW intensity is the quantitative distribution of IGW sources. Deep convection in the equatorial region serves as a powerful source of IGWs, which generates an equatorial maximum as a result of such a heterogeneity of sources. Taking account the aforementioned

latitudinal distribution, a fourth experiment (EXP4) was performed. The analytical expression is given as distribution (3) in Fig. 1, where a_{eq} = 0.00625 m s^{-1}.

Comparison of the zonal wind in EXP2 with EXP3, Fig. 3a, shows that the implementation of a latitude-inhomogeneous IGW intensity associated with the seasonal distribution mainly leads to changes in wind speeds at the heights of the observed maxima, while the wind reversal height at middle latitudes remain almost unchanged. An increase in the IGW intensity amplitude in the winter hemisphere weakens the stratospheric-mesospheric jet, which can also be estimated from the distribution of the zonal momentum flux divergence (Fig. 3c).

Implementation of a latitudinal distribution with equatorial IGW intensity maximum in EXP4, Fig. 3b, affects the height of the wind reversal at high latitudes of both hemispheres. Assuming that the IGW amplitudes at high latitudes are smaller due to the smaller number of sources, the upper boundary of the stratospheric-mesospheric jet is located at greater heights than for EXP2. In other words, at high latitudes, there is an increase in the acceleration of the mean flow due to the breaking of IGWs (Fig.

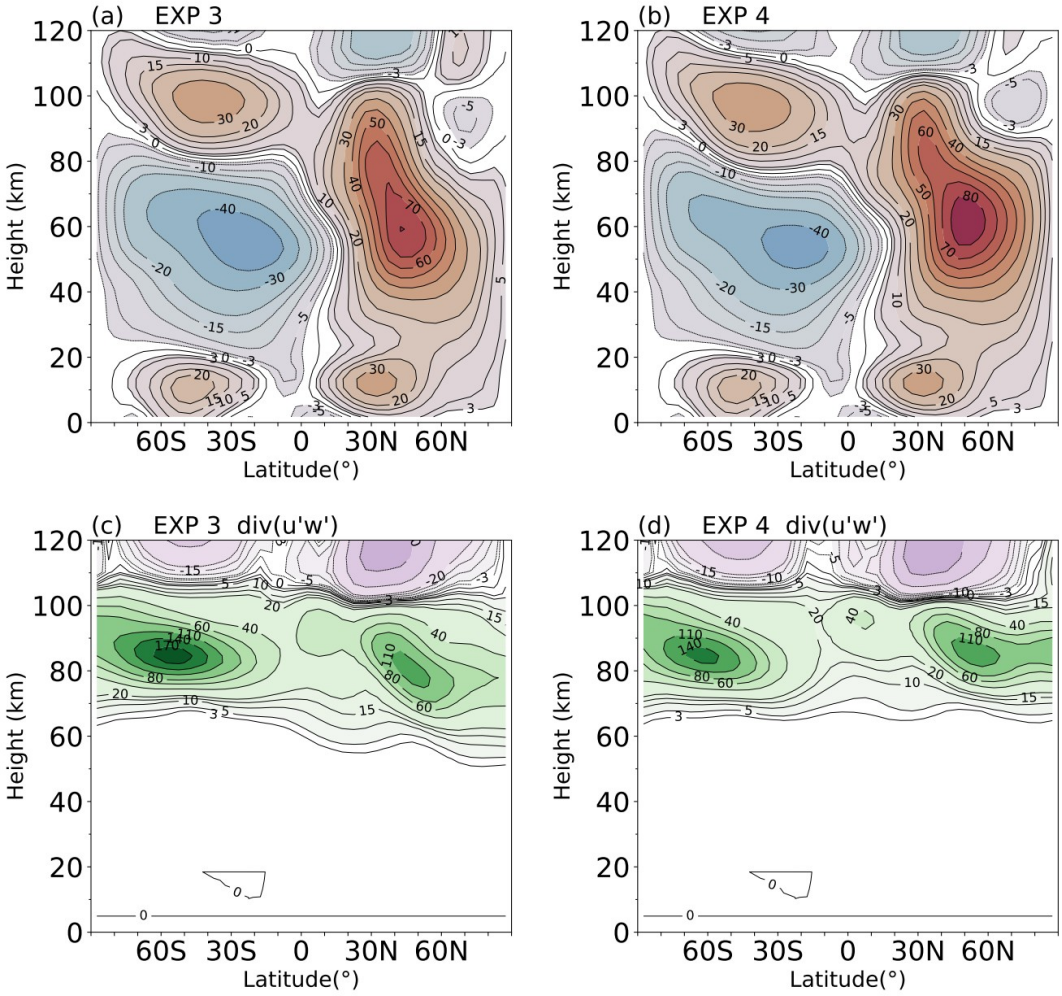

3d) which contributes to the strengthening of mesospheric zonal winds in this area.

Figure 3. As in Fig. 2, but for EXP3 and EXP4.

Fig. 4a shows the results of the EXP5, in which the IGW intensity distribution is presented as a sum of the distributions (2) and (3). A typical distribution of the zonal mean zonal wind for January according to the HWM 14 model (Drob et al., 2015) is shown in Fig. 4b. Some features of the zonal circulation for EXP5 are consistent with HWM 14 (Horizontal Wind Model 2014). In both hemispheres, wind reversal altitudes are identical to those of HWM 14. However, the maximum wind speeds of the stratospheric-mesospheric jet as simulated by MUAM are overestimated in the winter hemisphere and underestimated in the summer hemisphere compared to HWM 14.

It is of interest to study the seasonal distribution of the zonal wind in the MLT region. Fig. 5a shows the 2016-2017 mean zonal wind over Collm (51.3°N, 13.0°E) from meteor radar measurements (Korotyshkin et al., 2019). Fig. 5b represents the zonal wind distribution calculated using the MUAM model. The simulation was performed with the settings for EXP 5, i.e. the phase speeds were modified by the lower atmosphere winds, and their latitudinal distribution is a combination of distributions (2) and (3).

The MLT region zonal wind distribution according to radar observations demonstrates westerly winds in winter, circulation reversal in early spring, and a subsequent change in the wind regime in early autumn (Fig. 5a). The summer-spring zonal circulation is characterized by a change in wind circulation from easterly to westerly and in height. MUAM reproduces the general structure of the zonal circulation relatively well (Fig. 5b). The model shows westerly winds in winter with wind speeds that are consistent with meteor radar measurements, and a wind reversal during the spring-summer zonal circulation, which also agrees with radar observations. However, the MUAM also simulates a wind reversal at an altitude of about 95 km, which is not observed in radar observations in winter. Inconsistencies with observational data include a delay in the change of wind regimes from winter to summer. According to observations, this transition occurs in early March, but the model shows the wind reversal only in early May.

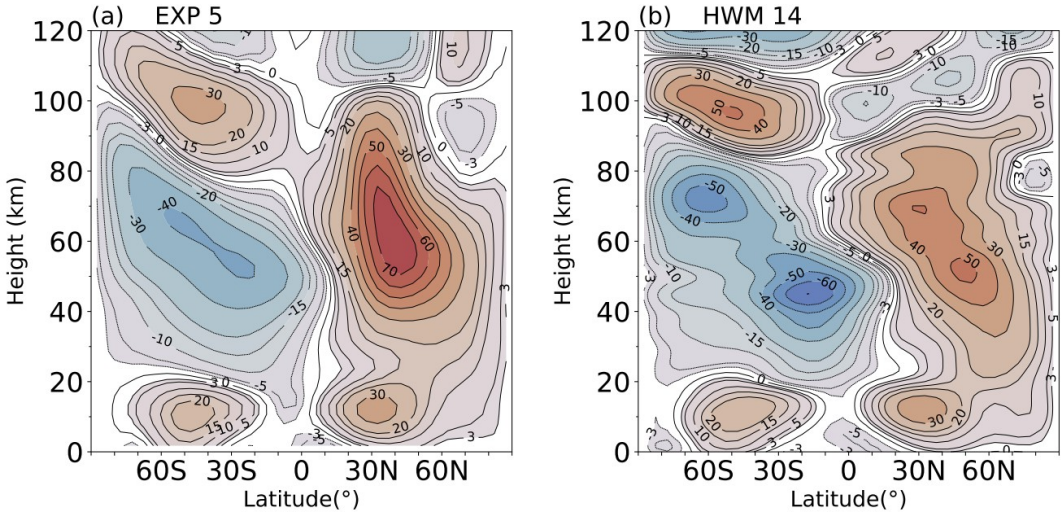

Figure 4. (a) zonal mean zonal wind (m s^{-1}) MUAM model, (b) zonal mean zonal wind (m s^{-1}) HWM 14 model.

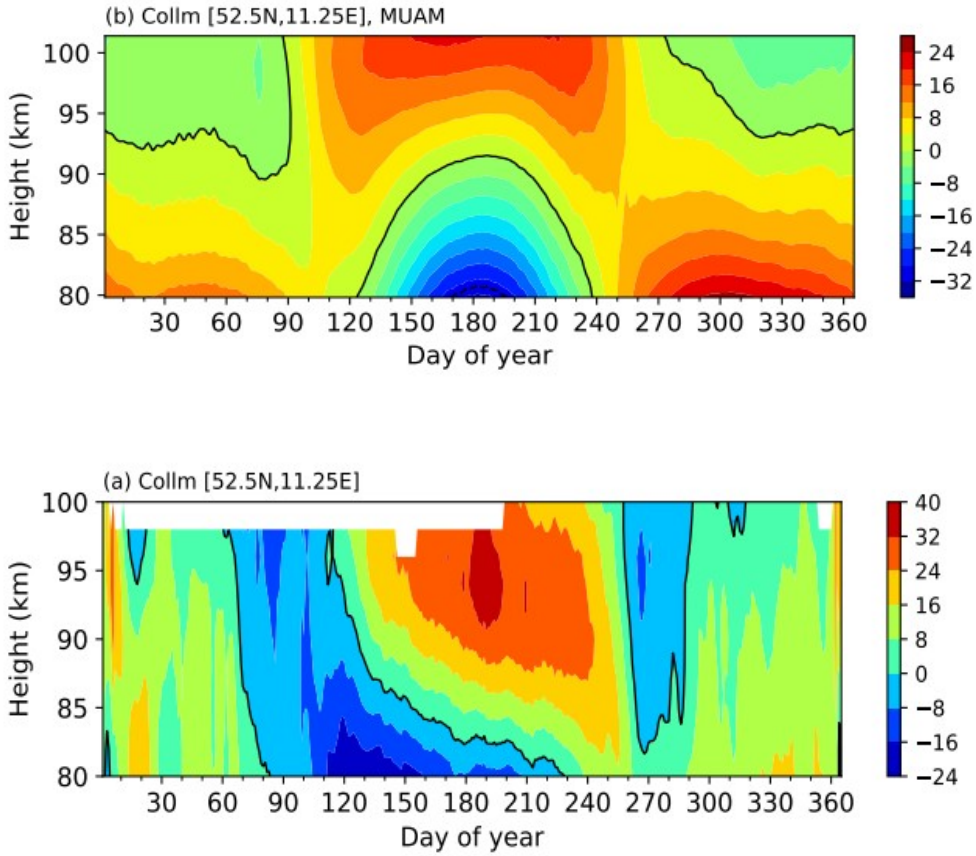

Figure 5. Zonal wind distribution at Collm from (a) meteor radar observations, (b) MUAM simulation.

3. Conclusions

In this paper we studied the sensitivity of the MUAM model to a slightly modified phase speed spectrum. The change has only been related to IGWs with slow phase speeds, the phase speed spectrum of which has been increased by the background flow. This modification has led to a vertical extension of the westerly jet in the winter hemisphere. The winter wind reversal have raised up to 100 km,

approximately the same reversal altitude as for the HWM 14 model, however, this effect is observed only in low and middle latitudes.

Two further numerical experiments have been carried out to study the sensitivity of the MUAM model to the observed inhomogeneity in the intensity of wave sources in the lower atmosphere. The distributions of sources depending on seasonal changes and intensity of convective processes were considered. The results shows that the zonal structure is most sensitive to the intensity of wave sources at high latitudes. Experiments with latitudinal modifications in the intensity of GW show that at low amplitudes, IGW dissipate at higher levels, thereby increasing the zonal wind reversal height. However, vertical propagation of the winter westerly wind is limited toa height of 90 km.

We also investigated the total effect of latitudinal distributions and the modified spectrum of phase speeds. The results of this numerical experiment (EXP5) is in good agreement with the data of the HWM 14 model in terms of the structure of the zonal mean zonal wind. Moreover, the MUAM model, adapted to the EXP5 IGW parameters, is capable of reproducing the major zonal circulation structures observed by the MLT wind radar.

Acknowledgements

This research has been supported by Deutsche Forschungsgemeinschaft through grant # JA 836/38-1 (NOSTHEM).

4. References

Drob, D. P., Emmert, J. T., Meriwether, J. W., Makela, J. J., Doornbos, E., Conde, M., Hernandez, G., Noto, J., Zawdie, K. A., McDonald, S. E., et al. 2015: An update to the Horizontal Wind Model (HWM): The quiet time thermosphere, Earth and Space Science, 2, 301– 319, doi:10.1002/2014EA000089.

Ebel, A., Berger, U., Krueger, B.C., 1995: Numerical simulations with COMMA, a global model of the middle atmosphere, SIMPO Newsletter, 12, 22-32.

Ermakova, T.S., Statnaya, I.A., Fedulina I.N., Suvorova, E.V., Pogoreltsev, A.I., 2017: Three-dimensional semi-empirical climate model of water vapor distribution and its implementation to the radiation module of the middle and upper atmosphere model, Russ. Meteorol. Hydrol., 42(9), 594–600, doi:10.3103/S1068373917090060.

Ermakova, T.S., Aniskina, O.G., Statnaya, I.A., Motsakov, M.A., Pogoreltsev, A.I., 2019: Simulation of the ENSO influence on the extra-tropical middle atmosphere, Earth, Planets and Space, 71:8, doi:10.1186/s40623-019-0987-9.

Fritts, D.C., Alexander M.J., 2003: Gravity wave dynamics and effects in the middle atmosphere, Rev. Geophys., 41 (D1), 1003, doi:10.1029/2001RG000106.

Fröhlich, K., Pogoreltsev, A., Jacobi, Ch., 2003: Numerical simulation of tides, Rossby and Kelvin waves with the COMMA-LIM model, Advances in Space Research, 32, 863–868, doi:10.1016/S0273-1177(03)00416-2.

Garcia, R. R., Marsh, D. R., Kinnison, D. E., Boville, B. A., Sassi, F., 2007: Simulation of secular trends in the middle atmosphere, 1950 – 2003, J. Geophys. Res., 112, D09301, doi:10.1029/2006JD007485.

Gavrilov, N. M., Fukao, S., 1999: A comparison of seasonal variations of gravity wave intensity observed with the middle and upper atmosphere radar with a theoretical model, J.Atmos. Sci., 56, 3485 – 3494, doi:10.1175/1520-0469(1999)056<3485:ACOSVO>2.0.CO;2.

Gavrilov, N. M., Jacobi, Ch., Kurschner D., 2001: Short-period variations of ionospheric drifts at Collm and their connection with the dynamics of the lower and middle atmosphere, Phys. Chem. Earth (C), 26(6), 459-464, doi:10.1016/S1464-1917(01)00031-9.

Gavrilov, N.M., Koval, A.V., 2013: Parameterization of mesoscale stationary orographic wave forcing for use in numerical models of atmospheric dynamics, Izv. Atm. Ocean Phys., 49(3), 244–251, doi:10.1134/S0001433813030067.

Gavrilov N.M., Koval, A.V., Pogoreltsev, A.I., Savenkova, E.N., 2015: Simulating influences of QBO phases and orographic gravity wave forcing on planetary waves in the middle atmosphere, Earth Planets Space, 67:86, doi: 10.1186/s40623-015-0259-2.

Jacobi, Ch., Fröhlich, K., Pogoreltsev, A., 2006: Quasi two-day-wave modulation of gravity wave flux and consequences for the planetary wave propagation in a simple circulation model, J. Atmos. Sol.-Terr. Phys., 68, 283-292, doi: 10.1016/j.jastp.2005.01.017.

Jakobs, H. J., Bischof, M., Ebel, A., Speth, P., 1986: Simulation of gravity wave effects under solstice conditions using a 3-d circulation model of the middle atmosphere, J. Atmos. Terr. Phys, 48, 1203-1223, doi:10.1016/0021-9169(86)90040-1.

Kobayashi, S., Ota, Y., Harada, Y., Ebita, A., Moriya, M., Onoda, H., Onogi, K., Kamahori, H., Kobayashi, C., Endo, H., Miyaoka, K., Takahashi, K., 2015: The JRA-55 Reanalysis: General Specifications and Basic Characteristics, J. Meteorol. Soc. Jpn. Sr. II, 93, 5–48, doi:10.2151/jmsj.2015-001.

Pogoreltsev, A.I., Vlasov, A.A., Fröhlich, K., Jacobi, Ch., 2007: Planetary waves in coupling th e lower and upper atmosphere // J.Atmos.Solar-Terr. Phys, 69, 2083-2101, doi:10.1016/j.jastp.2007.05.014

Pogoreltsev, A.I., Savenkova, E.N., Pertsev, N.N., 2014: Sudden stratospheric warmings: the role of normal atmospheric modes, Geomag. Aeron., 54, 357–372, doi:10.1134/S0016793214020169.

Suvorova, E.V., Pogoreltsev, A.I., 2011: Modeling of nonmigrating tides in the middle atmosphere, Geomag. Aeron., 51(1), 105–115, doi:10.1134/S0016793210061039.
Yiğit, E., Medvedev, A. S., 2009: Heating and cooling of the thermosphere by internal gravity waves, Geophys. Res. Lett. 36, L14807. doi:10.1029/2009GL038507.

Analysing the sensitivity of Arctic large-scale circulation to the regional radiation forcing over Europe using deep learning

Mehrdad, S.[1,✉], Sudhakar, D.[1], Jacobi, C.[1]

[1]*Institute for Meteorology, Stephanstr. 3, 04103 Leipzig,*
[✉]*e-mail: sina.mehrdad@uni-leipzig.de*

Summary: The Arctic large-scale circulation is governed by a wide range of factors. In order to investigate the sensitivity of the Arctic large-scale circulation to the regional radiative forcing over Europe, we conducted sensitivity experiments using a state-of-the-art atmosphere-land-ocean coupled model. Using advanced Deep Learning (DL) algorithms, we analyzed the Arctic circulation regimes response to negative radiative forcing anomalies over Europe. We examined different architectures for our DL algorithm to find the most suitable one for our analysis. We simultaneously analyzed the multiple fields of Mean Sea Level Pressure (MSLP) and 700 to 300 hPa layer Thickness (300-700-T) and their spatiotemporal patterns with the DL algorithm. The DL algorithms showed good skills in capturing the general structure of the large-scale circulation. The radiative forcing over Europe doesn't seem to induce new spatiotemporal patterns to the large-scale circulation, but modified the occurrence frequency of preferred circulation regimes.

Zusammenfassung: Die arktische großräumige Zirkulation wird von einer Vielzahl von Faktoren bestimmt. Um die Sensitivität der arktischen großräumigen Zirkulation auf den regionalen Strahlungsantrieb über Europa zu untersuchen, haben wir Sensitivitätsexperimente mit einem hochmodernen gekoppelten Atmosphäre-Land-Ozean-Modell untersucht. Unter Verwendung neuer Deep-Learning-Algorithmen (DL) analysierten wir die Reaktion der arktischen Zirkulationsregime auf negativen Strahlungsantriebsanomalien über Europa. Wir haben verschiedene Architekturen für unseren DL-Algorithmus untersucht, um die am besten geeignete für unsere Analyse zu finden. Wir haben die Felder des mittleren Drucks auf Meeresspiegelniveau und der Schichtdicke von 700 bis 300 hPa und ihre raumzeitlichen Muster mit dem DL-Algorithmus analysiert. Die DL-Algorithmen zeigten gute Ergebnisse bei der Erfassung der allgemeinen Struktur der großräumigen Zirkulation. Der Strahlungsantrieb über Europa scheint der großräumigen Zirkulation keine neuen raumzeitlichen Muster zuzufügen, veränderte aber die Häufigkeit des Auftretens bevorzugter Zirkulationsmuster.

1. Introduction

The analysis of the sensitivity of the atmospheric large-scale circulation to different forcing is a challenging task to do (Hannachi et al., 2017; Vavrus, 2018; Maher et al., 2019). A wide range of processes interactively contributes to generating the atmospheric large-scale circulation regimes (Jaiser et al., 2012; Li et al., 2015; Sandu et al., 2019). A common approach to analyzing the large-scale circulation response to

different forcing is to conduct idealized model sensitivity experiments (Li et al., 2015; Sandu et al., 2019). The mean state of the circulation is usually used to characterize the circulation response to the forcing and understand the underlying physical mechanisms (Jaiser et al., 2012, Hannachi et al., 2017). However, the forcing impact on the large-scale circulation dynamics and the local spatiotemporal circulation patterns still deserves attention.

The common methodologies used in detecting the signal in circulation response to the forcing, are unable to capture and analyze the spatiotemporal patterns in the circulation regimes (Cassano et al., 2006; Jaiser et al., 2012). Recently, Deep Learning (DL) has extraordinarily progressed our ability to recognize complex patterns in big datasets (LeCun et al., 2015). Deep autoencoders, a branch of DL algorithms, have been used successfully for clustering and anomaly detecting applications (Zhou and Paffenroth, 2017; Guo et al., 2017). The Convolutional Neural Networks (CNN), which usually act as the core of auto-encoders, have shown a promising performance to capture the spatiotemporal pattern in image-like datasets (Ji et al., 2012; LeCun et al., 2015; Rawat and Wang, 2017). They can capture the hierarchy of the local patterns in a dataset with several channels (LeCun et al., 2015; Rawat and Wang, 2017). Deep convolutional auto-encoders have shown great capabilities to capture the dynamic processes of the atmosphere (Weyn et al., 2019; Weyn et al., 2020).

In this study, we analyzed the results of sensitivity experiments with the local radiative forcing over Europe using a coupled model. We examined deep convolutional auto-encoders with different architectures to find the most suitable auto-encoder for our analysis. We used the selected auto-encoder to analyze the impact of the regional local radiative forcing over Europe on Arctic large-scale circulations. This gives us the advantages of using simultaneous multiple fields analysis of the circulation regimes and capturing the dynamical evolution of the circulation regimes.

2. Data and methodology

2.1 Model experiments

We analyzed results from two model experiments using the Max Planck Institute Earth System Model (MPI-ESM) coupled atmosphere-ocean–land surface model (Giorgetta et al., 2013). MPI-ESM consists of the atmospheric component ECHAM6 (Stevens et al., 2013) with T63L47 spectral resolution (about 1.8 in the horizontal, uppermost of the 47 levels at 0.01 hPa) and the ocean component Max Planck Institute Ocean Model (MPIOM) (Jungclaus et al., 2013), which applies an idealized control mapping grid of about 1.5° with 40 levels. The atmospheric composition, as well as other boundary conditions, are prescribed at pre-industrial conditions.

First, a control simulation was performed without any cloud modification (the control run). In the second experiment, an idealized regional cloud modification is forced over Europe (idealized location of 43°N to 58°N and 5°E to 25°E). Clouds have been modified in a way that they induced cooling radiative effects when they are present in the region. For every model time step, the cloud water content (q_l) is multiplied by a factor of 10 and the cloud ice water content (q_i) is multiplied by a factor of 0.1 in the region. The cloud modifications strongly depend on the presence and the thermodynamic phase of cloud layers in the atmosphere. These modifications perturb

the top of the atmosphere energy budget and consequently, affect the climate's energy budget. Both the simulations run for 30 years and include 6 ensemble members each.

2.2 DL algorithms

DL is a branch of machine learning that consists of successive layers of representations (LeCun et al., 2015). Each layer act as a transforming function that transfers the input to a new representation. These transformations are formed automatically in the training process by exposure to the training data. The use of layers with CNNs shows promising performance in computer vision as they use convolutional operations (Rawat and Wang, 2017). Convolutional layers (layers with CNN as their core) can learn local patterns in the dataset (Rawat and Wang, 2017). In this study, trying to capture the local process in large-scale circulation regime, we used CNNs as the core of every layer in our deep learning algorithms. The open-source python's library of Keras (Chollet, 2015) with Google's TensorFlow backend (Abadi et al., 2015) is used to implement the DL algorithms.

2.2.1 Data

The two atmospheric fields of Mean Sea Level Pressure (MSLP) and 700 to 300 hPa layer Thickness (300-700-T) were used to analyze the large-scale circulation (Figure 1). This helps us keep the important information in the dataset while preventing the DL algorithms' complexity and training computational cost. The thickness channel (300-700-T) adds complementary information about the weather systems to the dataset. Adding the layer thickness has been proved effective in data-derived weather predicting systems (Weyn et al., 2019; Weyn et al., 2020).

As we are interested in analyzing the Arctic large-scale circulation, only the data poleward of 30° N have been used. The data fields has been transferred to Lambert Azimuthal Equal-Area projection with a horizontal grid size of 53 km (corresponding to 1.5° which is close to the model original grid size). This projection preserves the weather system's scale independent of the location of the system. The data fields in this projection are well suited to be analyzed with CNN layers. As the patterns leaned by CNN layers are transfer invariant, the weather systems with the same scale can be captured independent of their location. One example of a data point of daily fields (with no time dimension) with MSLP and 300-700-T channels is illustrated in Figure 1. Both MSLP and 300-700-T fields have been normalized before feeding to DL algorithms.

Different configurations of the dataset are used for different DL algorithms. These configurations can be categorized into three classes of 1-D generative, n-D generative, and predictive configurations depending on the DL algorithm which the dataset is going to be used for training. In 1-D generative, the input and output of the DL algorithm are similar and consist of daily mean fields (1-D time dimension) of MSLP and 300-700-T. Every data point in this configuration is a 4-D array of (data point id, x, y, channel=1/2), where x and y are the projection axes (Figure 1), and channel refers to the two fields of MSLP and 300-700-T. In the n-D generative dataset, the input and output of the DL algorithm are also similar. However, they consist of stacking the sequence of daily mean fields (the sequence of n days for every point - n-D time dimension) of MSLP and 300-700-T. Thus, every data point in this configuration is a 5-d array of (data point id, n, x, y, channel), where n refers to the day number of the

data field relative to the starting day of the data point. For instance, if we have 8 sequences of days in our data point (8-D generative configuration), n can be an integer from 1 to 8 determining the day number relative to the starting day of the data point. We assigned the date of the first day of the data point to the whole data point. In the predictive configuration, the input and output of the DL algorithm are not similar. For each data point, we have daily sequences of data in the input and the corresponding output of the following daily sequences. Consequently, for each data point, the input data represents the daily sequences of data exactly before the sequence of the output data.

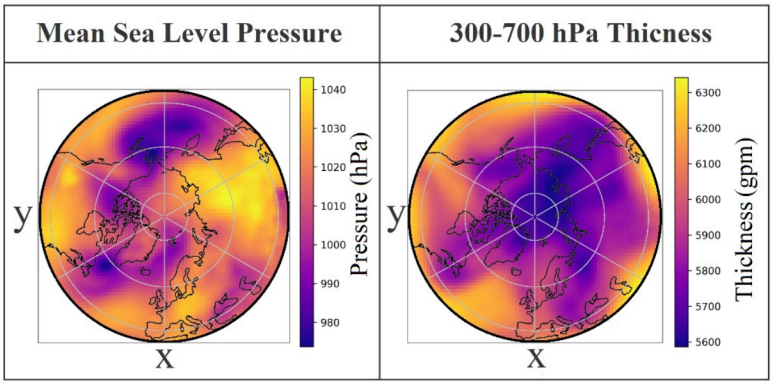

Figure 1: Example of daily fields (for the day 1869.01.21 for the control run) of Mean Sea Level Pressure (MSLP) and 300-700 hPa Thickness (300-700-T) for latitudes poleward of $30^{\circ}N$ *transferred to Lambert Azimuthal Equal-Area projection.*

Our model experiments consist of 30 years of simulations starting from 1850. We used roughly 25% of the whole dataset to validate the training process (validation dataset) and used the rest for training the DL algorithms (train dataset). In order to reliably train a DL algorithm, the validation dataset needs to be a good representative of the whole dataset. A good validation dataset should contain the inter-annual and intra-annual variability of the whole dataset. We used the whole year (including all seasons) data for every 4th year starting from 1851 for the validation dataset. The selected years for the validation dataset are the same for each DL algorithm.

2.2.2 Convolutional auto-encoder

An auto-encoder is a type of Machine Learning algorithms mostly used for coding the data. Auto-encoders consist of two main components: encoder and decoder. The encoder is basically a dimensionality reduction function that transfers the data from the data space (the space in which the data points are presented) to a latent space. The decoder can be considered as the inverse function of the encoder, which transfers the data points in the latent space to the data space. Both encoder and decoder (auto-encoder) are trained in a way that the latent space preserves the main structure of the data. Encoder and decoder with multiple layers of representation form deep auto-encoders. We call the encoder and decoder with convolutional layers of representation convolutional encoder and decoder, respectively. The auto-encoder structure (with 8-D generative configuration) is presented in Figure 2.

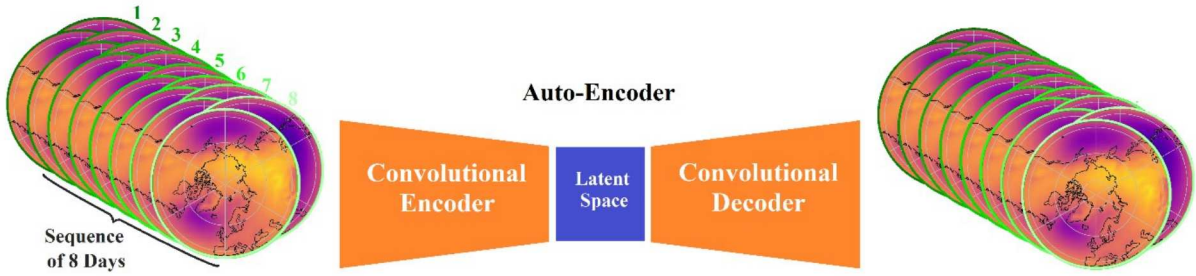

Figure 2: Generative Convolutional Auto-encoder with the 8-day sequences of MSLP and 300-700-T fields input/output (8-D generative configuration).

Exploiting the convolutional filters, convolutional auto-encoders can capture the spatial hierarchy of local patterns in the dataset. An illustrative example is given in Figure 3. To capture the dynamical patterns in datasets with time dimension, we used either 3d-CNN or Convolutional Long Short Term Memory (ConvLSTM) layers (Ji et al., 2012; Shi et al., 2015). These layers can capture dynamical patterns of spatial fields. We trained different convolutional auto-encoders to find the optimum architecture for analyzing the large-scale circulation regime. Based on their input and output shape, the convolutional auto-encoders can be categorized into two groups of generative and predictive convolutional auto-encoders.
As described above, in generative convolutional auto-encoders, the input and output are similar. Hence, a generative auto-encoder is trained in a way that it can be able to generate the input data point. However, in predictive convolutional auto-encoders, the input and output are not similar. In a predictive auto-encoder the output is the prediction fields for the input. I.e., given a sequence of data fields as an input (input data point) to the auto-encoder, the output should be the consecutive data fields of the input.

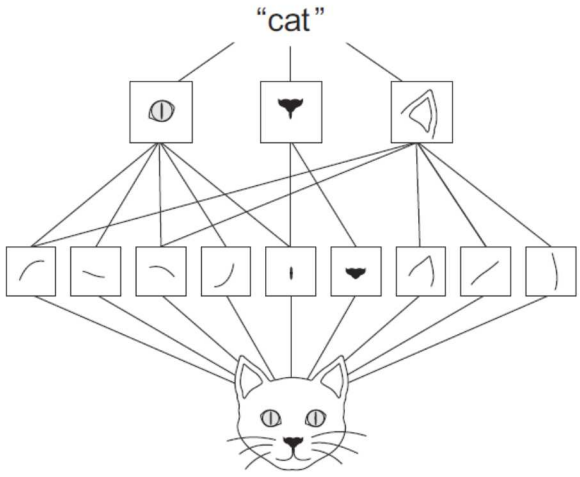

Figure 3: The spatial hierarchy of 2D convolutional filters. Local primary patterns combine to form large scale patterns (Chollet, 2021).

2.2.2.1 Auto-encoder architecture

In an attempt to find the optimum auto-encoder for analyzing the large-scale circulation, different architectures of convolutional auto-encoder have been used. The hyperparameters of the analyzed auto-encoder are presented in Table 3 of Appendix 1. Different auto-encoder architectures differ in being generative or predictive, layer type, layer configuration, input and output shape, and the latent space dimension. For

all the convolutional auto-encoders, we used mean square error (difference between the output of the auto-encoder and the expected output) and Adam optimizer (Kingma and Ba, 2014) as the training loss function and optimizer, respectively. The training process is restricted by the same early stopping conditioned on validation loss (the mean square error of the auto-encoder calculated for the validation dataset) for all the auto-encoders. If the validation loss will not reach a new minimum after 50 epochs of training, the training process is stopped and the auto-encoder weights corresponding to the validation loss minimum are restored. This minimum is called validation reconstruction loss and is saved for every auto-encoder to be used as an evaluation metric. The early stopping condition prevents the deep auto-encoders from overfitting while minimizing the validation loss.

2.2.3 Evaluation metrics

Two metrics, namely validation reconstruction loss and overfitting parameter are used to evaluate the auto-encoders performance. The validation reconstruction loss determines the auto-encoder performance in reconstructing the output fields, while the overfitting parameter measures the auto-encoder output generalization. The validation reconstruction loss is the minimum validation loss in the training process with the early stopping condition. The Overfitting Parameter (OP) is calculated as follows:

$$OP = \frac{VRL - TRL}{VRL} \times 100 \qquad \textit{Equation 1}$$

Where VRL is Validation Reconstruction Loss and TRL is Train Reconstruction Loss that is the training loss at the epoch when validation loss is minimized. Hence, the overfitting parameter determines the auto-encoder capability in overfitting to the train dataset. An auto-encoder with similar validation and training loss results in a low overfitting parameter.

3. Results and Discussion

3.1 Auto-encoder

We used auto-encoders to analyze the Arctic circulation sensitivity to local forcing over Europe. The auto-encoders have been used for two purposes: 1) anomaly detection and 2) regime classification. Before starting the analysis, we need to evaluate and determine the optimum auto-encoder.

3.1.1 Auto-encoder architecture

We examined each auto-encoder introduced in Table 3 of Appendix 1 based on their validation reconstruction loss and overfitting parameter values. The results are presented in Table 1. The whole dataset is used (the control run and the experiment dataset) to generate the values in Table 1. The detailed information about each auto-encoder is presented in Table 3 of Appendix 1 with the same number id. Table 1 shows that in general, the auto-encoders with a higher number of trainable parameters tend to produce larger overfitting parameter value. The auto-encoders with 3d-CNN layers tend to produce lower validation reconstruction loss, which shows the good performance of the 3d-CNN layers in capturing the spatiotemporal patterns in the dataset. Auto-encoder number 15 performed extraordinary in both the validation reconstruction loss and overfitting parameter. It is a generative convolutional auto-

encoder with the latent space dimension of 25600 that consists of 3d-CNN layers. The input and output of this auto-encoder are data points with sequences of 8 days daily mean fields (8-D generative configuration with the data space dimension: 107584). We used this auto-encoder architecture for our further analysis.

Table 1: *Auto-encoders evaluation.*

Nr	Validation loss	Overfitting parameters (%)
1	1.203×10^{-1}	0.08
2	1.183×10^{-1}	0.01
3	6.802×10^{-3}	0.49
4	1.926×10^{-3}	4.44
5	2.394×10^{-3}	18.94
6	9.131×10^{-4}	25.83
7	8.584×10^{-4}	32.90
8	8.581×10^{-4}	26.27
9	1.236×10^{-3}	45.65
10	4.610×10^{-4}	19.41
11	1.034×10^{-3}	30.94
12	9.249×10^{-4}	71.63
13	9.148×10^{-5}	27.18
14	9.501×10^{-5}	25.09
15	3.844×10^{-5}	6.37
16	1.482×10^{-4}	12.45
17	1.603×10^{-4}	32.35

3.2 Circulation anomaly

We can train and validate our selected auto-encoder by just using the model control run dataset. This way the auto-encoder will only learn the spatiotemporal patterns present in the model control dataset. These patterns represent the dynamical structure of circulation poleward of 30° N in the control run. As we used the 8-day sequences of daily mean fields for the selected auto-encoder, the dynamical structure with the temporal duration of less than 8 days can be captured. If we feed a data point that has a new spatiotemporal pattern (which was not present in the model control dataset), the auto-encoder would well perform in generating a proper output data point. Therefore, it is expected that the autoencoder produces large errors in generating data points with new patterns in them. Using measures like mean square error for a generated data point can be a good representative of the presence of new patterns in the data point.

We fed the radiation experiments dataset to the trained auto-encoder. Figure 4 shows the mean square error for all the data points in both the control and experiment datasets. Figure 4 shows that the auto-encoder mean square error shows a periodic seasonal pattern with higher values in wintertime for both datasets. The auto-encoder performs less well in generating the winter data points compared with the summer data points. This is most probably due to the presence of complex spatiotemporal patterns in the large-scale circulation of the northern hemisphere in boreal winter. Moreover, the mean square error for the radiation experiment did not show any anomalous behavior, which indicates that adding the radiation forcing does not add new dynamical processes to the large-scale circulation.

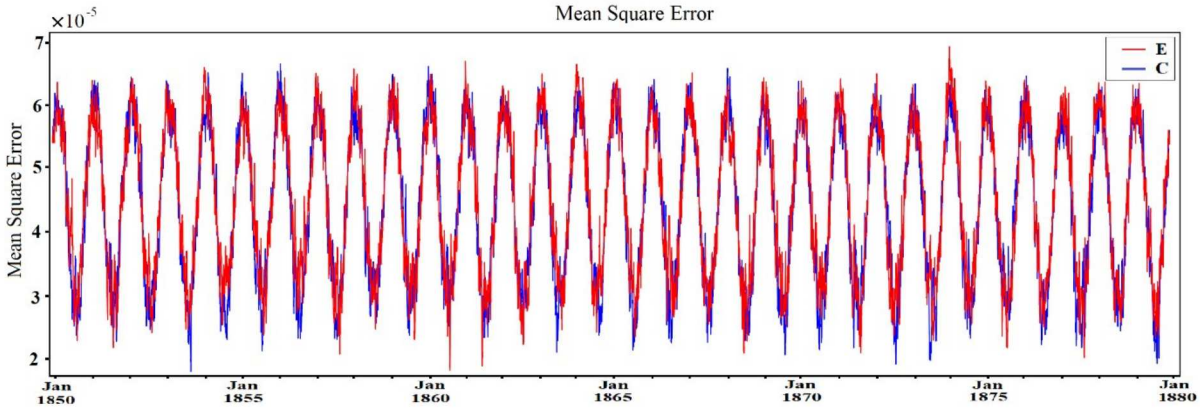

Figure 4: Mean Square Error for the Control run (blue) and the Radiation experiment (red) for data points from Jan 1850 to Jan 1880.

3.3 Latent space

Using auto-encoders, a data point can be transferred into a point in the latent space of the auto-encoder. This latent space is basically a feature space for the data points. In the convolutional auto-encoder, the latent space includes the spatiotemporal features of the dataset.

We trained the selected auto-encoder with the whole dataset (including both the control run and the experiment datasets) and used the latent space for clustering the circulation regime. The latent space has a lower dimension than the original data space but preserves the main structure of the data. The latent space is evaluated to see whether it can construct the data points mean. We calculated the mean for the whole dataset (with 8-D generative configuration) in both the data space and latent space (transferred using the encoder). The latent space mean is then transferred to the data space with the decoder to form the reconstructed mean. Both the data space mean and the reconstructed mean are in 8-D generative configuration. The corresponding difference between the data space mean and the reconstructed mean has the standard deviation of 0.46 hPa and 4.74 gpm for MSLP and 300-700-T fields, respectively. Figure 5 shows the mean (over the time dimension) of the reconstructed mean (first column), and the mean of the data space mean (second column), and their difference. Figure 5 shows that the spatial patterns of both MSLP and 300-700-T fields are similar in the data space mean and the reconstructed mean. Thus, we are able to reconstruct the data space mean using the latent space mean.

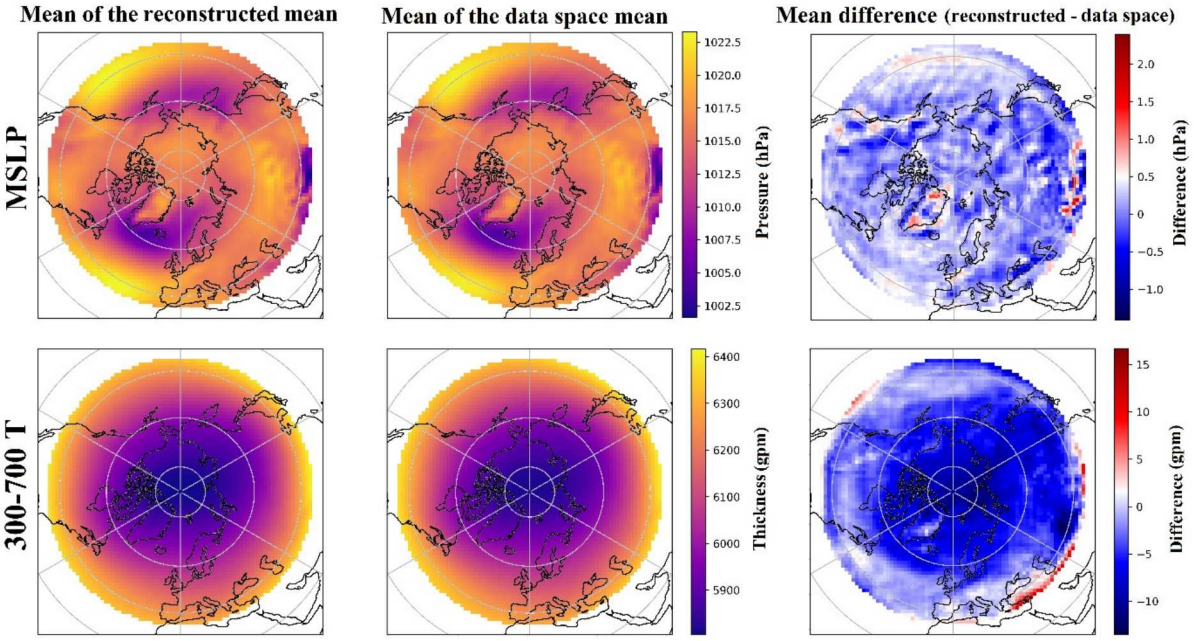

Figure 5: The mean MSLP (first row) and 300-700-T (second row) fields calculated for the reconstructed mean (first column) and the data space mean (second column) and their difference (third column).

The latent space has been used for clustering the circulation regime. To do so, we transferred all data points to the latent space and performed a k-mean clustering in the latent space. As k-mean uses the Euclidean distance to measure similarities, we have to make sure that data points close to each other in the latent space are also close in the data space. We tested the latent space continuity by the following method. First, we calculated the standard deviation for the data point distribution in the latent space (σ). Then we chose 10 random data points in the data space (normalized data space, namely data space with normalized MSLP and 300-700-T). We transferred these data points into the latent space using the encoder. For each data point, we added a random vector (with the values between 0 and 1) multiplied by 0.1σ and repeated this process for 100 times. Consequently, for every data point, we have 100 data points randomly distributed within 0.1σ distance from the point in the latent space. We transferred all these data points to the data space (normalized data space) using the decoder. After that, for each data point, we subtracted its neighboring 100 data points from its initial data point in the data space and calculated their standard deviation for all data points to get the mean standard deviation of 0.1σ displacement in latent space. We repeated the process for different factors of σ and the results are presented in Table 2. By increasing the displacement factor in the latent space, the mean standard deviation corresponds to the displacement in the data space increases. Hence, the neighbouring data points in the latent space are similar in the data space.

Table 2: *The mean standard deviation (MSD) of the difference of 12000 reconstructed data points from their neighbouring data points in latent space within different range of latent space standard deviation (σ).*

	0.1σ	0.2σ	0.3σ	0.4σ	0.5σ	0.6σ	0.7σ	0.8σ	0.9σ	1σ	2σ	3σ
MSD	0.0063	0.0067	0.0073	0.0080	0.0089	0.0098	0.0108	0.0119	0.0130	0.0142	0.0262	0.0391

3.4 Circulation clustering

We performed k-mean clustering with 12, 24, 60, 120, and 240 classes in the latent space. Here, we only show results of clustering with 12 classes. Each cluster center is a point in the latent space. We transferred these points to the data space (8-day sequences of data) using the decoder. Figure 6 illustrates the mean of cluster centers for the MSLP field (the 300-700-T field is not shown here). The occurrence frequency of different classes for the control run and the experiment is shown in Figure 7. Each cluster has its maximum occurrence in a specific month, and they cover all 12 months of the year (Figure 7). Hence, the clustering with 12 classes captures the main seasonal cycle of the circulation regime.

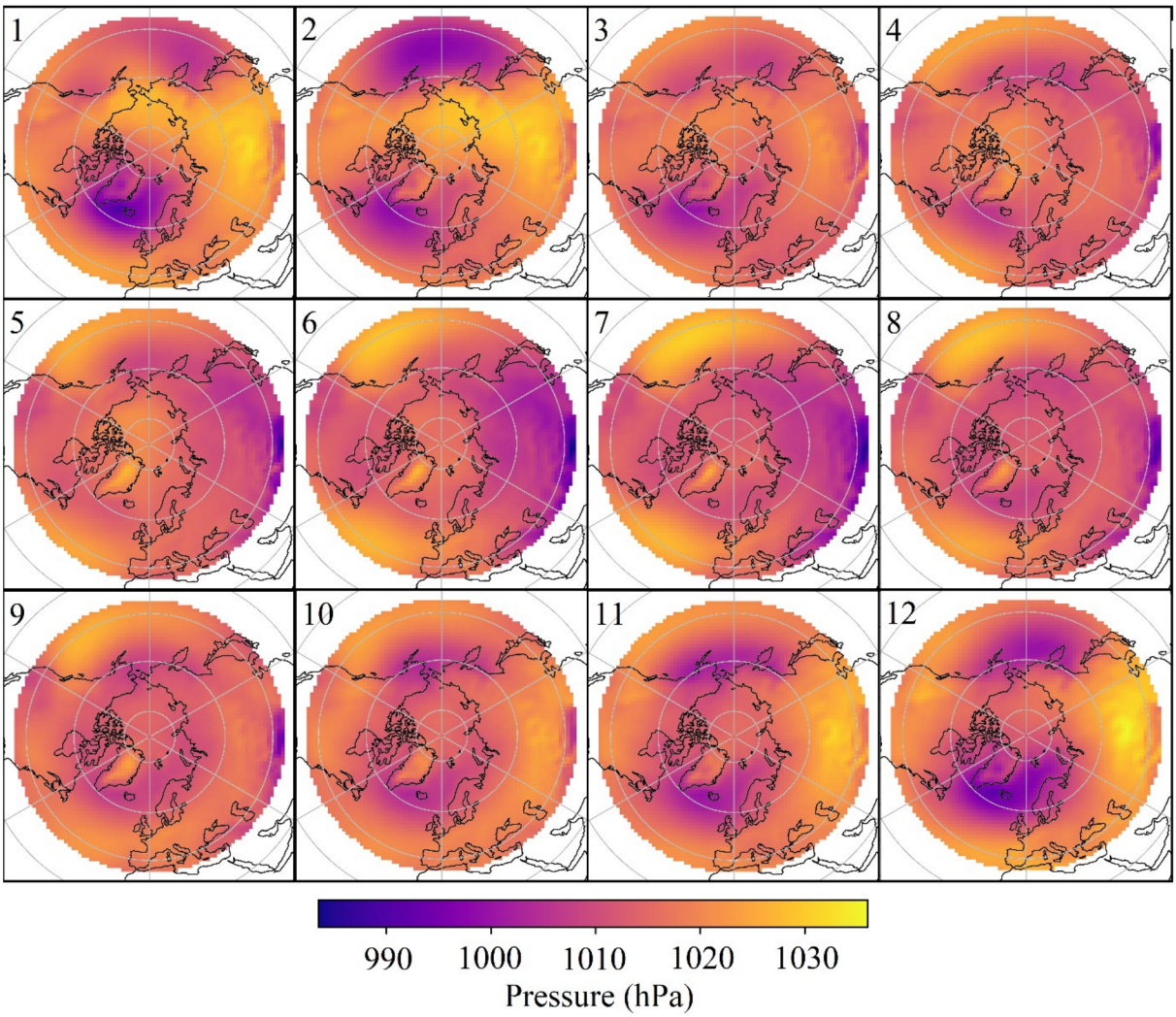

Figure 6: 8-day mean MSLP for classes' center using k-means clustering with 12 classes in latent space.

4. Conclusions and outlook

The deep auto-encoders show good skills in analyzing the large-scale circulation regime. The auto-encoders with 3d-CNN layers performed better considering the reconstruction loss and generalization. The latent space provided by the auto-encoder is basically a feature space that preserves the spatiotemporal structure of the whole dataset.

The anomaly detection using the deep auto-encoder suggested that the idealized radiation negative forcing over Europe does not introduce any new spatiotemporal pattern in the large-scale circulation regimes. The clustering analysis of the large-scale circulation using the deep auto-encoders for higher class numbers (not shown here) suggested that the radiative forcing may contribute to a disturbance in the occurrence frequency of some preferred circulation. However, further investigation is required to analyzed these preferred circulation regimes.

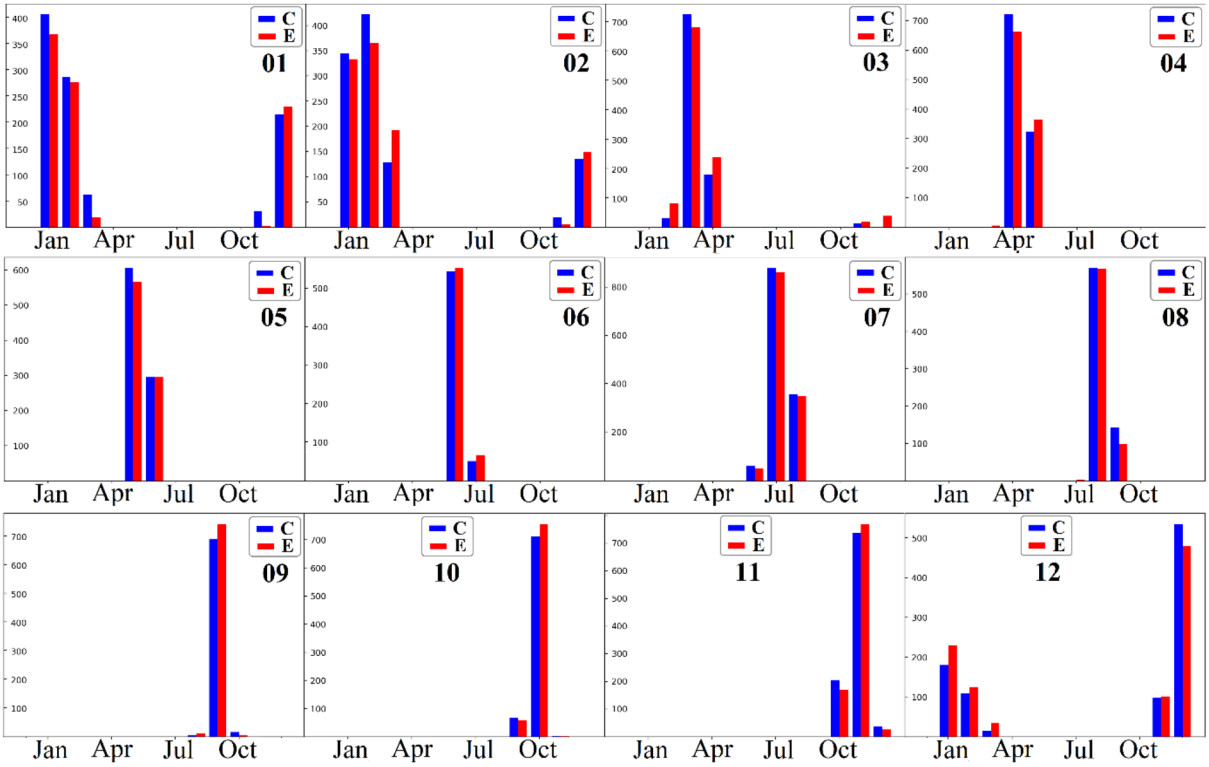

Figure 7: Monthly occurrence frequency of 12 classes in the Control run (blue) and the Radiation experiment (red)

Acknowledgements

We gratefully acknowledge the funding by the Deutsche Forschungsgemeinschaft (DFG, German Research Foundation) – Projektnummer 268020496 – TRR 172, within the Transregional Collaborative Research Center "ArctiC Amplification: Climate Relevant Atmospheric and SurfaCe Processes, and Feedback Mechanisms (AC)[3]

Appendix 1: Auto-encoders detailed architecture

Table 3 shows the architecture of different auto-encoders. D, F, M, N, R, U, and CNNT refer to Dense, Flatten, Max-pooling, batch Normalization, Reshape, Upsampling, and CNN Transpose layers, respectively. The superscripts of CNN, CNNT, and ConvLSTM determine the number of filters used by these layers. The superscript of D layers denotes the output shape of a Dense layer. The CNN's subscript determines whether the CNN is 2d or 3d. CNNs with strides is denoted by with CNN(s), and CNNs with valid padding is denoted by CNN(v). The same applies to CNNT. The subscripts for ConvLSTM layers determine whether the ConvLSTM layer returns sequences (3) or not (2). The subscripts in U and M determine whether they are 2d or 3d. M(t) is used when the max pooling also applies to the time

dimension. The same applies to U(t). In Table 3, the G/P column specifies whether the auto-encoder is generative (G) or predictive (P).

Table 3: *Auto-encoders architecture*

Nr	Input sequence	output sequence	Latent dimension	G/P	Encoder	Decoder
1	1	1	2	G	$CNN_2^{32}(s,v) - CNN_2^{32}(s,v)$ $- CNN_2^{32}(s,v) - CNN_2^{32}(s,v$ $- F - D^{32} - D^2$	$D^{32} - D^{20736} - R - CNNT_2^{32}(v)$ $- CNNT_2^{32}(v) - CNNT_2^2(v)$
2	1	1	3	*G*	$CNN_2^{32}(s,v) - CNN_2^{32}(s,v)$ $- CNN_2^{32}(s,v) - CNN_2^{32}(s,v$ $- F - D^{32} - D^3$	$D^{32} - D^{20736} - R - CNNT_2^{32}(v)$ $- CNNT_2^{32}(v) - CNNT_2^2(v)$
3	1	1	10	G	$CNN_2^{32}(s,v) - CNN_2^{32}(s,v)$ $- CNN_2^{32}(s,v) - CNN_2^{32}(s,v$ $- F - D^{32} - D^{10}$	$D^{32} - D^{20736} - R - CNNT_2^{32}(v)$ $- CNNT_2^{32}(v) - CNNT_2^2(v)$
4	1	1	20	G	$CNN_2^{32}(s,v) - CNN_2^{32}(s,v)$ $- CNN_2^{32}(s,v) - CNN_2^{32}(s,v$ $- F - D^{32} - D^{20}$	$D^{32} - D^{20736} - R - CNNT_2^{32}(v)$ $- CNNT_2^{32}(v) - CNNT_2^2(v)$
5	7	3	1600	*P*	$ConvLSTM_3^{32} - N$ $ConvLSTM_2^{64} - N$ $- CNN_2^{64} - M_2 - N$ $- CNN_2^{32} - M_2 - N$ $- CNN_2^{32} - M_2 - N$ $- CNN_2^{16} - M_2 - F$	$R - CNN_2^{32} - U_2 - N$ $CNN_2^{64} - U_2 - N$ $CNN_2^{30} - U_2 - N$ $- CNN_2^{16} - N - CNN_2^6 - R$
6	7	3	800	*P*	$- CNN_3^{64} - M_3 - N$ $- CNN_3^{64} - M_3(t) - N$ $- CNN_3^{64} - M_3(t) - N$ $- CNN_3^{32} - M_3 - F$	$R - CNNT_3^{64} - U_3(t) - N$ $- CNNT_3^{64} - U_3(t) - N$ $- CNNT_3^{32} - U_3 - N$ $- CNNT_3^{16} - U_3 - N - CNNT_3^2($
7	7	3	800	*P*	$- ConvLSTM_3^{64}(R) - M_3 - N$ $- ConvLSTM_3^{64}(R) - M_3 - N$ $- ConvLSTM_3^{64}(R) - M_3 - N$ $- ConvLSTM_2^{32}(R) - M_2 - N$	$R - CNNT_3^{64} - U_3(t) - N$ $- CNNT_3^{64} - U_3(t) - N$ $- CNNT_3^{32} - U_3 - N$ $- CNNT_3^{16} - U_3 - N - CNNT_3^2($
8	7	3	3200	*P*	$- CNN_3^{64} - M_3 - N$ $- CNN_3^{64} - M_3(t) - N$ $- CNN_3^{64} - M_3(t) - N$ $- CNN_3^{128} - M_3 - N - F$	$R - CNNT_3^{128} - U_3(t) - N$ $- CNNT_3^{64} - U_3(t) - N$ $- CNNT_3^{64} - U_3 - N$ $- CNNT_3^{32} - U_3 - N - CNNT_3^2$
9	7	3	200	*P*	$- CNN_3^{64} - M_3 - N$ $- CNN_3^{64} - M_3(t) - N$ $- CNN_3^{64} - M_3(t) - N$ $- CNN_3^{128} - M_3 - N$ $- F - D^{500} - D^{200}$	$D^{500} - D^{3200} - R$ $- CNNT_3^{128} - U_3(t) - N$ $- CNNT_3^{64} - U_3(t) - N$ $- CNNT_3^{64} - U_3 - N$ $- CNNT_3^{32} - U_3 - N - CNNT_3^2$
10	7	1	3200	*P*	$- CNN_3^{64} - M_3 - N$ $- CNN_3^{64} - M_3(t) - N$ $- CNN_3^{64} - M_3(t) - N$	$R - CNNT_3^{128} - U_3 - N$ $- CNNT_3^{64} - U_3 - N$ $- CNNT_3^{64} - U_3 - N$

					$-CNN_3^{128}-M_3-N-F$	$-CNNT_3^{32}-U_3-N-CNNT_3^2$
11	7	1	200	*P*	$-CNN_3^{64}-M_3-N$ $-CNN_3^{64}-M_3(t)-N$ $-CNN_3^{64}-M_3(t)-N$ $-CNN_3^{128}-M_3-N$ $-F-D^{500}-D^{200}$	$D^{500}-D^{3200}-R$ $-CNNT_3^{128}-U_3-N$ $-CNNT_3^{64}-U_3-N$ $-CNNT_3^{64}-U_3-N$ $-CNNT_3^{32}-U_3-N-CNNT_3^2$
12	7	3	25600	*P*	$-CNN_3^{64}-M_3-N$ $-CNN_3^{128}-M_3(t)-N$ $-CNN_3^{128}-M_3(t)-N$ $-CNN_3^{256}-N-F$	$R-CNNT_3^{256}-U_3(t)-N$ $-CNNT_3^{128}-U_3(t)-N$ $-CNNT_3^{64}-U_3-N$ $-CNNT_3^2-M_3$
13	7	1	46208	*P*	$ConvLSTM_3^{32}-N$ $ConvLSTM_2^{64}-N$ $-CNN_2^{64}-M_2-N$ $-CNN_2^{64}-N-CNN_2^{128}$ $-M_2-N-CNN_2^{128}-F$	$R-CNN_2^{128}-U_2-N$ $CNN_2^{64}-N$ $CNN_2^{32}-U_2-N$ $-CNNT_2^{16}(v)-CNNT_2^2(v)-R$
14	7	1	46208	*P*	$ConvLSTM_3^{50}-N$ $ConvLSTM_2^{64}-N$ $-CNN_2^{64}-M_2-N$ $-CNN_2^{64}-N-CNN_2^{128}$ $-M_2-N-CNN_2^{128}-F$	$R-CNN_2^{128}-U_2-N$ $CNN_2^{64}-N$ $CNN_2^{32}-U_2-N$ $-CNNT_2^{16}(v)-CNNT_2^2(v)-R$
15	8	8	25600	*G*	$-CNN_3^{128}-M_3(t)-N$ $-CNN_3^{128}-M_3(t)-N$ $-CNN_3^{256}-M_3(t)-N$ $-CNN_3^{256}-N-F$	$R-CNNT_3^{256}-U_3(t)-N$ $-CNNT_3^{128}-U_3(t)-N$ $-CNNT_3^{128}-U_3(t)-N$ $-CNNT_3^{64}(v)-CNNT_3^2$
16	8	8	700	*G*	$-CNN_3^{128}-M_3(t)-N$ $-CNN_3^{128}-M_3(t)-N$ $-CNN_3^{256}-M_3(t)-N$ $-CNN_3^{256}-M_3-N$ $-CNN_3^{256}-N-D^{700}$	$D^{6400}-R-CNNT_3^{256}$ $-U_3-N-CNNT_3^{256}-U_3(t)-$ $-CNNT_3^{128}-U_3(t)-N$ $-CNNT_3^{128}-U_3(t)-N$ $-CNNT_3^{64}(v)-CNNT_3^2$
17	8	8	200	*G*	$-CNN_3^{128}-M_3(t)-N$ $-CNN_3^{128}-M_3(t)-N$ $-CNN_3^{256}-M_3(t)-N$ $-CNN_3^{256}-M_3-N$ $-CNN_3^{256}-N-D^{200}$	$D^{6400}-R-CNNT_3^{256}$ $-U_3-N-CNNT_3^{256}-U_3(t)-$ $-CNNT_3^{128}-U_3(t)-N$ $-CNNT_3^{128}-U_3(t)-N$ $-CNNT_3^{64}(v)-CNNT_3^2$

5. References

Abadi, M., Agarwal, A., Barham, P., Brevdo, E., Brevdo, Z., Citro, C., et al., 2015. TensorFlow: Large-scale machine learning on heterogeneous systems. Retrieved from https://www.tensorflow.org/ (Software available from tensorflow.org

Cassano, J.J., Uotila, P. and Lynch, A., 2006. Changes in synoptic weather patterns in the polar regions in the twentieth and twenty-first centuries, part 1: Arctic. International Journal of Climatology: A Journal of the Royal Meteorological Society, 26(8),1027-1049, doi:10.1002/joc.1306.

Chollet, F., 2021. Deep learning with Python. Simon and Schuster.

Chollet, F., 2015. Keras. https://keras.io

Giorgetta, M.A., Jungclaus, J., Reick, C.H., Legutke, S., Bader, J., Böttinger, M., Brovkin, V., Crueger, T., Esch, M., Fieg, K. and Glushak, K., 2013. Climate and carbon cycle changes from 1850 to 2100 in MPI-ESM simulations for the Coupled Model Intercomparison Project phase 5. Journal of Advances in Modeling Earth Systems, 5(3), 572-597, doi: 10.1002/jame.20038.

Guo, X., Liu, X., Zhu, E. and Yin, J., 2017, November. Deep clustering with convolutional autoencoders. In International conference on neural information processing, 373-382, doi:10.1007/978-3-319-70096-0_39.

Hannachi, A., Straus, D.M., Franzke, C.L., Corti, S. and Woollings, T., 2017. Low-frequency nonlinearity and regime behavior in the Northern Hemisphere extratropical atmosphere. Reviews of Geophysics, 55(1), 199-234, doi:10.1002/2015RG000509.

Jaiser, R., Dethloff, K., Handorf, D., Rinke, A. and Cohen, J., 2012. Impact of sea ice cover changes on the Northern Hemisphere atmospheric winter circulation. Tellus A: Dynamic Meteorology and Oceanography, 64(1), 11595, doi:10.3402/tellusa.v64i0.11595.

Ji, S., Xu, W., Yang, M. and Yu, K., 2012. 3D convolutional neural networks for human action recognition. IEEE transactions on pattern analysis and machine intelligence, 35(1), 221-231, doi:10.1109/TPAMI.2012.59.

Jungclaus, J.H., Fischer, N., Haak, H., Lohmann, K., Marotzke, J., Matei, D., Mikolajewicz, U., Notz, D. and Von Storch, J.S., 2013. Characteristics of the ocean simulations in the Max Planck Institute Ocean Model (MPIOM) the ocean component of the MPI-Earth system model. Journal of Advances in Modeling Earth Systems, 5(2), 422-446, doi:10.1002/jame.20023.

Kingma, D.P. and Ba, J., 2014. Adam: A method for stochastic optimization. arXiv preprint arXiv:1412.6980.

LeCun, Y., Bengio, Y. and Hinton, G., 2015. Deep learning. nature, 521(7553), 436-444, doi:10.1038/nature14539.

Li, Y., Thompson, D.W. and Bony, S., 2015. The influence of atmospheric cloud radiative effects on the large-scale atmospheric circulation. Journal of Climate, 28(18), 7263-7278, doi:10.1175/JCLI-D-14-00825.1.

Maher, P., Gerber, E.P., Medeiros, B., Merlis, T.M., Sherwood, S., Sheshadri, A., Sobel, A.H., Vallis, G.K., Voigt, A. and Zurita-Gotor, P., 2019. Model hierarchies for understanding atmospheric circulation. Reviews of Geophysics, 57(2), 250-280, doi:10.1029/2018RG000607.

Rawat, W. and Wang, Z., 2017. Deep convolutional neural networks for image classification: A comprehensive review. Neural computation, 29(9), 2352-2449, doi:10.1162/neco_a_00990.

Sandu, I., van Niekerk, A., Shepherd, T.G., Vosper, S.B., Zadra, A., Bacmeister, J., Beljaars, A., Brown, A.R., Dörnbrack, A., McFarlane, N. and Pithan, F., 2019. Impacts of orography on large-scale atmospheric circulation. Npj Climate and Atmospheric Science, 2(1), 1-8, doi:10.1038/s41612-019-0065-9.

Shi, X., Chen, Z., Wang, H., Yeung, D.Y., Wong, W.K. and Woo, W.C., 2015. Convolutional LSTM network: A machine learning approach for precipitation nowcasting. Advances in neural information processing systems, 28.

Stevens, B., Giorgetta, M., Esch, M., Mauritsen, T., Crueger, T., Rast, S., Salzmann, M., Schmidt, H., Bader, J., Block, K. and Brokopf, R., 2013. Atmospheric component of the MPI-M Earth system model: ECHAM6. Journal of Advances in Modeling Earth Systems, 5(2), 146-172, doi:10.1002/jame.20015.

Vavrus, S.J., 2018. The influence of Arctic amplification on mid-latitude weather and climate. Current Climate Change Reports, 4(3), 238-249, doi:10.1007/s40641-018-0105-2.

Weyn, J.A., Durran, D.R. and Caruana, R., 2019. Can machines learn to predict weather? Using deep learning to predict gridded 500-hPa geopotential height from historical weather data. Journal of Advances in Modeling Earth Systems, 11(8), 2680-2693, doi:10.1029/2019MS001705.

Weyn, J.A., Durran, D.R. and Caruana, R., 2020. Improving data-driven global weather prediction using deep convolutional neural networks on a cubed sphere. Journal of Advances in Modeling Earth Systems, 12(9), e2020MS002109, doi:10.1029/2020MS002109.

Zhou, C. and Paffenroth, R.C., 2017, August. Anomaly detection with robust deep autoencoders. In Proceedings of the 23rd ACM SIGKDD international conference on knowledge discovery and data mining, 665-674, doi:10.1145/3097983.3098052.

Exploring aerosol-cloud interaction in Southeast Pacific marine stratocumulus during VOCALS regional experiment

Sudhakar, Dipu.[1,✉], **Johannes, Quaas.**[1]

[1] *Leipzig for Meteorology, Universität Leipzig, Germany*
✉*e-mail: dipu.sudhakar@uni-leipzig.de*

Summary: The marine stratocumulus clouds are highly sensitive to aerosol perturbations. In this study, we have explored the cloud susceptibility to aerosol using satellite observation and multi-model simulations over the Southeast Pacific Ocean (SEP). The climatology of satellite observation indicates that SEP is a relatively clean area with low aerosol optical depth (AOD). The SEP is a region of marine stratocumulus deck with cloud fraction (CF) reaching as high as 90% in many regions, with relatively low ($140\,cm^{-3}$) cloud droplet number concentration (CDNC) over the marine environment, and it increases as it moves towards the coast. The joint histogram analysis shows that the AOD-CDNC relation shows positive sensitivity and a non-linear CDNC-LWP (liquid water path) relationship; however, a negative sensitivity is dominant. The multi-model analysis shows that most models have a strong positive AOD-CDNC sensitivity, suggesting that the cloud albedo effect leads to net cooling. The general circulation models (GCM) reveal a negative radiative forcing (-0.28 to -1.36 $W\,m^{-2}$) at the top of the atmosphere (TOA) when using the flux method. It supports the positive AOD-CDNC sensitivity and the resulting negative radiative forcing in GCMs. However, the CDNC-LWP shows a diverse relation in the models. In the GCMs, the effect of cloud microphysics is not considered while estimating the net radiative forcing. To include the effect of cloud microphysics in the radiative forcing estimates, we have proposed a statistical approach to calculate the net radiative forcing. The results show that the net radiative forcing is sensitive to the LWP change due to the aerosol perturbation.

Zusammenfassung: Die marinen Stratocumulus-Wolken reagieren sehr empfindlich auf Aerosol-Störungen. In dieser Studie haben wir die Anfälligkeit der Wolken für Aerosol anhand von Satellitenbeobachtungen und Multi-Modellsimulationen über dem Südostpazifik (SEP) untersucht. Die Klimatologie der Satellitenbeobachtung zeigt, dass der SEP ein relativ sauberes Gebiet mit geringer Aerosol optischer Dicke (AOD) ist. Der SEP ist eine Region mit mariner Stratocumulus-Decke mit einer Wolkbedeckungsgrad (CF), der in vielen Regionen bis zu 90% erreicht, mit einer relativ niedrigen ($140\,cm^{-3}$) Wolkentröpfchenanzahlkonzentration (CDNC) über der marinen Umgebung, und sie nimmt in Richtung Küste zu. Die gemeinsame Histogramm-Analyse zeigt, dass die AOD-CDNC-Beziehung eine positive Sensitivität und eine nicht-lineare CDNC-LWP-Beziehung (Flüssigwasserpfad) aufweist; allerdings ist eine negative Sensitivität vorherrschend. Die Multi-Modellanalyse zeigt, dass die meisten Modelle eine stark positive AOD-CDNC-Empfindlichkeit aufweisen, was darauf hindeutet, dass der Wolkenalbedo-Effekt eine Nettokühlung bewirkt. Die allgemeinen Zirkulationsmodelle

(GCM) zeigen einen negativen Strahlungsantrieb (-0,28 bis -1,36 $\mathrm{W\,m^{-2}}$) am Oberrand der Atmosphäre (TOA), wenn die Flussmethode verwendet wird. Dies unterstützt die positive AOD-CDNC-Empfindlichkeit und den daraus resultierenden negativen Strahlungsantrieb in GCMs. Der CDNC-LWP zeigt jedoch unterschiedliche Abhängigkeiten in den Modellen. In den GCMs wird die Wirkung der Wolkenmikrophysik bei der Abschätzung des Netto-Strahlungsantriebs nicht berücksichtigt. Um die Auswirkungen der Wolkenmikrophysik auf den Strahlungsantrieb einzubeziehen, haben wir einen statistischen Ansatz zur Berechnung des Nettostrahlungsantriebs gewählt. Die Ergebnisse zeigen, dass der Nettostrahlungsantrieb empfindlich auf die LWP-Änderung durch die Aerosolstörung reagiert.

1 Introduction

Aerosols, clouds, and their interaction continue to be the primary contributor to the uncertainty in assessing the Earth's radiation budget estimates (Forster et al., 2021; Mülmenstädt and Feingold, 2018). Atmospheric aerosols can act as cloud condensation nuclei that modulate cloud micro and macrophysical properties (Twomey, 1977; Charlson et al., 1992). Twomey (1977) reported the relation between aerosol concentration, cloud droplet number concentration (CDNC) and cloud albedo. It hypothesized that an increased aerosol loading could modify the CDCN, which enhances the cloud albedo, commonly known as radiative forcing due to aerosol-cloud interaction (Bellouin et al., 2020; Forster et al., 2021). Further, at higher CDNC, the LWP may enhance or decrease, subjected to rapid adjustments to aerosol-cloud interactions (Albrecht, 1989). Thus, aerosols influence the cloud via modifying microphysical processes and substantially impact their radiative forcing (Menon et al., 2002). Satellite imagery has been proven that ship tracks (Goren and Rosenfeld, 2012) and smoke plumes (Goren and Rosenfeld, 2015) are evidence of aerosol-cloud interaction and subsequent radiative effect.

Quantifying the mechanisms responsible for aerosol radiative forcing and its representation in models has been proven to be challenging. Nevertheless, several studies investigated the aerosol-cloud interaction and estimated radiative forcing with a wide range of uncertainty (Twomey, 1977; Menon et al., 2008; Quaas et al., 2008; Wood et al., 2011). The uncertainty may arise from wide observational scales and platforms (McComiskey and Feingold, 2012).

In-situ observation plays a crucial role in unfolding the uncertainties in aerosol-cloud interaction. The VAMOS (Variability of the American Monsoon Systems) Ocean-Cloud-Atmosphere-Land study (VOCALS, Wood et al., 2011) is an international program designed to understand the physical and chemical processes of the coupled climate system of the Southeast Pacific (SEP). The VOCALS campaign is categorized into the VOCAL regional experiment (in-situ observations) and the VOCAL numerical model experiment. The Weather Research and Forecasting model coupled to Chemistry (WRF-chem) and COnsortium for Small-scale MOdeling - Aerosols and Reactive Trace gases (COSMO-ART) are the regional models actively participating in the VOCALS modelling experiment. They have compared the aerosol and cloud characteristics over the SEP with observation and are in good agreement (Wood et al., 2011; Wyant et al., 2015). Additionally, Min et al. (2012) reported a strong correlation between satellite observation, specifically aerosol and cloud optical properties, with the VOCALS in-situ

measurements.

This study explores the aerosol-cloud interaction over the SEP during the VOCALS experiment. For this, we have used satellite observations and multi-model simulations (both regional and global models) to explore the aerosol-cloud interaction over the SEP during the VOCALS experiment. Further, to have a better representation of radiative forcing due to the aerosol-cloud interaction, we have proposed a new statistical method to calculate radiative forcing by considering the cloud's optical properties. Detailed descriptions of numerical models, satellite data sets, and the statistical approach are given in section 2. Results of the analysis have been described in section 3, and the summary and conclusions are presented in section 4.

2 Data and methods

2.1 Regional models

In this study, we have considered simulations from the regional model, WRF-Chem (Grell et al., 2005), and COSMO-ART (Vogel et al., 2006). In both cases, the simulations were carried out for the time period of 15 October to 15 November 2008, which were run continuously in free-running mode. There are two sets of WRF-chem model simulations carried out by the University of Iowa (IOWA, Saide et al., 2012) and the Pacific Northwest National Laboratory (PNNL, Yang et al., 2012). The IOWA simulation uses the lateral boundary condition from the National Centers for Environmental Prediction (NCEP) global Final Analysis (FNL), and the PNNL uses the lateral boundary condition from the NCEP's Global Forecast System (GFS) analyses. The COSMO-ART has been configured, and simulations are carried out by the Karlsruhe Institute of Technology (KIT) research group. The COSMO-ART is based on the mesoscale model system (Vogel et al., 2006). It replaces the meteorological module with an optional weather forecast model COSMO of the Deutscher Wetterdienst (DWD). The modelling system consists of gas-phase chemistry, and aerosol dynamics are online coupled with the COSMO model. The model is initialized and forced with the reanalysis data, the global meteorological model GME (Global Model of the Earth). A detailed description of the above-mentioned regional models can be obtained from Wang et al. (2011), Wood et al. (2011), and Wyant et al. (2015).

2.2 Global models

Although several GCMs are also contributed to VOCALS Rex, we have considered the Aerosol Comparison between Observations and Models (AeroCom, Myhre et al., 2013). For this study, we have considered the following models: (i) the global aerosol-climate model ECHAM6-HAM (European Center for Medium-range Weather Forecasting model, Hamburg version, Zhang et al., 2012), (ii) GISS-modelE (ModelE version of the Goddard Institute for Space Studies, Koch et al., 2011), (iii) GFDL (Geophysical Fluid Dynamics Laboratory, Golaz et al., 2011), (iv) HadGEM3 (Hadley Center Global Environmental Model with the United Kingdom Chemistry and Aerosols, Bellouin et al., 2011), and (v) two versions of SPRINTARS (Spectral Radiation Transport Model for Aerosol Species, Takemura et al., 2009) models. The above models are driven by Aero-

Com emissions for the years 1850 and 2000 (Myhre et al., 2013). A detailed description of nudging and other model treatments is illustrated in Ghan et al. (2016). To study the aerosol-cloud interaction, we have used the GCMs with AeroCom emissions for the year 2000 with three hourly outputs. The aerosol-cloud sensitivity analysis is restricted to the marine stratocumulus clouds over the SEP during the VOCALS intensive experiment from 15 October 2008 to 15 November 2008. Further, the statistical method to calculate radiative forcing is only applied to the AeroCom GCMs. Because the statistical method uses the mean/median change in the LWP over the marine stratocumulus over SEP, that can be estimated only from the simulations with and without aerosol perturbation. Hence, we have used present-day and pre-industrial AeroCom solutions to calculate the change in LWP due to aerosol perturbation. A list of models used in this study, along with their resolutions, is given in Table 1.

2.3 Satellite observation

We have also used data from the Moderate Resolution Imaging Spectroradiometer (MODIS, Platnick et al., 2017) onboard the Aqua satellite. The MODIS satellite delivers daily information on the average cloud and aerosol properties within a 1° × 1° degree resolution (MODIS Level-3 product), with near-global coverage. The primary quantities of interest when investigating aerosol-cloud interaction are aerosol optical depth (AOD) and cloud effective radius (r_e), together with total liquid water path (LWP) and optical depth (τ_c) of the cloud. Although CDNC is not retrieved directly, it can be estimated using τ_c and r_e that uses the adiabatic assumption (Quaas et al., 2006), is given by; CDNC = $\alpha\, \tau_c^{0.5}\, r_e^{-2.5}$, where $\alpha = 1.37 \times 10^{-5}\, m^{-0.5}$. The CDNC is then filtered for single-layer liquid clouds with a cloud-top temperature greater than 268 K and pixels with a cloud fraction greater than 0.9. Additionally, a cloud optical depth of less than two is excluded from the analysis (Gryspeerdt et al., 2019). The CDNC is a crucial parameter for aerosol-cloud interaction because it influences cloud albedo by directly linking with aerosol sources (Wood et al., 2011). The uncertainties in the derived CDNC arise mainly from the cloud droplet effective radius (Grosvenor et al., 2018; Quaas et al., 2006). Further, they suggested that in the broken cloud regime and at the low zenith angle, the uncertainties are higher in the satellite retrieval of CDNC.

Table 1: *Details of models used in this study:*

No.	Models	Type	Model Resolutions
1.	WRF-Chem	Regional	0.25° × 0.25°
2.	COSMO-ART	Regional	0.01° × 0.05°
3.	ECHAM-HAM	GCM	2.50° × 2.5°
4.	HadGEM3	GCM	1.25° × 1.875°
5.	GFDL	GCM	2.50° × 2.5°
6.	GISS	GCM	2.50° × 2.5°
7.	SPRINTARS	GCM	2.50° × 2.5°

In both regional and GCMs, the top cloud CDNC is considered, and the analysis was restricted to liquid phase clouds. The sensitivity cloud microphysics on aerosol perturbation is studied using the joint histograms analysed following Gryspeerdt et al. (2016). In the joint histogram, for instance, the conditional probability is defined as the probability of finding a certain LWP given that a certain CDNC has been observed (CP = [P (LWP | CDNC) × 100]).

2.4 Radiative forcing

Atmospheric aerosols play an important role in modifying the Earth's radiation budget (Menon et al., 2002; Forster et al., 2007). An aerosol perturbation which alters the radiative balance at the top of the atmosphere (TOA) is aerosol radiative forcing. It results in a negative forcing (cooling) at TOA that partly offsets greenhouse warming. The global mean net radiative forcing estimate at TOA is -0.5 Wm^{-2} with an uncertainty of a factor of 2 (Forster et al., 2007). In the global model TOA, radiative forcing is defined as the difference between the radiative fluxes in the absence (pristine pre-industrial) and the presence of aerosol (present-day) (Loeb and Manalo-Smith, 2005). This radiative flux perturbation is a valid option for studying the forcing in different models (Lohmann et al., 2010). In this study, we have used AeroCom models (detailed description in section 2.2) with a baseline state of the atmosphere under pre-industrial conditions and the present state of the atmosphere under present-day conditions (Myhre et al., 2013). From these simulations, aerosol radiative forcing can be expressed as,

$$\Delta F_f = (F_{net}^{\downarrow} - F_{net}^{\uparrow})_{PD} - (F_{net}^{\downarrow} - F_{net}^{\uparrow})_{PI}$$
where, F_{net} = Shortwave + Longwave, PD = Present day, and PI = Pre-industrial (1)

Similarly, from the pre-industrial and present-day model simulation, one can also estimate the net radiative forcing at TOA using cloud optical properties. For this, one can use a joint histogram of CDNC (N_d) and LWP (L), one can choose most likely LWP corresponding to mean/median CDNC (N_d) for present-day and pre-industrial scenarios, the difference between the two LWP (L) is Δ L. With present-day τ_c, N_d, Δ L and assuming one of the g (asymmetry parameter)values (for example, g = 0.85), one can calculate the change in planetary albedo $\Delta\alpha$

$$\Delta\alpha = \frac{5}{6}\frac{(1-g)(a_2-a_1)}{(\tau_c(1-g)+a_2)^2}\frac{\tau_c}{L}\Delta L$$

Where a_1 and a_2 are constants, the corresponding values are 0.092, 1.43 respectively . Along with the TOA, incoming solar radiation $F_s^{\downarrow}$ and fractional coverage with liquid clouds f_{liq} yields TOA radiative forcing and can be expressed as (Quaas et al., 2008),

$$\Delta F_c = -f_{liq}F_s^{\downarrow}\Delta\alpha \quad (2)$$

In this study, the radiative forcing is representative of the months October and November, the intensive VOCALS experiment period and the forcing estimates are restricted to GCMs.

3 Results

3.1 Satellite climatology: aerosol optical depth and cloud optical properties

The monthly climatology of MODIS aqua-derived aerosol and cloud optical properties over SEP has been analyzed for the period of 15 October to 15 November 2004 - 2014. Fig. 1 shows the climatology of the spatial distribution of AOD, cloud fraction (CF), LWP,

and CDNC, respectively. The figure shows that the SEP is a region of low AOD, and it varies between 0.05 to 0.6 (Fig. 1 a). The relatively high AOD can be noticed over the land and adjoining areas. The increased aerosol loading over the land and the adjacent regions is due to the transport of polluted air mass from continental sources (Twohy et al., 2013). The climatological pattern of AOD indicates that SEP is a relatively clean area. The CF climatology suggests that over the oceanic region, the CF exceeds 50% (0.5), and reaches as high as 90% in most parts (Fig. 1 b). Muhlbauer et al. (2014) reported that marine stratocumulus exhibits different morphologies of cellular mesoscale convection, in which the CF is largest for closed mesoscale cellular convection with a mean of about 90% on a global scale. Fig. 1 c shows the LWP climatology with a significant increase over the land relative to the marine environment. The offshore LWP values exceed 250 gm^{-2}, with high values seen over the northwest region, whereas, over the maritime atmosphere, the LWP is observed below 100 gm^{-2}. Aircraft observation during the VOCALS experiment also reported a similar LWP pattern over SEP (Wyant et al., 2015). Further, the CDNC climatology, which is derived from MODIS cloud effective radius (r_e) and cloud optical depth (τ_c), also demonstrates an increase as it moves towards the coast. The offshore low CDNC indicates the existence of broad marine stratocumulus. Over the open ocean, the CDNC values are below 140 cm^{-3}, whereas in the coastal region, it ranges between 200 to 400 cm^{-3}. The climatological values are also in close agreement with VOCALS observation, in which the average CDNC ranges between 80 and 400 cm^{-3} (Zheng et al., 2011).

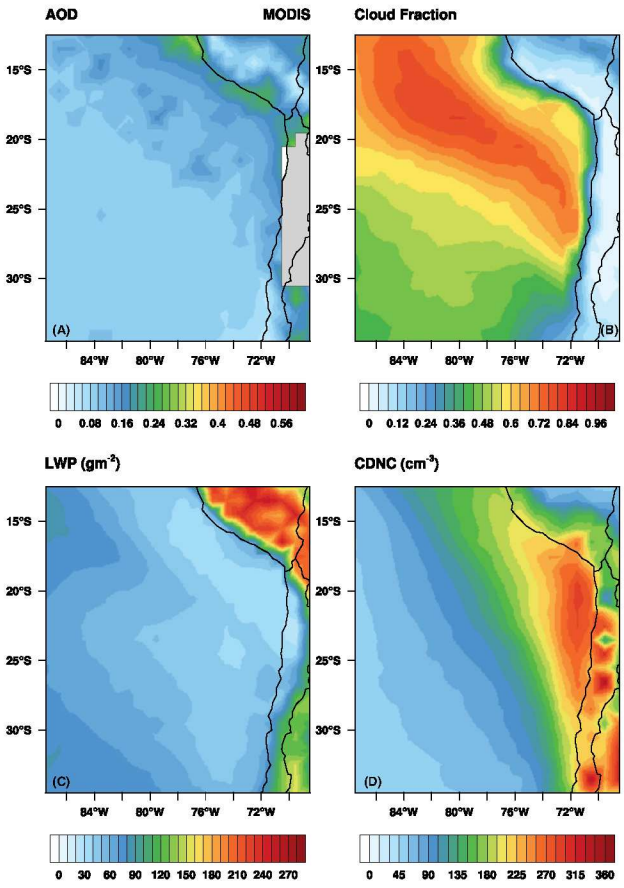

Figure 1: *MODIS climatology (2001-2014) of (a) aeroosl optical depth (AOD), (b) cloud fraction (CF, %), (c) liquid water path (LWP, g m^{-2}), and (d) cloud droplet number concentration (CDNC, c m^{-3}) over the SEP.*

3.2 Aerosol cloud interaction

3.2.1 Satellite analysis

The sensitivity of CDNC to AOD/LWP is investigated using the joint histogram analysis described by (Gryspeerdt et al., 2016). It relies on conditional probability, and the joint

histograms are normalized such that each column adds to unity. Fig. 2 shows the relation between AOD/CDNC-CDNC/LWP derived from the satellite observation over the SEP. Both monthly and climatological AOD-CDNC show a nonlinear relationship. For low AOD, the sensitivity to CDC is negative, with maximum condition probability seen along the negative slope. Then the AOD increases with increasing CDNC (Fig. 1 a and b), with maximum condition probability observed along the positive slope. The strong CDNC-AOD sensitivity at higher AOD is in agreement with previous studies (Quaas et al., 2008; Gryspeerdt et al., 2016). The nonlinearity in AOD-CDNC relation may arise from the poor retrieval of MODIS AOD below 0.05 along with CDNC retrieval uncertainty. Hence care must be taken in interpreting the AOD-CDNC relation (Gryspeerdt et al., 2016). Even though the AOD-CDNC relationship is nonlinear, the dominant relation is positive, especially for the AOD between 0.5 to 1.

In the case of CDNC-LWP relation, both the monthly and the climatology also show a similar pattern (Fig. 2 c and d). In both cases, the relationship is nonlinear, with a slight increase in LWP for the lower CDNC (< 20 cm^{-3}), then decreases with the increasing CDNC. Further, the maximum conditional probability is observed along the nonlinearity curve of the CDNC-LWP relation. Gryspeerdt et al. (2019) also reported a similar nonlinear CDNC-LWP sensitivity over the Global Oceans using satellite data. Although the joint histogram analysis shows a nonlinear relationship, the dominant tendency in both cases is a negative sensitivity.

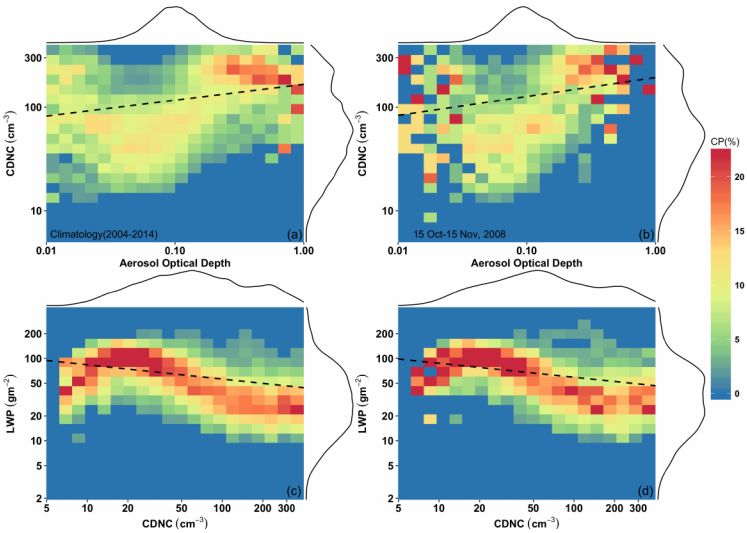

Figure 2: *The MODIS satellite-derived joint histogram for AOD-CDNC (a), climatology for the period 2004 to 2014, (b) monthly time scale (15 October to 15 November 2008), and the joint histogram for CDNC-LWP (c) climatology for the period 2004 to 2014, (d) monthly time scale (15 October to 15 November 2008). The dotted line in each plot represents the linear regression. CP(%) is condition probability: the probability of finding a certain CDNC(LWP) given that a certain AOD(CDNC) has been observed. The marginal plots are the probability density function (PDF) for the respective variables.*

3.2.2 Model analysis

Fig. 3 illustrates the AOD-CDNC sensitivity in the regional and global models. Both WRchem model shows a strong positive AOD-CDNC relationship (the maximum condition probability lies along the positive slope), while the COSMO-ART shows a weak AOD-CDNC sensitivity (Fig. 3 a, b, and c). As the aerosol increases, the CDNC also increases, which suggests a strong cloud lifetime effect in the WRF-chem model. In the case of COSMO-ART, the AOD-CDNC sensitivity is very weak because of the distribution of

AOD and CDNC in the model. In the COSMO-ART, the AOD values range between 0.01 and 0.2, whereas in the WRF, it ranges between 0.02 to 0.8. While the COSMO-ART simulated CDNC ranges between 5 to 300 cm^{-3} with a PDF (probability density function) the peak centred at 60 cm^{-3}. Although the WRF-Chem CDNC also shows similar distribution to that of the COSMO model, it is broader in the WRF-chem models. The GCMs, also show a diverse AOD-CDNC sensitivity, with most models showing a

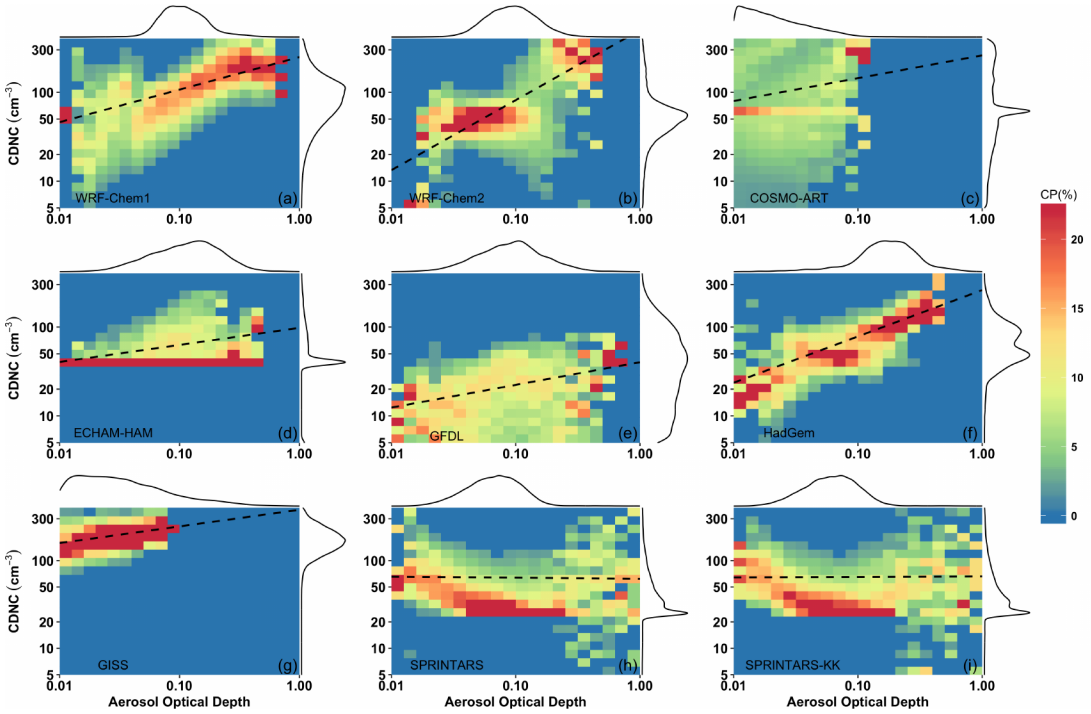

Figure 3: *The AOD-CDNC joint histogram for (a) WRF-Chem (IOWA), (b) WRF-Chem (PNNL), (c) COSMO-ART, (d) ECHAM-HAM, (e) GFDL, (f) HadGem, (g) GISS, (h) SPRINTARS, and (k) SPRINTARS-KK. The figure description is the same as Fig. 1.*

positive AOD-CDNC relation. In the case of ECHAM-HAM (Fig. 3 d), the maximum CP is lining along constant CDNC (50 cm^{-3}) because the lower limit of the prescribed CDNC is 40 cm^{-3}, although the rest of the plot shows a positive sensitivity. The models such as GFDL, HdGem, and GISS show a relatively strong positive AOD-CDNC sensitivity, with maximum CP appearing along the positive slope (Fig. 3 e, f, and g). At the same time, the SPRINTARS models show a weak AOD-CDNC sensitivity. Both SPRINTARS shows negative AOD-CDNC relation for the lower AODs, with maximum CP appearing along the negative slope. For higher AODs, the histograms are randomly distributed (Fig. 3 h and i).

The CDNC-LWP relationship from the regional and global model over the SEP is illustrated in Fig. 4. Both WRF-chem simulations show a strong negative CDNC-LWP relationship (Fig. 4 a and b), with maximum CP appearing along the negative slope. However, the COSMO-ART shows a strong positive relationship, with peak CP appearing along the positive slope (Fig.4 c). Again, the distinct CDNC-LWP relationship within the regional model arises due to the treatment of the microphysical processes in the models. Although the LWP distribution is similar in the regional models, the CDNC distribution in the COSMO-ART model is narrow compared to the WRF-chem.

Furthermore, the CDNC-LWP relationship in the global model also shows a diverse

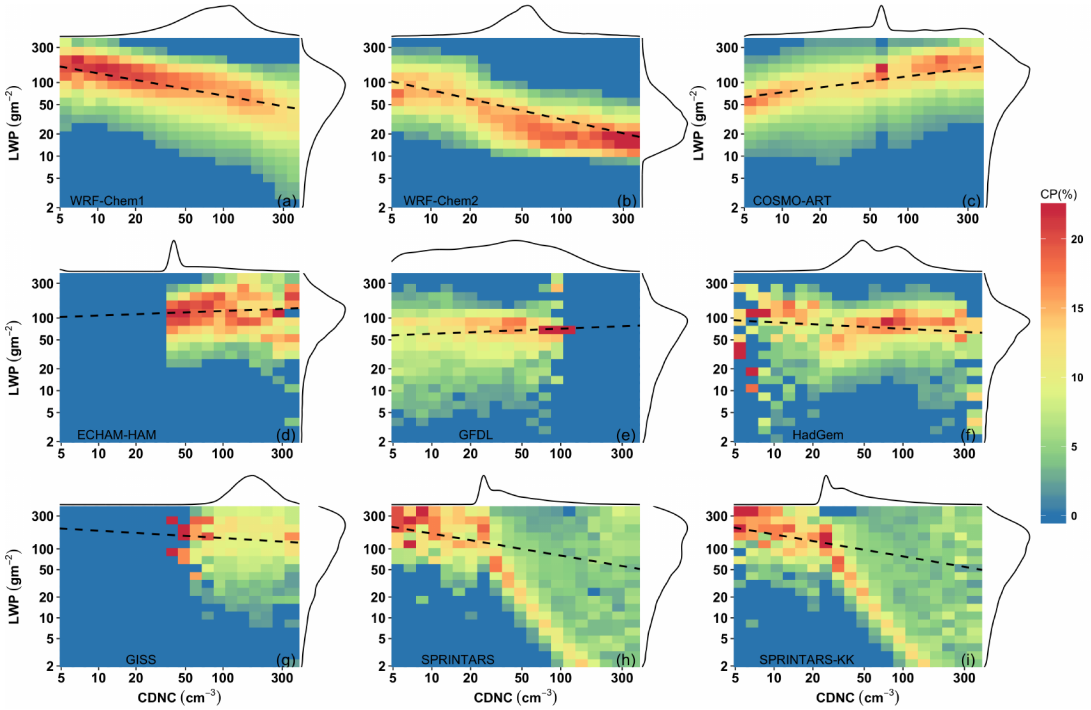

Figure 4: *The CDNC-LWP joint histogram for (a) WRF-Chem (IOWA), (b) WRF-Chem (PNNL), (c) COSMO-ART, (d) ECHAM-HAM, (e) GFDL, (f) HadGem, (g) GISS, (h) SPRINTARS, and (k) SPRINTARS-KK. The figure description is the same as Fig. 1.*

relationship. The ECHAM-HAM and the GFDL models show a somewhat positive relationship (Fig. 4 d and e). In contrast, a negative CDNC-LWP relationship dominates in the models HadGem, GISS and the SPRINTARS, respectively (Fig. 4, f, g, and h). Similar to the regional models, the diverse CDN-LWP relationship also arises due to the CDNC distribution in the respective models. In ECHAM-HAM and SPRINTARS, the CDNC distribution is narrow compared to other GCMs. However, all the GCMs show similar LWP distribution.

3.3 Radiative forcing estimates

The anthropogenic aerosol radiative forcing is estimated using two different methods. The first method uses the top of the atmosphere (TOA) flux between pre-industrial and present-day simulations (equation 1). The second method uses statistical relation using planetary albedo and cloud properties (equation 2). In this study, the radiative forcing estimates are restricted to the GCMs only (AeroCom models), focusing on the VOCALS region and experiment period. The GCM estimated aerosol radiative forcing is provided in Table 2. Even though the aerosol effect and the cloud microphysics are parameterized differently in the GCMs, in the flux method, all the GCMs are able to produce a net negative radiative forcing at the TOA (net cooling) similar to the global average. The multi-model flux-derived radiative forcing ranges from -1.03 to -3.58 W m^{-2}. The wide ranges of GCM radiative forcing are also reported in the previous studies (Quaas et al., 2009).

Table 2: *The net (Shortwave + Longwave) radiative forcing at the TOA over SEP:*

No	Models	ΔF_c at TOA ($W m^2$)		AOD		CDNC ($c m^{-3}$)		LWP ($g m^{-2}$)	
		Flux method	Statistical method	PD	PI	PD	PI	PD	PI
1	ECHAM-HAM	-1.64	-0.47	0.074	0.067	67	55	102.10	107.52
2	GFDL	-1.25	-3.29	0.076	0.058	22	11	61.84	46.77
3	HadGEM3	-3.58	0.78	0.098	0.072	73	56	75.11	72.16
4	GISS	-1.59	0.49	0.062	0.054	177	138	133.10	192.84
5	SPRINTARS	-1.03	1.05	0.071	0.063	50	47	111.80	111.71
6	SPRINTARS*	-1.08	1.08	0.066	0.058	51	47	96.39	95.23

R.F.: Radiative Forcing;
PD: Present Day
PI: Pre-Industrial
SPRINTARS*: SPRINTARS-KK

However, the negative radiative forcing didn't show any signs of the aerosol-cloud interaction (diverse CDNC-LWP sensitivity in GCMs); the statistical method could circumvent it. Similar to the diverse CDNC-LWP relation, the radiative forcing estimated using the statistical method shows different forcing in the GCMs. The ECHAM-HAM and GFDL models show similar radiative forcing (negative) in the statistical and the flux method. In the flux method, the estimated radiative forcings are -0.47 and -3.29 $W m^{-2}$, respectively, for the ECHAM-HAM and GFDL. The rest of the models depict positive radiative forcing of 0.776, 0.495, 1.051, and 1.08 $W m^{-2}$, respectively, for the models HadGEM3, GISS, and SPRINTARS. The CDNC-LWP joint histogram analysis shows a positive CDNC-LWP sensitivity in ECHAM-HAM and GFDL models. It implies that, as the CDNC increases, the LWP also increases, which leads to a negative radiative forcing. However, the rest of the GCMs are susceptible to a negative CDNC-LWP sensitivity, resulting in the positive radiative forcing. The statistical approach accounts for the effect of aerosol on the cloud's microphysical properties in the climate models, resulting in the diverse magnitude of the radiative forcing. Further, it can be due to the cloud microphysics (marine stratocumulus) parameterization in respective GCMs. The global liquid cloud fraction climatology from the GCMs shows large spatial and inter-model variability. Besides the SPRINTERS models, SEP marine stratocumulus clouds are represented quite well in the models, with varying magnitudes, though. Additionally the cloud representation in the GCMs, the factor contributing to the statistical radiative forcing is the sign of the ΔL (change in LWP, $\Delta L = \overline{L_{pd}} - \overline{L_{pi}}$). Thus, it is noticed that in the ECHAM-HAM and GFDL models, marine stratocumulus clouds are more susceptible to aerosols ($-\Delta L$), resulting in a negative radiative forcing. However, in other GCMs, the marine stratocumulus clouds are not susceptible to aerosol perturbation ($+\Delta L$), resulting in a positive radiative forcing.

4 Summary and conclusions

The aerosol-cloud interaction in the marine stratocumulus cloud over the SEP has been invested using satellite observation and multi-model simulations. The MODIS climatology of AOD indicates that SEP is a region of relatively low aerosol loading. The SEP coastal and adjoining regions are relatively polluted compared to the maritime atmo-

sphere. Over the SEP, the MODIS AOD varies between 0.1 to 0.6. The CF climatology shows there is a persistent cloud cover over the ocean, which attributes to the marine stratocumulus deck over the SEP. The annual mean CF exceeds 60% in most regions, except over the coast, where topographic irregularities exist. The corresponding LWP is dominant over the coastal region, which varies between 30 to 300 $\mathrm{g\,m^{-3}}$. Additionally, the CDNC climatology shows a latitudinal gradient with maximum CDNC observed in the coastal region. It is consistent with previous studies (Wyant et al., 2015).

To explore the cloud susceptibility to aerosol loading, we have used a joint histogram of AOD-CDNC and CDNC-LWP. The MODIS satellite analysis shows that on both monthly and climatological time scales, the AOD-CDNC relation shows a dominant positive relation, despite the non-linearity at lower AOD. In contrast, the CDNC-LWP shows a negative sensitivity. A positive AOD-CDNC suggests the cloud albedo effect in the marine stratocumulus clouds (Twomey, 1977; Albrecht, 1989). However, the CDNC-LWP relation shows that the cloud albedo effect (a positive CDNC-LWP relation) is observed only at lower CDNC. The CDNC-LWP relation is dominant, with a negative CDNC-LWP sensitivity that accounts for the cloud droplet entrainment and evaporation (Han et al., 2002).

Further, we have explored aerosol-cloud interaction over the SEP using regional and climate model simulations. The joint histogram analysis shows that both WRF-chem models show a relatively strong AOD-CDNC relation in the regional model compared to the COSMO-ART model. The weak AOD-CDNC relationship in the COSMO-ART model may be due to the poor representation of aerosols in the model compared to WRF-chem. The PDF shows that the AOD distribution is skewed to the right in the COSMO-ART. However, the CDNC shows the normal distribution in the COSMO-ART, which is comparable with WRF-chem. Furthermore, besides the SPRINTERS model, the GCMs also show a positive AOD-CDNC sensitivity over the SEP region. In the case of the CDNC-LWP sensitivity, both the WRF-chem models show a strong negative relationship. At the same time, in the COSMO-ART, the CDNC-LWP shows a strong positive relationship. Likewise, the Aerocom models also depict a diverse CDNC-LWP relationship. In ECHAM-HAM and the GFDL model, a positive CDNC-LWP relation is observed, whereas a negative CDNC-LWP relation is seen in HadGEM, GISS, and SPRINTARS models, respectively.

From the satellite analysis, it is noticed that the AOD-CDNC relation mainly accounts for the cloud lifetime or cloud albedo effect. However, the non-linear CDNC-LWP relation suggests both cloud albedo and entrainment effects. In the case of AOD-CDNC sensitivity derived from the models, most of the model represents the cloud albedo effect. It suggests that, as the aerosol concentration increases, the CDNC also increases, leading to the cloud albedo effect, consequently, a negative radiative forcing. Notably, all the GCMs reveal a negative radiative forcing at the TOA while using the flux method, which is similar to the global mean radiative forcing. However, the radiative forcings are diverse when we use the statistical method, which would also consider the effect of LWP sensitivity to aerosol perturbation. The above analysis suggests that the flux-derived radiative forcing results in net cooling at the TOA irrespective of the model, even though aerosol and cloud parameterizations are treated differently. Further, the GCM models are tuned radiatively to get similar radiative forcing at the TOA. So our analysis suggests that the statistical approach using planetary albedo and cloud properties would be more

appropriate for radiative forcing estimates in which aerosol-mediated indirect effects are also considered. Importantly, the statistical method assumes that the CDNC-LWP sensitivity is linear and the LWP is susceptible to aerosol loading. However, recent studies (in addition to this analysis) suggest that the CDNC-LWP relation is non-linear (Gryspeerdt et al., 2019). So further research would be needed to improve the statistical method to predict the radiative forcing.

Acknowledgements

This study has been carried out as a part of the Aerosols, Clouds, Precipitation and Climate (ACPC) initiative. We thank the VOCALS and KIT group for providing the regional model simulations.

References

Albrecht, B. A.: Aerosols, Cloud Microphysics, and Fractional Cloudiness, Science, 245, 1227–1230, doi:10.1126/science.245.4923.1227, URL http://science.sciencemag.org/content/245/4923/1227, 1989.

Bellouin, N., Rae, J., Jones, A., et al.: Aerosol forcing in the Climate Model Intercomparison Project (CMIP5) simulations by HadGEM2-ES and the role of ammonium nitrate, Journal of Geophysical Research: Atmospheres, 116, n/a–n/a, doi:10.1029/2011JD016074, URL http://dx.doi.org/10.1029/2011JD016074, d20206, 2011.

Bellouin, N., Quaas, J., Gryspeerdt, E., et al.: Bounding global aerosol radiative forcing of climate change, Rev. Geophys., 58, e2019RG000 660, doi:10.1029/2019RG000660, 2020.

Charlson, R. J., Schwartz, S. E., Hales, J. M., et al.: Climate Forcing by Anthropogenic Aerosols, Science, 255, 423–430, doi:10.1126/science.255.5043.423, URL https://science.sciencemag.org/content/255/5043/423, 1992.

Forster, P., Ramaswamy, V., Artaxo, P., et al.: Changes in Atmospheric Constituents and in Radiative Forcing, pp. 129–234, Cambridge University Press, Cambridge, United Kingdom and New York, NY, USA, 2007.

Forster, P., Storelvmo, T., Armour, K., et al.: The Earth's Energy Budget, Climate Feedbacks, and Climate Sensitivity. In *Climate Change 2021: The Physical Science Basis. Contribution of Working Group I to the Sixth Assessment Report of the Intergovernmental Panel on Climate Change* [Masson-Delmotte, V., P. Zhai, A. Pirani, S.L. Connors, C. Péan, S. Berger, N. Caud, Y. Chen, L. Goldfarb, M.I. Gomis, M. Huang, K. Leitzell, E. Lonnoy, J.B.R. Matthews, T.K. Maycock, T. Waterfield, O. Yelekçi, R. Yu, and B. Zhou (eds)], chap. 7, Cambridge University Press. In Press., 2021.

Ghan, S., Wang, M., Zhang, S., et al.: Challenges in constraining anthropogenic aerosol effects on cloud radiative forcing using present-day spatiotemporal variability, Proceedings of the National Academy of Sciences, 113, 5804–5811, doi:10.1073/pnas.1514036113, URL http://www.pnas.org/content/113/21/5804.abstract, 2016.

Golaz, J.-C., Salzmann, M., Donner, L. J., et al.: Sensitivity of the Aerosol Indirect Effect to Subgrid Variability in the Cloud Parameterization of the GFDL Atmosphere General Circulation Model AM3, Journal of Climate, 24, 3145–3160, doi:10.1175/2010JCLI3945.1, URL https://doi.org/10.1175/2010JCLI3945.1, 2011.

Goren, T. and Rosenfeld, D.: Satellite observations of ship emission induced transitions from broken to closed cell marine stratocumulus over large areas, Journal of Geophysical Research: Atmospheres, 117, n/a–n/a, doi:10.1029/2012JD017981, URL http://dx.doi.org/10.1029/2012JD017981, d17206, 2012.

Goren, T. and Rosenfeld, D.: Extensive closed cell marine stratocumulus downwind of Europe—A large aerosol cloud mediated radiative effect or forcing?, Journal of Geophysical Research: Atmospheres, 120, 6098–6116, doi:10.1002/2015JD023176, URL http://dx.doi.org/10.1002/2015JD023176, 2015JD023176, 2015.

Grell, G. A., Peckham, S. E., Schmitz, R., et al.: Fully coupled "online" chemistry within the WRF model, Atmospheric Environment, 39, 6957–6975, doi:https://doi.org/10.1016/j.atmosenv.2005.04.027, URL https://www.sciencedirect.com/science/article/pii/S1352231005003560, 2005.

Grosvenor, D. P., Sourdeval, O., Zuidema, P., et al.: Remote Sensing of Droplet Number Concentration in Warm Clouds: A Review of the Current State of Knowledge and Perspectives, Reviews of Geophysics, 56, 409–453, doi:https://doi.org/10.1029/2017RG000593, URL https://agupubs.onlinelibrary.wiley.com/doi/abs/10.1029/2017RG000593, 2018.

Gryspeerdt, E., Quaas, J., and Bellouin, N.: Constraining the aerosol influence on cloud fraction, Journal of Geophysical Research: Atmospheres, 121, 3566–3583, doi:10.1002/2015JD023744, URL http://dx.doi.org/10.1002/2015JD023744, 2015JD023744, 2016.

Gryspeerdt, E., Goren, T., Sourdeval, O., et al.: Constraining the aerosol influence on cloud liquid water path, Atmos. Chem. Phys., 19, 5331–5347, doi:10.5194/acp-19-5331-2019, URL https://acp.copernicus.org/articles/19/5331/2019/, 2019.

Han, Q., Rossow, W. B., Zeng, J., and Welch, R.: Three Different Behaviors of Liquid Water Path of Water Clouds in Aerosol–Cloud Interactions, Journal of the Atmospheric Sciences, 59, 726–735, doi:10.1175/1520-0469(2002)059<0726:TDBOLW>2.0.CO;2, URL https://doi.org/10.1175/1520-0469(2002)059<0726:TDBOLW>2.0.CO;2, 2002.

Koch, D., Bauer, S. E., Genio, A. D., et al.: Coupled Aerosol-Chemistry–Climate Twentieth-Century Transient Model Investigation: Trends in Short-Lived Species and Climate Responses, Journal of Climate, 24, 2693–2714, doi:10.1175/2011JCLI3582.1, URL https://doi.org/10.1175/2011JCLI3582.1, 2011.

Loeb, N. G. and Manalo-Smith, N.: Top-of-Atmosphere Direct Radiative Effect of Aerosols over Global Oceans from Merged CERES and MODIS Observations, Journal of Climate, 18, 3506–3526, doi:10.1175/JCLI3504.1, URL https://doi.org/10.1175/JCLI3504.1, 2005.

Lohmann, U., Rotstayn, L., Storelvmo, T., et al.: Total aerosol effect: radiative forcing or radiative flux perturbation?, Atmospheric Chemistry and Physics, 10, 3235–3246, doi:10.5194/acp-10-3235-2010, URL https://www.atmos-chem-phys.net/10/3235/2010/, 2010.

McComiskey, A. and Feingold, G.: The scale problem in quantifying aerosol indirect effects, Atmospheric Chemistry and Physics, 12, 1031–1049, doi:10.5194/acp-12-1031-2012, URL https://www.atmos-chem-phys.net/12/1031/2012/, 2012.

Menon, S., Genio, A. D. D., Koch, D., and Tselioudis, G.: GCM Simulations of the Aerosol Indirect Effect: Sensitivity to Cloud Parameterization and Aerosol Burden, Journal of the Atmospheric Sciences, 59, 692–713, doi:10.1175/1520-0469(2002)059<0692:GSOTAI>2.0.CO;2, URL https://doi.org/10.1175/1520-0469(2002)059<0692:GSOTAI>2.0.CO;2, 2002.

Menon, S., Genio, A. D., Kaufman, Y., et al.: Analyzing signatures of aerosol-cloud interactions from satellite retrievals and the GISS GCM to constrain the aerosol indirect effect, Journal of Geophysical Research, 113, 1–15, doi:10.1029/2007JD009442, 2008.

Min, Q., Joseph, E., Lin, Y., et al.: Comparison of MODIS cloud microphysical properties with in-situ measurements over the Southeast Pacific, Atmospheric Chemistry and Physics, 12, 11 261–11 273, doi:10.5194/acp-12-11261-2012, URL https://www.atmos-chem-phys.net/12/11261/2012/, 2012.

Muhlbauer, A., McCoy, I. L., and Wood, R.: Climatology of stratocumulus cloud morphologies: microphysical properties and radiative effects, Atmospheric Chemistry and Physics, 14, 6695–6716, doi:10.5194/acp-14-6695-2014, URL https://www.atmos-chem-phys.net/14/6695/2014/, 2014.

Mülmenstädt, J. and Feingold, G.: The Radiative Forcing of Aerosol-Cloud Interactions in Liquid Clouds: Wrestling and Embracing Uncertainty, Curr. Clim. Chang. Rep., 4, 23–40, doi:10.1007/s40641-018-0089-y, URL https://doi.org/10.1007/s40641-018-0089-y, 2018.

Myhre, G., Samset, B. H., Schulz, M., et al.: Radiative forcing of the direct aerosol effect from AeroCom Phase II simulations, Atmospheric Chemistry and Physics, 13, 1853–1877, doi:10.5194/acp-13-1853-2013, URL https://www.atmos-chem-phys.net/13/1853/2013/, 2013.

Platnick, S., Meyer, K. G., King, M. D., et al.: The MODIS Cloud Optical and Microphysical Products: Collection 6 Updates and Examples From Terra and Aqua, IEEE Trans. Geosci. Remote Sens., 55, 502–525, doi:10.1109/TGRS.2016.2610522, 2017.

Quaas, J., Boucher, O., and Lohmann, U.: Constraining the total aerosol indirect effect in the LMDZ and ECHAM4 GCMs using MODIS satellite data, Atmospheric Chemistry and Physics, 6, 947–955, doi:10.5194/acp-6-947-2006, URL https://www.atmos-chem-phys.net/6/947/2006/, 2006.

Quaas, J., Boucher, O., Bellouin, N., and Kinne, S.: Satellite-based estimate of the direct and indirect aerosol climate forcing, Journal of Geophysical Research: Atmospheres, 113, n/a–n/a, doi:10.1029/2007JD008962, URL http://dx.doi.org/10.1029/2007JD008962, d05204, 2008.

Quaas, J., Ming, Y., Menon, S., et al.: Aerosol indirect effects â€“ general circulation model intercomparison and evaluation with satellite data, Atmospheric Chemistry and Physics, 9, 8697–8717, doi:10.5194/acp-9-8697-2009, URL https://www.atmos-chem-phys.net/9/8697/2009/, 2009.

Saide, P. E., Spak, S. N., Carmichael, G. R., et al.: Evaluating WRF-Chem aerosol indirect effects in Southeast Pacific marine stratocumulus during VOCALS-REx, Atmospheric Chemistry and Physics, 12, 3045–3064, doi:10.5194/acp-12-3045-2012, URL https://acp.copernicus.org/articles/12/3045/2012/, 2012.

Takemura, T., Egashira, M., Matsuzawa, K., et al.: A simulation of the global distribution and radiative forcing of soil dust aerosols at the Last Glacial Maximum, Atmospheric Chemistry and Physics, 9, 3061–3073, doi:10.5194/acp-9-3061-2009, URL https://www.atmos-chem-phys.net/9/3061/2009/, 2009.

Twohy, C. H., Anderson, J. R., Toohey, D. W., et al.: Impacts of aerosol particles on the microphysical and radiative properties of stratocumulus clouds over the southeast Pacific Ocean, Atmospheric Chemistry and Physics, 13, 2541–2562, doi:10.5194/acp-13-2541-2013, URL https://www.atmos-chem-phys.net/13/2541/2013/, 2013.

Twomey, S.: The Influence of Pollution on the Shortwave Albedo of Clouds, Journal of the Atmospheric Sciences, 34, 1149–1152, doi:10.1175/1520-0469(1977)034<1149:TIOPOT>2.0.CO;2, URL https://doi.org/10.1175/1520-0469(1977)034<1149:TIOPOT>2.0.CO;2, 1977.

Vogel, B., Hoose, C., Vogel, H., and Kottmeier, C.: A model of dust transport applied to the Dead Sea Area, Meteorologische Zeitschrift, 15, 611–624, doi:10.1127/0941-2948/2006/0168, URL http://dx.doi.org/10.1127/0941-2948/2006/0168, 2006.

Wang, H., Rasch, P. J., and Feingold, G.: Manipulating marine stratocumulus cloud amount and albedo: a process-modelling study of aerosol-cloud-precipitation interactions in response to injection of cloud condensation nuclei, Atmospheric Chemistry and Physics, 11, 4237–4249, doi:10.5194/acp-11-4237-2011, URL https://www.atmos-chem-phys.net/11/4237/2011/, 2011.

Wood, R., Mechoso, C. R., Bretherton, C. S., et al.: The VAMOS Ocean-Cloud-Atmosphere-Land Study Regional Experiment (VOCALS-REx): goals, platforms, and field operations, Atmospheric Chemistry and Physics, 11, 627–654, doi:10.5194/acp-11-627-2011, URL https://www.atmos-chem-phys.net/11/627/2011/, 2011.

Wyant, M. C., Bretherton, C. S., Wood, R., et al.: Global and regional modeling of clouds and aerosols in the marine boundary layer during VOCALS: the VOCA intercomparison, Atmospheric Chemistry and Physics, 15, 153–172, doi:10.5194/acp-15-153-2015, URL https://www.atmos-chem-phys.net/15/153/2015/, 2015.

Yang, Q., Gustafson Jr., W. I., Fast, J. D., et al.: Impact of natural and anthropogenic aerosols on stratocumulus and precipitation in the Southeast Pacific: a regional modelling study using WRF-Chem, Atmospheric Chemistry and Physics, 12, 8777–8796, doi:10.5194/acp-12-8777-2012, URL https://www.atmos-chem-phys.net/12/8777/2012/, 2012.

Zhang, K., O'Donnell, D., Kazil, J., et al.: The global aerosol-climate model ECHAM-HAM, version 2: sensitivity to improvements in process representations, Atmospheric Chemistry and Physics, 12, 8911–8949, doi:10.5194/acp-12-8911-2012, URL https://www.atmos-chem-phys.net/12/8911/2012/, 2012.

Zheng, X., Albrecht, B., Jonsson, H. H., et al.: Observations of the boundary layer, cloud, and aerosol variability in the southeast Pacific near-coastal marine stratocumulus during VOCALS-REx, Atmospheric Chemistry and Physics, 11, 9943–9959, doi:10.5194/acp-11-9943-2011, URL https://www.atmos-chem-phys.net/11/9943/2011/, 2011.

Variation of cloud horizontal sizes and cloud fraction over Europe 1985–2018 in high-resolution satellite data

Linke, O.[1,✉], **Quaas, J.**[1]

[1] *Leipzig Institute for Meteorology, Leipzig University*
✉*e-mail: olivia.linke@uni-leipzig.de*

Summary: Aerosol-cloud interactions are a major uncertainty in estimating the anthropogenic climate change. Adjustments of cloud properties to an aerosol perturbation concern among others the cloud fraction, and have been emphasised as particularly complex.

Cloud adjustments can generate important responses on the distribution of cloud horizontal sizes. We derive the cloud-size distribution as observational constraint for the cloud-fraction response from high-resolution Landsat satellite data. The goal is to carry out long-term trends in cloud sizes and cloud fraction over Europe during 1985–2018 to investigate the impact of major aerosol reductions during that time. Landsat data with a high spatial resolution of 30 m was preprocessed via the web-based platform Google Earth Engine to evade the obstacle of high computational effort and time to handle the comprehensive data archive.

The observed multidecadal trends indicate a widespread increase in cloud fraction during 1985–2018. This corresponds to a decrease in the number of small clouds of several 10–100 m cloud length, whereas larger clouds (1 km and more), which contribute more to the cloud fraction, became more numerous. We confirm this by showing a large-scale decrease of the power-law exponent describing the relative abundance of small and large clouds in the cloud-size distribution. Even though we can interpret the observed changes in cloud properties as significant trends, we do not explicitly identify a clear aerosol signal. Untangling the pure aerosol effect from other confounding factors (e.g., the local meteorology) is therefore left as an outlook for subsequent studies.

Zusammenfassung: Aerosol-Wolken-Wechselwirkungen stellen eine große Unsicherheit in der Quantifizierung des anthropogenen Klimawandels dar. Die sekundären Anpassungen von Wolken an eine Veränderung atmosphärischer Aerosolkonzentrationen betreffen beispielsweise den Wolken-Bedeckungsgrad und sind besonders komplex. Wolkenanpassungen können sich in der Veränderung der Wolkengrößen-Verteilung widerspiegeln. Wir präsentieren eine Methode, um mittels Beobachtungen der Wolkengrößen-Verteilung zeitliche Veränderungen in Aerosol-Wolken-Wechselwirkungen nachzuweisen.

Wolkengrößen-Verteilung und Wolkenbedeckungsgrad wurden mittels hochauflösender Satellitendaten der Landsat-Serie berechnet. Das Ziel ist es, langjährige Trends im Wolkenbedeckungsgrad über Europa im Zeitraum 1985–2018 herzuleiten und ggf. den Einfluss stark rückläufiger Aerosolkonzentrationen während dieser Zeit zu identifizieren. Landsat-Daten haben eine räumliche Auflösung von bis zu 30 Metern. Um die damit verbundenen großen Datenmengen prozessieren zu können, nutzen wir die Web-basierte Plattform Google Earth Engine.

Unsere langjährigen Trends zeigen eine großskaligen Zunahme im Wolkenbedeckungsgrad zwischen 1985 und 2018. Dies ist zurückzuführen auf einen relativen Rückgang in der Anzahl kleinerer Wolken (einige 10 bis 100 Meter Länge), während größere Wolken (mehrere Kilometer), welche mehr zum Bedeckungsgrad beitragen, häufiger wurden. Dies zeigt sich im negativen Trend des Power-Law-Exponenten der Wolkengrößen-Verteilung, welcher die relative Anzahl kleiner und großer Wolken beschreibt. Auch wenn sich diese Beobachtungen als signifikante Trends herausstellen, identifizieren wir darin kein klares Aerosol-Signal. Die Isolierung des puren Aerosoleffekts von anderen beeinflussenden Faktoren, wie der lokalen Meteorologie, bietet einen Ansatzpunkt für aufbauende Studien.

1 Introduction

Clouds are important regulators of the Earth's energy balance due to their strong impact on fluxes of incoming shortwave radiation (SWR), and outgoing longwave radiation (LWR) that is emitted by the Earth. Since clouds interact with both SWR and LWR, small changes in cloud properties may have important implications on the Earth radiation budget (Boucher et al., 2013; Cubasch et al., 2013).

Several human impacts have the potential to alter cloud characteristics and abundance. Among these are changes in anthropogenic aerosol emissions. Aerosol particles serve as cloud condensation nuclei (CCN) in almost all liquid-water nucleation processes, thereby mediating cloud radiative properties (Lohmann and Feichter, 2005). Aerosol-cloud interactions (ACIs) have an important impact on the top-of-the-atmosphere (TOA) radiative effect, but still contribute largely to the uncertainty in quantifying anthropogenic climate change (Boucher et al., 2013).

It is commonly known that changes in the amount of aerosol particles can impact the number concentration of cloud droplets which affects the cloud albedo (Twomey, 1974). However, there are conflicting results on the sign of the RF arising from cloud adjustments, making it particularly challenging to understand the full impact of ACIs (e.g., Jiang et al., 2006; Xue et al., 2008; Small et al., 2009).

Those adjustments concern the aerosol effect on cloud properties like the cloud lifetime, liquid water path (LWP), and the cloud fraction (CF): It is likely that an increased state of pollution corresponds to more numerous, but smaller droplets at initially unchanged LWP (Twomey, 1974). Some clouds (e.g., warm boundary layer clouds) can adjust to the smaller droplets through the suppression of precipitation. This process is widely known as "lifetime effect" as it potentially extends the residence time of cloud condensate (Albrecht, 1989).

However, several model-based and observational studies reinforce that a non-linear relationship exists within the cloud adjustments (e.g., Jiang et al., 2006; Xue et al., 2008; Small et al., 2009). Other processes can feed back on cloud radiative properties as a consequence of initially changed CCN. Those processes include possible evaporation feedbacks that can reduced cloudiness as a consequence of an increase in aerosol concentrations. The feedbacks thereby counteract the lifetime effect and have the potential to offset a significant fraction of the Twomey effect (Gryspeerdt et al., 2018).

We speculate on the role of cloud horizontal sizes and propose that small and large clouds likely show different responses to changing aerosol concentrations: The addition

of aerosols may increase the size of large clouds as they are less susceptible to evaporation drying. On the other hand, if small, non-precipitating cumulus clouds experience an aerosol perturbation, they can respond in a manner incongruent with the lifetime effect, due to their higher surface-to-volume ratio, which feeds back positively on the cloud size (Jiang and Feingold, 2006; Xue and Feingold, 2006; Small et al., 2009).

Based upon this, we enforce the hypothesis that through a changing aerosol concentration the cloud-size distribution (CSD) shifts as response to either lifetime and/or evaporation feedbacks. This potentially provides an observational constraint for the aerosol effects on cloud lifetime and CF which are often assumed to be correlated (Jiang et al., 2006).

To test this hypothesis, we make use of the large-scale reduction of the aerosol load over Europe during past decades: We estimate the CF response by deriving CSDs from high-resolution Landsat data during the period where aerosol concentrations haven been decreasing. The satellite data was provided and preprocessed by the web-based platform Google Earth Engine (GEE) to manage the vast amount of data. A main attempt of this study was to show the capability of exploiting the Landsat-GEE community for deriving trends in CSD and CF over Europe during 1985–2018.

The leading scientific questions of this work are defined as the following: 1) What cloud changes have occurred during recent decades? 2) Are the trends real or spurious, and if real, can they be attributed to the European aerosol decrease since the late 1980s?

This section is followed by a methodological description of estimating CSDs and CF from satellite data. Results are presented as pan-European and long-term averaged CSD firstly. Secondly, we show interannual trends of CSD and CF over Europe 1985–2018. Finally, results are discussed in terms of potential ACIs over Europe from a reduction in aerosols.

2 Data and methods

The cloud-size distribution n is commonly known to follow a negative sloping power-law relation in terms of the cloud length L (or area):

$$n(L) = \alpha L^{-\beta}. \tag{1}$$

The power-law distribution was previously documented for satellite observations and large eddy simulations, and also applies for global data sets. The latter has been demonstrated by Wood and Field (2011). We follow their method and derive $n(L)$ by adding up the total number of clouds N_i with lengths between (approximately logarithmic) bin boundaries $L_{\mathrm{i}-}$ and $L_{\mathrm{i}+}$, and dividing by the respective bin width and total transect length D_{tot}:

$$n(L) = \frac{N_{\mathrm{i}}}{D_{\mathrm{tot}}(L_{\mathrm{i}+} - L_{\mathrm{i}-})}. \tag{2}$$

For a given cloud field that conforms to a power-law distribution, the cloud fraction can be derived by integrating $Ln(L)$ over L,

$$\mathrm{CF}(L_{\min}, L_{\max}) = \int_{L_{\min}}^{L_{\max}} Ln(L)dL, \tag{3}$$

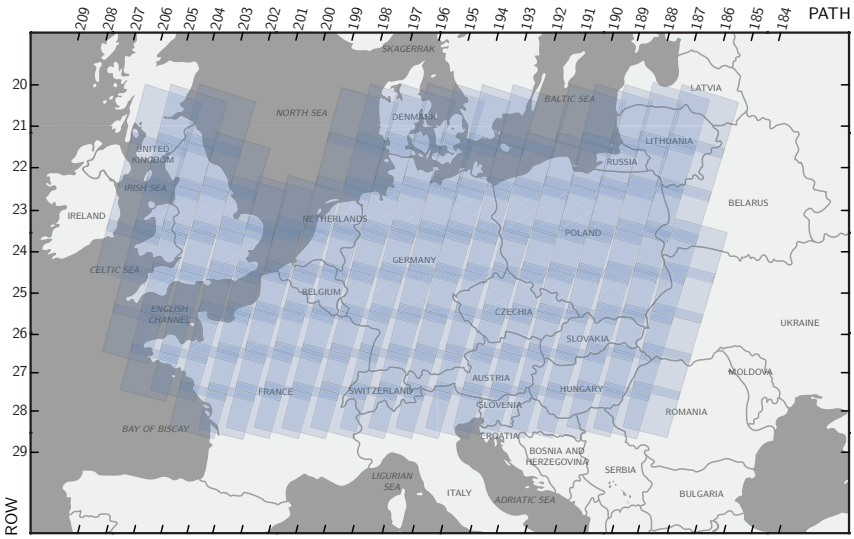

Figure 1: *European research domain showing all Landsat footprints in the region. The spatial attribution follows the path/row WRS-2.*

with $L_{\min}$ and $L_{\max}$ being the smallest and largest detectable scale, respectively.

We use Landsat data from 1985 to 2018 which provides a powerful tool to resolve cloud fields at 30 m horizontal size. To take full advantage of the massive data amount, we use GEE which provides access to high-performance computing resources to process large geospatial data volumes. We use data from the USGS Collection-1 Tier-1 TOA reflectance archive from Landsat 5, 7 and 8. Data from Landsat 7 was included only within 1999–2003 due to a scan-line correction failure which would have affected the results onward from May 2003. Also, the year 2012 is not represented here due to the data gap following the fail of the Landsat-6 mission.

Landsat images are provided within so called footprints/tiles that are spatially classified by satellite path and row according to Worldwide Reference System-2 (WRS-2). Figure 1 gives a map of all tiles considered as our research domain. In total, 143 Landsat tiles were chosen to represent a wide range of the European continent. Each tile has an approximate horizontal size of 200×200 km, and contains around 7000×7000 pixels on average, with 8–11 bands depending on the Landsat mission.

All files within the data collection were passed on to a cloud-masking GEE internal algorithm. From the binary mask, we derive cloud lengths in two different sampling directions (in North-South and West-East alignment) by counting horizontally contiguous cloud pixels between the clear boundaries. A simplified sketch of a cloud-mask example and the sampling in each direction is illustrated in Fig. 2. If the first or last pixel of a given stripe contains a cloud, the corresponding cloud length is initially excluded due to the chance of extending beyond the satellite scene. Each Landsat pixel has a horizontal resolution of 30 m.

We calculate the CSD corresponding to Eq. 2. By ignoring all clouds touching the scene boundary, a size-dependent sampling bias arises since large clouds are more likely being excluded. Wood and Field (2011) address this error by introducing a correction term to Eq. 2. However, applying the correction to the Landsat data was set aside here, since the main interest was to quantify how the CSD changes over the years. Since the image size among all Landsat files does not show distinct variations, the error can be

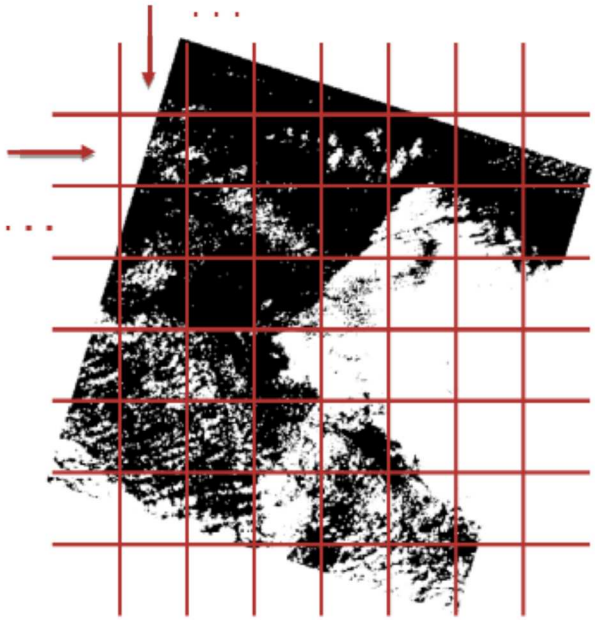

Figure 2: *Sketch of stripe-wise cloud size sampling in the cloud mask (here: white=cloudy pixel, black=non-cloudy pixel). Horizontally contiguous cloud pixel are counted together to add up to a respective cloud length value. The cloud sampling directions are in North-South and West-East alignment. Therefore, each satellite image is scanned twice foe cloud sizes. The resolution of each Landsat image is 30 m.*

considered an equal impact on the results and thereby cancels by looking at temporal changes.

To quantify interannual changes, we fit the observed CSD to Eq. 1 to derive the horizontal exponent β. The exponent is used to determine the pivoting of the CSD over the years (i.e., the change in the frequency of occurrence among the cloud-size classes). Finally, the CF is calculated via Eq. 3, with power-law parameters α and β derived from the power-law fit.

3 Results

We first show the pan-European CSD as a temporal average by grouping together the data for the entire period 1985–2018. Secondly, the data was grouped for each year individually to carry out interannual records of CSD and CF over Europe and potentially detect an aerosol impact.

The single pan-European CSD (Fig. 3) closely matches a power-law relation that spans over three orders of magnitude of cloud size, from 30 m to 30 km. The middle sloping line (black) shows the best regression ($r = 0.996$) between observation and power-law fit. The overall power-law exponent is estimated with $\beta = 1.73$. The blue and green lines represent exponents of $\beta = 1.5$ and $\beta = 1.9$, respectively, to visualise the impact of variable parameters on the CSD. For clouds larger than approximately 30 km length, the distribution deviates from the power law (scale break).

Looking at each Landsat footprint individually, again, all size distributions closely match a power-law relationship (not shown here), with significant individual correlations

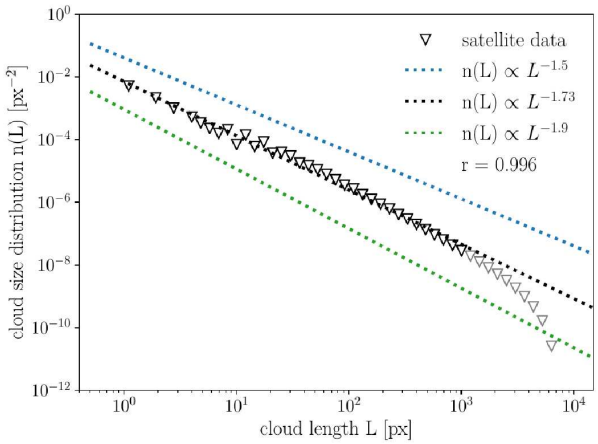

Figure 3: *Observed pan-European CSD, $n(L)$ on the y-axis as temporal average for the time period 1985–2018 (triangles). The exponent β of the power-law is estimated with $\beta = 1.73$. Pearson's correlation coefficient for the regression is $r = 0.996$. 50 logarithmically spaced bins are used to display the distribution. For larger cloud sizes, the distribution deviates from the power-law due to a horizontal scale break (gray triangles).*

between observation and fit. The power-law exponent over Europe spatially varies with $1.63 \leq \beta \leq 1.83$, so that the overall scaling exponent can be quantified as $\beta = 1.73 \pm 0.10$ to account for regional variations.

3.1 Interannual cloud-size distribution trends

Trends in the CSD are derived by grouping the cloud sizes per year, so that each time step accounts for an annual average of the distribution. We do not account for seasonality.

The pan-European trend of the horizontal exponent β during 1985–2018 is represented in Fig. 4. Panel (a) accounts for data averaged over all 143 Landsat tiles of the research domain. The data indicate an overall dropping horizontal exponent over Europe. The overall trend is not monotonic and includes a period of increasing β during 2000–2010.

However, not all time series within individual Landsat footprints give trends that are statistically significant. Panel (b) only includes the data of satellite footprints with robust trends. To ensure the practicability of the linear trend model, we filter among the tiles by excluding all local trends with linear correlation coefficients below 0.4, and a root-mean-square error (RMSE) above the domain-average value.

When including only robust individual time-series, the trend increases from $-1.6 \cdot 10^{-3}$ to $-3.7 \cdot 10^{-3}$ per year with larger correlation ($r = 0.81$), while increasing the error range due to the reduced amount of data (only 21 grid boxes passed the filtering procedure). The corresponding tiles that passed the significance filter are marked in Fig. 5, showing the spatial distribution of trends widespread over Europe. From the 21 tiles that passed the filtering, 17 are found on land and appear in the map as crosses within the respective region.

All statistically significant grid-box trends support a long-term decrease in the power-law exponent. The corresponding regions are mostly found over Germany and in some parts of France, Great Britain, and the Benelux. Considering the entire domain, regions

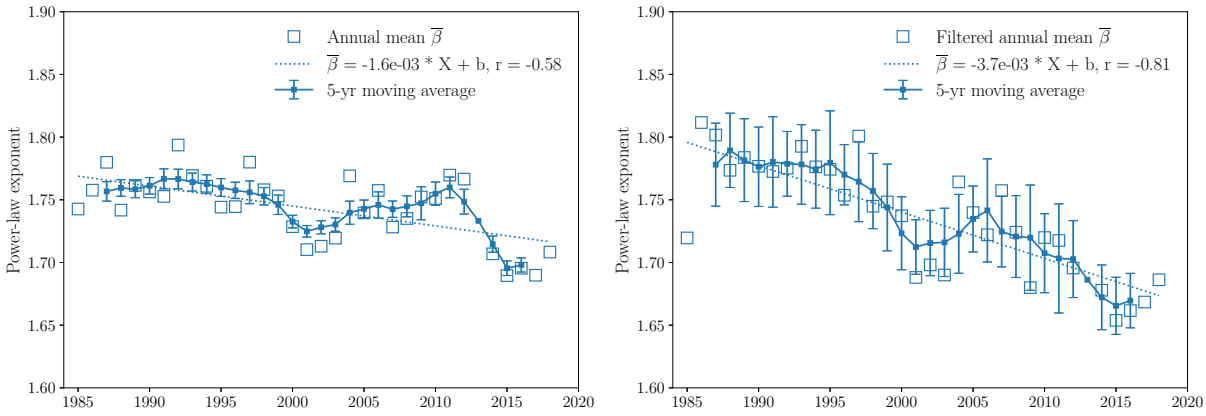

(a) (b)

Figure 4: *Pan-European trends of the power-law scaling exponent $\overline{\beta}$ 1985–2018, (a) without filtering, and (b) after filtering, as raw data (larger empty squares), and low-frequency variability (5-yr moving average time series; filled smaller squares). The filtering in (b) excludes all Landsat footprints with individual correlation coefficients $r < 0.4$, and a RMSE > $\overline{RMSE}$ (domain average), respectively. Error bars are indicated as standard error of mean. A linear regression fit is used to derive the trend in $\overline{\beta}$ 1985–2018.*

with negative trends dominate the geographic pattern.

In summary, there was an overall dropping horizontal scaling exponent describing the CSD over Europe during 1985–2018, with locally significant trends supporting the result. The negative trend corresponds to a large-scale pivoting of the negative power-law slope as result of both a decreased number of small clouds, and an increase in the number of larger cloud fields. The latter was not specifically shown here, but confirmed by considering the pan-European trend of cloud number separately within different size bins: Smaller cloud bins indicated a negative trend, whereas for larger clouds the number increased over the years.

3.2 Interannual cloud fraction trends

In a final step, records of CF are derived by integrating the CSD according to Eq. 3. The contribution of clouds with horizontal scales from 30 m to 30 km (1 px to 1000 px) to the CF is henceforth referred to as "total" CF. This should not be associated with the real cloud cover, but the partial CF from clouds within the size range satisfying a power-law distribution. The actual CF was reduced not only by considering a limited range of cloud horizontal sizes, but also since all cloud fields outranging the Landsat footprint dimension (~ 200 km) are automatically neglected. The same applies for clouds touching the boundaries of the satellite scene. Moreover, Landsat T1 data precautionarily excludes heavily clouded scenes from the data set due to low quality conditions. Therefore, it can be assumed that in reality the CF was larger.

Fig. 6 shows the pan-European trend in the total CF over Europe (blue), and moreover, the individual contribution from different cloud size bins. The partial CF is derived as contribution from clouds with 30–300 m (1–10 px), 300–3000 m (10–100 px), and

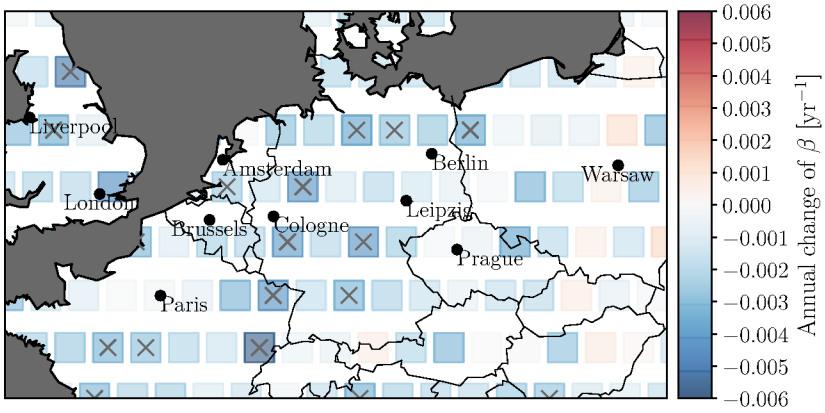

Figure 5: *Tile-specific trends of power-law exponent β during 1985–2018. Regions marked with cross indicate statistically significant trends with individual linear correlation coefficient $r > 0.4$, and RMSE $< \overline{RMSE}$. From a total of 143 Landsat tiles, 21 met the significance criteria, from which 17 are found on land and indicated within the map.*

3 km–30 km (100–1000 px) length, respectively, by correspondingly adjusting the limits of integration.

The total CF indicates an overall increase during 1985–2018 over Europe with 0.04 % per year accounting for the entire domain, and 0.15 % per year within the filtered data set. An increasing CF trend is further notable for the contribution from medium-sized and large clouds, but with decreasing significance towards smaller cloud sizes. For the smallest size bin, a slight reduction in the contribution to the CF is evident from the corresponding data. The contribution of partial CF to the total CF is dominated by large-scaled clouds. This is in agreement with our observed power-law exponent β: If the value of the exponent is below the scaling threshold 2, then large clouds dominate the CF, but with values larger than 2, small clouds contribute more to the overall CF (for more information see Wood and Field, 2011). Consequently, the overall trend in CF is also dominated by changes within larger cloud fields, due to $\beta < 2$.

By applying the statistical filter to the time series, each individual trend (partial and total CFs) is intensified and appears increasingly monotonic. However, from all 143 tiles only 9 (8, 6, 12) passed the thresholds to contribute to the filtered trend of total CF (partial CFs from 1–10, 10–100, 100–1000 px, respectively). The corresponding regions are marked in the map of Fig. 7, showing the spatial distribution of trends in total CF during the period 1985–2018.

Most grid-box trends show a widespread increase in CF over Europe. Grids with significant trends are exclusively positive, supporting the filtered time series that gives the average of these areas in panel (b) of Fig. 6. Some larger connected parts of Europe indicate negative trends, especially in eastern Germany extending towards the Czech Republic, and the Benelux, but with little statistical significance. Therefore, it can be concluded that there was a widespread increase in CF over Europe during 1985–2018.

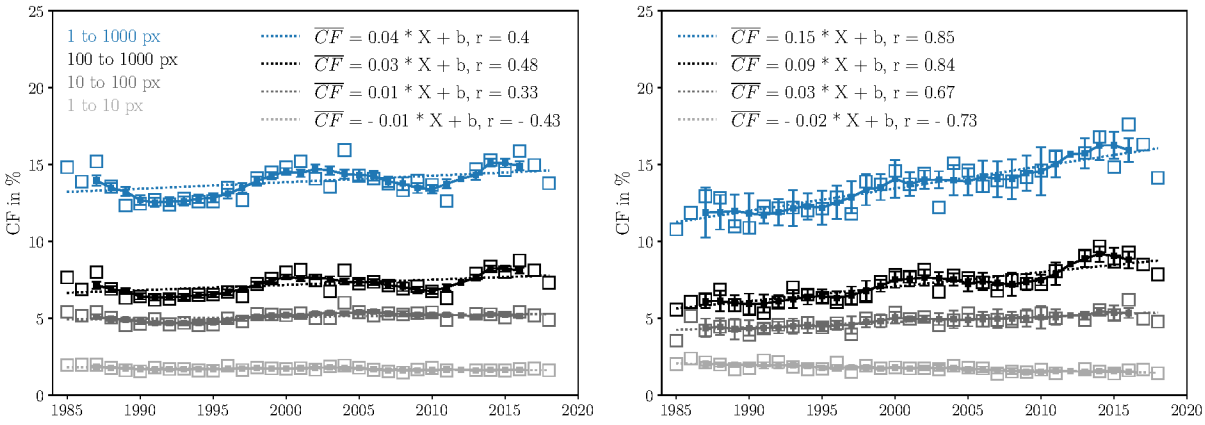

(a) (b)

Figure 6: *Pan-European trends in CF 1985–2018, (a) without filtering, and (b) after filtering for statistical significance, as raw data (larger empty squares), and low-frequency variability (5-yr moving average; filled smaller squares). The filtering excludes all Landsat footprints with trends r* < 0.4, *and RMSE* $> \overline{RMSE}$. *From the total of 143 tiles, 9 passed the filtering in the total CF (blue). Error bars give the standard error of mean, and a linear regression fit is used to derive the overall trend 1985–2018. CF trends were derived separately as contribution from clouds within different size ranges by correspondingly adjusting the limits of integration. All clouds with 30 m to 30 km (1–1000 px) length are contributing to the "total" CF.*

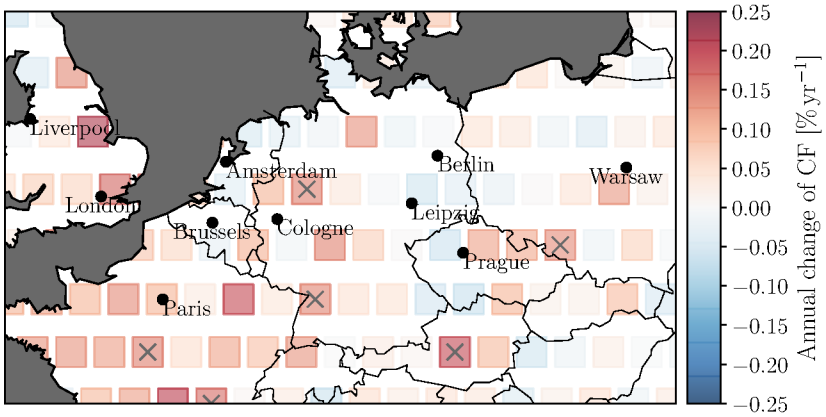

Figure 7: *Grid-box trends of total CF during 1985–2018. Regions marked with cross indicate statistically significant trends with individual linear correlation coefficient r* > 0.4, *and RMSE* $< \overline{RMSE}$. *From a total of 143 Landsat tiles, 9 met the significance criteria, from which 6 are found on land and indicated within the map.*

4 Discussion

For deriving trends in cloudiness over Europe we adapt the method of Wood and Field (2011) to determine CSDs by cloud segment length. The primary result of deriving an overall CSD over Europe including the entire Landsat collection is the emergence of a power-law fit that spans over three orders of magnitude of cloud horizontal scales ranging from 30 m to 30 km. The quantification of the overall exponent with $\beta = 1.73$ is in good agreement with previous studies using observational data sets but also from numerical simulations (Guillaume et al., 2018). The power-law is further valid when breaking down the data set to account for regional and annual distributions. The tile-specific power-law exponent remained below the scaling threshold 2. This supports the common knowledge that the cloud cover is dominated by larger clouds, whereas the contribution to the number density increases towards smaller cloud sizes.

To circle back to the previously defined research question, our first attempt was to identify potential cloud changes in our data set of CSDs during past decades. The pan-European trend in the CSD indicates a large-scale decrease in the number of small clouds, together with an increase in the relative abundance of larger cloud fields of several 100 m length and more. The reduction/increase in the number of small/large clouds reflects in the corresponding trends of partial CFs. Overall, there was an increase in the total CF during 1985–2018 widespread over Europe, which becomes monotonic by filtering the entire data for robust trends among the grid boxes.

But are there trends real, and if so, can they be attributed to the European aerosol decrease since the late 1980s? The cloud record is in alignment with the findings of Norris and Wild (2007), who showed an overall dropping downward solar cloud-cover radiative effect due to an increasing CF during 1987–2002. They estimate the enhancement in cloudiness with $+0.9 \pm 1.7$ % per decade. The Landsat data set accounts for a CF trend of +0.4 % per decade within the unfiltered trend, and +1.5 % per decade for the filtered time-series, which matches the estimated range of Norris and Wild (2007).

Norris and Wild (2007) attribute the cloud record to natural weather and climate variability since a long-term increase in cloud cover occurred at the same time as aerosol concentrations decreased. However, this argumentation alone might not be enough to exclude a major impact of the European aerosol concentration decrease. Clouds can adjust through other processes than precipitation suppression. However, according to recent conclusions of Rosenfeld et al. (2019), the isolation of the pure aerosol effect most likely results in an overall positive correlation that is indeed mainly mediated by the aerosol effect on coalescence and precipitation.

Another point of interest is the role of cloud horizontal sizes in the cloud adjustments. Our hypothesis suggests that individual cloud-size classes might respond in a different manner to an aerosol perturbation: Smaller clouds are more exposed to entrainment drying due to their surface-to-volume ratio. However, our observational data suggests a decrease in the number of smaller clouds and the corresponding partial CF, even though aerosol loads have been dropping. The opposite is true for larger clouds, which would not be expected from a pure aerosol impact.

Rosenfeld et al. (2019) attribute negative aerosol-CF relationships from previous studies to an effect of local meteorology. The CF response appears to be strongly tied to atmospheric conditions (e.g., ambient relative humidity) that can obscure the actual

aerosol effect. But do local meteorological conditions reflect in our observed CF trend?

For individual cloud records among the grid boxes, the trends were mostly weak and of low statistical significance, so that the signal-to-noise ratio would justify the attribution to natural variability. Moreover, local minima within the cloud record fall together with noteworthy drought years, e.g., 2003, 2015, and 2018 (see again Fig. 6 (a) and (b), without low-frequency filter). Those drought events are mostly driven by precipitation deficits and rising temperatures (Hanel et al., 2018). This gives us another indication of a likely impact of local meteorology on the CF trend. Additionally, a negative aerosol-CF relationship has been found in several studies before, and was interpreted as effect of local meteorology and climate variations (Sato and Suzuki, 2019).

The remaining question is whether cloud changes are entirely explained by natural internal variability or whether they can be attributed to ACIs by further resolving the data set spatially and temporally. By mapping annual grid-box trends, some areas show a decrease in CF (e.g., Benelux regions, parts of Eastern Germany and Czech Republic). However, these trends are not significant and interpreting them within the context of ACIs is premature. It remains unclear what else impacts the cloud record and to what extent local trends are individually affected.

5 Summary and conclusions

In this study, we derive CSD and CF trends over Europe during 1985–2018, including satellite data from Landsat 5 to 8. During this time, the European aerosol burden experienced a large-scale decrease, which has likely led to a decrease in cloud albedo onward from the late 1980s (Krüger and Graßl, 2002; Norris and Wild, 2007). However, ACIs might have been additionally mediated by cloud adjustments concerning properties like the CF.

So far, scientists have not reached a consensus on the sign of the aerosol-CF relationship due to the coexistence of precipitation suppression (Albrecht, 1989), and evaporation feedbacks (Ackerman et al., 2004; Small et al., 2009) which might either increase, or decrease cloudiness through an increase in aerosol numbers. We use the CSD as observational link, derived from the Landsat-GEE data catalogue and computational routines. Due to its general spectral characteristics and long-term data record, Landsat data has the potential to carry out multidecadal cloud studies.

Our derived European CSD follows the expected power-law relation, and shows a larger relative abundance of small clouds over large clouds. The co-variation of slope and intercept of the power-law distribution further allows for the derivation of CFs from the represented clouds sizes. The observations indicate an increase within the pan-European CF during 1985–2018, thereby suggesting a negative relationship between aerosol amount and CF. However, considering the results of recent studies, the isolated aerosol-CF effect is more likely represented by a positive relationship (Gryspeerdt et al., 2016; Rosenfeld et al., 2019).

We still consider the change in CSD and CF a real trend. However, based on current knowledge it is more likely that other confounding factors contributed to the trend rather than the European aerosol reductions. We speculate on the impact of local meteorology and climate variability which can obscure the aerosol impact on clouds.

As articulated before, additional data (e.g., trends in temperature and precipitation) need to be considered within the chain of causality between aerosol amount and CF to isolate potential adjustments embedded in ACIs. More attention should be payed to robust trends indicated within individual cases, as they might outweigh both the effect of natural variability, and spurious trends from satellite retrieval anomalies. This topic is left as an outlook for subsequent studies.

Acknowledgements

We acknowledge the processing service Google Earth Engine for providing a platform for algorithm development which allowed us to preprocess and download high-resolution Landsat. The authors would like to thank Oliver Lahr for providing Fig. 1.

References

Ackerman, A. S., Kirkpatrick, M. P., Stevens, D. E., and Toon, O. B. (2004). The impact of humidity above stratiform clouds on indirect aerosol climate forcing. *Nature*, 432(7020):1014.

Albrecht, B. A. (1989). Aerosols, Cloud Microphysics, and Fractional Cloudiness. *Science*, 245(4923):1227–1230.

Boucher, O., Randall, D., Artaxo, P., Bretherton, C., Feingold, G., Forster, P., Kerminen, V.-M., Kondo, Y., Liao, H., Lohmann, U., et al. (2013). Clouds and aerosols. In *Climate change 2013: the physical science basis. Contribution of Working Group I to the Fifth Assessment Report of the Intergovernmental Panel on Climate Change*, pages 571–657. Cambridge University Press.

Cubasch, U., Wuebbles, D., Chen, D., Facchini, M., Frame, D., Mahowald, N., and Winther, J. (2013). Introduction. In *Climate change 2013: the physical science basis. Contribution of Working Group I to the Fifth Assessment Report of the Intergovernmental Panel on Climate Change*, pages 119–158. Cambridge University Press.

Gryspeerdt, E., Goren, T., Sourdeval, O., Quaas, J., Mülmenstädt, J., Dipu, S., Unglaub, C., Gettelman, A., and Christensen, M. (2018). Constraining the aerosol influence on cloud liquid water path. *Atmospheric Chemistry and Physics Discussions*, 2018:1–25.

Gryspeerdt, E., Quaas, J., and Bellouin, N. (2016). Constraining the aerosol influence on cloud fraction. *Journal of Geophysical Research: Atmospheres*, 121(7):3566–3583.

Guillaume, A., Kahn, B. H., Yue, Q., Fetzer, E. J., Wong, S., Manipon, G. J., Hua, H., and Wilson, B. D. (2018). Horizontal and Vertical Scaling of Cloud Geometry Inferred from CloudSat Data. *Journal of the Atmospheric Sciences*, 75(7):2187–2197.

Hanel, M., Rakovec, O., Markonis, Y., Máca, P., Samaniego, L., Kyselỳ, J., and Kumar, R. (2018). Revisiting the recent European droughts from a long-term perspective. *Scientific reports*, 8(1):1–11.

Jiang, H. and Feingold, G. (2006). Effect of aerosol on warm convective clouds: Aerosol-cloud-surface flux feedbacks in a new coupled large eddy model. *Journal of Geophysical Research: Atmospheres*, 111(D1).

Jiang, H., Xue, H., Teller, A., Feingold, G., and Levin, Z. (2006). Aerosol effects on the lifetime of shallow cumulus. *Geophysical Research Letters*, 33(14).

Krüger, O. and Graßl, H. (2002). The indirect aerosol effect over Europe. *Geophysical Research Letters*, 29(19):31–1–31–4.

Lohmann, U. and Feichter, J. (2005). Global indirect aerosol effects: a review. *Atmospheric Chemistry and Physics*, 5(3):715–737.

Norris, J. R. and Wild, M. (2007). Trends in aerosol radiative effects over Europe inferred from observed cloud cover, solar "dimming", and solar "brightening". *Journal of Geophysical Research: Atmospheres*, 112(D8).

Rosenfeld, D., Zhu, Y., Wang, M., Zheng, Y., Goren, T., and Yu, S. (2019). Aerosol-driven droplet concentrations dominate coverage and water of oceanic low-level clouds. *Science*, 363(6427):eaav0566.

Sato, Y. and Suzuki, K. (2019). How do aerosols affect cloudiness? *Science*, 363(6427):580–581.

Small, D. J., Chuang, P., Feingold, G., and Jiang, H. (2009). Can aerosol decrease cloud lifetime? *Geophysical Research Letters - GEOPHYS RES LETT*, 36.

Twomey, S. (1974). Pollution and the planetary albedo. *Atmospheric Environment (1967)*, 8(12):1251 – 1256.

Wood, R. and Field, P. R. (2011). The Distribution of Cloud Horizontal Sizes. *Journal of Climate*, 24(18):4800–4816.

Xue, H. and Feingold, G. (2006). Large-Eddy Simulations of Trade Wind Cumuli: Investigation of Aerosol Indirect Effects. *Journal of the Atmospheric Sciences*, 63(6):1605–1622.

Xue, H., Feingold, G., and Stevens, B. (2008). Aerosol Effects on Clouds, Precipitation, and the Organization of Shallow Cumulus Convection. *Journal of the Atmospheric Sciences*, 65(2):392–406.

Forschungsbericht 2021
Bearbeitete Forschungsprojekte

Institut für Meteorologie

Direktor Prof. Dr. M. Wendisch

Allgemeine Meteorologie; Manfred Wendisch
AG Atmosphärische Strahlung

Koordination des Schwerpunktprogramms 1294 "Atmosphären- und Erdsystemforschung mit dem Forschungsflugzeug HALO (High Altitude and Long Range Research Aircraft)"
HALO coordination project

Schlagworte: flugzeuggetragene Forschung

Projektleiter: M. Wendisch (m.wendisch@uni-leipzig.de)
Professor Dr. Joachim Curtius, Goethe-Universität Frankfurt am Main, Institut für Atmosphäre und Umwelt

Projektmitarbeiter: Anja Schwarz, Jörg Schmidt

Projektbeginn: 2010
Projektende: 2021

Beschreibung
Das Ziel des Antrages ist die zentrale Koordination des SPP 1294 'Atmosphären- und Erdsystemforschung mit HALO' (HALO: HighAltitude and Long Range Research Aircraft, Hochfliegendes und weitreichendes Forschungsflugzeug). Das Projekt dient der Förderung der Zusammenarbeit und Kommunikation innerhalb der HALO Missionsteams und den individuellen Projektpartnern, die im SPP eingebunden sind. Die drei Koordinatoren (M. Wendisch, Universität Leipzig; J. Curtius, Universität Frankfurt am Main; M. Scheinert, Technische Universität Dresden) vertreten den SPP gegenüber der DFG, dem Wissenschaftlichen Lenkungsausschuss (WLA) für HALO, dem HALO Projektteam des Deutschen Zentrums für Luft- und Raumfahrt (DLR-FX) und der Öffentlichkeit. Der DFGAnteil an den Missionskosten wird an der Universität Leipzig zentral verwaltet. Die Finanzmittel für Maßnahmen zur Förderung der Gleichstellung werden verwaltet, und die Ausbildung der jungen Wissenschaftler wird koordiniert. Monatliche Telefonkonferenzen der drei Koordinatoren, jährlich Statusseminare und thematische Workshops werden organisiert. Spezielle Sitzungen auf internationalen Konferenzen und Veröffentlichungen von Spezialausgaben in internationalen Zeitschriften werden initiiert und befördert. Die SPP Internet-Seite wird überarbeitet, fortlaufend aktualisiert und gewartet. Um die Arbeit der Koordinatoren zu unterstützen, werden eine halbe Position eines Wissenschaftlichen Administrators und eine Stelle für einen HALO Nutzerkoordinator beantragt.

Description

The goal of this proposal is the central coordination of the SPP 1294 'Atmospheric and Earth System Research with HALO' (HALO: High Altitude and Long Range Research Aircraft). The project serves the promotion of cooperation and communication among the HALO mission teams and the individual project participants involved in the SPP. The three coordinators (M. Wendisch, University of Leipzig; J.Curtius, University of Frankfurt am Main; M. Scheinert, Dresden University of Technology) represent the SPP at the DFG, the scientific steering committee of HALO (WLA: Wissenschaftlicher Lenkungsausschuss), the HALO project team of the German Aerospace Center (DLR-FX), and the public. The DFG share of the mission costs will be centrally administered by the University of Leipzig. The funds for measures to promote gender equality are managed, and the training of young researchers is coordinated. Monthly teleconferences of the three coordinators, annual status seminars, and topical workshops will be organized. Special sessions at international conferences and publications of special issues are initiated and pursued. The SPP web page will be revised, continuously updated, and maintained. To support the three coordinators in conducting these tasks, funding of a half-time position of a Scientific Administrator and a HALO User Coordinator is applied for.

Mittelgeber: DFG WE 1900/24-1, Projekt number 179953493 and Projekt number 316646266

Kampagnenantrag für die HALO-(AC)³ Mission: Arktische Luftmassentransformationen während Warmlufteinschüben und Kaltluftausbrüchen
Umbrella Proposal for the HALO-(AC)³ Mission: Arctic Air-Mass Transformations During Warm Air Intrusions and Marine Cold Air Outbreaks

Schlagworte: flugzeuggetragene Forschung

Projektleiter: M. Wendisch (m.wendisch@uni-leipzig.de)

Projektmitarbeiter: N.N.

Projektbeginn: 2020
Projektende: 2023

Beschreibung
Das Ziel des Antrages ist die zentrale Koordination des SPP 1294 'Atmosphären- und Erdsystemforschung mit HALO' (HALO: HighAltitude and Long Range Research Aircraft, Hochfliegendes und weitreichendes Forschungsflugzeug). Das Projekt dient der Förderung der Zusammenarbeit und Kommunikation innerhalb der HALO Missionsteams und den individuellen Projektpartnern, die im SPP eingebunden sind. Die drei Koordinatoren (M. Wendisch, Universität Leipzig; J. Curtius, Universität Frankfurt am Main; M. Scheinert, Technische Universität Dresden) vertreten den SPP gegenüber der DFG, dem Wissenschaftlichen Lenkungsausschuss (WLA) für HALO, dem HALO Projektteam des Deutschen Zentrums für Luft- und Raumfahrt (DLR-FX) und der Öffentlichkeit. Der DFG-Anteil an den Missionskosten wird an der Universität Leipzig zentral verwaltet. Die Finanzmittel für Maßnahmen zur Förderung der Gleichstellung werden verwaltet, und die Ausbildung der jungen Wissenschaftler wird koordiniert. Monatliche Telefonkonferenzen der drei Koordinatoren, jährlich Statusseminare und thematische Workshops werden organisiert. Spezielle Sitzungen auf internationalen Konferenzen und Veröffentlichungen von Spezialausgaben in internationalen Zeitschriften werden initiiert und befördert. Die SPP Internet-Seite wird

überarbeitet, fortlaufend aktualisiert und gewartet. Um die Arbeit der Koordinatoren zu unterstützen, werden eine halbe Position eines Wissenschaftlichen Administrators und eine Stelle für einen HALO Nutzerkoordinator beantragt.

Description
So far, observations of air-mass transformations in the Arctic have mostly been conducted from a fixed local position. Only few aircraft-based samplings of air-mass properties over a limited regional area have been reported. This Eulerian point of view does not permit the observations of air-mass modifying processes along their meridional pathway, which are required for model validations. Therefore, we propose a quasi-Lagrange approach following air-masses to and from the Arctic to observe the air-mass transformation processes during warm air intrusions and cold air outbreaks, whereby we focus on warm air intrusions, which have been observed much less frequently in the past. This quasi-Lagrange approach requires a long-endurance airborne facility, which may carry the necessary equipment for the observations. HALO with its exceptional endurance and high lifting capacity is most suited for these observations.

Mittelgeber: DFG Projekt number 442647689

Einfluss der Eiskristallform auf den Strahlungseffekt von arktischen Zirren: Messungen und Repräsentation in numerischen Wettervorhersagemodellen
Influence of the ice crystal shape on radiative effects of Arctic cirrus: Observations and representation in numerical weather prediction models

Schlagworte: flugzeuggetragene Messungen, Wolken, Strahlungsantrieb, Zirren

Projektleiter: M. Wendisch (m.wendisch@uni-leipzig.de)

Projektmitarbeiter: Johannes Röttenbacher

Projektbeginn: 2021
Projektende: 2023

Beschreibung
Flugzeuggetragenen Messungen der solaren und thermisch-infraroten atmosphärischen Strahlung sollen verwendet werden, um den Strahlungseffekt von Zirren in hohen Breiten zu quantifizieren und dessen Repräsentation in numerische Wettervorhersagemodellen zu evaluieren. Diese Zielstellung basierend auf den Erkenntnissen des vorangegangenen Projektes, in dem eine hohe Sensitivität des Strahlungsschemas im ECMWF Integrated Forecast System (IFS) bezüglich der Parametrisierung der Strahlungseigenschaften von Eiskristallen nachgewiesen werden konnte. Für arktischen Zirrus muss diese Analyse auf das Strahlungsbudget im thermisch-infraroten Wellenlängenbereich erweitert werden, da in der Arktis (Polarnacht), die solare Strahlung einen geringen bis nicht-vorhanden Anteil am Energiebuget ausmacht. Das Projekt ist in den HALO Missionen Cirrus-HL (High Latitude) und HALO-(AC)^3 (ArctiC Amplification: Climate Relevant Atmospheric and SurfaCe Processes, and Feedback Mechanisms) eingebunden. Beide Missionen nutzen das Forschungsflugzeug HALO, um arktische Wolken mit neuesten aktiven und passiven Fernerkundungsmethoden sowie in situ Messungen der Wolkeneigenschaften zu charakterisieren. In diesem Projekt werden Messungen der von den Wolken reflektierten solaren und der

emittierten thermisch-infraroten Strahlung durchgeführt. Dazu wird ein neues breitbandiges Radiometersystem, ein spektrales Albedometer und ein abbildendes Infrarotkamera verwendet, um das Strahlungsbudget oberhalb und unterhalb der Zirren zu quantifizieren. Basierend auf diesen Messungen, wird der Strahlungseffekt der Zirren berechnet und in Abhängigkeit der Wolkeneigenschaften analysiert. Besonders wird hier untersucht, in wie weit sich typisch arktische Randbedingungen wie das reflektierende Meereis und langlebige niedrige Wolken auf den Strahlungseinfluss der Zirren auswirken. Des Weiteren wird untersucht, wie diese Strahlungseffekte von arktischen Zirren in numerischen Wettervorhersagemodellen repräsentiert werden. Dazu werden die im Modell vorhergesagten Strahlungseffekte mit den Messungen verglichen. In mehreren Schritten, werden Strahlungstransfermodellen mit unterschiedlichen Parametrisierungen der Strahlungseigenschaften von Eiskristall verwendet, um die Unsicherheiten in Bezug auf das Strahlungsschema und die prognostizieren Wolkeneigenschaften zu separieren.

Description
Based on the sensitivity of the ECMWF radiation scheme to the parametrization of ice crystal radiative properties observed in the completed project for ice clouds in mid-latitudes, the continuation of the project aims to extends this model evaluation for the radiative effects of cirrus in high-latitudes. For Arctic cirrus, the analysis needs to be extended to the thermal-infrared radiation budget, which dominates due to the lag of solar radiation and depends on cloud altitude, thickness and ice crystal properties. Therefore, the project is embedded in the proposed HALO missions Cirrus-HL (High Latitude) and HALO-$(AC)^3$ (ArctiC Amplification: Climate Relevant Atmospheric and SurfaCe Processes, and Feedback Mechanisms), which both aim to investigate Arctic clouds by state of the art airborne remote sensing (active and passive) and cloud microphysical in situ observations. Within this project, measurements of the cloud-reflected solar and emitted thermal infrared radiance and irradiance with a new broadband radiometer system, a spectral albedometer, and a thermalinfrared imager are proposed to quantify the radiative energy budget above and below Arctic cirrus. Based on the observations, the cirrus radiative effect will be derived and evaluated with respect to its dependence on cloud macrophysical and microphysical properties, and the special Arctic environment (sea ice, persistent low clouds). We will evaluate how well the cirrus and their radiative effects are represented in numerical weather prediction models. The comparison will be performed in the observational space of irradiances and radiances instead of cloud properties. Therefore, the output of the numerical weather prediction (NWP) models will be converted by radiative transfer models into the observed radiation quantities. Operational and experimental radiation schemes will be tested and compared to the observed radiation quantities to identify the reasons of potential differences between model and observation. The airborne observations and the radiative transfer simulations will be used to corroborate the hypothesis: “The radiative effects of Arctic cirrus, which significantly depend on their macrophysical and microphysical properties such as the ice crystal shape, can be used to validate numerical weather prediction models.” To address this hypothesis, the proposed study will focus on five specific science questions: (A) How variable are the radiative effects by Arctic cirrus on different horizontal scales (e.g., contrail cirrus, cirrus in air mass transformation)? (B) How strong the radiative effects depend on the presence of sea ice and low clouds? (C) Do observed ice crystal shapes of Arctic cirrus lead to a significant change of cloud radiative effects? (D) Do NWP models realistically represent the radiative effects of Arctic cirrus? (E) Can we use spectral solar and thermal-infrared radiation measurements to constrain potential uncertainties of NWP models?

Mittelgeber: DFG, SPP 1294, Projekt number 316500630

SFB/Transregio 172 „Arktische Verstärkung“
Zentrale Dienstleistungen, Verwaltung und Koordinierung (Z01)
Central services, administration and coordination (Z01)

Schlagworte: Arktis.

Projektleiter:
M. Wendisch (m.wendisch@uni-leipzig.de)
Prof. Dr. Susanne Crewell, Universität zu Köln, Institut für Geophysik und Meteorologie
Prof. Dr. Justus Notholt, Universität Bremen, Institut für Umweltphysik

Projektmitarbeiterin: Dr. Marlen Brückner

Projektbeginn: 2016
Projektende: 2023

Beschreibung
Innerhalb des TR 172 Antrages werden Mittel für die zentrale Koordinierung beantragt. Dieses Teilprojekt dient dazu, die Kooperationen und Kommunikation im Verbund unter den einzelnen wissenschaftlichen Projekten und Clustern zu fördern. Aus diesem Grund werden monatliche Videokonferenzen, halbjährliche Meetings, jährliche wissenschaftliche Konferenzen, als auch spezielle Workshops organisiert und durchgeführt. Die Mittel für Gleichstellungsmaßnahmen werden dazu verwendet um junge Wissenschaftler/innen in Zusammenarbeit mit lokalen Graduiertenschulen zu trainieren. Die internationale Präsenz des TR 172 wird etabliert. Eine Internetseite wird erstellt und implementiert. Die logistische Organisation und wissenschaftliche Planung von intensiven Messkampagnen innerhalb des TR 172 werden durch das Projekt Z01 unterstützt. Öffentlichkeitsarbeit zwischen den verschiedenen Partnern wird organisiert und koordiniert.

Description
Funds for the central coordination of TR 172 are requested within this proposal. The project serves the promotion of cooperation and communication among the individual scientific projects and clusters. Monthly video conferences, biannual general assemblies, annual scientific conferences, as well as topical workshops will be organized and conducted. The funds for measures to promote gender equality are managed the training of young researchers is coordinated, in collaboration with local graduate schools. The international visibility of TR 172 will be fostered. A web page will be set up and maintained. The logistic organization and scientific planning of the extensive observational campaigns within TR 172 will be supported by project Z01. Public outreach activities will be organized and coordinated between the different partners.

Mittelgeber: DFG, TRR 172, Projekt number 268020496

SFB/Transregio 172 „Arktische Verstärkung“
Modul integriertes Graduiertenkolleg (MGK*)
Integrated Research Training Group (MGK*)

Schlagworte: Arktis.

Projektleiter:
M. Wendisch (m.wendisch@uni-leipzig.de)
Prof. Dr. Susanne Crewell, Universität zu Köln, Institut für Geophysik und Meteorologie
Prof. Dr. Justus Notholt, Universität Bremen, Institut für Umweltphysik

Projektmitarbeiterin: Dr. Marlen Brückner

Projektbeginn: 2020
Projektende: 2023

Beschreibung
Ziel des Projektes ist es eine Integrated Research Training Group (IRTG) innerhalb von (AC) 3 einzurichten, um junge Forscher (Doktoranden und Postdocs) bei der Entwicklung ihrer wissenschaftlichen Unabhängigkeit zu unterstützen und sie auf den Arbeitsmarkt in Wissenschaft, in verschiedenen Bereichen der Industrie, oder in der wissenschaftlichen Verwaltung vorzubereiten. Das im Rahmen der IRTG geplante Qualifizierungsprogramm wird dazu beitragen, das Wissen und die Fähigkeiten junger Forscher zu vertiefen und ihre Unabhängigkeit zu fördern.

Description
The project will establish an Integrated Research Training Group (IRTG) within (AC)3 to support young researchers (Phd students and Postdocs) in their development of scientific independence, and prepare them for positions in academia, industry, in various fields, or in administration. The qualification programme planned within the IRTG will help to deepen their knowledge and skills of young researchers and promote their independence.

Mittelgeber: DFG, TRR 172, Projekt number 268020496

SFB/Transregio 172 „Arktische Verstärkung“
Fesselballongetragene Messungen des Energiebudgets in der wolkenbedeckten Zentralarktis (A02)
Tethered balloon-borne energy budget measurements in the cloudy central Arctic (A02)

Schlagworte: Arktis, ballongetragene Messungen, Energiebilanz, Strahlungsabkühlung.

Projektleiter: M. Wendisch (m.wendisch@uni-leipzig.de)
Dr. Holger Siebert, Leibniz-Institut für Troposphärenforschung e.V. (TROPOS)

Projektmitarbeiter: Michael Lonardi

Projektbeginn: 2016
Projektende: 2023

Beschreibung
Während der Expedition MOSAiC im Frühsommer (April bis Juni) 2020 werden fesselballongetragene Messungen von einer Eisschollenstation analysiert. Basierend auf den

gewonnenen Messungen werden wir typische Werte und Profile von Turbulenz, Strahlung, Aerosolpartikeln und wolkenmikrophysikalische Eigenschaften während der Entstehung von stratiformen Grenzschichtwolken in der Zentralarktis sammeln. Wir fokussieren uns hier auf lokale Aspekte der bewölkten Grenzschicht auf die Arktische Verstärkung, wobei auch entfernte Prozesse wie Advektion berücksichtigt werden.

Description
Tethered balloon-borne measurements from an ice-floe camp during the MOSAiC expedition in early summer (April-June) 2020 will be analysed. On the basis of the collected data we will quantify typical values and profiles of turbulence, radiation, aerosol particle and cloud microphysical properties during the life-time of stratiform ABL clouds in the central Arctic. Here we focus on local aspects of the cloudy ABL on Arctic amplification, although remote processes such as advection will also be considered.

Mittelgeber: DFG, TRR 172, Projekt number 268020496

SFB/Transregio 172 „Arktische Verstärkung“
Einfluss von tiefen Wolken auf die arktische atmosphärische Grenzschichtturbulenz und -Strahlung (A03)
Impact of low-level clouds on Arctic atmospheric boundary layer turbulence and radiation (A03)

Schlagworte: Arktis, flugzeuggetragene Messungen, Energiebilanz, Strahlungsabkühlung.

Projektleiter: M. Wendisch (m.wendisch@uni-leipzig.de)
Dr. Christof Lüpkes, Alfred-Wegener-Institut Helmholtz-Zentrum für Polar- und Meeresforschung

Projektmitarbeiter: Sebastian Becker

Projektbeginn: 2016
Projektende: 2023

Beschreibung
Um den Einfluss von atmosphärischen Grenzschichtwolken auf die Arktische Verstärkung zu verstehen, sind detaillierte Studien der wolkenbedingten Prozesse, welche die arktische Grenzschicht und das Energiebudget beeinflussen, unabdingbar. Wir schlagen zwei Hauptziele für die zweite Phase vor. Ersteres bezweckt ein besseres Verständnis des Einflusses der Jahreszeit auf Wolken und deren verbundene Grenzschichtprozesse und das Energiebudget. Zweites Ziel beinhaltet die Untersuchung der Wolken während eines Lagrangeschen Luftmassentransports. Um diese Ziele zu erreichen, werden drei Messkampagnen mit den Polar5/6 Flugzeugen sowie mit HALO (High Altitude and Long Range Research Aircraft) durchgeführt.

Description
To understand the role of atmospheric boundary layer clouds in Arctic amplification, detailed studies of cloud–related processes influencing the ABL and the atmospheric energy budget are indispensable. We propose two major goals for phase II. The first one aims at a better understanding of the seasonal dependence of the cloud impact on the ABL processes and energy budget. The second objective includes to investigate the changing cloud impact during Lagrangian

air mass transports. To reach these goals, we will perform three campaigns using the AWI Polar 5/6 aircraft and the High Altitude and Long Range Research Aircraft (HALO).

Mittelgeber: DFG, TRR 172, Projekt number 268020496

SFB/Transregio 172 „Arktische Verstärkung“
Einfluss von Bodenheterogenität auf den Strahlungsantrieb und Ableitung von Aerosol- und Wolkeneigenschaften in der Arktis (C01)
Influence of surface heterogeneity on radiative forcing and retrieval of aerosol and cloud properties in the Arctic (C01)

Schlagworte: Arktis, flugzeuggetragene Messungen, Eis- und Schneealbedo, BRDF

Projektleiter: M. Wendisch (m.wendisch@uni-leipzig.de)
Dr. Georg Heygster (bis 12/2019), Universität Bremen, Institut für Umweltphysik (IUP)
Dr. Marcel Nicolaus (Seit 01/2020), Alfred-Wegener-Institut Helmholtz-Zentrum für Polar- und Meeresforschung
Dr. Gunnar Spreen, (seit 01/2020), Universität Bremen, Institut für Umweltphysik Abteilung für Erdfernerkundung

Projektmitarbeiterin: Dr. Evelyn Jäkel

Projektbeginn: 2016
Projektende: 2023

Beschreibung
Die Bodenheterogenität und zeitliche Entwicklung der Bodeneigenschaften des Arktischen Ozeans beeinflussen den Strahlungsenergietransfer durch die Kopplung von Atmosphäre, Meereis und Ozean im arktischen Klimasystem. Strahlungseffekte durch Interaktionen dieser Komponenten sind nicht gut verstanden, allerdings können sie eine entscheidende Rolle im arktischen Klimasystem spielen. Wir werden Flugzeugmessungen der vorangegangenen Kampagnen ACLOUD, PAMARCMiP, und AFLUX analysieren und neue Messungen während MOSAiC und HALO-(AC) hoch 3 sammeln. Zusätzlich werden wir Satellitendaten (MERIS, Sentinel-3) für unsere Analyse verwenden.

Description
The spatial heterogeneity and temporal evolution of surface properties of the Arctic Ocean influence the radiative energy transfer through the coupled compartments (atmosphere, sea ice, open ocean) of the Arctic climate system. Radiative effects of interactions between these components are not well studied, however, they may play an important role in the Arctic climate system. We will analyse airborne data from the previous ACLOUD, PAMARCMiP, and AFLUX campaigns, and collect new measurements during the planned MOSAiC and HALO-(AC) observations. In addition, we will use satellite data (MERIS, Sentinel-3) in our analysis.

Mittelgeber: DFG, TRR 172, Projekt number 268020496

SFB/Transregio 172 „Arktische Verstärkung“
Charakterisierung von arktischen Mischphasenwolken durch flugzeuggetragene in-situ Messungen und Fernerkundung (B03)
Characterization of Arctic mixed-phase clouds by airborne in-situ measurements and remote sensing (B03)

Schlagworte: Arktis, flugzeuggetragene Messungen, Mischphasenwolken.

Projektleiter: Dr. André Ehrlich (a.ehrlich@uni-leipzig.de)
Professor Dr. Susanne Crewell, Universität zu Köln, Institut für Geophysik und Meteorologie
Professor Dr. Andreas Macke, Leibniz-Institut für Troposphärenforschung e.V. (TROPOS)

Projektmitarbeiter: Elena Ruiz, Marcus Klingebiel

Projektbeginn: 2016
Projektende: 2023

Beschreibung
Dieses Teilprojekt kombiniert flugzeuggetragene Fernerkundung der Vertikalsäule und den Strahlungseffekt von Wolken mittels in-situ mikrophysikalischen Messungen von Wolken- und Aerosolpartikeln. Da die vorangegangenen Kampagnen lediglich Momentaufnahmen der arktischen Bedingungen geliefert haben, werden wir diese Messungen mit zwei weiteren Kampagnen ausbauen, um die saisonalen und regionalen Unterschiede von Wolken- und Aerosoleigenschaften und deren Beitrag zur Arktischen Verstärkung systematisch zu untersuchen. Die beobachteten Wolken- und Aerosoleigenschaften werden untereinander verlinkt und für unterschiedliche Aspekte kategorisiert, um Änderungen der Aerosol-Wolken-Wechselwirkung unter verschiedenen Bedingungen zu identifizieren, welche mehr oder weniger häufig bedingt durch die Arktische Verstärkung zu beobachten sind.

Description
We aim to combine airborne remote sensing of the vertical column and the radiative impact of clouds with in–situ microphysical measurements of cloud and aerosol properties. As the completed campaigns represent only a snapshot of Arctic conditions, we aim to extend these measurements by two major campaigns to systematically investigate seasonal and regional differences of cloud and aerosol properties and their contribution to Arctic amplification. The observed cloud and aerosol properties will be linked to each other and categorized for different issues to identify changes of aerosol-cloud interaction under different conditions, which are expected to occur more/less frequently due to Arctic amplification.

Mittelgeber: DFG, TRR 172, Projekt number 268020496

SFB/Transregio 172 „Arktische Verstärkung“
Analyse und Vorhersage des Transports und der Transformation von Arktischen Luftmassen (Warmlufteinschübe und Kaltluftausbrüche)
Analysis and forecast of transport and transformation of Arctic air masses (warm air intrusions, cold air outbreaks)

Schlagworte: Arktis, Luftmassentransport.

Projektleiter: Dr. Michael Schäfer (michael.schaefer@uni-leipzig.de)

Projektmitarbeiter: Benjamin Kirbus

Projektbeginn: 2020
Projektende: 2023

Beschreibung
Im Frühjahr 2022 werden Messungen mit dem deutschen Forschungsflugzeug HALO (High Altitude and Long Range Research Aircraft) im Rahmen von HALO- (AC) ³ (www.halo-spp.de) durchgeführt. Ziel sind Fernerkundungsmessungen, um die Auswirkungen von Wolken auf atmosphärische Grenzschichtprozesse und den Energiehaushalt in der Arktis zu untersuchen. Mit HALO wollen wir einen Lagrange-Ansatz verfolgen, um dasselbe Wolkensystem innerhalb von mehreren Tagen zu untersuchen und die Entwicklung der eingebetteten Wolken zu charakterisieren. In diesem Zusammenhang sind Warmlufteinschübe und Kaltluftausbrüche von besonderem Interesse. Sie bleiben in der Regel mehrere Tage bestehen und können große Mengen an Wärme und Feuchtigkeit über große Entfernungen in die Arktis oder aus der Arktis transportieren, wodurch die Wolkenmorphologie auf ihrem Weg beeinflusst wird. Um die Wolkenbildung / -entwicklung entlang solcher Transportwege von Anfang an zu erfassen, müssen Warmlufteinbrüche und Kaltluftausbrüche rechtzeitig vorhergesagt werden. Der Kern dieses Projekts besteht darin, ein Prognosetool zu entwickeln, es während der HALO- (AC) 3-Kampagne anzuwenden und anschließend zu validieren. Darüber hinaus werden die Luftmasseneigenschaften, die Wolkenentwicklung und ihr Einfluss auf die Strahlungseigenschaften analysiert.

Description
In spring 2022 airborne remote sensing in the Arctic will be used to study the cloud impact on atmospheric boundary layer processes and the energy budget. The measurements will be performed using the German research aircraft HALO (High Altitude and Long range research aircraft) within the framework of HALO-(AC)³ (www.halo-spp.de). With HALO, we aim to follow a Lagrangian approach to sample the same cloud system in the course of several days to investigate the embedded cloud evolution. In this regard, warm air intrusions and cold air outbreaks are of special interest. They usually persist for several days and are capable to transport large amounts of heat and moisture over huge distances into the Arctic or out of it, influencing the cloud morphology on its way. To capture the cloud formation/evolution along such transport paths from the very beginning, it is necessary to forecast warm air intrusions and cold air outbreaks in time. The core of this project is to develop a forecast tool, apply it during the HALO-(AC)3 campaign, and to validate it afterwards. Furthermore, the air-mass characteristics, the cloud evolution, and their influence on radiative properties will be evaluated.

Mittelgeber: Universität Leipzig, Doktorandenförderung

SFB/Transregio 172 „Arktische Verstärkung“
Evaluierung der ECMWF und ICON Vorhersagequalität von arktischen Wolkeneigenschaften mit Hilfe von flugzeuggetragenen Messungen

Evaluation of ECMWF and ICON forecast quality of cloud properties using airborne dropsonde and cloud measurements in the Arctic

Schlagworte: Arktis, flugzeuggetragene Messungen, Mischphasenwolken.

Projektleiter: Dr. Michael Schäfer (michael.schaefer@uni-leipzig.de)

Projektmitarbeiter: Hanno Müller

Projektbeginn: 2021
Projektende: 2024

Beschreibung
In den letzten Jahren hat sich die Leistung numerischer Wettervorhersagemodelle wie ECMWF oder ICON stetig verbessert. Ihre horizontale und vertikale Auflösung wurde erhöht, während die Unsicherheit ihrer vorhergesagten Parameter und die erforderliche Rechenzeit verringert werden konnten. Daher wurden solche Modelle zu einem wertvollen Instrument, um das Auftreten verschiedener Wolkentypen in bestimmten synoptischen Situationen zu untersuchen, was insbesondere in arktischen Regionen mit spärlichen lokalen Beobachtungen von entscheidender Bedeutung ist. Darüber hinaus helfen die Modelle in wissenschafltich interessante synoptische Situationen zu identifizieren und unterstützen die Planung geeigneter Flugmuster zur Untersuchung von arktischen Wolken. In früheren Kampagnen (ACLOUD, AFLUX oder MOSAiC-ACA) wurden zahlreiche Dropsonden- und Wolkenmessungen (in-situ, Fernerkundung) erfasst. Das Ziel dieses Projekts ist es, diese Daten zu verwenden, um die ECMWF- und ICON-Prognosequalität von Wolkeneigenschaften in der Arktis in unterschiedlichen synoptischen Situationen zu bewerten.
Es sind Profildaten von Temperatur und Luftfeuchtigkeit aus Dropsonde-Messungen zu verwenden, die während mehrerer Forschungsflüge nördlich von Spitzbergen in früheren Kampagnen erfasst wurden. Zusätzliche Kamera-, Radar- und Lidar-Messungen stehen zur Verfügung, um die Wolkensituation während der Flüge zu charakterisieren. Die Ergebnisse sollen zu einer quantitativen Bewertung der Vorhersagequalität von EZMW und ICON führen, die 2022 in weiteren Luftkampagnen wie HALO- (AC) 3 getestet wird.

Description
During the past years, the performance of numerical weather prediction models like ECMWF or ICON improved steadily. Their horizontal and vertical resolution have been increased, while the uncertainty of their predicted parameters and the required computational time could be reduced. Therefore, such models became a valuable tool to investigate the occurrence of different cloud types in specific synoptic situations, which is crucial especially in Arctic regions, where local observations are sparse. Furthermore, in such regions, they help to identify interesting upcoming cloud situations and to design most suited flight patterns for airborne campaigns. During past campaigns (ACLOUD, AFLUX, or MOSAiC-ACA) numerous dropsonde and cloud (in-situ, remote sensing) measurements have been collected. The objective of this project is to use these data to evaluate the ECMWF and ICON forecast quality of cloud properties in the Arctic in different synoptic situation.
Profile data of temperature and humidity from dropsonde measurements shall be used, which were captured during several research flights North of Svalbard during past campaigns. Additional image data, radar, and lidar measurements are available to further characterize the cloud situation during the flights. The results shall lead to a quantitative evaluation of the prediction quality of ECMWF and ICON, which will be tested during further airborne campaigns like HALO-(AC)3 in 2022.

Mittelgeber: Universität Leipzig, Doktorandenförderung

Entwicklung von tropischer hochreichender Konvektion abgeleitet aus bodengebundenen abbildenden Spektroradiometermessungen
Evolution of tropical deep-convective clouds derived from ground-based imaging spectroradiometer measurements

Schlagworte: Konvektive Wolken, atmosphärische Strahlung, bodengebundene Fernerkundung

Projektleiter: M. Wendisch (m.wendisch@uni-leipzig.de)

Projektmitarbeiterin: Kátia Mendes de Barros (katia.mendes_de_barros@uni-leipzig.de)

Projektbeginn: 2017
Projektende: 2021

Beschreibung
Im Rahmen des Projekts soll aus bodengebundenen Wolkenseitenmessungen der reflektierten Strahlung mittels eines abbildenden Spektrometersystems von tropischer hochreichender Konvektion auf das Vertikalprofil der mikrophysikalischen Eigenschaften der Wolke geschlossen werden. Damit soll die vertikale Entwicklung von hochreichender Konvektion, die eine wesentliche klimarelevante Rolle spielt, unter Berücksichtigung des Einflusses von Aerosolpartikeln und von thermodynamischen Bedingungen auf das Tropfenwachstum charakterisiert werden. Die geplanten Messungen sollen auf einem 320 m hohen Messturm (ATTO: Amazonian Tall Tower Observatory), der kürzlich im brasilianischen Regenwald errichtet wurde, stattfinden. ATTO ist mit Messgeräten ausgestattet, die meteorologische, chemische und Aerosolparameter liefern. Die Messregion bietet ideale Beobachtungsbedingungen mit klar definierten Jahreszeiten (Regen- und Trockenzeit), täglicher Konvektion und variablen Aerosolbedingungen. Aus den Messungen eines neuen abbildenden Spektrometersystems, SPIRAS (SPectral Imaging Radiation System) sollen Vertikalprofile der thermodynamischen Phase und der Partikelgröße mit hoher zeitlicher und räumlicher Auflösung und mit Hilfe von adaptierten Verfahren unter Verwendung von dreidimensionalen Strahlungstransportsimulationen abgeleitet werden. Damit sollen vertikale Bereiche, die das Tropfenwachstum beschreiben (Diffusion, Koaleszenz, Mischphasenbereich und Vereisung), identifiziert werden. Zusätzliche Messungen einer Infrarotkamera und eines scannenden Depolarisations-Lidars werden für die Höhen- und Temperaturbestimmung der beobachteten Wolkenelemente herangezogen. Zusätzlich werden die Polarisationsmessungen des Lidars zur Bestimmung der thermodynamischen Phase verwendet, um den wichtigen Phasenübergang zu identifizieren. Mit Hilfe der gewonnenen Daten werden außerdem Annahmen (Effektivradius als konservative Wolkeneigenschaft) wie sie von Ableitungsverfahren zur Bestimmung von mikrophysikalischen Wolkenprofilen aus Satellitenmessungen gemacht werden, überprüft.

Description
Specifically, the project will derive the vertical profile of microphysical properties of tropical deep-convective clouds (DCC) from ground-based measurements of reflected radiation from cloud sides by an imaging spectroradiometer system. This general objective is to characterize the vertical

evolution of DCCs, which play an important role in the Earths climate system. The evolution will be studied with respect to the impact of aerosol and thermodynamic conditions on the cloud particle growth. The planned measurements will be performed on the new Amazonian Tall Tower Observatory (ATTO), of 320 m height situated in the Amazon Basin near the equator. ATTO is equipped with instruments to measure micrometeorological and atmospheric chemical variables, as well as aerosol properties. It provides ideal observation conditions with clear seasons (wet and dry season), and daily occurrence of DCCs in a highly variable environment with respect to concentrations and types of aerosol particles. The new imaging spectroradiometer system, SPIRAS (SPectral Imaging Radiation System), will be used to derive vertical profiles of thermodynamic phase and cloud effective radius with high temporal and spatial resolution by means of adapted methods based on three-dimensional radiative transfer simulations. In this way vertical zones characterizing the droplet growth (diffusion, coalescence, mixed-phase, and glaciation) will be identified. Auxiliary measurements by an infrared camera and a scanning depolarization Lidar will be used to estimate the height and the temperature of the observed cloud element. Additionally, polarization measurements by Lidar will support the retrieval of the thermodynamic phase which is important to identify the phase transition. By means of the data obtained we will validate assumptions (effective particle radius as conservative cloud property) of retrieval methods for satellite-based observations to derive microphysical profiles.

Mittelgeber: DFG WE 1900/34-1, Projekt number 310366544

Fernerkundung und Strahlungsantrieb von Inhomogenen Passatwind-Cumuli
Remote Sensing and Radiative Forcing of Inhomogeneous Trade-Wind Cumuli

Schlagworte: Passatwind-Cumuli, atmosphärische Strahlung, flugzeuggetragene Fernerkundung

Projektleiter: M. Wendisch (m.wendisch@uni-leipzig.de)

Projektmitarbeiterin: Anna Luebke

Projektbeginn: 2019
Projektende: 2022

Beschreibung
Das Hauptziel des Projektes besteht in der Quantifizierung des großskaligen Strahlungsantriebes von flachen Passatwind Cumulus-Wolken als Funktion der makro- und mikrophysikalischen Wolkeneigenschaften, der räumlichen Anordnung der Wolken, und der mesoskaligen Vertikalbewegung. Wir kombinieren makro-, mikrophysikalische und Strahlungseigenschaften von Passatwindwolken, welche von flugzeuggetragenen Fernerkundungsbeobachtungen und in-situ Strahlungsmessungen abgeleitet werden. Diese Messungen werden an Bord von HALO (High Altitude and Long Range Research Aircraft) während der Messkampagne EUREC4A (ElUcidating the Role of Cloud-Circulation Coupling in ClimAte) östlich von Barbados im Februar 2020 gewonnen. Um die relevanten Wolken- und Strahlungsdaten ableiten zu können, werden wir die Instrumentierung von HALO erweitern durch (i) eine multispektrale thermisch-infrarote Kamera, und (ii) auf- und abwärts gerichtete, halbräumliche Breitband-Pyranometer und Pyrgeometer. Die breitbandigen Radiometer werden solare und terrestrische Strahlungsflussdichtemessungen liefern, um den atmosphärischen Strahlungshaushalt in Flughöhe zu quantifizieren. Die thermisch-

infrarote Kamera wird die Helligkeitstemperatur in verschiedenen Spektralbändern mit hoher räumlicher (5 Meter) und zeitlicher (20 Hz) Auflösung bestimmen. Diese Geräte wurden noch nicht auf HALO eingesetzt. Deshalb besteht ein wichtiger Teil des vorgeschlagenen Arbeitsplanes in intensiven Tests und Kalibrierungen der neuen Geräte und der Entwicklung von Software zur Handhabung und Auswertung der Daten. Die thermisch-infrarote Kamera wird verwendet, um Wolkenprodukte abzuleiten. Dies umfasst Felder der Temperatur am Wolkenoberrand, Flüssigwasserpfad und Effektivradien. Die Felder werden statistisch analysiert, um den Bedeckungsgrad, den Grad der Organisation, und die Wolkengrößenverteilung zu erhalten. Die Daten werden mit atmosphärischen Parametern (Temperatur-/Feuchteprofile, Hintergrundaerosol, großskalige Divergenz) korreliert. Die Beobachtungen mit den Breitband-Radiometern werden in Kombination mit den Feldern der Wolkeneigenschaften, die von den Messungen mit der thermisch-infraroten Kamera abgeleitet werden, analysiert. Die Quantifizierung des Wolken-Strahlungsantriebes für unterschiedliche Wolkenbedeckungen sowie Wolkenoberkantentemperaturen wird zeigen, wie empfindlich der Wolken-Strahlungsantrieb im Hinblick auf makroskopische Eigenschaften und die Anordnung der Passatwolken ist. Eine Parametrisierung dieser Empfindlichkeiten hilft bei der Beschreibung von Passatwind-Wolken in numerischen Wettervorhersage- und globalen Klimamodellen.

Description
The core objective of the project is to quantify the large-scale radiative forcing of shallow trade-wind cumuli as a function of the cloud macrophysical and microphysical properties, the cloud spatial organization, and the mesoscale vertical motion. We will combine macrophysical, microphysical, and radiative properties of trade-wind cumuli obtained from airborne remote sensing cloud observations and in situ irradiance measurements aboard the High Altitude and Long Range Research Aircraft (HALO) during the EUcidating the Role of Cloud-Circulation Coupling in ClimAte (EUREC4A) campaign east of Barbados in February 2020.To retrieve the relevant cloud and radiation data, we will extend the instrumentation of HALO by (i) a multi-wavelength thermal infrared (IR) imager, and (ii) pairs of upward and downward looking, hemispheric broadband pyranometers and pyrgeometers. These broadband radiometers will provide solar and terrestrial irradiance measurements to quantify the atmospheric radiation budget at flight level. The thermal IR imager will map the cloud top brightness temperatures at different thermal IR spectral bands with high spatial (5 m) and temporal (20 Hz) resolution. The instruments were not operated on HALO yet. Therefore, a crucial part of the proposed work plan is related to extensive tests and calibrations of the new instruments and developing tools for handling and post processing the data. The thermal IR imager will be used to develop an IR-based cloud product, providing maps of cloud top temperature, cloud liquid water path and cloud effective droplet size. The maps will be analysed statistically to obtain the cloud fraction, degree of clustering, and cloud size distributions. The data will be correlated with atmospheric parameters (temperature/humidity profiles, background aerosol, large-scale divergences). The observations of the broadband radiometers will be analysed in combination with the maps of cloud properties derived from the thermal IR imager. Quantifying the cloud radiative forcing for scenes of trade-wind cumuli with different cloud fraction, degree of clustering, and cloud top temperatures will indicate how sensitive the cloud radiative forcing is with respect to the macroscopic properties and organization of trade-wind cumuli. Parameterizing this sensitivity provides a tool to evaluate the representation of trade-wind cumuli in numerical weather prediction models and global climate models.

Mittelgeber: DFG Projekt Nummer 422897361

EUREC4A Rahmenantrag - Untersuchung der Bedeutung der Koppelung zwischen Wolken und Zirkulation im Klimasystem
EUREC4A mission proposal - Elucidating the Role of Cloud-Circulation Coupling in Climate

Schlagworte: Passatwind-Cumuli, atmosphärische Strahlung, flugzeuggetragene Fernerkundung

Projektleiter: Felix Ament (Univeristät Hamburg), M. Wendisch (m.wendisch@uni-leipzig.de)

Projektmitarbeiterin: Anna Luebke

Projektbeginn: 2019
Projektende: 2022

Beschreibung
Das Project finanziert den univesitären Anteil der Missionskosten der HALO Mission EUcidating the Role of Cloud-Circulation Coupling in ClimAte (EUREC4A) in dem die Universität Leipzig mit einem Einzelprojekt (siehe „Fernerkundung und Strahlungsantrieb von Inhomogenen Passatwind-Cumuli“, DFG Projekt Nummer 422897361) vertreten ist.

Description
The project funds the university part of the mission cost of the HALO mission EUcidating the Role of Cloud-Circulation Coupling in ClimAte (EUREC4A) in which the Leipzig University participates with a research project (see “Remote Sensing and Radiative Forcing of Inhomogeneous Trade-Wind Cumuli” DFG Project Number 422897361).

Mittelgeber: DFG Projekt Nummer 423239633

Anwendung von Eisoberflächen- und Strahlungsdaten in der Luft basierend auf MOSAiC Beobachtungen für Oberflächenalbedoparametrisierungen der zentralen Arktis
Application of airborne ice surface and radiation data based on MOSAiC observations for surface albedo parameterizations of the central Arctic (ALIBABA)

Schlagworte: Arktis, Oberflächenalbedo, hubschraubergetragene Messungen, MOSAiC

Projektleiter: M. Wendisch (m.wendisch@uni-leipzig.de)

Projektmitarbeiter: Tim Sperzel

Projektbeginn: 2021
Projektende: 2024

Beschreibung
Das Ziel des Projekts ALIBABA ist die direkte Anwendung der fluggestützten Strahlungs- und Kameradaten, die mit der Hubschrauber-Schleppsonde „HELiPOD“ während MOSAiC erhoben werden. Damit soll der Einfluss von Wolken-Inhomogenitäten auf die Eigenschaften der Rückstreuung solarer Strahlung von arktischen Eisflächen quantifiziert werden. Es werden verschie-

dene Skalen von 0.25 km bis 10 km betrachtet, die für regionale Klimamodelle und die horizontale Auflösung von Satelliten charakteristisch sind. Für diese räumlichen Skalen stellen die Oberflächen-Reflexionseigenschaften oft eine Mischung von verschiedenen Oberflächen-Arten dar, wie z.B. offenes Wasser, pures Eis, mit Schnee bedecktes Eis -und Schmelztümpel. Dreidimensionale (3D) Strahlungstransportsimulationen sollen mit den Messungen der komplexen Oberflächen-Reflexionseigenschaften kombiniert werden. Die Albedo und die direktionale Reflexion der individuellen Oberflächenarten sollen aus den großflächigen Beobachtungen unter Berücksichtigung der von Einstrahlungsänderungen (Wolkenbedeckung, Sonnenstand) abgeleitet werden. Dadurch soll die zeitliche Entwicklung der Reflexionseigen-schaften der verschiedenen Oberflächenarten über einen längeren Zeitraum dokumentiert werden (MOSAiC-Messungen Mai bis August 2020). Damit können Parametrisierungen der Oberflächen-Albedo für Klimamodelle wie HIRHAM-NAOSIM und ICON evaluiert und verbessert werden.

Description
The aim of the project ALIBABA is the direct application of the airborne radiation and camera data obtained with the helicopter borne meteorological sonde “Helipod” during MOSAiC (Multidisciplinary drifting Observatory for the Study of Arctic Climate). The data are used to quantify the impact of cloud inhomogeneity on the solar reflection properties of Arctic surfaces on typical spatial scales (0.25 – 10 km) covered by regional climate models and satellite footprint sizes. For such spatial scales, the surface reflection properties may feature a mixture of different surface types such as open water, bare ice, snow covered ice, and melt ponds. Three-dimensional (3D) radiative transfer modeling will be combined with measurements of such complex surface reflection properties. The subtype albedo and directional reflection will be extracted from areal surface observations considering effects of illumination changes (cloud occurrence, solar zenith angle). By that, the temporal evolution of the individual subtypes of reflection properties during the course of MOSAiC (May – August 2020) will be documented. That will help to evaluate and improve the surface albedo parameterization scheme of climate models such as HIRHAM-NAOSIM and ICON.

Mittelgeber: BMBF Projekt Nummer 232101570

Hochatmosphäre, Christoph Jacobi
Upper Atmosphere

Large-scale dynamical impacts on regional Arctic climate change
Der Einfluss großräumiger Dynamik auf regionale arktische Klimaänderungen

Schlagworte: Arktische Verstärkung, Klimavariabilität

Projektleiter: Prof. Dr. Christoph Jacobi (jacobi @ rz.uni-leipzig.de), Prof. Dr. Johannes Quaas (johannes.quaas @ uni-leipzig.de)

Projektmitarbeiter: Sina Mehrdad

Projektbeginn: 1.1.2016
Projektende: 31.12.2023

Beschreibung
Das Projekt umfasst die Wechselwirkung zwischen der variablen großskaligen Zirkulation und regionalen arktischen Klimaänderungen und der Diagnose der arktischen Verstärkung auf regionaler Skala als Reaktion auf Variationen großskaliger Zirkulation in der Vergangenheit sowie in Klimaszenarien zukünftigen Klimwandels. Es werden hierzu Reanalysedaten und CMIP5-Modellergebnisse herangezogen und eigene Modellsimulationen durchgeführt. Die Kopplung von Troposphäre und Stratosphäre als wichtiger Bestandteil der Variabilität der polaren Atmosphäre wird auch mit numerischen Simulationen untersucht.

Mittelgeber: Deutsche Forschungsgemeinschaft, SFB-Transregio 172

Lokaler Schwerewellenantrieb auf die mittlere Atmosphäre: Bildung, Auswirkungen, und Langzeittrends
Middle atmosphere localized gravity wave forcing: Formation, impact and longterm evolution (MATELO-FILE)

Schlagworte: Schwerewellen, mittlere Atmosphäre, Brewer-Dobson-Zirkulation, Klimawandel

Projektleiter: Prof. Dr. Christoph Jacobi (jacobi @ rz.uni-leipzig.de)

Projektmitarbeiter: Dr. K. Karami

Projektbeginn: 1.5.2021
Projektende: 30.4.2024

Beschreibung
MATELO-FILE beinhaltet die Bestimmung, Analyse und Simulation von Schwerpunkten stratosphärischer Schwerewellenaktivität sowie deren Auswirkungen auf die Dynamik der mittleren Atmosphäre. Zu diesem Zweck werden die relevanten Regionen auf Basis von Beobachtungs-, Reanalyse- und Modelldaten identifiziert, indem Schwerewellenparameter sowie die Hintergrundzirkulation untersucht werden. Aus diesen Analysen werden die Auslöser der erhöhten Schwerewellenaktivität sowie meteorologische Bedingungen, die solche Schwerpunkte hervorrufen, abgeleitet. Darauf aufbauend wird mit Hilfe mehrjähriger Zeitreihen aus ERA5 und CMIP6-Datensätzen untersucht, ob sich die Aktivität solcher Schwerpunktregionen verändert hat. Um die Wechselwirkung von lokal verstärkter Schwerewellenaktivität mit der Zirkulation der mittleren Atmosphäre zu untersuchen, was die Anregung atmosphärischer Wellen sowie mögliche Kompensationsmechanismen umfasst, werden Experimente mit dem UA-ICON GCM sowie einem weiteren mechanistischen Zirkulationsmodell durchgeführt. Derartige Herangehensweisen ermöglichen es zu untersuchen, (i) wie Bereiche verstärkter Schwerewellenaktivität in Klimamodellen reproduziert werden, (ii) was der Einfluss von Schwerewellen auf die Zirkulation ist und (iii) wie diese sich in einem sich ändernden Klima anpassen. Das Projekt ist eine Kooperation zwischen dem LIM und dem Department Atmosphärenphysik, Karls-Universität Prag.

Description
The MATELO-FILE project focuses on the detection, analysis, and modelling of stratospheric gravity wave (GW) hotspots and their effect on the dynamics of the middle atmosphere. To this end, we will identify GW hotspots on the basis of observations, reanalysis data and model output by analysing different GW parameters, and also background conditions. From these analyses we will deduce possible GW sources as well as meteorological conditions that favour the generation of GW hotspots. Based on these results fromthe datasets partly covering several decades, we will also investigate the temporal development of these GW hotspots to investigatein how far the GW hotspot activity has changed during the last decades. To analysethe interactionprocessesof these GW hotspots with the circulation of the middle atmosphere (the wave forcing itself as well as a compensation mechanism), experiments with the UA-ICON global circulation model and a further mechanistic circulation modelwill be performed. This will enable us toinvestigate (i) how the GW hotspots and their effects are reproduced in climate models, (ii) their influence on circulation changes in a changing climate, and (iii) how they react on a changing climate. The project is a cooperation between LIM and the Department of Atmospheric Physics, Charles University in Prague.

Mittelgeber: Deutsche Forschungsgemeinschaft (DFG JA 836/47-1)

Verzögerte Antwort der Ionosphäre auf Variationen des solaren EUV (DRIVAR)
Delayed response of the ionosphere to solar EUV variability (DRIVAR)

Schlagworte: Ionosphäre, solare Variabilität

Projektleiter: Prof. Dr. Christoph Jacobi (jacobi @ rz.uni-leipzig.de)

Projektmitarbeiter: R. Vaishnav

Projektbeginn: 1.5.2017
Projektende: 30.11.2021

Beschreibung
Das ionosphärische Plasma reagiert auf Änderungen der ionosphärischen EUV und UV-Strahlung auf der Zeitskala der solaren Rotation mit einer Verzögerung von 1-2 Tagen. Es wird angenommen, dass diese Verzögerung auf Transportprozesse von der unteren Ionosphäre in die F-Region zurück zu führen ist, doch wurden bislang nur begrenzte Modelluntersuchungen durchgeführt, um diesen Zusammenhang zu belegen. Innerhalb von DRIVAR sollen die Prozesse, die für die ionosphärische Verzögerung verantwortlich sind, durch umfassende Datenanalyse und Modellierung untersucht werden. Verschiedene solare Proxies sowie spektral aufgelöste EUV- und UV-Flüsse aus Satellitenmessungen werden verwendet und zusammen mit ionosphärischen Parametern analysiert, welche aus GPS-Radiookkultationsmessungen, Ionosondenmessungen und GPS-Gesamtelektronenmessungen stammen. Letztere haben sowohl den Vorteil einer globalen Abdeckung als auch einer z.T. räumlich hoher Auflösung. Die ionosphärsche Verzögerung wird auf verschiedenen Zeitskalen ionosphärischer Variation (Tage, solare Rotation, saisonal) untersucht, und regionale Abhängigkeiten werden analysiert. Wegen des komplexen Charakters der involvierten Prozesse in der Thermosphäre und Ionosphäre werden Experimente mit numerischen Modellen benötigt, um die der Verzögerung zugrundeliegenden Prozesse physikalisch zu

untersuchen. Wir verwenden das Coupled Thermosphere Ionosphere Plasmasphere Electrodynamics (CTIPe), um die Verzögerung zu simulieren und führen Sensitivitätsstudien durch um die zur ionosphärischen Verzögerung führenden Prozesse im Detail zu analysieren. Die Ergebnisse von DRIVAR werden zu einem verbesserten Verständnis ionosphärischer Prozesse führen und werden insbesondere in der Vorhersage ionosphärischer Variabilität Anwendung finden, z.B. bei der Analyse und Vorhersage von GNSS- Positionsfehlern.

Description
The ionospheric plasma reacts on solar EUV and UV variations in the course of the solar rotation with a time delay of 1-2 days. This delay is assumed to be owing to transport processes from the lower ionosphere to the F region, but only limited modeling has been performed so far to prove this hypothesis.
Within DRIVAR, the processes responsible for the ionospheric delay will be investigated through comprehensive data analyses and modeling. Different kinds of solar proxies as well as spectral EUV and UV fluxes from satellite observations will be used and analyzed together with ionospheric parameters from GPS radio occultations and ionosondes, and, providing both global and high-resolution coverage, GPS total electron content maps. In particular, the ionospheric delay will be analyzed at different time scales (short-term, solar rotation, seasonal time scale), and the regional dependence of the delay will be analyzed.

Mittelgeber: Deutsche Forschungsgemeinschaft (DFG JA 836/33-1)

Nicht-zonale Strukturen der Dynamik der Mesosphäre/unteren Thermosphäre in mittleren Breiten (NOSTHEM)
Non-zonal Structures of Mesosphere/lower Thermosphere Dynamics at Middle Latitudes (NOSTHEM)

Schlagworte: mittlere Atmosphäre; Radarmessungen

Projektleiter:
Prof. Dr. Christoph Jacobi (jacobi @ rz.uni-leipzig.de)

Projektmitarbeiter: F. Lilienthal, K. Kandieva

Projektbeginn: 1.9.2018
Projektende: 31.8.2022

Beschreibung
In NOSTHEM sollen zonale Unterschiede des mittleren Windes, Gezeitenparameter, planetarer Wellen und Schwerewellen in der Mesosphäre und unteren Thermosphäre untersucht und erklärt werden. Ihr Einfluss auf die Repräsentativität einzelner Messungen für ein zonales Mittel von mittlerem Wind und Wellen wird bestimmt werden. Dies soll eine quantitative Einschätzung der Unsicherheiten von mittlerer Klimatologie, Langzeittrends und Maßen für die Variabilität auf der Basis einzelner Messungen ermöglichen. Der Beitrag nicht-zonaler Strukturen auf die mittlere Zirkulation und ihre Variabilität wird bestimmt. Hemisphärische Analysen von Wellen und Zirkulation in der unteren und mittleren Atmosphäre werden verwendet, um deren Rolle bei der Bildung longitudinaler Unterschiede zu klären. Dies wird auch die Frage beantworten, ob die schon

seit langem beobachteten Unterschiede des mesosphärischen Windes über Mittel- und Osteuropa signifikant sind und wenn ja, welche Prozesse zu deren Auftreten beitragen.
In NOSTHEM werden Beobachtungen zweier praktisch identischer VHF-Meteorradare auf ähnlicher geographischer Breite, aber mit 36° Längenunterschied herangezogen. Daher kann daraus der Beitrag nicht-zonaler Strukturen zur lokalen Klimatologie und Variabilität ermittelt werden. Um ein umfassendes hemisphärisches Bild zu erhalten, werden die lokalen Radarmessungen durch Satellitenbeobachtungen und Reanalysedaten ergänzt, sowie numerische Simulationen mit einem Zirkulationsmodell der mittleren Atmosphäre durchgeführt.
Die Hauptziele von NOSTHEM sind (1) eine quantitative Darstellung von Ähnlichkeiten und Unterschieden der mesosphärischen/thermosphärischen Zirkulation an zwei Längengraden, (2) eine Erweiterung dieser Analyse durch hemisphärische Daten und (3) eine Quantifizierung der Rolle von Wellen bei der Ausprägung der Zirkulation an einzelnen Orten. Als Endziel werden nicht-zonale Strukturen und ihre Gründe und die zu ihnen führenden Prozesse geklärt, und auch Hinweise für die Interpretation von Klimatologie und Variabilität an einzelnen Orten in Bezug auf die gesamthemisphärische Dynamik gegeben.
NOSTHEM wird als Kooperation des Instituts für Meteorologie, Universität Leipzig und des radiophysikalischen Departments, Universität Kasan gemeinsam durchgeführt.

Description
During NOSTHEM, longitudinal differences of mean winds, tidal parameters, and planetary and gravity waves in the mesosphere/lower thermosphere (MLT) will be analyzed and interpreted. The influence of these differences on the representativeness of single sites for describing zonal means of winds and wave parameters will be quantified. This will allow us to quantitatively estimate the uncertainty of mean climatology, long-term trends, and measures of interannual variability observed at single sites. The contribution of non-zonal structures to mean circulation and its variability will be determined. Hemispheric analyses of lower and middle atmosphere waves and circulation parameters will be used to analyze the role of these in establishing longitudinal differences. This will then resolve the question whether there is a significant difference between the mid-latitude MLT wind regimes in Western and Eastern Europe, and which are the underlying processes leading to these differences.
The NOSTHEM project will make use of the two very similar VHF meteor radar observations at similar latitude, but with a 36° difference in longitude in order to specify quantitatively the influence of non-zonal structures on mean circulation, waves and tides. In order to obtain a comprehensive picture of non-zonal structures in the MLT dynamics, the concurrent observations of winds and temperatures using VHF radars at Collm and Kazan will be completed by numerical modeling using a circulation model of the middle atmosphere, satellite observations, and reanalyses.
Main goals of NOSTHEM are (1) a quantitative description of similarities and differences of MLT circulation parameters at two longitudes, (2) an extrapolation of this analysis to the full hemispheric view based on satellite observations and modeling, and (3) a quantitative estimation of the role of waves in the specific characteristic of circulation parameters at single sites. As a final goal, we shall explain longitudinal differences through their underlying processes, and also provide guidelines for the interpretation of both mean climatology and trend analyses made at single sites in terms of their representativeness for hemispheric dynamics.
NOSTHEM is carried out in cooperation between the Institute for Meteorology, Universität Leipzig and the Department of Radiophysics, Institute of Physics, Kazan Federal University, Russian Federation.

Mittelgeber: Deutsche Forschungsgemeinschaft (DFG JA 836/38-1)

Wellenkopplung der mittleren und oberen Atmosphäre: Jahr-zu-Jahr-Variabilität und Langzeittrends (VACILT)
Wave coupling processes of the middle and upper atmosphere: Interannual and long-term variability (VACILT)

Schlagworte: mittlere Atmosphäre; Hochatmosphäre, Langzeittrends

Projektleiter: Prof. Dr. Christoph Jacobi (jacobi @ rz.uni-leipzig.de)

Projektmitarbeiter: A. Kuchar

Projektbeginn: 1.5.2019
Projektende: 30.6.2022

Beschreibung
Die langfristigen Änderungen in der Hochatmosphäre werden durch dynamische Prozesse der darunterliegenden Schichten beeinflusst. Diese meteorologischen Einflüsse werden vor allem durch Wellen hervorgerufen, die sich von der unteren Atmosphäre in die Thermosphäre ausbreiten. Indem sie Energie und Impuls transportieren, modifizieren sie thermosphärische und ionosphärische Parameter. Wellen in der Atmosphäre werden nicht nur vom Zustand der unteren und mittleren Atmosphäre beeinflusst, sondern weisen auch Langzeittrends auf. Daher trägt nicht nur die bekannte Abkühlung durch die Zunahme von Treibhausgasen zu langfristigen Änderungen in der Thermosphäre bei, sondern auch Trends der Wellenaktivität, so dass eine umfassende Beschreibung hochatmosphärischer Variabilität auch Trends der Wellen beinhalten muss.
Um die Auswirkung von Wellen auf die Kopplung von mittlerer und oberer Atmosphäre zu quantifizieren, zielt das Projekt VACILT auf die Beobachtung und Simulation von Wellen, sowie die Quantifizierung ihrer Variabilität und die Analyse ihrer Auswirkungen auf die Thermosphäre. Dazu werden langfristige (> 30 Jahre) Radarbeobachtungen herangezogen und Ergebnissen einer Langzeitsimulation mit dem GAIA-Erdsystemmodell gegenübergestellt, welche wiederum durch Beobachtungen thermosphärischer Parameter gestützt werden.
Die GAIA-Analysen erlauben es, die Auswirkungen atmosphärischer Wellen in der Thermosphäre zu quantifizieren und mit der Variabilität der atmosphärischen Zirkulation in Verbindung zu bringen. Die Ergebnisse werden mit Hilfe von Sensitivitätsstudien unter Verwendung eines mechanistischen Zirkulationsmodells gestützt.
Die Ziele von VACILT sind demnach die folgenden: (1) Quantifizierung der Variabilität der Wellen in der mittleren Atmosphäre auf der Basis von Radarbeobachtungen und GAIA-Analysen (2) quantitative Bestimmung der Auswirkung von Wellenkopplung auf die Hochatmosphäre und (3) die umfassende Analyse des Beitrags von Wellen auf Trends in der Thermosphäre/Ionosphäre, gegenüber dem Beitrag von Treibhausgasen und deren Änderung. Das Erreichen dieser Ziele wird die Rolle von Wellen auf die Thermosphäre/Ionosphäre klären, und hat damit direkte Anwendung z.B. in der Vorhersage der Genauigkeit von Kommunikations-/Navigationssignalen.
VACILT ist ein gemeinsames Projekt der Universität Leipzig mit dem Leibniz-Institut für Atmosphärenphysik, Kühlungsborn und dem Department of Earth and Planetary Sciences, Universität Kyushu, Japan. Damit können die Ressourcen der jeweiligen Partner, nämlich Radarbeobachtungen und mechanistische Modelle auf deutscher, Erdsystemmodellierung und thermosphärischer Satellitenanalysen auf japanischer Seite, optimal kombiniert werden.

Description

The long-term variations of the upper atmosphere are influenced by dynamical processes in the underlying atmosphere. These meteorological influences are mainly due to atmospheric waves propagating from the lower atmosphere to the thermosphere. Transferring energy and momentum, they modify thermospheric and ionospheric parameters. Atmospheric waves not only reflect dynamical features of the lower/middle atmosphere, but also exhibit long-term trends. Consequently, not only the widely known greenhouse gas cooling contributes to thermospheric long-term changes, but atmospheric wave trends also, and a comprehensive description of upper atmosphere trends will have to include this wave variability and trends.

To quantify the effect of lower and middle atmosphere wave coupling on upper atmosphere dynamics, VACILT aims at observing, modeling, and rigorously quantifying interannual and long-term changes of lower and middle atmosphere waves and their effects in the upper atmosphere. To this end, long-term (> 30 years) radar observations will be analyzed with respect to waves and mean circulation trends. These analyses will be compared with results of a long-term, lower atmosphere driven simulation of the GAIA Earth System Model, which in turn will be supported by the analysis of thermospheric observations.

From the GAIA analyses, the lower atmosphere forcing on the thermosphere due to waves will be quantified. The variability of this forcing will be determined and interpreted in the context of lower atmosphere variability. To substantiate the results, sensitivity experiments with a mechanistic model will be performed.

Main goals of VACILT are (1) a quantitative description of interannual and long-term variability and trends in the middle atmosphere and thermosphere by analyzing the mean circulation and wave parameters from Earth System Model, supported by ground-based and satellite observations. (2) Quantitative estimates of the degree of wave coupling effects in the upper atmosphere . (3) comprehensive analysis of the role of middle-upper atmosphere wave coupling in forcing upper atmosphere long-term trends and variations, in relation to other drivers like greenhouse gas cooling.

Reaching these goals will elucidate the role of waves for the thermosphere/ionosphere and can for example be applied to predicting the accuracy of communication/navigation signals. VACLIT is a joint project between Universität Leipzig and the Leibniz Institute of Atmospheric Physics, Kühlungsborn, Germany and the Department of Earth and Planetary Sciences, University of Kyushu, Japan.

Mittelgeber: Deutsche Forschungsgemeinschaft (DFG JA 836/43-1)

Theoretische Meteorologie; Johannes Quaas
AG Wolken und globales Klima

Probabilistic attribution of extreme precipitation to aerosol perturbations (PATTERA)

Schlagworte: Attribution, Klima-Extremereignisse, Aerosol-Konvektions-Wechselwirkung

Projektleiter:
Koordinator: Andreas Hense, Universität Bonn (ahense@uni-bonn.de)
J. Quaas (johannes.quaas@uni-leipzig.de)

Projektmitarbeiter: Dr. Ribu Cherian (ribu.cherian@uni-leipzig.de)

Projektbeginn: 1.3.2020
Projektende: 28.2.2023

Beschreibung
Der Klimawandel wirkt sich insbesondere über Änderungen in Extermereignissen auf die Gesellschaft aus; hierbei stellen Extremniederschläge und Blitzeinschläge aus hochreichender Konvektion (Gewitter) besondere Gefahren dar. Anthropogene Änderungen der Atmosphärenzusammensetzung können Veränderungen in solchen Ereignissen bewirken. Anders als Treibhausgase und globale Erwärmung haben Emissionen von Aerosolpartikeln möglicherweise einen unmittelbaren Einfluss auf Konvektion. Das Projekt PATTERA wird (i) die Einflüsse von Aerosolen auf Konvektion, wie sie im ICON-Atmosphärenmodell simuliert werden, evaluieren, wobei vorhandene hochaufgelöste Simulationen, Multi-Modell-Ensembles und bodengebundene Beobachtungen als Referenz genutzt werden. Es wird weiterhin (ii) mit dem Ansatz probabilistischer Ursachenzuordnung (attribution; Ensemblesimulation tatsächlicher und hypothetischer – faktischer und kontrafaktischer – Bedingungen) die Auswirkungen von anthropogenen Aerosolen auf Extremniederschlag und Blitze untersuchen. In einer möglichen zweiten Phase können diese Untersuchungen auf die globale Skala ausgeweitet werden.

Mittelgeber: BMBF

Contrast between hemispheres in aerosol impact on cloud erosion (CHANCE)

Schlagworte: Neuseeland, Aerosol-Wolken-Wechselwirkungen, Hemisphärischer Unterschied

Projektleiter:
Koordinator: J. Quaas (johannes.quaas@uni-leipzig.de)
Gilles Bellon, University of Auckland (gilles.bellon@auckland.ac.nz)

Projektmitarbeiter: Samuel Kwakye (samuel.kwakye@uni-leipzig.de)

Projektbeginn: 1. 4. 2020
Projektende: 31.12.2022

Beschreibung
Die Frage, wie anthropogene Verschmutzungspartikel, sogenannte Aerosole, Wolken, und dadurch die Energiebilanz des Erdsystems beeinflussen, ist eine der wichtigsten Fragen bezüglich der Physik des Klimawandels. Hierbei spielen vor allem niedrige Wolken eine Rolle, und der wichtigste Wolkentyp bezüglich des Einflusses auf die Strahlung sind Stratokumuluswolken. Besonders interessant und mit besonders großer Unsicherheit behaftet ist dabei, inwiefern Stratokumulus auf einen anfänglichen Anstieg der Wolkentröpfchenkonzentration, Nd, aufgrund der anthropogenen Aerosolemissionen, reagieren (Wolkenanpassungen). Dabei sind zwei gegenläufige Senkenprozesse zu untersuchen: (i) Wolkenauflösung via Niederschlagsbildung – höhere Nd führen zu verzögerter Niederschlagsbildung, längerer Wolkenlebensdauer und damit zu einem stärkeren abkühlenden Effekt der Wolken. (ii) Wolkenauflösung durch turbulente Mischung mit der Umgebung und Tröpfchenverdunstung. Bei höhrerer Nd verdunsten die Tröpfchen durch größeres Oberfläche-Volumen-Verhältnis schneller – der gegenteilige Effekt. CHANCE baut auf neuen, komplementären Entwicklungen in Neuseeland und Deutschland auf: Neue Ansätze für die Darstellung und Untersuchung des Wolkenlebenszyklus anhand von hochaufgelösten Modelle (Auckland/NZ) sowie die führende universitäre Rolle in den Entwicklungen des ICON-Atmosphärenmodells (Leipzig/D). Dies ermöglicht wolkenauflösende – mit realistischer Darstellung der Wolkensenkenprozesse – bis globale Simulationen. CHANCE verbindet die Modellierung mit eingehenden Analysen von Beobachtungsdaten insbesondere von Satelliten und wird Stratokumulus für eine große Bandbreite an Wetterbedingungen und Aerosolkonzentrationen in den beiden unterschiedlichen Hemisphären simulieren; die beiden Wolkenauflösungsprozesse eingehend analysieren; die Modelle prozessorientiert mit Satellitendaten evaluieren und damit Modellverbesserungen vorschlagen; und schließlich den Aerosol-Wolken-Strahlungsantrieb quantifizieren.

Mittelgeber: BMBF

---

innovative MachIne leaRning to constrain Aerosol-cloud CLimate Impacts (iMIRACLI)

Schlagworte: Aerosol-Wolken-Wechselwirkungen, Maschinelles Lernen, Datenwissenschaften

Projektleiter:
Koordinator: Philip Stier, Universität Oxford (philip.stier@physics.ox.ac.uk)
J. Quaas (johannes.quaas@uni-leipzig.de)

Projektmitarbeiter: Jessenia Gonzalez Villarreal (jessenia.gonzalezv@uni-leipzig.de)
Julien Lenhardt (julien.lenhardt@uni-leipzig.de)

Projektbeginn: 1.1.2020
Projektende: 31.12.2023

Beschreibung

Climate change is one of the most urgent problems facing mankind. Implementation of the Paris climate agreement relies on robust scientific evidence. Yet, the uncertainty of non-greenhouse gas forcing associated with aerosol-cloud interactions limits our constraints on climate sensitivity. Radically new ideas are required. While the majority of radiative forcing estimates are model based, model uncertainties remain too large to achieve the required uncertainty reductions. The quantification of aerosol cloud climate interactions in Earth Observation data is thus one of the major challenges of climate science. Progress has been hampered by i) the difficulty to disentangle aerosol effects on clouds and climate from their covariability with confounding factors, ii) retrieval issues, iii) a very low signal-to-noise ratio and on the other hand computationally, due to the scale of the "big" datasets (100s of Tb) and their heterogeneity.
Such "big data" challenges are not unique to climate science but occur across a wide range of data sciences. However, innovative techniques and tools developed by the data mining and machine learning community have not yet found their way into climate sciences and climate scientists are currently not trained to capitalise on these advances.
This Marie Curie ITN will train the next generation of climate & data scientists through synergies between climate research and modern data sciences. Its innovative training plan will match students (and supervisors) from climate and data backgrounds, provide them with training in state of the art data and climate science techniques which will be applied to key uncertainties in current climate research. Partners from the data-science and space industry will be closely involved in the projects and provide real-world training opportunities in a commercial context. This will produce a new generation of climate and data scientists, ideally trained for employment in science or commercial data applications.

Mittelgeber: Europäische Union, Horizon 2020, Marie Curie Innovative Training Network

---

Advancing the Science for Aviation and ClimAte (ACACIA)

Schlagworte: Einfluss von Flugverkehr auf Klima, Aerosol – Wolken – Wechselwirkungen, Kondensstreifen

Projektleiter:
Koordinator: Robert Sausen, Deutsches Zentrum für Luft- und Raumfahrt, Institut für Physik der Atmosphäre (Robert.Sausen@dlr.de)
J. Quaas (johannes.quaas@uni-leipzig.de)

Projektmitarbeiterin: Sajedeh Marjani (sajedeh.marjani@uni-leipzig.de)

Projektbeginn: 1.1.2020
Projektende: 31.12.2022

Beschreibung
Non-CO2 emissions of aviation may impact climate as much as aviation's carbon dioxide (CO2) emissions do. However, the impact the non-CO2 effects (e.g., ozone and methane from NOx emissions, contrails, indirect aerosol effects) is associated with much larger uncertainties, some of these effects might result in a relatively large cooling. ACACIA has four aims for scientifically based and internationally harmonised policies and regulations for a more climate-friendly aviation system. (1) We will improve scientific understanding of those impacts that have the largest

uncertainty, in particular, the indirect effect of aviation soot and aerosol on clouds. (2) We will identify needs for international measurement campaigns to constrain our numerical models and theories with data and we will formulate several design options for such campaigns. (3) Putting all aviation effects on a common scale will allow providing an updated climate impact assessment. Uncertainties will be treated in a transparent way, such that trade-offs between different mitigation strategies can be evaluated explicitly. This helps our final aim (4) to provide the knowledge basis and strategic guidance for future implementation of mitigation options, giving robust recommendations for no-regret strategies for achieving reduced climate impact of aviation. To this end, ACACIA brings together research across scales (from plume to global scale), from the laboratory experiments to global models, and it proceeds from fundamental physics and chemistry to the provision of recommendations for policy, regulatory bodies, and other stakeholders in the aviation business. Additionally, ACACIA will cooperate with international partners, both research institutions and organisations.

Mittelgeber: Europäische Union, Horizon2020

Modellierung von Aerosolen und Aerosol-Wolken-Wechselwirkungen in der Arktis (D02)
Modelling aerosols and aerosol-cloud interactions in the Arctic (D02)

Schlagworte: Arktischer Klimawandel, Aerosol-Wolken-Wechselwirkungen, Modellierung

Projektleiter: Johannes Quaas, Universität Leipzig (johannes.quaas@uni-leipzig.de)

Projektmitarbeiterin: Iris Papakonstantinou-Presvelou (i.presvelou@uni-leipzig.de)

Projektbeginn: 1.1.2016
Projektende: 31.12.2023

Beschreibung
In diesem Beitrag zum SFB/Transregio $(AC)^3$ soll mit Hilfe von globaler Modellierung in Kombination mit verschiedenen Beobachtungen der Einfluss anthropogener Aerosole auf den arktischen Klimawandel untersucht werden. In Kooperation mit dem Leibniz-Institut für Troposphärenforschung liegt hierbei der Schwerpunkt auf dem Meridionaltransport der Aerosole (TROPOS) und der Wechselwirkung von Aerosol mit Wolken (LIM).

Mittelgeber: Deutsche Forschungsgemeinschaft (DFG) TRR 172 $(AC)^3$

Arktische Rückkopplungsprozesse in Klimamodellen (E01)
Assessment of Arctic feedback processes in climate models (E01)

Schlagworte: Arktischer Klimawandel, Feedbacks, Modellierung

Projektleiter: Johannes Quaas, Universität Leipzig (johannes.quaas@uni-leipzig.de)

Projektmitarbeiterin: Olivia Linke (olivia.linke@uni-leipzig.de)

Projektbeginn: 1.1.2016
Projektende: 31.12.2023

Beschreibung
In diesem Beitrag zum SFB/Transregio $(AC)^3$ sollen mit Hilfe von globaler Modellierung in Kombination mit verschiedenen Beobachtungen die verschiedenen Klima-Feedback-Mechanismen quantifiziert und in den Klimamodellen evaluiert werden. Spezielles Augenmerk ist hierbei in Kooperation mit der Uni Köln auf dem Wolken-Feedback.

Mittelgeber: Deutsche Forschungsgemeinschaft (DFG) TRR 172 $(AC)^3$

Atmosphären-Modelldaten: Datenqualität, Kurationskriterien und DOI-Branding
Atmospheric model data: data quality, curation criteria, and doi-branding

Projektleiter: Prof. Dr. Johannes Quaas (johannes.quaas@uni-leipzig.de)

Projektmitarbeiter: Dr. Jan Kretzschmar (jan.kretzschmar@uni-leipzig.de)

Projektbeginn: 1.6.2019
Projektende: 31.05.2022

Beschreibung
Der Austausch und die Interpretation von Klimamodelldaten sind weit über die Klimaforschungsgemeinschaft hinaus von Bedeutung, werden jedoch aktuell durch das Fehlen übergreifender qualitätssichernder Maßnahmen und abgestimmter Kurationskriterien erschwert. In der Meteorologie und Klimaforschung bereits etablierte Datenqualitäts- und Datenkurationsstandards zur Gewährleistung effektiver Teil- und Nachnutzbarkeit der Forschungsdaten finden primär in großen, international koordinierten Modellvergleichsstudien (MIPs, z.B. Coupled Model Intercomparison Project - CMIP) ihre Anwendung. In diesem Vorhaben werden diese auf CMIP fußenden Standards und Konventionen im Austausch mit den Fachcommunities systematisch in weiteren Bereichen der Meteorologie und Klimaforschung angepasst: Zum einen an die Bedürfnisse kleinerer MIPs, für die eine volle CMIP-Adaptierung nicht sinnvoll erscheint und zu aufwändig ist. Zum anderen in der Stadtklimaforschung mit ihren sehr hochauflösenden Daten, einem Forschungsbereich ohne etablierten Datenstandard. Die Ergebnisse werden in der Praxis auf existierende Atmosphärenmodelldaten angewendet (Datenaufbereitung sowie Langzeitarchivierung) und auf ihre universelle Nutzbarkeit hin evaluiert. Die Ergebnisse etablieren zudem auf weitere Bereiche der Klimaforschung anwendbare Blaupausen für Kurationskriterien und Standardisierungen, die eine Reproduzierbarkeit und Prüfbarkeit signifikant erhöhen und darüber hinaus eine interdisziplinäre Nachnutzung von Klimamodelldaten unterstützen. Darüber hinaus wird, um Nachnutzern die Auswahl von Forschungsdaten zu erleichtern, zum einen eine fachspezifische Erweiterung des DataCite Metadatenschemas vorgenommen. Eine zwingend mit einem DOI-Branding verbundene, für Nutzer deutlich sichtbare, anspruchsvollere Qualitätsprüfung für disziplinspezifische Daten und Kurationsprozesse stärkt die Wertigkeit der DataCite DOIs und erhöht das Vertrauen bei der Nachnutzung. Zum anderen wird im Sinne der FAIR-Prinzipien ein maschinenlesbares Fachvokabular auf Basis von DCAT (W3C Data

Catalog Vocabulary) bereitgestellt. Eine nachhaltige Anwendung des universellen Datenstandards, der Prozesse zur Kuratierung und Qualitätssicherung sowie auch die Vergabe fachspezifischer DataCite DOI's werden durch die Angebote der beiden beteiligten Infrastrukturdienstleister dauerhaft gesichert und die Etablierung über den Bereich der Meteorologie und Klimaforschung hinaus ermöglicht. Die Verbindung von national und international stark vernetzten Partnern aus der Klimaforschung (Universität Hamburg, Universität Leipzig) mit einem Infrastrukturbetreiber aus der Klimaforschung (DKRZ) sowie der Zentralen Fachbibliothek für Technik und Naturwissenschaften (TIB) im AtMoDat-Konsortium bürgt für eine hochwertige, alle Aspekte dieses Vorhabens abdeckende Kompetenz und eine weitreichende, nachhaltige Aufnahme der Ergebnisse in diesem Forschungsgebiet. AtMoDat ist darüber hinaus fachübergreifend Impulsgeber für Verbesserungen im Forschungsdatenmanagement.

Mittelgeber: BMBF Bundesministerium für Bildung und Forschung, 16QK02B

Besser bestimmes Aerosolforcing für verbesserte Klimaprojektionen (FORCES)
Constrained aerosol forcing for improved climate projections (FORCES)

Projektleiter: Prof. Dr. Johannes Quaas (johannes.quaas@uni-leipzig.de)

Projektmitarbeiter: Dr. Dipu Sudhakar (dipu.sudhakar@uni-leipzig.de)
Enrico Metzner (enrico.metzner@uni-leipzig.de)
Iris Papakonstantinou-Presvelou (iris.presvelou@uni-leipzig.de)

Projektbeginn: 1.10.2019
Projektende: 28.02.2024

Beschreibung
FORCES strebt eine bessere Quantifikation des Klimaantriebs durch Aerosole an, mit dem Ziel, Klimavorhersagen zu verbessern.

Description
FORCES aims at constraining the aerosol-climate forcing in order to improve climate projections.

Mittelgeber: Europäische Union

Besser bestimmte Unsicherheit für multi-dekadische Klimavorhersagen (CONSTRAIN)
Constraining uncertainty of multi decadal climate projections (CONSTRAIN)

Projektleiter: Prof. Dr. Johannes Quaas (johannes.quaas@uni-leipzig.de)
Projektmitarbeiterin: Dr. Karoline Block (karoline.block@uni-leipzig.de)
Olivia Linke (olivia.linke@uni-leipzig.de)

Projektbeginn: 1.6.2019
Projektende: 30.05.2023

Beschreibung
Verschiedene unsichere Aspekte in multi-dekadischen Klimavorhersagen werden in CONSTRAIN besser bestimmt, darunter effektiver Strahlungsantrieb und transiente Klimasensitivität.

Description
Several uncertain aspects for multi-decadal climate projections will be constrained in CONSTRAIN, among which the effective radiative forcing and transient climate sensitivity.

Mittelgeber: Europäische Union

FOR 2820 Teilprojekt: Einfluss von Vulkanen auf Wolken (VolCloud)
FOR 2820 Teilprojekt: Cloud response to Volcanic eruptions (VolCloud)

Projektleiter: Prof. Dr. Johannes Quaas (johannes.quaas@uni-leipzig.de)
Projektmitarbeiterin: Mahnoosh Haghighatnasab (mahnoosh.haghighatnasab@uni-leipzig.de)

Projektbeginn: 1.3.2019
Projektende: 30.11.2022 (verlängert bis 30.11. 2022)

Beschreibung
Wolken spielen eine Schlüsselrolle für die Energiebilanz der Erde. Sie reagieren auf Änderungen in Aerosolen auf verschiedene Weise, und diese Reaktionen sind jeweils einerseits mit großen Unsicherheiten behaftet und andererseits potentiell sehr relevant in ihrer Auswirkung auf Energiebilanz und Klima. (i) Flüssigwasserwolken werden von Aerosol, das als Wolkenkondensationskeim (CCN) dient, verändert. Die Tröpfchenkonzentration wird vergrößert, und dies hat Veränderungen von mikrophysikalischen Wolken- und Niederschlagsprozessen einerseits, und Wolkendynamik (etwa das Einmischen von trockener Umgebungsluft) andererseits zur Folge. Hierbei ist es vor allem wichtig, die Änderung von Bedeckungsgrad und Flüssigwasserweg der Wolken zu quantifizieren. (ii) Eis- und Mischphasenwolken werden, je nach Eisbildungsmechanismus, durch CCN, aber auch Eiskeime verändert. Veränderungen der komplexen Wolken- und Niederschlagsprozesse sind die Folge. (iii) Die Störung der Energiebilanz bedeutet Änderungen in thermodynamischen Profilen und Zirkulation durch schnelle Anpassungen, auf die Wolken wiederum reagieren. Es ist die Summe aus den ursprünglichen Wolkenänderungen und diesen Anpassungen, aus denen sich die effektive Änderung der Strahlungsbilanz zusammensetzt. (iv) Wird hochreichende Konvektion beeinflusst, können Gewitter sich intensivieren, und der Transport zwischen Troposphäre und Stratosphäre kann verändert werden. Dies hat möglicherweise bedeutende Auswirkungen auf die Zirkulation und das Klima. Diese Fragestellungen sind besonders im Kontext von Vulkanausbrüchen relevant: (a) ein Vulkanausbruch bedeutet eine vergleichsweise gut definierte und gegebenenfalls bedeutende Störung des atmosphärischen Aerosols, aus exogener Quelle. Die Beobachtung der Wolkenreaktion auf einen Vulkanausbruch ist daher eine einzigartige Gelegenheit, um Aerosol-Wolken-Niederschlags- Wechselwirkungen zu untersuchen. (b) Die Reaktion der Wolken beeinflusst die Auswirkung des Vulkanausbruchs auf die Strahlung. Es ist daher essentiell, die Wolkenreaktion angemessen zu quantifizeren, um die Klimawirkung zu beurteilen. VolCloud geht diese Fragen und Herausforderungen an, indem drei verschiedene Typen von Vulkanausbrüchen in der Vergangenheit untersucht werden (eine massive Änderung des troposphärischen Sulfats durch den Holuhraun; eine Eruption, die auch Eiskeime emittiert hat, von Eyjafjallajökull; sowie die größte

von Satelliten beobachtete Eruption, Mt. Pinatubo). Hierbei werden Modellsimulationen mit detaillierter Darstellung von Wolken und Aerosol mit Wolkensystem-auflösender Diskretisierung (ICON-NWP-ART, 2 km Auflösung) in Kombination mit Satellitebeobachtung aus passiver und – soweit verfügbar – aktiver Fernerkundung. VolCloud arbeitet eng mit den anderen VolImpact-Projekten zusammen, wobei insbesondere die Möglichkeiten der höheraufgelösten, aber beschränkteren Simulationen einerseits und der gröber aufgelösten, aber globalen Simulationen einerseits ausgewertet werden.

Description
Clouds are a key modulator of the Earth energy budget. They respond to perturbations in aerosol in various ways, and all these pathways are uncertain yet of potentially very large importance when assessing the impact of the aerosol perturbation on the Earth energy budget and on climate. (i) Liquid-water clouds respond to the perturbation in aerosols serving as cloud condensation nuclei (CCN). Cloud droplet number concentration is perturbed, and this entails perturbations to cloud- and precipitation microphysical processes, but also to cloud dynamics responses (e.g. altered entrainment rates of dry air into the clouds). The most relevant question is how cloud fraction and cloud liquid water paths respond to this perturbation. (ii) Ice- and mixed- phase clouds respond to both CCN and ice nucleating particle concentration changes, depending on the ice formation mechanism. Modifications of intricate cloud and precipitation processes follow. (iii) The change in the energy budget leads to alterations in thermodynamic profiles and in atmospheric circulation via rapid adjustments, and clouds respond to these as well. It is the sum of the initial cloud perturbation and these adjustments that composes the effective perturbation of the Earth energy budget. (iv) When deep convective clouds are altered, thunderstorms may become more intense, and transport from the troposphere into the stratosphere may be altered, with strong consequences for circulation and climate. These questions are particularly relevant when considered in the context of volcanic eruptions for two reasons: (a) the volcanic eruption is a relatively well-defined and occasionally strong perturbation to the atmospheric aerosol concentration that is exogenous to the atmosphere system. The observation of the cloud response to volcanic eruption thus is a unique opportunity to study the aerosol- cloud-precipitation interactions. (b) the cloud response may strongly modulate, and likely enhance, the radiative impact of a volcanic eruption. It is thus crucial to adequately quantify the cloud response, in order to assess the climate response. VolCloud will address these questions and challenges by investigating three different types of past volcanic eruptions (a massive sulfur perturbation to the troposphere, Holuhraun; an eruptive perturbation that also emitted INP, Eyjafjallajökull; and the largest eruption in the satellite era, Mt. Pinatubo) using model simulations with a detailed cloud and aerosol representation, resolving cloud systems (ICON-NWP-ART at 2 km resolution), in combination with satellite observations from passive and – where available – active remote sensing. VolCloud intensely collaborates with the other projects within VolImpact, reaching out to what can be learned from simulations at finer but in extent more limited, and coarser but global scale.

Mittelgeber: DFG Deutsche Forschungsgemeinschaft ,QU 311/23-1

Klimamodell-PArametrisierungen – Revision mit Hilfe von RAdar (PARA)
Climate model PArameterizations informed by RAdar (PARA)

Projektleiter: Prof. Dr. Johannes Quaas (johannes.quaas@uni-leipzig.de)

Projektmitarbeiterin: Sabine Hörnig (sabine.hoernig@uni-leipzig.de)

Projektbeginn: 1.1.2019
Projektende: 30.06.2022

Beschreibung
Die adäquate Darstellung diabatischer Wolken- und Niederschlagsprozesse ist eine besondere Herausforderung für Klimamodelle, da diese räumlich nicht aufgelösten Prozesse mittels subskaliger Parameterisierungen repräsentiert werden. Diese müssten mit Hilfe von Beobachtungen und/oder prozessauflösenden Simulationen erstellt und evaluiert werden. Radarpolarimetrie liefert die am Besten geeingeten Beobachtungen für die Wolken- und Niederschlagsmikrophysik dank der Ableitung mikrophysikalischer Zustandsgrößen und der Prozesserkennung. In der ersten Phase von PROM wird das Projekt PARA die räumliche Heterogenität des Eiswassergehalts sowie die Niederschlagsbildung über de Eisphase betrachten; in der zweiten Phase wird die Betrachtung von Mischphasenprozessen wie Bereifung, und die Rolle der Variabilität der Partikelanzahlkonzentration hinzukommen. PARA betrachtet dabei mit Hilfe von polarimetrischen Radarbeobachtungen und der Evaluierung und Revision der Parametrisierungen im ICON-Klimamodell die vier Prozesse, die für die Bestimmung von aus der Eisphase gebildeten Niederschlag am Boden relevant sind: (i) die Eisbildung und die räumliche Heterogenität des Eiswassergehalts auf bezüglich des ICON-GCM subskaligen Dimensionen, (ii) die Rolle dieser Variabilität für die Schneebildung durch den Aggregationsprozess, (iii) das Schmelzen von Schnee bei Temperaturen über 0°C, und (iv) die Verdunstung von Regen unterhalb der Schmelzschicht.

Description
An adequate representation of moist diabatic processes in clouds and precipitation in climate models is challenging, because these spatially unresolved processes are subject to sub-grid parameterizations, which must be informed by observations and/or models resolving these processes. Radar polarimetry provides most suitable observations on cloud and precipitation microphysics via microphysical retrievals and process fingerprints. PARA will focus in Phase I of PROM on ice water content heterogeneity and precipitation generation via the ice phase and concentrate on mixed-phase processes including riming and the role of particle number concentration variability in Phase II. PARA will investigate four processes both by polarimetric radar retrievals and the evaluation and revision of their representation in the ICON general circulation model: (i) ice generation and spatial heteorogeneity of ice water content at ICON-GCM sub-grid scales, (ii) the role of both in snow formation like aggregation, (iii) melting of snow falling through the 0°C isotherm, and (iv) evaporation of rain below the melting layer.

Mittelgeber: DFG Deutsche Forschungsgemeinschaft, QU 311/21-1

Wolkentröpfchenanzahlkonzentration aus mit Atmosphärenmodellierung verbesserten Satellitenbeobachtungen für die Analyse von Aerosol-Wolken-Wechselwirkungen (CDNC4aci)
Cloud Droplet Number Concentration – satellite retrievals Advanced by Atmospheric models for Assessing Aerosol-Cloud Interactions (CDNC4aci)

Projektleiter: Prof. Dr. Johannes Quaas (johannes.quaas@uni-leipzig.de)

Projektmitarbeiter: Dr. Tom Goren (tom.goren@uni-leipzig.de)

Projektbeginn: 1.4.2021
Projektende: 31.3.2024

Beschreibung
Die Wechselwirkungen zwischen Aerosolen und Wolken führen zu einem effektiven Strahlungsantrieb, der eine wesentliche Unsicherheit beim Verständnis und Interpretation des beobachteten Klimawandels darstellt. Es werden globale Daten benötigt, um die relevanten Prozesse besser zu quantifizieren, aber eine Schlüsselgröße - die Konzentration der Wolkentröpfchenzahl (CDNC, Nd) - ist in operationellen Produkten nicht verfügbar. Aufbauend auf Vorarbeiten wird CDNC4aci in enger Wechselwirkung zwischen Beobachtungen und Modellen auf zuverlässige Nd-Werte von Satelliten hinarbeiten: Neu verfügbare wolkenauflösende Simulationen ermöglichen die Entwicklung und Verfeinerung der Retrievals. Diese Daten werden umgekehrt dazu verwendet, das Verständnis und die Quantifizierung der Aerosol-Wolken-Wechselwirkungen im Modell und bei der statistischen Analyse zu verbessern. Konkret wird das Projekt multi-angulare und polarimetrische Beobachtungen für bessere Nd-Daten einbeziehen, es wird die Retrievalansätze unter Verwendung einer modellgestützten vertikalen Wolkenschichtung in Abhängigkeit vom Wolkenregime überarbeiten. Das Projekt wird die Informationen über Wolkenprozesse in den Daten mit Hilfe von Modellsensitivitätsanalysen untersuchen, es wird Modell und Daten durch Vorwärtssimulationen vergleichbar machen und die Aerosol-Wolken-Wechselwirkungen in einem globalen Modell, das unter Verwendung der Daten und des Prozessverständnisses verbessert wird, analysieren. Das Ziel ist eine konsistente Quantifizierung des Aerosol-Wolken-Antriebs zwischen Modell und Datenanalyse.

Description
Aerosol-cloud interactions imply an effective radiative forcing that is a key uncertainty when understanding and interpreting observed climate change. Global data are needed to better quantify the relevant processes, but a key quantity – the cloud droplet number concentration (CDNC, Nd) - is not available from operational products. Building on preliminary work, CDNC4aci will work towards reliable retrievals of Nd from satellites in close observations – model interaction: newly-available cloud-resolving simulations will inform the retrieval development and refinement, and the data, in turn, will be used to improve understanding and quantification of aerosol-cloud interactions in the model and from statistical analysis. Specifically, the project will include multi-angle and polarimetric observations for better Nd data, it will revise retrieval approaches using model-informed cloud vertical stratification conditioned on cloud regime and thoroughly quantify and correct retrieval errors and biases and assess aerosol-cloud interaction processes from data. The project will assess the cloud-process information in the retrieved data using model sensitivity analyses, it will make model and data comparable by forward-simulating measured polarized radiances and retrieval products, and assess aerosol-cloud interactions in a global model evaluated using the data and the process understanding in model-data assessment. The final goal is a consistent quantification of the aerosol-cloud forcing between model and data analysis.

Mittelgeber: DFG Deutsche Forschungsgemeinschaft, QU 311/27-1

Wolkenänderungen durch die Umkehr des Aerosoltrends über China: Beobachtungsdaten – Modell Synergie von regionaler zu großer Skala (Cloudtrend)
Cloudiness change with aerosol trend reversal over China: data-model synergy from regional to large scale (Cloudtrend)

Projektleiter: Prof. Dr. Johannes Quaas (johannes.quaas@uni-leipzig.de)

Projektmitarbeiterin: Dr. Hailing Jia (hailing.jia@uni-leipzig.de)

Projektbeginn: 1.4.2021
Projektende: 31.3.2024

Beschreibung
Die Reaktion von Wolken auf anthropogene Änderungen der Atmosphärenzusammensetzung stellt eine große Unsicherheit bei der Quantifizierung des globalen Klimawandels dar. Ein sehr wichtiger Aspekt dabei ist die Änderung von Wolken durch Aerosolemissionen. In Bezug auf diese Aerosol-Wolken-Wechselwirkungen hat sich in neuen Studien herausgestellt, dass die wesentliche Unbekannte die Änderung der horizontalen Wolkenausdehnung (Bedeckungsgrad) in Anpassung an Wolkentröpfchenkonzentrationsänderungen ist. Cloudtrend wird das Verständnis und die Quantifizierung dieses Problems substantiell verbessern, indem es auf drei Schlüsselideen aufbaut: (i) die stark ansteigenden und dann abnehmenden anthropogenen Aerosolemissionen über China im 21. Jahrhundert bieten eine einzigartige Gelegenheit für die Detection und Attribution von aerosolabhängigen Wolkenänderungen in Beobachtungsdaten, die für diese Periode in hoher Qualität vom Boden und von Satelliten zur Verfügung stehen; (ii) neue Modellier- und Datenanalysewerkzeuge stehen zur Verfügung, einschließlich verbesserter Satellitendaten für Wolkenmikrophysik und Wolkenregimedefinitionen, sowie die CMIP6 Multi-Modell-Daten; und (iii) die Datenanalyse und Klimamodellierung auf großer Skala kann dank neuer Ansätze aus maschinellem Lernen systematisch von den hochaufgelösten regionalen Daten und Modellen lernen. Das Projekt wird durch die Synergie in der Expertise an der Nanjing University of Information Science and Technology (Schwerpunkt auf den regionalen Referenzdaten und -modellen) und der Universität Leipzig (Schwerpunkt auf der großen Skala) möglich gemacht.

Description
The response of clouds to anthropogenic changes in atmospheric composition constitutes a large uncertainty when quantifying the effective forcing of global climate change. One key element is the response of clouds to aerosol emissions. In these aerosol-cloud interactions, it emerges currently as the key question how cloud horizontal extent, or cloud fraction, changes in adjustment to cloud droplet number concentration changes. Cloudtrend will substantially improve the understanding and quantification for this problem by building on three key ideas: (i) the very strong increasing then decreasing trends in anthropogenic aerosol emissions over China in the 21st Century provide a unique opportunity for a detection and attribution of aerosol-induced cloudiness changes in the high-quality data available from the surface and from satellites; (ii) new modelling and data analysis tools are available, including better satellite retrievals of cloud microphysics and new regime definitions, as well as the new CMIP6 multi-model data; and (iii) the large-scale data analysis and global climate modelling is proposed to systematically learn from the regional, high-quality data and modelling. The project is possible thanks to the synergy between the expertise in the teams at the Nanjing University of Information Science and Technology (regional focus) and the University of Leipzig (large-scale focus).

Mittelgeber: DFG Deutsche Forschungsgemeinschaft, QU 311/28-1

Wechselwirkung zwischen meridionalen Ozean-Wärmetransporten und regionalen Prozessen im Arktischen Ozean (D04)
Interaction of meridional ocean heat transports and regional processes in the Arctic Ocean (D04)

Projektleiter: Prof. Dr. Rüdiger Gerdes, Alfred-Wegener-Institut, Helmholtz-Zentrum für Polar- und Meeresforschung, Prof Dr. Torsten Kanzow, Alfred-Wegener-Institut, Helmholtz-Zentrum für Polar- und Meeresforschung, Dr. Marc Salzmann (marc.salzmann@uni-leipzig.de)

Projektmitarbeiter: Enrico Paul Metzner (enrico.metzner@uni-leipzig.de), Finn Heukamp, Alfred-Wegener-Institut, Helmholtz-Zentrum für Polar- und Meeresforschung

Projektbeginn: 1.1.2020
Projektende: 31.12.2023

Beschreibung
In diesem Teilprojekt sollen die ozeanischen Prozesse besser verstanden werden, welche die Reaktion des arktischen Klimasystems (insbesondere Wärmeflüsse zwischen Ozean und Atmosphäre) auf die Erwärmung der Atmosphäre aufgrund von Treibhausgasen ausmachen. Hierfür sollen regionale und globale Modelle genutzt sowie existierende Ergebnisse von globalen Klimamodellen analysiert werden. Ein Fokus wird auf der Barentssee liegen, wo starke Oberflächen-Wärmeflüsse den Export von Wasser und Meereis an der Meeresoberfläche fördern. Dieser Export wird durch das entsprechende Einströmen atlantischen Wassers kompensiert, welches den positiven Rückkopplungskreislauf schließt. Diese Prozesse können aufgrund ihres Einflusses auf die Schichtung des Ozeans und der Entstehung Wassers hoher Dichte zur weiteren Erwärmung der Arktis beitragen.

Description
This project investigates the oceanic processes which shape the response of the arctic climate system (especially ocean-atmosphere heat fluxes) to greenhouse gas warming using regional and global climate models and analyzing existing model results. A focus will be on the Barents Sea, where strong surface heat fluxes promote the export of water and sea ice at the surface. This export is compensated by inflow of Atlantic water, closing a positive feedback loop. Due to their influence on the ocean stratification and the formation of high density waters these processes can contribute to increased Arctic warming.

Mittelgeber: DFG Projekt Nummer 423239633

Junior-Professorin Dr. Heike Kalesse-Los

Fernerkundung; Heike Kalesse-Los
AG Fernerkundung der Atmosphäre und das Arktische Klimasystem

Bodengebundene Fernerkundung der Atmosphäre zur Verbesserung der Charakterisierung mikrophysikalischer Wolkeneigenschaften sowie der Leistungsprognose erneuerbarer Energien
Ground-based remote sensing of the atmosphere for improving the characterization of microphysical cloud properties and for improving the load prediction of renewable energies

Schlagworte: bodengebundene Fernerkundung, erneuerbare Energien, Wolkenretrieval, DACAPO-PESO, EUREC4A

Projektleiter: H. Kalesse-Los (heike.kalesse@uni-leipzig.de), A. Ehrlich (a.ehrlich@uni-leipzig.de), M. Schäfer (michael.schaefer@uni-leipzig.de), M. Wendisch (m.wendisch@uni-leipzig.de)

Projektmitarbeiter: AP1: M. Lochmann (moritz.lochmann@uni-leipzig.de), AP2: W. Schimmel (willi.schimmel@uni-leipzig.de), AP3: Johannes Stapf (johannes.stapf@uni-leipzig.de) und Teresa Vogl (teresa.vogl@uni-leipzig.de)

Projektbeginn: 1.9.2018
Projektende: 28.2.2022

Beschreibung
Die bodengebundene Fernerkundung der Atmosphäre dient sowohl der Grundlagenforschung von Wolken und Niederschlag, als auch im operationellen Dienst der Wettervorhersage als ein wichtiger Baustein für die Leistungsprognose erneuerbarer Energien. Innerhalb dieses Projekts gibt es zwei Hauptzielstellungen: Zum einen wird analysiert werden, wie künstliche neuronale Netze (KNN) zur Leistungsprognose von Photovoltaik- und Windkraftanlagen optimiert werden können, wenn zusätzliche Daten von Wetterstationen und bodengebundenen Fernerkundungsmessungen implementiert werden. Zum anderen sollen in zwei weiteren Teilprojekten für Wolkenbeobachtungen Ableitungsalgorithmen (Retrievals) weiterentwickelt werden, um die Bestimmung von Wolkeneigenschaften zu verbessern und zu erweitern. Dabei stehen Messgerätesynergien zur Ableitung der Wolkentröpfchenkonzentration sowie die Entwicklung anwendungsspezifischer KNN zur Charakterisierung der Verteilung von Flüssigwasser in Mischphasenwolken im Vordergrund.

Das Projekt ist in drei Arbeitspakete unterteilt:
AP1: Test des Einflusses zusätzlicher Messdaten von Wetterstationen und aus der bodengebundenen Fernerkundung auf die Leistungsprognose von PV- und Windkraft-Anlagen mittels künstlicher Neuronaler Netze (KNN)

AP2: Entwicklung eines auf Wolkenradar- und Lidar basierendem KNN zur Detektion von Flüssigwasser in Wolken

AP3: Entwicklung einer auf synergistischen Fernerkundungsmessungen basierenden Methode zur Ableitung der Wolkentröpfchenkonzentration

Description
Ground-based remote sensing of the atmosphere serves both, the basic research of clouds and precipitation, and in the operational service of weather forecasting as an important building block for the power prognosis of renewable energies. Within this project there are two main objectives: Firstly, it will be analysed how artificial neural networks (ANN) can be optimized for power forecasting of Photovoltaics (PV) and wind turbines, if additional data from weather stations and

ground-based remote sensing measurements are implemented. On the other hand, in two further subprojects for cloud observations, retrieval algorithms will be developed to improve and extend the determination of cloud properties. The focus will be on instrument synergies for the derivation of cloud droplet concentrations and the development of application-specific ANN for the characterization of the distribution of liquid water in mixed-phase clouds.

The project is divided into three work packages:
AP1: Testing the influence of additional measurement data from weather stations and ground-based remote sensing on the power prognosis of PV and wind power plants using artificial neural networks (ANN)
AP2: Development of a cloud radar and lidar based ANN for detection of liquid water in clouds
AP3: Development of a cloud droplet concentration retrieval based on synergistic remote sensing observations

Mittelgeber: ESF - Sächsische Aufbaubank (SAB), Antragsnummer: 100339509

PICNICC - Durch CCN und INP beeinflusste Polarimetrie in Zypern und Chile – Abschätzung von hemisphärischen Kontrasten in radarpolarimetrischen Größen und deren Beziehung zu Unterschieden in der Aerosolbelastung
Polarimetry Influenced by CCN aNd INP in Cyprus and Chile (PICNICC):
An assessment of hemispheric cloud polarimetric contrasts and its relation to differences in aerosol load

Schlagworte: Radarpolarimetrie, DACAPO-PESO, Wolkenmikrophysik, Aerosol-Wolken-Wechselwirkung

Projektleiter: H. Kalesse-Los (heike.kalesse@uni-leipzig.de)
Dr. P. Seifert, Leibniz Institut für Troposphärenforschung (TROPOS)

Projektmitarbeiter: Prof. J. Quaas (johannes.quaas@uni-leipzig.de)
Teresa Vogl (teresa.vogl@uni-leipzig.de), A. Teissiere (TROPOS)

Projektbeginn: 1.11.2018
Projektende: 31.12.2023

Beschreibung
Das Verständnis von mikrophysikalischen Wachstumsprozessen in Mischphasenwolken wie Aggregation und Bereifung beruht auf einer gründlichen Charakterisierung der in der Wolke vorhandenen Flüssigphase. In dieser Studie wird eine einzigartige Messmöglichkeit mit einer erweiterten Fernerkundungsinstrumentensuite genutzt, die polarimetrische Radarbeobachtungen bei mehreren Wellenlängen auf der Nord- und Südhalbkugel beinhaltet, um die Millimeterwellenlängen-Radarpolarimetrieforschung für mikrophysikalische Prozessstudien voranzubringen. Die übergeordnete Hypothese, die in diesem Projekt untersucht wird, ist, dass Mischphasen-Wolkenprozesse anfällig für Aerosolstörungen sind. Wir postulieren, dass:
A) Die Aggregation wird bei hohen Aerosolbelastungen und damit verbundenen höheren INP (Ice Nucleating Particle)-Konzentrationen häufiger erfolgen, da höhere Eiskristallkonzentrationen die Aggregation begünstigen.

B) Bereifung von Eiskristallen wird häufiger auftreten, wenn aufgrund einer Knappheit von INP anhaltende unterkühlte Flüssigkeitsschichten auftreten.
Um diese Hypothesen anzugehen, wird die Häufigkeit des Auftretens von Aggregation und Bereifung in mehrjährigen Datensätzen charakterisiert, die bei Feldexperimenten in der Aerosol-Lasten-Atmosphäre über Limassol, Zypern und der unberührten Region Punta Arenas, Chile, erhalten wurden und werden. Die beobachtete Reaktion von Mischphasen-Wolkenprozessen auf Aerosolstörungen wird im Zusammenhang mit einer Modellsensitivitätsstudie von Simulationen mit einer wolkensystemauflösenden (1 km) Version des ICON-NWP für die gesamten Beobachtungszeiträume für regionale Bereiche um die Beobachtungsstandorte in Zypern und Chile gestellt, die von Radar-Fortsimulationen begleitet werden.

Description
Understanding mixed-phase cloud processes such as aggregation and riming relies on a thorough characterization of the liquid phase present in the cloud. For this study we propose to use a unique measurement opportunity with an extended remote-sensing instrument suite including triple-frequency polarimetric radar observations on the Northern and Southern hemisphere to bring forward millimeter wavelength radar polarimetry research for microphysical process studies. The overarching hypothesis that we would like to study within this project is that mixed-phase cloud processes are susceptible to aerosol perturbations. We postulate that
A) Aggregation will be more frequent for high aerosol loads and associated higher ice nucleating particle (INP) concentrations because higher ice crystal concentrations favor aggregation.
B) Riming will be more frequent where sustained supercooled liquid layers occur due to a scarcity of INP.
To address these hypotheses, we will characterize the frequency of occurrence of aggregation and riming in multi-year datasets obtained during institutional-funded field experiments in the aerosol-burden atmosphere above Limassol, Cyprus and the pristine region of Punta Arenas, Chile. For that purpose, we will make slanted linear depolarization (SLDR) polarimetric observations with a Ka-band radar a versatile technique for classification of hydrometeors in mixed-phase clouds.
The observed response of mixed-phase cloud processes to aerosol perturbations will be put in context to a model sensitivity study of simulations with a cloud-system-resolving (1 km) version of the ICON-NWP for the entire observation periods for regional domains around the observations sites in Cyprus and Chile that are accompanied by radar forward simulations.

Mittelgeber: DFG KA 4162/2-1

Einfluss von Wasserrinnen im Meereis und Polynyas auf arktische Wolkeneigenschaften – B07
(Influence of sea ice leads or polynyas on Arctic cloud properties – B07)

Schlagworte: Arktische Verstärkung, Arktische Wolken, bodengebundene Fernerkundung von Wolken

Projektleiter: H. Kalesse-Los (heike.kalesse@uni-leipzig.de)

Projektmitarbeiter: Pablo Saavedra-Garfias (pablo.saavedra@uni-leipzig.de)

Projektbeginn: 01.01.2020
Projektende: 31.12.2023

Beschreibung
Die winterliche Meereisbedeckung ist charakterisiert durch verschiedenste Brüche unterschiedlichsten Levels. Wasserrinnen und Polynyas führen zu erheblichen Wärme- und Feuchteflüssen vom relativ warmen Ozean zur kalten Atmosphäre. Damit beeinflussen sie die Struktur der atmosphärischen Grenzschicht, Wolkenbedeckung und das Energiebudget an der Oberfläche und ebenfalls den chemischen Austausch zwischen Atmosphäre und Ozean. Um den Einfluss von Meereisrinnen und Polynyas auf Wolken zu quantifizieren, werden mikro- und makrophysikalische Eigenschaften von bodennahen Wolken während auflandigen Winden in Anwesenheit von Meereisrinnen oder Polynyas verglichen mit Wolken während auflandigen Wind über einer geschlossenen Eisdecke.

Description
The wintertime Arctic sea ice area is characterised by different degrees of fracturing. Leads and polynyas result in a substantial heat and moisture flux from the relatively warm ocean to the cold atmosphere. They thus alter the atmospheric boundary layer structure, cloud cover, and the surface energy budget and also affect atmosphere-ocean chemical exchanges. To quantify the influence of leads or polynyas on clouds, the micro- and macrophysical properties of surface-coupled clouds during onshore winds in the presence of leads or polynyas will be compared to clouds observed during onshore winds in closed sea-ice conditions.

Mittelgeber: Projektnummer 268020496 innerhalb von TRR 172 „Arktische Verstärkung (AC)^3“

Ein neuartiger Retrievalansatz zur Ableitung troposphärischer Temperatur- und Feuchteprofile unter allen Wetterbedingungen für eine verbesserte Quantifizierung von Verdunstungsraten

(A novel synergistic retrieval approach to enable tropospheric temperature and humidity profiling under all weather conditions for an improved quantification of evaporation rates)

Schlagworte: Instrumentensynergie, bodengebundene Fernerkundung, Niederschlag, Neuronale Netze, optimale Schätzung, Wasserdampfprofile, Temperaturprofile, Verdunstungsraten, Abkühlungsraten

Projektleiter: A. Foth (andreas.foth@uni-leipzig.de)
Projektmitarbeiter: A. Foth (andreas.foth@uni-leipzig.de)

Projektbeginn: 1.4.2020
Projektende: 31.03.2023

Beschreibung
Die ständige Weiterentwicklung und Verbesserung der Wetter- und Klimamodelle stellt die Fernerkundung der Atmosphäre vor große Herausforderungen. Für die Evaluierung der Modelle werden immer besser aufgelöste Messungen und Methoden benötigt. Herkömmliche Ansätze scheitern hier vor allem an fehlenden kontinuierlichen Beobachtungen der Temperatur und Feuchte bei allen Wetterbedingungen und insbesondere bei Regen. Ein Windprofiler ist allerdings auch bei solchen Bedingungen in der Lage Vertikalinformationen der Temperatur- und Feuchtegradienten zu messen. Der hier vorgeschlagene neuartige Ansatz aus einer Synergie aus Windprofiler (inklusive Radio Acoustic Sounding System), Ramanlidar, Mikrowellenradiometer und

Wolkenradar ermöglicht eine automatisierte und kontinuierliche Erstellung von Temperatur- und Feuchteprofilen sogar bei Niederschlägen.

Langzeitbeobachtungen an Meteorologischen Observatorium in Lindenberg werden genutzt, um aussagekräfige Statistiken über die Verdunstungs- und Abkühlungsraten zu erstellen. Die Ergebnisse werden für verschiedene Bedingungen wie stratiformen und konvektiven Niederschlag und für verschiedenen Jahreszeiten evaluiert. Dies wird den Modellieren helfen, die Parametrisierungen der Verdunstungsraten in kleinskaligen Modellen zu evaluieren.

Description
Steady improvements of weather and climate models are challengeing for remote sensing of the atmosphere. For the evaluation of the models highly resolved measurements and methods are necessary. Usual approaches fail due to the lack of continuous observation of temperature and humidity profiles during all weather conditions, especially during precipitation. A wind profiling radar enables the measurement vertical profiles of temperature and humidity gradients. The novel approach based on synergy between eind profiling radar (with Radio Acoustic Sounding System), Raman lidar, microwave radiometer, and cloud radarenables an automated and continuous observation of temperature and humidity profiles even during precipitation. The used variational approach (optimal estimation) provides a robust tool for the combination of different instruments including the uncertainties of the single systems.

Longterm observation at the meterological observatory Lindenberg will be used to estimate robust statistics about evaporation and cooling rates. The results will be evaluated for differenet conditions as stratiform or convective precipitation or for different seasons. The outcome will help modellers to evaluate the parametrizations of evaporation rates in small-scale models.

Mittelgeber: Deutsche Forschungsgemeinschaft (DFG FO 1285/2-1)

Aerosole und Wolken, Matthias Tesche
Aerosols and Clouds

Partikel in Aerosol-Wolken Wechselwirkungen: Schichtung, Konzentration und Wolkenlebenszyklus
Particles in Aerosol Cloud Interactions: stratification, CCN/INP concentrations, and Cloud lifecycle (PACIFIC)

Schlagworte: Aerosol-Wolken-Wechselwirkungen, Satellitenfernerkundung, Wolkenverfolgung, Wolken- und Eiskeime

Projektleiter: Dr. Matthias Tesche (matthias.tesche@uni-leipzig.de)

Projektmitarbeiter: Dr. Peter Bräuer, Dr. Torsten Seelig, Dr. Diego Villanueva, Fani Alexandri, Goutam Choudhury, Felix Müller

Projektbeginn: 01.01.2019
Projektende: 31.12.2022

Beschreibung
Aerosolpartikel sind von herausragender Bedeutung für die Bildung von Wolken, da sie als Wolkenkondensationskerne in Flüssigwasserwolken and als Eiskeime in eisenthaltenden Wolken wirken. Veränderungen der Aerosolkonzentration in der Atmosphäre beeinflussen die Reflektivität, die Entwicklung, die Wasserphase, die Lebenszeit und die Regenrate von Wolken. Diese Prozesse werden als Aerosol-Wolken-Wechselwirkungen bezeichnet. Obwohl ihr Einfluss auf das Klima der Erde seit Jahrzenten einen Schwerpunkt der Atmosphärenforschung bildet, ist unser derzeitiger Wissensstand, so wie er im letzten Bericht des Weltklimarates zusammengefasst wurde, dass Aerosol-Wolken-Wechselwirkungen die größte Unsicherheit zu unserem Verständnis des Klimawandels beiträgt.
PACIFIC wird unser Verständnis von Aerosol-Wolken-Wechselwirkungen durch zwei Innovationen verbessern: (1) die Charakterisierung der für diese Prozesse relevanten Aerosolpartikel und (2) die Untersuchung der zeitlichen Veränderung der Eigenschaften von Wolken im Verlauf ihres Lebenszyklus. Untersuchungen von Aerosol-Wolken-Wechselwirkungen mit Geräten auf polarumlaufenden Satelliten sind auf Wolkenbeobachtungen zu festen Zeiten beschränkt. Die für solche Studien benötigte Information der Anzahl vorhandener Wolkenkondensationskerne wird derzeit aus säulenintegrierten optischen Aerosoleigenschaften abgeschätzt. Eine ähnliche Methodik zur Abschätzung der Konzentration von Eiskeimen existiert nicht, da deren Eigenschaften von der Art und Größe der Partikel abhängen. Daher sind zur Zeit keinen Studien von Aerosol-Wolken-Wechselwirkungen auf eisenthaltende Wolken basierend auf Fernerkundungsmessungen möglich. Die quantitative Abschätzung der Bedeutung von Aerosolen in Aerosol-Wolken-Wechselwirkungen verlangt, dass Informationen über die räumliche Verteilung von Wolkenkondensationskernen und Eiskeimen vorhanden sind. Das Projekt strebt an bisher nicht erhältliche Informationen über die Konzentration von Wolkenkondensationskernen und Eiskeimen aus weltraumgetragenen Lidarmessungen zu erlangen. Dessweiteren wird die Entwicklung von Wolken vor und nach der Punktbeobachtung mir polarumlaufenden Geräten dadurch charakterisiert, dass diese Wolken in zeitlich aufgelösten Beobachtungen von geostationären Geräten verfolgt werden. Die neuartige Information wird dann zum Studium der Effekte von Wolkenkondensationskernen und Eiskeimen auf die Helligkeit, den Flüssig- und Eiswassergehalt, die Tropfen- und Eiskristallgröße, die Entwicklung, die Wasserphase und die Regenrate von Wolken in verschiedenen Wolkenregimen verwendet. Besonderes Augenmerk wird dabei auf eine umfassende Berücksichtigung der meteorologischen Rahmenbedingungen gelegt werden. Die Ergebnisse von PACIFIC sind von Bedeutung für die Untersuchung und Verbesserung des Verhaltens von Klimamodellen.

Description:
Atmospheric aerosol particles are of great importance for cloud formation in the atmosphere because they are needed to act as cloud condensation nuclei (CCN) in liquid-water clouds and as ice nucleating particles (INP) in ice-containing clouds. Changes in aerosol concentration affect the albedo, development, phase, lifetime and rain rate of clouds. These aerosol-cloud interactions (ACI) and the resulting climate effects have been in the focus of atmospheric research for several decades. Nevertheless, the IPCC still concludes that ACI cause the largest uncertainty in assessing climate change as they are understood only with medium confidence.
PACIFIC will improve our understanding of ACI by enhancing the representation of the aerosols relevant for cloud processes and by quantifying temporal changes in cloud properties throughout

the cloud life cycle. ACI studies using polar-orbiting sensors are limited to snap-shot observations of clouds. CCN concentrations for assessing ACI are currently estimated from column- integrated optical aerosol parameters. There is no such proxy of INP concentrations for remote-sensing studies of aerosol effects on cold clouds as INP activity depends on aerosol type and size. Quantifying the role of aerosols in ACI requires knowledge of the spatial and vertical distribution of CCN and INP. The project aims to obtain unprecedented insight in CCN and INP concentrations from spaceborne lidar data. In addition, the development of clouds before and after the snap-shot view of polar-orbiting sensors is characterised by tracking those clouds in time-resolved geostationary observations. This novel information will be used to study the effects of CCN and INP on the albedo, liquid and ice water content, droplet and crystal size, development, phase and rain rate of clouds within different regimes carefully accounting for the meteorological background. The findings of PACIFIC are crucial for assessing and improving the performance of climate models.

Mittelgeber: Bundesministerium für Bildung und Forschung (BMBF) und Deutscher Akademischer Austauschdienst (DAAD), MOPGA-GRI Senior Research Grant PACIFIC (57429422)

MAMiP – Mehrschichtige Arktische Mischphasenwolken: Beobachtungen
Multilayer Arctic Mixed-Phased Clouds: Observations (MAMiP:O)

Projektleiter: Dr. Matthias Tesche (matthias.tesche@uni-leipzig.de)

Projektmitarbeiterin: Dr. Peggy Achtert

Projektbeginn: 01.07.2021
Projektende: 30.06.2024

Beschreibung
Wolken spielen eine zentrale Rolle in der Kopplung der Atmosphäre mit der Erdoberfläche. Diese Verbindung wird durch den direkten Strahlungstransport im solaren und terrestrischen Wellenlängenbereich sowie den Austausch latenter Energie in der Form von Feuchteflüssen und Niederschlag hergestellt. Im Gegensatz zu anderen Orten auf der Erde können Wolken in der Arktis mit ihrer im Vergleich zur Erdoberfläche oft wärmeren Wolkenoberkante eine erwärmende Wirkung auf der Erdoberfläche ausüben. Der Fokus in der Untersuchung arktischer Wolken lag bisher auf sogenannten Einschichtwolken, welche sich in der Regel am Oberrand der planetaren Grenzschicht bilden. Wolken, die in einer anderen Höhe oder in mehreren Höhen gleichzeitig auftreten (Mehrschichtwolken), könnten allerdings einen Einfluss auf die Energiebilanz der Erdoberfläche ausüben, der sich von dem der umfangreich untersuchten Einschichtwolken unterscheidet. Dies hat mehrere Gründe: (i) den komplexen Strahlungstransport im Vergleich zu Einschichtwolken, (ii) der Einfluss oberer Wolken auf die diabatische Abkühlung darunter liegender Wolken und (iii) Eiskristalle, die aus oberen in die unteren Wolken fallen, können durch Eisimpfung die Wasserphase der unteren Wolken verändern und damit die Bildung von Mischphasenwolken im Temperaturbereich des heterogenen Gefrierens ermöglichen.
MAMiP:O strebt an die Lücken in unserem wissenschaftlichen Verständnis arktischer Mehrschichtwolken durch die systematische Auswertung von Fernerkundungsmessdaten zu schließen. Folgende Fragen sollen beantwortet werden:
1. Wie häufig treten Mehrschichtwolken im Vergleich zu Einschichtwolken auf?

2. Kann das Auftreten arktischer Einschicht- und Mehrschichtwolken aus aktiven und passiven Satellitenbeobachtungen abgeleitet werden?
3. Wie oft tritt Eiskristallimpfung in arktischen Mischphasenwolkensystemen auf?
4. Welche Faktoren bestimmen die Eiskristallimpfung? Lösen sich geimpfte Wolken auf oder verdicken sie sich?

Description:
Arctic clouds with their warm cloud tops (compared to the surface) can have a warming effect on the atmosphere. So far, studies of Arctic clouds have focussed on single-layer clouds, which form at boundary layer top. The radiative effect of clouds that occur at multiple heights simultaneously (multi-layer clouds) can be very different from that of single-layer clouds. This is because of (i) more complex radiative transport, (ii) adiabatic cooling of lower clouds, and (iii) glaciation of lower clouds as a result of ice-crystal seeding from upper cloud layers.
MAMiP will address gaps in our scientific understanding of Arctic multi-layer clouds through four questions:
1. What is the occurrence rate of Arctic multi-layer clouds compared to single-layer clouds?
2. What is the occurrence rate of ice-crystal seeding in Arctic multi-layer clouds?
3. Can simulations of Arctic multi-layer clouds with cloud-resolving models reproduce observations and provide insight into the dominating processes?
4. Which factors determine ice-crystal seeding? What happens to seeded clouds?

MAMiP:O will analyse observations beyond the MOSAiC data set. In MAMiP:M, the observed cases will be simulated with a cloud-resolving model to investigate the connection between radiative and microphysical processes, the predictability of multi-layer clouds, and their effect on the radiative budget at the surface.

Mittelgeber: Bundesministerium für Bildung und Forschung (BMBF), Förderkennzeichen 03F0891A

Maximilian Maahn
AG drOPS - clouD and pRecipitation Observations for Process Studies

---

Charakterisierung der räumlichen Variabilität von Eiswassergehalt in und unter Mischphasenwolken (B08)
Characterising the spatial variability of ice water content in and below mixed-phase clouds (B08)

Schlagworte: Arktischer Klimawandel, Fernerkundung, Mischphasenwolken

Projektleiter: Maximilian Maahn, Universität Leipzig (maximilian.maahn@uni-leipzig.de)

Projektmitarbeiterin: Nina Maherndl (nina.maherndl@uni-leipzig.de)

Projektbeginn: 1.1.2021

Projektende: 31.12.2023

Beschreibung
Die Prozesse, die die räumliche Variabilität des Eiswassergehalts (IWG) in Mischphasenwolken (MPW) bestimmen, sind nicht ausreichend erforscht. Deswegen wird ein Forschungsprojekt vorgeschlagen, welches sich explizit dem Verständnis und der Quantifizierung dieser Prozesse widmet. Es ist zwar eine Herausforderung, diese MPW Prozesse direkt zu beobachten, jedoch können Fingerabdrücke der dominierenden MPW Prozesse in verbesserten Flugzeugbeobachtungen von IWG und Schneefallrate (SR) identifiziert werden. Dafür werden Beobachtungen verwendet, die während der ACLOUD Kampagne 2017 sowie weiteren (AC)3 Flugzeug Kampagnen gemacht wurden, bzw. die bei der für 2021 geplanten HALO-(AC)3 Kampagne gemacht werden. Bei ACLOUD und HALO-(AC)3 flogen bzw. fliegen mindestens zwei Flugzeuge in einer Tandemformation wodurch kollokierte in situ und Fernerkundungsmessungen zur Verfügung stehen. Auf Basis dieser seltenen Tandemdatensätze wird ein nahtloses Umkehr Verfahren (engl. Retrieval) entwickelt, welches auf der Bayesschen Optimal Estimation Theorie basiert: Die flugzeuggebundenen Fernerkundungs- und in situ Daten werden kombiniert, um die in situ Daten nicht nur für die Datenpunkte zu verwenden, an denen sie gemessen wurden, sondern für alle vom Radar erfassten Wolkenbereiche. Dafür wird ihr Gewicht im Umkehr Verfahren proportional zum Abstand zwischen Radar und in situ Messung unter Berücksichtigung der Autokorrelationslängen der gemessenen Parameter gewählt. Dadurch kann berücksichtigt werden, wie sich der Informationsgehalt der in situ Messungen mit zunehmendem Abstand verringert. So können alle verfügbaren Informationen kombiniert werden und die vertikale und horizontale Variabilität von IWG und SR in und unter Wolken kann mit hoher räumlicher Auflösung bestmöglich bestimmt werden. Basierend auf den verbesserten Beobachtungsverfahren wird die beobachtete IWG Variabilität mit andern Mikro- und Makrophysikalischen Wolkeneigenschaften (z.B. dominierender Eispartikelwachstumsprozess, Wolkentyp, Flüssigwassergehalt, Wolkendicke, Variabilität von Wolkenphase an der Wolkenoberseite, turbulente Koppelung mit der Oberfläche) verknüpft. Ein besonderer Fokus wird auf die vertikale IWG Variabilität und den daraus resultierenden Einfluss auf die Massenflüsse von Eiskristallen gelegt. Dafür kann man nicht nur auf die umfangreichen Flugzeugmessungen zurückgreifen, sondern auch auf die bodengebundenen Beobachtungen in Ny-Ålesund und von der PASCAL Kampagne. Dadurch werden nicht nur die Prozesse identifiziert, die für die Quellen und Senken von IWG in der Atmosphäre am wichtigsten sind, sondern auch auf welchen räumlichen Skalen diese Prozesse aktiv sind. Simulationen mit dem ICON-LEM Atmosphärenmodel werden analysiert, um Unterschiede in der Darstellung von IWG zu identifizieren. Durch Anwendung der gleichen mikro- und makrophysikalischen Wolkenklassifikationen wie bei den Beobachtungen werden die Modellparametrisierungen identifiziert, die verbessert werden müssen.

Description
The processes determining spatial variability of ice water content (IWC) in mixed-phase clouds (MPCs) are not sufficiently understood. Therefore, we propose a project targeted at understanding and quantifying these processes. While it is challenging to observe MPC processes directly, we will advance techniques for quantifying IWC and snowfall rate (SR) with low uncertainty from airborne radar measurements so that we are able to observe fingerprints of the dominating processes. We will use data collected during the (AC)3 aircraft campaigns with a particular focus on the ACLOUD campaign performed in 2017, and the upcoming HALO-(AC)3 campaign planned within the current phase of (AC)3. For these campaigns, at least two closely collocated aircraft are flying in formation for obtaining collocated in situ and remote sensing observations. We will use these rare data

collected during tandem flights to develop a seamless Bayesian Optimal Estimation retrieval for obtaining IWC and SR from combined radar and in situ measurements along a flight track 'curtain'. We will develop a novel retrieval approach where the in situ data are exploited not only for the observation point where they were obtained, but for the whole curtain by scaling their weight proportional to the autocorrelation lengths of the microphysical properties. By this, we can consider how the information content of the in situ instruments is reduced with increasing distance between in situ and remote sensing observation volume. Such a retrieval can combine all available information from radar and in situ observations and will close an important gap in our ability to observe the vertical and horizontal spatial variability of IWC in clouds with high accuracy and high spatial resolution. Based on the improved observations, we will link the observed IWC variability to other microphysical and macrophysical cloud properties (among others, dominating particle growth process, cloud type, liquid water content, cloud depth, cloud top phase variability, surface coupling). A particular emphasis will be put on vertical IWC variability and the resulting impact on precipitation mass fluxes. For this, we can rely on the extensive supporting aircraft data sets, but also on ground-based observations in Ny-Ålesund and during the PASCAL campaign. By this, we will identify the processes most relevant for IWC sources and sinks as well as the spatial scales on which these processes are active. Model simulations using ICON-LEM will be analysed for quantifying differences in the representation of IWC. By comparing to the same microphysical and macrophysical cloud classifications used for the observations, we will identify which model MPCs parameterisations need to be improved.

Mittelgeber: Deutsche Forschungsgemeinschaft (DFG) TRR 172 (AC)^3

Publikationen
LIM 2021

Autor Name	Vorname	weitere Autoren	Titel	ID, DOI Publikationsort
Amarillo	A.	Carreras, H. A., **Krisna, T.**, Mignola, M., Busso, I. T., **Wendisch, M.**	Exploratory analysis of carbonaceous PM2.5 species in urban environments: Relationship with meteorological variables and satellite data	doi: 10.1016/j.atmosenv.2020.117987 Atmos. Environm. 245, 117987 (2021)
Braga	R. C.	Ervens, B., Rosenfeld, D., Andreae, M. O., Förster, J.-D., Fütterer, D., Hernández Pardo, L., Holanda, B. A., Jurkat-Witschas, T., Krüger, O. O., Lauer, O., Machado, L. A. T., Pöhlker, C., Sauer, D., Voigt, C., Walser, A., **Wendisch, M.**, Pöschl, U., and Pöhlker, M. L.	Cloud droplet formation at the base of tropical convective clouds: closure between modeling and measurement results of ACRIDICON–CHUVA	doi: 10.5194/acp-21-17513-2021 Atmos. Chem. Phys., 21, 17513–17528 (2021)
Braga	R. C.	Rosenfeld, D., Krüger, O. O., Ervens, B., Holanda, B. A., **Wendisch, M.**, **Krisna, T.**, Pöschl, U., Andreae, M. O., Voigt, C., and Pöhlker, M. L.	Linear relationship between effective radius and precipitation water content near the top of convective clouds: measurement results from ACRIDICON–CHUVA campaign	doi: 10.5194/acp-21-14079-2021 Atmos. Chem. Phys., 21, 14079–14088 (2021)
Egerer	Ulrike	**Ehrlich, A.**, **Gottschalk, M.**, Neggers, R. A. J., Siebert, H., and **Wendisch, M.**	Case study of a humidity layer above Arctic stratocumulus and potential turbulent coupling with the cloud top	doi: 10.5194/acp-21-6347-2021 Atmos. Chem. Phys., 21, 6347–6364 (2021)
Foth	**Andreas**	Zimmer, J., **Lauermann, F.,** and **Kalesse-Los, H.**	Evaluation of micro rain radar-based precipitation classification algorithms to discriminate between stratiform	doi: 10.5194/amt-14-4565-2021 Atmos. Meas. Tech., 14, 4565-4574 (2021)

			and convective precipitation	
Geet	George	Stevens, B., Bony, S., Pincus, R., Fairall, C., Schulz, H., Kölling, T., Kalen, Q. T., **Klingebiel, M.**, Konow, H., Lundry, A., Prange, M., and Radtke, J.	JOANNE: Joint dropsonde Observations of the Atmosphere in tropical North atlaNtic meso-scale Environments	doi: essd-13-5253-2021 Earth Syst. Sci. Data, 13, 5253–5272 (2021)
Geet	George	Stevens, B., Bony, S., **Klingebiel, M.**, and Vogel, R.	Observed Impact of Mesoscale Vertical Motion on Cloudiness	doi: 10.1175/JAS-D-20-0335.1 J. Atmos. Sci., 78(8), 2413-2427 (2021)
Herber	A.	**Becker, S.** , Belter, H. J. , Brauchle, J. , **Ehrlich, A. , Klingebiel, M.** , Krumpen, T. , Lüpkes, C., Mech, M. , Moser, M. and **Wendisch, M.**	MOSAiC Expedition: Airborne Surveys with Research Aircraft POLAR 5 and POLAR 6 in 2020	doi: 10.48433/BzPM_0754_2021 Berichte zur Polar- und Meeresforschung = Reports on polar and marine research, Bremerhaven, Alfred Wegener Institute for Polar and Marine Research, 754 , 99 p. (2021)
Hernández Pardo	Lianet	Machado, L. A. T., Morrison, H., Cecchini, M. A., Andreae, M. O., Pöhlker, C., Pöschl, U., Rosenfeld, D., Vendrasco, E. P., Voigt, C., **Wendisch, M.**, Pöhlker, M. L.	Observed and simulated variability of droplet spectral dispersion in convective clouds over the Amazon	doi: 10.1029/2021JD035076 J. Geophys. Res., 126, e2021JD035076 (2021)
Jäkel	**Evelyn**	Carlsen T., **Ehrlich A., Wendisch M.**, **Schäfer M.**, **Rosenburg S.**, Nakoudi K., Zanatta M., Birnbaum G., Helm V., Herber A., Istomina L., Mei L., Rohde A.	Measurements and Modeling of Optical-Equivalent Snow Grain Sizes under Arctic Low-Sun Conditions	doi: 10.3390/rs13234904 Remote Sensing, 13(23), 4904 (2021)
Konow	Heike	Ewald, F., George, G., Jacob, **M., Klingebiel**, M., Kölling, T., **Luebke, A. E.**, Mieslinger, T., Pörtge, V., Radtke, J., **Schäfer, M.**, Schulz, H., Vogel, R., Wirth, M., Bony, S., Crewell, S., **Ehrlich, A.**, Forster, L., Giez, A., Gödde, F., Groß, S., Gutleben, M., Hagen, M., Hirsch, L., Jansen, F., Lang, T., Mayer, B., Mech, M., Prange, M., Schnitt, S., Vial, J., Walbröl, A., **Wendisch, M.**, **Wolf, K.**, Zinner,	EUREC^{4}A's HALO	doi: 10.5194/essd-13-5545-2021 Earth Syst. Sci. Data, 13, 5545–5563 (2021)

		T., Zöger, M., Ament, F., and Stevens, B.		
Klingebiel	**Marcus**	Konow, H., and Stevens, B.	Measuring Shallow Convective Mass Flux Profiles in the Trade Wind Region	doi: 10.1175/JAS-D-20-0347.1 J. Atmos. Sci., 78(10), 3205-3214 (2021)
Mei	Linlu	Rozanov, V., **Jäkel, E.**, Cheng, X., Vountas, M., and Burrows, J. P.	The retrieval of snow properties from SLSTR Sentinel-3 – Part 2: Results and validation	doi: 10.5194/tc-15-2781-2021 The Cryosphere, 15, 2781–2802 (2021)
Siebert	Holger	Szodry, K.-E., Egerer, U., Wehner, B., Henning, S., Chevalier, K., Lückerath, J., Welz, O., Weinhold, K., **Lauermann, F.**, **Gottschalk, M.**, **Ehrlich, A.**, **Wendisch, M.**, Fialho, P., Roberts, P. F. G., Allwayin, N., Schum, S., Shaw, R. A., Mazzoleni, C., Mazzoleni, L., Nowak, J. L., Malinowski, S., Karpinska, K., Kumala, W., Czyzewska, D., Luke, E. P., Kollias, P., Wood, R., Mellado, J. P.	Observations of aerosol, cloud, turbulence, and radiation properties at the top of the marine boundary layer over the Eastern North Atlantic Ocean: The ACORES campaign	doi:10.1175/BAMS-D-19-0191.1 Bull. Am. Meteorol. Soc., 102, E123—E147 (2021)
Stapf	**Johannes**	**Ehrlich, A.**, and **Wendisch, M.**	Influence of thermodynamic state changes on surface cloud radiative forcing in the Arctic: a comparison of two approaches using data from AFLUX and SHEBA	doi: 10.1029/2020JD033589 J. Geophys. Res., 126, e2020JD033589 (2021)
Stevens	Bjorn	**Ehrlich, A., Klingebiel**, **M.**, **Röttenbacher, J., Schäfer**, **M., Wendisch**, **M., Wolf, K.**, **Schmidt, J.**, et al.	EUREC^{4}A	doi: 10.5194/essd-13-4067-2021 Earth Syst. Sci. Data, 13, 5253–5272 (2021)
Sun	Bin	**Schäfer, M.**, **Ehrlich, A.**, **Jäkel, E.**, and **Wendisch, M.**	Influence of atmospheric adjacency effect on top-of-atmosphere radiances and its correction in the retrieval of Lambertian surface reflectivity	doi:10.1016/j.rse.2021.112543 Rem. Sens. of Envir., 263, 112543 (2021)

			based on three-dimensional radiative transfer	
Tan	Ivy	Sotiropoulou, G., Taylor, P., Zamora, L., **Wendisch, M.**	A review of the factors influencing Arctic liquid-containing clouds: progress and outlook	doi: 10.1002/essoar.10508308.1 Earth and Space Science Open Archive, 54pp (2021)
Wendisch	**Manfred**	D. Handorf, I. Tegen, R. A. J. Neggers, and G. Spreen	Glimpsing the ins and outs of the Arctic atmospheric cauldron	doi: 10.1029/2021EO155959 Eos, 102 (2021)
He	Maosheng	Forbes, J.M., Li, G., **Jacobi, Ch.** und Hoffmann, P.	Mesospheric Q2DW interactions with four migrating tides at 53°N latitude: Zonal wavenumber identification through dual-station approaches	doi: 10.1029/2020GL092237 Geophys. Res. Lett., 48, e2020GL09223 (2021)
Karagodin-Doyennel	Arseniy	Rozanov, E., **Kuchar, A.**, Ball, W., Arsenovic, P., Remsberg, E., Jöckel, P., Kunze, M., Plummer, D. A., Stenke, A., Marsh, D., Kinnison, D. und Peter, T.	The response of mesospheric H_2O and CO to solar irradiance variability in models and observations}	doi: 10.5194/acp-21-201-2021 Atmos. Chem. Phys. 21, 201-216 (2021)
Jacob	**Christoph**	**Lilienthal, F**., Korotyshkin, D., Merzlyakov, E. und Stober, G.	Influence of geomagnetic disturbances on mean winds and tides in the mesosphere/lower thermosphere at midlatitudes	doi: 10.5194/ars-19-185-2021 Adv. Radio Sci., 19, 185–193 (2021)
Pedatella	Nicholas M.	Liu, H.-L., Conte, J. F., Chau, J. L., Hall, C., **Jacobi, Ch**., Mitchell, N. und Tsutsumi, M.	Migrating semidiurnal tide during the September equinox transition in the Northern Hemisphere	doi: 10.1029/2020JD033822 J. Geophys. Res. Atmos. 126, e2020JD033822 (2021)
Vaishnav	**Rajesh**	**Jacobi, Ch.**, Berdermann, J., Codrescu, M.,und Schmölter, E.	Role of eddy diffusion in the delayed ionospheric response to solar flux changes	doi: 10.5194/angeo-39-641-202 Ann. Geophys., 39, 641–655 (2021)

Vaishnav	**Rajesh**	Jin, Y., Mostafa, Md. G., Aziz, S. R., Zhang, S.-R. und **Jacobi, Ch.**	Study of the upper transition height using ISR observations and IRI predictions over Arecibo	doi: 10.1016/j.asr.2020.10.010 Adv. Space Res., 68, 2177-2185 (2021)
Vaishnav	**Rajesh**	Schmölter, E., **Jacobi, Ch.**, Berdermann, J. und Codrescu, M.	Ionospheric response to solar EUV radiation variations: Comparison based on CTIPe model simulations and satellite measurements	doi: 10.5194/angeo-39-341-2021 Ann. Geophys., 39, 341–355 (2021)
Merzlyakov	Eugeny	Korotyshkin , D., **Jacobi Ch.** und **Lilienthal, F.**	Long-period meteor radar temperature variations over Collm (51°N, 13°E) and Kazan (56°N, 49°E)	doi: 10.1016/j.asr.2021.02.014 Adv. Space Res., 67, 3250–3259 (2021)
Pisoft	**Petr**	Sacha, P., Polvani, L. M., Añel, J. A., de la Torre, L., Eichinger, R., Foelsche, U., Huszar, P., **Jacobi, Ch.**, Karlicky, J, **Kuchar, A.,** Miksovsky, J., Zak, M. und Rieder, H. E.	Stratospheric contraction caused by increasing greenhouse gases	doi: 10.1088/1748-9326/abfe2b Environ. Res. Lett. 16, 064038 (2021)
Šácha	Petr	**Kuchař, A.**, Eichinger, R., Pisoft, P., **Jacobi, Ch.** und Rieder, H. E.	Diverse dynamical response to orographic gravity wave drag hotspots - a zonal mean perspective	doi: 10.1029/2021GL093305 Geophys, Res. Lett., 48, e2021GL093305 (2021)
Stober	Gunter	**Kuchař, A.**, Pokhotelov, D., Liu, H., Liu, H.-L., Schmidt, H., **Jacobi, Ch.**, Baumgarten, K., Brown, P., Janches, D., Murphy, D., Kozlovsky, A., Lester, M., Belova, E., Kero, J. und Mitchell, N.	Interhemispheric differences of mesosphere-lower thermosphere winds and tides investigated from three whole-atmosphere models and meteor radar observations	doi: 10.5194/acp-21-13855-2021 Atmos. Chem. Phys., 21, 13855-13902 (2021)
Campbell-Brown	Margaret D.	Stober, G., **Jacobi, Ch.,** Kero, J., Kozlovsky, A. und Lester, M.	Radar observations of Draconid outbursts	doi: 10.1093/mnras/stab2174 Mon. Not. R. Astron. Soc., 57, 852–857 (2021)
Dipu	**Sudhakar**	**Quaas, J.**, Quaas, M., Rickels, W., **Mülmenstädt, J.** und Boucher, O.	Substantial Climate Response outside the Target Area in an Idealized Experiment of	doi: 10.3390/cli9040066 Climate,9, 66 (2021)

			Regional Radiation Management	
Jia	**Hailing**	Ma, X., Fangqun, Y. und Quaas, J.	Significant underestimation of radiative forcing by aerosol–cloud interactions derived from satellite-based methods	doi: 10.1038/s41467-021-23888-1 Nature Communications, 12, 3649 (2021)
Mülmenstädt	**Johannes**	**Salzmann, M.,** Kay, J. E., Zelinka, M. D., Ma, P.-L., **Nam, C.**, **Kretschmar, J.**, S. **Hörnig, S.** und **Quaas, J.**	An underestimated negative cloud feedback from cloud lifetime changes	doi: 10.1038/s41558-021-01038-1 Nat. Clim. Change, 11, 508–513 (2021)
Quaas	**Johannes**	Gryspeerdt, E., Vautard. R. und Boucher, O.	Climate impact of aircraft-induced cirrus assessed from satellite observations before and during COVID-19	doi: 10.1088/1748-9326/abf686 Environ. Res. Lett., 16, 064051 (2021)
Senf	Fabian	Tegen, I. und **Quaas, J.**	Absorbing aerosol decreases cloud cover in cloud-resolving simulations over Germany	doi: 10.1002/qj.4169 Quart. J. Roy. Meteorol. Soc., 147, 4083–4100 (2021)
Ansmann	Albert	Ohneiser, K., Mamouri, R.-E., Knopf, D. A., Veselovskii, I., Baars, H., Engelmann, R., **Foth, A.**, Jimenez, C., Seifert, P., Barja, B.	Tropospheric and stratospheric wildfire smoke profiling with lidar: mass, surface area, CCN, and INP retrieval	doi: 10.5194/acp-21-9779-2021 Atmos. Chem. Phys., 21, 9779–9807 (2021)
Foth	**Andreas**	Zimmer, J.**, Lauermann, F.** und **Kalesse-Los, H.**	Evaluation of micro rain radar-based precipitation classification algorithms to discriminate between stratiform and convective precipitation	doi: 10.5194/amt-14-4565-2021 Atmos. Meas. Tech., 14, 4565–4574 (2021)
Hartmann	Markus	Gong, X., Kecorius S., van Pinxteren, M. , **Vogl, T.,** Welti, A., Wex, H., Zeppenfeld, S., Herrmann, H., Wiedensohler, A. und Stratmann, F.	Terrestrial or marine – indications towards the origin of ice-nucleating particles during melt season in the European Arctic up to 83.7° N	doi: 10.5194/acp-21-11613-2021 Atmos. Chem. Phys., 21, 11613–11636 (2021)

Stephan	Claudia Christine	Schnitt, S., Schulz, H., Bellenger, H., de Szoeke, S. P., Acquistapace, C., Baier, K., Dauhut, T., Laxenaire, R., Morfa-Avalos, Y., Person, R., Quiñones Meléndez, E., Bagheri, G., Böck, T., Daley, A., Güttler, J., Helfer, K. C., Los, S. A., Neuberger, A., **Röttenbacher, J.**, Raeke, A., Ringel, M., Ritschel, M., Sadoulet, P., Schirmacher, I., Stolla, M. K., Wright, E., Charpentier, B., Doerenbecher, A., Wilson, R., Jansen, F., Kinne, S., Reverdin, G., Speich, S., Bony, S., and Stevens, B.	Ship- and island-based atmospheric soundings from the 2020 EUREC^{4}A field campaign	doi: 10.5194/essd-13-491-2021 Earth Syst. Sci. Data, 13, 491–514 (2021)
Trömel	Silke	Simmer, C., Blahak, U., Blanke, A., **Doktorowski, S.**, Ewald, F., Frech, M., Gergely, M., Hagen, M., Janjic, T., Kalesse-Los, H., Kneifel, S., Knote, C., Mendrok, J., Moser, M., Köcher, G., Mühlbauer, K., Myagkov, A., Pejcic, V., Seifert, P., Shrestha, P., Teisseire, A., von Terzi, L., Tetoni, E., **Vogl, T.**, Voigt, C., Zeng, Y., Zinner, T. und **Quaas, J.**	Overview: Fusion of radar polarimetry and numerical atmospheric modelling towards an improved understanding of cloud and precipitation processes	doi: 10.5194/acp-21-17291-2021 Atmos. Chem. Phys., 21, 17291–17314 (2021)
Vogl	**Teresa**	Hrdina, A., Thomas, C. K.	Choosing an optimal β factor for relaxed eddy accumulation applications across vegetated and non-vegetated surfaces	doi: 10.5194/bg-18-5097-2021 Biogeosciences, 18, 5097–5115 (2021)
Kezoudi	Maria	**Tesche, M.,** Smith, H., Tsekeri, A., Baars, H., Dollner, M., Estellés, V., Bühl, J., Weinzierl, B., Ulanowski, Z., Müller, D., and Amiridis, V.	Measurement report: Balloon-borne in situ profiling of Saharan dust over Cyprus with the {UCASS} optical particle counter	doi:10.5194/acp-21-6781-2021 Atmos. Chem. Phys., 21, 6781–6797 (2021)
Seelig	**Torsten**	Deneke, H., **Quaas, J.**, **Tesche, M.**	Life cycle of shallow marine cumulus clouds from geostationary satellite	doi: 10.1029/2021jd035577 J. Geophys. Res. Atmos., 126,

			observations	e2021JD035577 (2021)
Tesche	**Matthias**	Achtert, P. und Pitts, M.C.	On the best locations for ground-based polar stratospheric cloud (PSC) observations	doi:10.5194/acp-21-505-2021 Atmos. Chem. Phys., 21 ,505–516 (2021)
Tyagi	Bhishma	**Choudhury,** G., Vissa, N.K.,Singh, J., und **Tesche, M.**	Redefining the hotspot pollution regions over India by understanding the changed pollution scenario during COVID-19	doi: 10.1016/j.envpol.2020.116354 Environ. Pollut., 271, 116354 (2021)
Kulie	Mark S.	Pettersen, C., Merrelli, A. J., Wagner, T. J., Wood, N. B., Dutter, M., Beachler, D., Kluber, T., Turner, R., Mateling, M., Lenters, J., Blanken, P., **Maahn, M.**, Spence, C., Kneifel, S., Kucera, P. A., Tokay, A., Bliven, L. F., Wolff, D. B., and Petersen, W. A.	Snowfall in the Northern Great Lakes: Lessons learned from a multi-sensor observatory	doi: 10.1175/BAMS-D-19-0128.1 Bull. Amer. Meteor. Soc., 102, E1317–E1339 (2021)
Luke	Edward P.	Yang, F., Kollias, P.. Vogelmann, A. M. und **Maahn, M.**	New insights into ice multiplication using remote-sensing observations of slightly supercooled mixed-phase clouds in the Arctic	doi: 10.1073/pnas.2021387118 Proc. Natl. Acad. Sci. U.S.A., 118, e2021387118 (2021)
Maahn	**Maximilian**	Goren, T., Shupe, M. D., und de Boer, G.	Liquid containing clouds at the North Slope of Alaska demonstrate sensitivity to local industrial aerosol emissions	doi: 10.1029/2021GL094307 Geophys. Res. Lett., 48, e2021GL094307 (2021)
Raabe	**Armin**	Starke M. und Ziemann A.	Acoustic Tomography	in: Foken T. (ed.), Handbook of Atmospheric Measurements. Chapt. 35, 1093-1117, Springer (2021)
Raabe	**Armin**	und Holstein, P	Akustik und Raumklima	doi: 10.1007/978-3-658-33324-9

				Springer Fachmedien Wiesbaden
Rodrigues	Italo Sampaio	Gomes Costa, C. A., **Raabe A.**, Medeiros, P. H. A. und de Araújo, J. C.	Evaporation in Brazilian dryland reservoirs: Spatial variability and impact of riparian vegetation	doi: 10.1016/j.scitotenv.2021.149059 Sci. Total Environ., 797, 149059 (2021)

Gremium Mitgliedschaft

Prof. Dr. Manfred Wendisch:

Seit 2010	Koordinator des DFG-SPP (Schwerpunktprogramm) 1294 zu HALO (High Altitude and Long Range Research Aircraft), gemeinsam mit Prof. J. Curtius (Uni Frankfurt am Main) und Mirko Scheinert (TU Dresden)
Seit 2011	Ordentliches Mitglied der Sächsischen Akademie der Wissenschaften
Seit 2012	Gewähltes Mitglied im IRC (Internationale Strahlungskommission) innerhalb von IAMAS
Seit 2012	Vize-Sprecher der „Leibniz-Graduate School on Clouds, Aerosols, and Radiation (LGS-CAR)“
Seit 2015	Mitglied des Wissenschaftlichen Beirats des Deutschen Wetterdienstes (DWD)
Seit 2015	Mitglied des Programmrates des „Hans-Ertel-Zentrum für Wetterforschung (HErZ)“ des DWD
Seit 2016	Mitglied des Präsidiums der Sächsischen Akademie der Wissenschaften
Seit 2016	Stellvertretender Vorsitzender des Wissenschaftlichen Lenkungsausschuss (WLA) für HALO (High Altitude and Long Range Research Aircraft)
Seit 2016	Sprecher des Sonderforschungsbereiches SFB-Transregio 172: “Arktische Verstärkung: Klimarelevante Atmosphären- und Oberflächenprozesse, und Rückkopplungsmechanismen (AC)^3”
Seit 2016	Koordinator des YOPP (Year of Polar Prediction) Task Teams zu Flugzeuggetragenen Messplattformen
Seit 2017	Mitglied des Projekt-Kommittees für MOSAiC (**M**ultidisciplinary drifting **O**bservatory for the **S**tudy of **A**rct**i**c **C**limate), Team Koordinator für Flugzeugoperation
Seit 2017	Mitglied DFG-Senatskommission für Erdsystemforschung
Seit 2019	Mitglied der International Commission on Atmospheric Chemistry and Global Pollution, ICACGP, of the International Association of Meteorology and Atmospheric Science IAMAS. http://www.icacgp.org
Seit 2020	Mitglied des deutschen Nationalkomitees SCAR/IASC (Scientific Committee on Arctic Research / International Arctic Science Committee)
Seit 2020	Mitglied des Kuratoriums des Alfred-Wegener-Instituts, Helmholtz-Zentrum für Polar- und Meeresforschung (AWI)
Seit 2020	Mitglied im DFG Fachkollegium 313 «Atmosphären- und Klimaforschung» für das Fach 313-01 «Physik und Chemie der Atmosphäre», Stellvertretender Sprecher
Seit 2020	Vorsitzender des Wissenschaftlichen Beirats des Deutschen Wetterdienstes (DWD)
Seit 2020	Vize-Präsident IRC (Internationale Strahlungskommission) innerhalb von IAMAS
Seit 2021	Gewähltes Mitglied im Senat der Universität Leipzig

Prof. Dr. Christoph Jacobi:
Mitglied im Vorstand der Meteorologischen Gesellschaft, Sektion Mitteldeutschland
Leiter der Division II „Aeronomic Phenomena“ der IAGA
Leiter der Arbeitsgruppe II-D der IAGA: „External Forcing of the Middle Atmosphere“
Vorsitzender der Mitgliederversammlung des TROPOS

Prof. Dr. Johannes Quaas:
Lead Author, Intergovernmental Panel on Climate Change (IPCC), Working Group I, 6th Assessment Report

Vorsitz, Sektion Mitteldeutschland, Deutsche Meteorologische Gesellschaft
Mitglied im Fakultätsrat, Fakultät für Physik und Geowissenschaften
Mitglied im Wissenschaftlichen Beirat, Leibniz-Institut für Troposphärenforschung
Scientific Steering Committee, Aerosols-Clouds-Precipitation and Climate Initiative

Jun.-Prof. Dr. Heike Kalesse:
Deutsche Meteorologische Gesellschaft – DACH 2022 Programmkomittee

Dr. Maximilian Maahn:
Member ESA WIVERN (wind velocity radar nephoscope) Mission Advisory Group

Mitgliedschaften in Redaktionskollegien, Herausgebergremien

Prof. Dr. Manfred Wendisch:

Seit 2008	Ko-Editor “Journal on Atmospheric Measurement Techniques”
Seit 2019	Mitglied im Editorial Board des *Bulletin of the American Meteorological Society* (*BAMS*) (Subject Matter Editor for Aerosol and Cloud Physics)

Prof. Dr. Christoph Jacobi:

Annales Geophysicae	Editor-in-Chief
Mitteilungen der DMG	Mitglied Redaktionsteam

Prof. Dr. Johannes Quaas:
Atmospheric Chemistry and Physics

PD Dr. Matthias Tesche:

Atmos. Chem. Phys.	Co-Editor

Dr. Maximilian Maahn:
Associate Editor: Atmospheric Measurement Techniques

173

Mitarbeitende am LIM 2021

Name	E-Mail-Adresse
Alexandri, Fani	fani.alexandri@uni-leipzig.de
Becker, Sebastian	sebastian.becker@uni-leipzig.de
Block, Karoline	karoline.block@uni-leipzig.de
Bräuer, Peter	peter.braeuer@uni-leipzig.de
Brückner, Marlen	m.brueckner@uni-leipzig.de
Cherian, Ribu	ribu.cherian@uni-leipzig.de
Choudhury, Goutam	goutam.choudhury@uni-leipzig.de
Ehrlich, André	a.ehrlich@uni-leipzig.de
Foth, Andreas	andreas.foth@uni-leipzig.de
Gonzalez Villarreal, Jessenia	jessenia.gonzalesv@uni-leipzig.de
Goren, Tom	tom.goren@uni-leipzig.de
Haghighatnasab, Mahnoosh	mahnoosh.haghighatnasab@uni-leipzig.de
Hörnig, Sabine	sabine.hoernig@uni-leipzig.de
Jacobi, Christoph	jacobi@rz.uni-leipzig.de
Jäkel, Evelyn	evi.jaekel@uni-leipzig.de
Jia, Hailing	hailing.jia@uni-leipzig.de
Kaiser, Falk	fkaiser@rz.uni-leipzig.de
Kalesse-Los, Heike	heike.kalesse@uni-leipzig.de
Kandieva, Kanykei	Kanykei.Kandieva@uni-leipzig.de
Karami, Khalil	khalil.karami@uni-leipzig.de
Kirbus, Benjamin	benjamin.kirbus@uni-leipzig.de
Klingebiel, Marcus	marcus.klingebiel@uni-leipzig.de
Kretzschmar, Jan	jan.kretzschmar@uni-leipzig.de
Kuchar, Ales	ales.kuchar@uni-leipzig
Kwakye, Samuel	samuel.kwakye@uni-leipzig.de
Lenhardt, Julien	julien.lenhardt@uni-leipzig.de
Lindemann, Simone	simone.lindemann@uni-leipzig.de
Linke, Olivia	olivia.linke@uni-leipzig.de
Lochmann, Moritz	moritz.lochmann@uni-leipzig.de
Lonardi, Michael	michael.lonardi@uni-leipzig.de
Luebke, Anna	anna.luebke@uni-leipzig.de
Maahn, Maximilian	maximilian.maahn@uni-leipzig.de
Maherndl, Nina	nina.maherndl@uni-leipzig.de
Marjani, Sajadeh	sajedeh.Marjani@uni-leipzig.de
Mehrdad, Sina	sina.mehrdad@uni-leipzig.de
Metzner, Enrico	enrico.metzner@uni-leipzig.de
Müller, Felix	felix.mueller.2@uni-leipzig.de

Müller, Hanno	hanno.mueller@uni-leipzig.de
Papakonstantinou-Presvelo, Iris	i.presvelou@uni-leipzig.de
Quaas, Johannes	johannes.quaas@uni-leipzig.de
Rehnert, Jutta	rehnert@uni-leipzig.de
Röttenbacher, Johannes	johannes.roettenbacher@uni-leipzig.de
Saavedra Garfias, Pablo	pablo.saavedra@uni-leipzig.de
Salzmann, Marc	marc.salzmann@uni-leipzig.de
Schäfer, Michael	michael.schaefer@uni-leipzig.de
Schandert, Katrin	schandrt@rz.uni-leipzig.de
Schimmel, Willi	willi.schimmel@uni-leipzig.de
Schmidt, Jörg	joerg.schmidt@uni-leipzig.de
Schwarz, Anja	anja.schwarz@uni-leipzig.de
Seelig, Torsten	torsten.seelig@uni-leipzig.de
Seydel, Birgit	birgit.seydel@uni-leipzig.de
Sperzel, Tim Robert	tim.sperzel@uni-leipzig.de
Sudhakar, Dipu	dipu.sudhakar@uni-leipzig.de
Tesche, Matthias	matthias.tesche@uni-leipzig.de
Tesche-Achtert, Peggy	peggy.achtert@uni-leipzig.de
Vaishnav, Rajesh Ishwardas	rajesh_ishwardas.vaishnav@uni-leipzig.de
Vogl, Teresa	teresa.vogl@uni-leipzig.de
Wendisch, Manfred	m.wendisch@uni-leipzig.de
Wolter, Steffen	steffen.wolter@uni-leipzig,de

Anzahl der Studierenden am Institut für Meteorologie

Bachelor of Science Meteorologie

Datum	Semester	1.FS	2. FS	3.FS	4.FS	5.FS	6. FS	7.FS	8.FS	9. FS	10.FS	>10.FS	gesamt
15.10.21	WS 20/21	40	0	27	0	24	4	12	0	4	1	0	112
15.10.20	WS 20/21	34	1	32	7	21	0	9	2	2		1	109
15.10.19	WS 19/20	58		17		12		9					96
15.10.18	WS 18/19	48		14		9		5					76
15.10.17	WS 17/18	37		17		7		5					66
15.10.16	WS 16/17	48		7		5		3					63
15.10.15	WS 15/16	35		5		9		3					52
15.10.14	WS 14/15	35		14		15		3		3		1	71
15.10.13	WS 13/14	39		23		21		13		4			100
15.10.12	WS 12/13	60		29	1	22	2	16	1	2			133
15.10.11	WS 11/12	60		27		26	1	19		1			134
15.10.10	WS 10/11	64		34		20							118
15.10.09	WS 09/10	67	0	21	0	20	0						108
15.10.08	WS 08/09	71	0	28	0	12							111
15.10.07	WS 07/08	98	0	15									113
13.12.06	WS 06/07	31											31

Master of Science Meteorologie

Datum	Semester	1.FS	2. FS	3.FS	4.FS	5.FS	6. FS	gesamt
15.10.21	WS20/21	8	0	13	0	0	0	21
15.10.20	WS20/21	14	4	6	1	3	1	29
15.10.19	WS 19/20	9		5		5		19
15.10.18	WS18/19	5		5		9		19
15.10.17	WS 17/18	5		9		10		24
15.10.16	WS 16/17	9		13		17		39
15.10.15	WS 15/16	13		19		18		50
15.10.14	WS 14/15	19		18		16		53
15.10.13	WS 13/14	18		16		20		54
15.10.12	WS 12/13	18		20	1	15		54
15.10.11	WS 11/12	21		17		10		48
15.10.10	WS 10/11	20		9		5		34
15.10.09	WS 09/10	11						11

Ausbildung Diplom-Meteorologie beendet

Diplom Meteorologie													
Datum	Semester	1.FS	2. FS	3.FS	4.FS	5.FS	6. FS	7.FS	8.FS	9. FS	10.FS	>10.FS	Meteo_Diplom
15.10.2013	WS 13/14											2	2
17.10.2012	WS 12/13											3	3
16.10.2011	WS 11/12											3	3
15.10.2010	WS 10/11											14	14
15.10.2009	WS 09/10								0	14	0	7	21
15.10.2008	WS 08/09						0	14	0	23	1	25	63
15.10.2007	WS 07/08				0	22	0	26	1	18	2	19	88
13.12.2006	WS 06/07		0	40	0	36	0	24	2	14	1	17	175
15.10.2005	WS 05/06	109	0	49	0	30	2	16	1	17	1	13	237
08.12.2004	WS 04/05	97	0	35	1	20	0	19	0	12	1	15	200
03.12.2003	WS 03/04	68	1	25	0	20	1	13	1	12	1	13	155
14.10.2002	WS 02/03	45	0	19	0	16	0	15	1	12	1	9	118
06.12.2001	WS 01/02	43	0	21	0	16	0	13	0	7	0	5	105
07.12.2000	WS 00/01	41	1	27	0	22	0	8	0	6	1	6	112
01.12.1999	WS 99/00	40	0	24	0	9	0	9	0	6	1	6	95
16.12.1998	WS 98/99	36	0	11	0	17	1	9	1	5	0	8	88
10.11.1997	WS 97/98	29	0	17	0	10	1	8	0	7	0	4	76

Abschlussarbeiten Institut für Meteorologie 2021

Bachelorarbeiten 2021

Gebauer, Henriette: Statistische Analyse der urbanen Konvektionseffizienz auf Quartiersebene und daraus abgeleiteter Empfehlungen zur Anpassung an den Klimawandel

Wetzel, Bruno: Untersuchung zur Bestimmung der Konzentration, Eigenschaften und Quellen arktischer Eiskeime

Al Hajjar, Mohamed Khaled: Fallstudie: Analyse arktischer Warmlufteinschübe Mitte April 2020 am Forschungsschiff Polarstern im Bezug auf den Langstrecken-Transport von Feuchtigkeit

Bischay, Julian: Analyse von Wolkenprodukten aus passiven Messungen anhand simulierter EarthCARE-Daten

Federau, Meike: Statistische Analyse von extremen Niederschlagsereignissen mit einer Kombination von Wolkenradar und Distrometer

Gaudeck, Tom: Is there a difference in the cloud top temperature of Arctic low-level clouds in single-layer and multi-layer systems?

Seiffert, Hennes: Analyse der vertikalen Veränderung des Niederschlags in Leipzig

Stöckel, Willy: Bestimmung des Bodenwärmestroms in Gründächern

Walter, Gregor Anton: Stratospheric smoke layers in the Nothern and Southern Hemisphere: Impact of pyrocumulonimbus convection and self-lifting effects

Lipken, Friederike: Strahlungseffekte des Brandaerosols während der extremen arktischen Wald- und Fläachenbrände der Jahre 2019 und 2020

Masterarbeiten 2021

Röttenbacher, Johannes: Further developement of an algorithm to determine cirrus cloud dynamics

Martin, Anna: Determination of radiation couplings in climate change simulations: Analysis with two different linearization methods

Promotionen 2021

Geißler, Christoph: Quarterdiurnal tide in the middle atmosphere

Egerer, Ulrike: A new set of tethered balloon-borne instrument payloads for collocated turbulence and radiation measurements in the cloudy Arctic boundary layer - first applications

Kretzschmar, Jan: Improving the representation of Arctic clouds in atmospheric models across scales using observations
Mewes, Daniel: Large-scale Horizontal energy fluxes into the Arctic analyzed using self-organizing maps

Ruiz Donoso, Elena: Small-scale structure of thermodynamic phase in Arctic mixed-phase clouds observed with airborne remote sensing during the ACLOUD campaign

Schacht, Jacob: Black carbon aerosol in the Arctic: Ageing, transport and radiative effects

Santiago Villanueva Ortiz, Diego: A story of dust and ice --- constraining dust-driven immersion freezing in climate models using spaceborne retrievals

Hartmann, Markus: Ice nucleating particles in the Arctic - A story of their abundance, properties and possible origin from the Little Ice Age to the current age of unpreceded Arctic warming

Stieger, Bastian Andreas: Highly time-resolved and long-time quantification of inorganics and low-molecular-weight organic acids in the gas and particle phases at the research station Melpitz

Sun, Jia: Temporal and spatial variability of black carbon mass concentrations and size-resolved particle number concentrations in Germany ranging from city street to high Alpine environments

Ishwardas Vaishnav, Rajesh: Delayed ionospheric response to solar EUV/UV radiation variations

Zhao, Jiangyue: Particle exposure in German dwellings: Particle number and mass size distributions, indoor particle dynamics, and source apportionment

Wissenschaftliche Mitteilungen aus dem Institut für Meteorologie der Universität Leipzig

Band 1	*A. Raabe, G. Tetzlaff* und *W. Metz* (Edn.), 1995: Meteorologische Arbeiten aus Leipzig I
Band 2	*R. Devantier*, 1995: Wolkenbildungsprozesse über der südwestlichen Ostsee - Anwendungen eines neuen Wolkenschemas in einem mesoskaligen Modell
Band 3	*J. Laubach*, 1996: Charakterisierung des turbulenten Austausches von Wärme, Wasserdampf und Kohlendioxid über niedriger Vegetation anhand von Eddy-Korrelations-Messungen
Band 4	*A. Raabe* und *J. Heintzenberg* (Edn.), 1996: Meteorologische Arbeiten aus Leipzig II
Band 5	Wind- und Seegangsatlas für das Gebiet um Darß und Zingst *D. Hinneburg, A. Raabe* und *G. Tetzlaff*, 1997: Teil I: Windatlas
Band 6	*W. von Hoyningen-Huene* und *G. Tetzlaff* (Edn.), 1997: Sediment and Aerosol Teil I: Beiträge zur Alfred-Wegener-Konferenz, Leipzig 1997 Teil II: Aktuelle Beiträge aus dem Institut für Meteorologie
Band 7	*B.-R. Beckmann*, 1997: Veränderungen in der Windklimatologie und in der Häufigkeit von Sturmhochwassern an der Ostseeküste Mecklenburg-Vorpommerns
Band 8	*P. Posse*, 1997: Bestimmung klimarelevanter Parameter des maritimen Aerosols unter besonderer Berücksichtigung der Nichtkugelform realer Aerosolteilchen
Band 9	*A. Raabe, K. Arnold* und *J. Heintzenberg* (Edn.),1998: Meteorologische Arbeiten aus Leipzig III
Band 10	Wind- und Seegangsatlas für das Gebiet um Darß und Zingst, Teil II, 1998: *D. Hinneburg, A. Raabe* und *G. Tetzlaff*: Vergleich Windatlas –Beobachtungsdaten; *M. Börngen, H.-J. Schönfeldt, F. Riechmann, G. Panin* und *G. Tetzlaff*: Seegangsatlas; *M. Stephan* und *H.-J. Schönfeldt*: Sedimenttransportatlas
Band 11	*J. Rissmann, 1998*: Der Einfluss langwelliger Strahlungsprozesse auf das bodennahe Temperaturprofil
Band 12	*A. Raabe, K. Arnold* und *J. Heintzenberg* (Edn.), 1999:Meteorologische Arbeiten aus Leipzig IV
Band 13	*U. Müller, W. Kuttler und G. Tetzlaff (Edn.)*, 1999: Workshop Stadtklima 17. / 18. 02. 1999 in Leipzig
Band 14	*R. Surkow, 1999*: Optimierung der Leistungsverfügbarkeit von Windenergie durch ihre Integration in Wind-Biogas-Hybridanlagen
Band 15	*N. Mölders*, 1999: Einfache und akkumulierte Landnutzungsänderungen und ihre Auswirkungen auf Evapotranspiration, Wolken- und Niederschlagsbildung
Band 16	G. Tetzlaff und U. Grünewald (Edn.), 1999:2. Tagung des Fachausschusses Hydrometeorologie 15./16. 11. 1999 in Leipzig
Band 17	A. Raabe und K. Arnold (Edn.), 2000: Meteorologische Arbeiten aus Leipzig V
Band 18	K. Arnold, 2000: Ein experimentelles Verfahren zur Akustischen Tomographie im Bereich der atmosphärischen Grenzschicht
Band 19	*A. Ziemann*, 2000: Eine theoretische Studie zur akustischen Tomographie in der atmosphärischen Grenzschicht
Band 20	*Ch. Jacobi*, 2000: Midlatitude mesopause region dynamics and its coupling with lower and middle atmospheric processes
Band 21	*M. Klingspohn*, 2000: Interdekadische Klimavariabilität über dem Nordatlantik – Statistische Analysen und Modellstudien –
Band 22	*A. Raabe* und *K. Arnold* (Edn.), 2001: Meteorologische Arbeiten aus Leipzig VI
Band 23	*K. Arnold, A. Ziemann, G. Tetzlaff, V. Mellert* und *A. Raabe* (Edn.), 2001: International Workshop Tomography and Acoustics: Recent developments and methods 06. - 07.03.2001 in Leipzig
Band 24	*O. Fanenbruck*, 2001: Ein thermophysiologisches Bewertungsmodell mit Anwendung auf das Leipziger Stadtgebiet
Band 25	*M. Lange*, 2001: Modellstudien zum CO_2-Anstieg und O_3-Abbau in der mittleren Atmosphäre und Einfluss des Polarwirbels auf die zonale Symmetrie des Windfeldes in der Mesopausenregion
Band 26	*A. Raabe* und *K. Arnold* (Edn.), 2002: Meteorologische Arbeiten aus Leipzig VII
Band 27	*M. Simmel*, 2002: Ein Modul zur spektralen Beschreibung von Wolken und Niederschlag in einem Mesoskalenmodell zur Verwendung auf Parallelrechnern
Band 28	*H. Siebert*, 2002: Tethered-Balloon Borne Turbulence Measurements in the Cloudy Boundary Layer
Sonderband	*G. Tetzlaff* (Hrsg.), 2002:- Atmosphäre - Aktuelle Beiträge zu Luft, Ozon, Sturm, Starkregen und Klima
Band 29	*U. Harlander*, 2003: On Rossby wave propagation in atmosphere and ocean
Band 30	*A. Raabe* und *K. Arnold* (Edn.), 2003: Meteorologische Arbeiten aus Leipzig VIII
Band 31	*M. Wendisch*, 2003: Absorption of Solar Radiation in the Cloudless and Cloudy Atmosphere
Band 32	*U. Schlink*, 2003: Longitudinal Models in Biometeorology: Effect Assessment and Forecasting of Ground-level Ozone
Band 33	*H. Heinrich*, 2004: Finite barotrope Instabilität unter synoptischem Antrieb
Band 34	*A. Raabe* und *K. Arnold* (Edn.), 2004: Meteorologische Arbeiten aus Leipzig IX

Band 35 *C. Stolle*, 2004: Three-dimensional imaging of ionospheric electron density fields using GPS observations at the ground and on board the CHAMP satellite

Band 36 *A. Raabe* und *K. Arnold* (Edn.), 2005: Meteorologische Arbeiten (X) und Jahresbericht 2004 des Institutes für Meteorologie der Universität Leipzig

Band 37 *A. Raabe* und *K. Arnold* (Edn.), 2006: Meteorologische Arbeiten (XI) und Jahresbericht 2005 des Institutes für Meteorologie der Universität Leipzig

Band 38 *K. Fröhlich*, 2006: The Quasi Two-Day Wave – its impact on zonal mean circulation and wave-wave interactions in the middle atmosphere

Band 39 *K. Radtke, 2006: Zur Sensitivität von Starkwindfeldern gegenüber verschiedenen meteorologischen Parametern im Mesoskalenmodell LM*

Band 40 K. Hungershöfer, *2007: Optical Properties of Aerosol Particles and Radiative Transfer in Connection with Biomass Burning*

Band 41 *A. Raabe* (Hrsg.), 2007: Meteorologische Arbeiten (XII) und Jahresbericht 2006 des Institutes für Meteorologie der Universität Leipzig

Band 42 *A. Raabe* (Hrsg.), 2008: Meteorologische Arbeiten (XIII) und Jahresbericht 2007 des Institutes für Meteorologie der Universität Leipzig

Band 43 *A. Kniffka, 2008*: Einfluss der Inhomogenitäten von Aerosol, Bodenalbedo und Wolken auf das aktinische Strahlungsfeld der Atmosphäre

Band 44 *M. Barth, 2009*: Akustische Tomographie zur zeitgleichen Erfassung von Temperatur- und Strömungsfeldern

Band 45 *A. Raabe* (Hrsg.), 2009: Meteorologische Arbeiten (XIV) und Jahresbericht 2008 des Institutes für Meteorologie der Universität Leipzig

Band 46 *G. Stober, 2009:* Astrophysical Studies on Meteors using a SKiYMET All-Sky Meteor Radar

Band 47 *A. Raabe* (Hrsg.), 2010: Meteorologische Arbeiten (XV) und Jahresbericht 2009 des Institutes für Meteorologie der Universität Leipzig

Band 48 *A. Raabe* (Hrsg.), 2011: Meteorologische Arbeiten (XVI) und Jahresbericht 2010 des Institutes für Meteorologie der Universität Leipzig

Band 49 *A. Raabe* (Hrsg.), 2012: METTOOLS_VIII Tagungsband

Band 50 *A. Raabe* (Hrsg.), 2012: Meteorologische Arbeiten (XVII) und Jahresbericht 2011 des Institutes für Meteorologie der Universität Leipzig

Band 51 *A. Raabe* (Hrsg.), 2013: Meteorologische Arbeiten (XVIII) und Jahresbericht 2012 des Institutes für Meteorologie der Universität Leipzig

Band 52 A. Raabe (Hrsg.), 2014: Meteorologische Arbeiten (XIX) und Jahresbericht 2013 des Institutes für Meteorologie der Universität Leipzig

Band 53 *A. Raabe* (Hrsg.), 2015: Meteorologische Arbeiten (XX) und Jahresbericht 2014 des Institutes für Meteorologie der Universität Leipzig

Band 54 *A. Raabe* (Hrsg.), 2016: Meteorologische Arbeiten (XXI) und Jahresbericht 2015 des Institutes für Meteorologie der Universität Leipzig

Band 55 *A. Raabe, M.Wendisch* (Hrsg.), 2017: Meteorologische Arbeiten (XXII) und Jahresbericht 2016 des Institutes für Meteorologie der Universität Leipzig

Band 56 *A. Raabe, M.Wendisch* (Hrsg.), 2018: Meteorologische Arbeiten (XXIII) und Jahresbericht 2017 des Institutes für Meteorologie der Universität Leipzig

Band 57 *A. Raabe, M.Wendisch* (Hrsg.), 2019: Meteorologische Arbeiten (XXIV) und Jahresbericht 2018 des Institutes für Meteorologie der Universität Leipzig

Band 58 *M.Wendisch* (Hrsg.), 2020: Meteorologische Arbeiten (XXV) und Jahresbericht 2019 des Institutes für Meteorologie der Universität Leipzig

Band 59 *M.Wendisch* (Hrsg.), 2021: Meteorologische Arbeiten (XXVI) und Jahresbericht 2020 des Institutes für Meteorologie der Universität Leipzig

Band 60 M.Wendisch (Hrsg.), 2022: Meteorologische Arbeiten (XXVII) und Jahresbericht 2021 des Institutes für Meteorologie der Universität Leipzig

Wissenschaftliche Mitteilungen aus dem Institut für Meteorologie der Universität Leipzig

Band 60 (2022):

Meteorologische Arbeiten XXVII
Jahresbericht 2021

ISBN 978-3-9823985-0-1

Die einzelnen Beiträge dieses Heftes wurden in einem internen Verfahren begutachtet

Abbildung auf Umschlag

Institutsgebäude – Leipziger Institut f. Meteorologie (LIM)

Herausgegeben im Selbstverlag:
Institut für Meteorologie, Universität Leipzig

Herausgeber:
M. Wendisch

Bestellungen richten Sie bitte an:

Institut für Meteorologie, Universität Leipzig
Stephanstr. 3
D-04103 Leipzig

Tel: 0341 - 9732850
Fax: 0341 - 9732899
E-Mail: birgit.seydel@uni-leipzig.de
Preis pro Band: 20,– €